UNIVERSIDADE FEDERAL DE SANTA CATARINA
CAMPUS FLORIANÓPOLIS
PROGRAMA DE PÓS-GRADUAÇÃO EM ENGENHARIA MECÂNICA

KELVIN GUESSI DOMICIANO

THEORETICAL AND EXPERIMENTAL ANALYSIS OF A DIFFUSION BONDED ULTRA-THIN COPPER LOOP HEAT PIPE

FLORIANÓPOLIS
2021

Kelvin Guessi Domiciano

Theoretical and experimental analysis of a diffusion bonded ultra-thin copper loop heat pipe

Dissertação submetida ao Programa de pós-graduação em Engenharia Mecânica da Universidade Federal de Santa Catarina para a obtenção do título de mestre em engenharia mecânica.
Orientador: Prof.(a) Marcia Barbosa Henriques Mantelli, Ph.D.
Coorientador: Juan Pablo Florez Mera, Dr. Eng.

Florianópolis
2021

Ficha de identificação da obra elaborada pelo autor,
através do Programa de Geração Automática da Biblioteca Universitária da UFSC.

Domiciano, Kelvin Guessi
THEORETICAL AND EXPERIMENTAL ANALYSIS OF A DIFFUSION BONDED ULTRA-THIN COPPER LOOP HEAT PIPE / Kelvin Guessi Domiciano ; orientador, Marcia Barbosa Henriques Mantelli, coorientador, Juan Pablo Florez Mera, 2021.
151 p.

Dissertação (mestrado) - Universidade Federal de Santa Catarina, Centro Tecnológico, Programa de Pós-Graduação em Engenharia Mecânica, Florianópolis, 2021.

Inclui referências.

1. Engenharia Mecânica. 2. Ultra-thin flat loop heat pipe. 3. Thermal performance. 4. Diffusion bonding of UTLHP. I. Barbosa Henriques Mantelli, Marcia. II. Florez Mera, Juan Pablo. III. Universidade Federal de Santa Catarina. Programa de Pós-Graduação em Engenharia Mecânica. IV. Título.

Kelvin Guessi Domiciano

Theoretical and experimental analysis of a diffusion bonded ultra-thin copper loop heat pipe

O presente trabalho em nível de mestrado foi avaliado e aprovado por banca examinadora composta pelos seguintes membros:

Prof.(a) Marcia Barbosa Henriques Mantelli, Ph.D.
Universidade Federal de Santa Catarina

Juan Pablo Florez Mera, Dr. Eng.
Universidade Federal de Santa Catarina

Prof. Paulo Henrique Dias dos Santos, Dr.
Universidade Tecnológica Federal do Paraná

Prof. Fernando Henrique Milanese, Dr.
Universidade Federal de Santa Catarina

Certificamos que esta é a **versão original e final** do trabalho de conclusão que foi julgado adequado para obtenção do título de mestre em Engenharia Mecânica.

Documento assinado digitalmente
Paulo de Tarso Rocha de Mendonca
Data: 04/06/2021 14:24:26-0300
CPF: 149.822.691-49
Verifique as assinaturas em https://v.ufsc.br

Prof. Paulo de Tarso Rocha de Mendonça. Dr.
Coordenador do Programa

Documento assinado digitalmente
Marcia Barbosa Henriques Mantelli
Data: 04/06/2021 10:30:45-0300
CPF: 025.041.158-06
Verifique as assinaturas em https://v.ufsc.br

Prof.(a) Marcia Barbosa Henriques Mantelli, Ph.D.
Orientador(a)

Florianópolis, 07 de maio de 2021.

Este trabalho é dedicado aos meus queridos pais, irmãos, avó e amigos.

AGRADECIMENTOS

Agradeço imensamente meus pais pela oportunidade e auxílio durante esses dois anos. Aos meus irmãos Renato e Cauã que sempre estiveram presentes. Ao restante da minha família, particularmente a minha Vó Maria, na qual sempre me apoiou.

À minha orientadora Professora Marcia Mantelli na qual me forneceu suporte com seus conhecimentos e uma oportunidade única de trabalhar na área de microgravidade. Ainda, ao coorientador Juan Pablo que me apoiou durante as atividades no laboratório.

Aos meus amigos e colegas que me acompanharam desde o início desta jornada e também àqueles que encontrei durante a minha caminhada. Dentro todos, destaco a Larissa Krambeck que sempre esteve presente para auxiliar em qualquer dificuldade. Aos outros integrantes da microgravidade, Gustavo Siedel e Jonas que se empenharam em ajudar a finalizar o projeto. Ao Caluga que forneceu conhecimento necessário para o andamento do projeto. Por fim, ao Luis Betancur na qual orientou meu primeiro contato com o laboratório e sempre se manteve a disposição.

Ainda, agradeço àqueles do Labtucal que de alguma maneira me auxiliaram neste período.

Àqueles amigos não mencionados, mas não esquecidos, que me apoiaram.

Por fim, agradeço a todos mencionados e também ao Daniel, Matheus e Elvis pelo tempo de distração e diversão durante a pesquisa, em momentos de celebração pelos nossos sucessos.

Ou escreves algo que valha a pena ler, ou fazes algo acerca do qual valha a pena escrever. (Benjamin Franklin, 1790)

RESUMO

Tubos de calor planos em circuito utilizam da mudança de fase de um fluido de trabalho para transferir altas taxas de calor, tornando-os adequados para aplicações em dispositivos eletrônicos, como smartphones. Na presente dissertação, é proposto um método de fabricação de tubos de calor planos em circuito ultrafinos com espessuras inferiores a 1,6 mm, que preservam a eficiência de dispositivos de transferência de calor comumente utilizados. Tubos de calor em circuito com 1,6; 1,2 e 0,9 mm de espessura são fabricados utilizando tecnologia de sinterização e união por difusão. Os dispositivos de transferência de calor possuem uma estrutura porosa de cobre em pó, localizada no interior do evaporador, a qual fornece a força motriz necessária para a circulação do fluido de trabalho. Uma estrutura secundária localizada na linha de líquido, na qual possui as mesmas propriedades da localizada no evaporador, é utilizada para garantir que o fluido condensado retorne ao evaporador. Uma bancada é desenvolvida para avaliar o desempenho térmico do tubo de calor, onde é simulada o resfriamento de um processador (chip), típica aplicação eletrônica do presente dispositivo, os quais são analisados termicamente, tendo como fonte fria a convecção natural do ar a uma temperatura ambiente de 24 ± 1 ºC, sendo testados nas posições: horizontal, vertical (assistida pela gravidade) e vertical invertido (contra gravidade). Dois fluidos de trabalho diferentes são analisados: etanol e água destilada. Uma modelagem matemática, baseada em circuitos térmicos equivalentes, balanço de energia e massa e queda de pressão, é proposta como ferramenta de projeto para prever o desempenho térmico do dispositivo projetado. O método de fabricação proposto provoca poucas deformações em todo o dispositivo. A investigação experimental mostra que a estrutura porosa secundária é essencial para a circulação do fluido de trabalho. Os dados experimentais confirmam que, reduzindo a espessura, o desempenho térmico dos tubos de calor diminui, devido principalmente à maior taxa transferência de calor por condução, na qual não participa na mudança de fase, e ao menor confinamento do fluido de trabalho. O tubo de calor em circuito ultrafino com maior espessura, 1,6 mm, apresenta a menor resistência térmica de 0,20 ºC/W, transportando 8 W/cm². Reduzindo a espessura em 50%, o desempenho térmico piora em, aproximadamente, três vezes. Ainda, o modelo teórico demonstra ser uma ferramenta promissora de projeto destes dispositivos, uma vez que foi capaz de predizer o funcionamento dos tubos de calor em circuito.

Palavras-chave: Tubos de calor plano em circuito ultrafinos. Desempenho térmico. União por difusão de UTLHP.

RESUMO EXPANDIDO

Introdução

Nos últimos anos, o avanço da tecnologia permitiu a produção de eletrônicos ultrafinos e compactos, como projetores portáteis, tablets e smartphones. Esse progresso aumenta a geração de calor interna nesses sistemas, devido à redução do tamanho do processador em chip, o aumento sua densidade e a maior velocidade de processamento. Portanto, questões relacionadas ao gerenciamento térmico têm se tornado essenciais em diversas aplicações. Ainda assim, esses dispositivos sofrem com elevados gradientes de temperatura devido aos altos fluxos de calor e à não uniformidade das fontes de dissipação de calor no equipamento. Apesar dos esforços para melhorar os sistemas de refrigeração tradicionais, o fluxo de calor rejeitado aumenta a cada ano, podendo atingir 14 W/cm². Desta forma, os eletrônicos alcançam elevadas temperaturas, o que diminui sua vida útil. O desenvolvimento de soluções de resfriamento mais eficientes e compactas se tornou indispensável para a miniaturização dos eletrônicos. Dentre as soluções de resfriamento mais promissoras estão os tubos de calor, que consistem em dispositivos que utilizam a mudança de fase do fluido de trabalho para transferir o calor, de forma passiva, de um lado aquecido para um dissipador de calor. Além dos tubos de calor convencionais, os tubos de calor em circuito (LHPs) têm sido amplamente pesquisado devido a algumas vantagens: capacidade de transportar calor em curtas e longas distâncias, alta flexibilidade e funcionamento independente da ação da gravidade. Os principais desafios dos tubos de calor em circuito com espessuras finas (UTLHPs) consistem no processo de fabricação, que pode causar deformações, e no desempenho térmico eficiente. Portanto, a ênfase da presente pesquisa é o desenvolvimento de tubos de calor em circuito ultrafinos planos para aplicação em eletrônicos, como smartphones. Além disso, busca-se adquirir o conhecimento do processo de miniaturização e fabricação desses dispositivos de transferência de calor.

Objetivos

No presente trabalho, pretende-se concentrar esforços no desenvolvimento de tubos de calor ultrafinos em circuito a fim de melhorar os modelos teóricos a serem utilizados na concepção destes dispositivos de transferência de calor, de forma a validar os resultados teóricos com os dados experimentais. Neste contexto, é apresentado o processo de fabricação do UTLHP e da estrutura capilar, onde são aplicados diferentes processos de união por difusão e sinterização. Finalmente, uma análise do desempenho térmico de UTLHPs é realizada com diferentes espessuras.

Metodologia

Inicialmente é apresentada uma revisão bibliográfica dos principais trabalhos e autores na área de tubos de calor em circuito planos. Posteriormente, são discutidos os princípios físicos fundamentais que regem o funcionamento desses dispositivos de transferência de calor, detalhando cada componente dos LHPs. A geometria escolhida para o LHP possui foco na aplicação em eletrônicos, como os smartphones. Os dispositivos fabricados possuem duas estruturas capilares localizadas no evaporador e linha de líquido. Ambas consistem de pó de cobre sinterizado com a mesma composição e propriedades. Uma descrição detalhada do processo de sinterização da estrutura capilar e da união por difusão é apresentada. Para analisar o desempenho térmico do LHP, uma bancada experimental baseada na geometria de um processador em chip de smartphone é proposta. Um modelo teórico é apresentado com objetivo de predizer o comportamento térmico do LHP, como temperatura de operação, resistência térmica, queda de pressão e taxa de transferência de calor por condução do evaporador para

linha de líquido. Por fim, analisa-se os resultados do desempenho térmico do dispositivo e comparados com os dados experimentais.

Resultados e discussão

Os resultados mostram que a união por difusão é um método de fabricação conveniente, pois causa poucas deformações no dispositivo de transferência de calor ultrafino. É constatado que a estrutura capilar adicional na linha de líquido é necessária para o funcionamento do tubo de calor em circuito ultrafino na posição horizontal. Os resultados experimentais mostram que o volume total de fluido de trabalho dentro do dispositivo de transferência de calor afeta diretamente em seu desempenho térmico. Como esperado, os dados experimentais confirmam que reduzindo a espessura dos tubos de calor, seu desempenho térmico diminui, devido às perdas de calor por condução de calor e maior confinamento do fluido de trabalho. Na orientação horizontal, o tubo de calor de circuito ultrafino com etanol e 1,6 mm de espessura total inicia seu funcionamento com um fluxo de calor de 2 W/cm². O menor valor de resistência térmica de 0,20 ºC/W é alcançado a 8 W/cm². Reduzindo a espessura da parede em 50%, ou seja, 0,5 mm de espessura, o dispositivo de transferência de calor para seu funcionamento com 7 W/cm², provavelmente devido a área do condensador não ser suficiente. Para este UTLHP, a menor resistência térmica é de 0,72 ºC/W com 3 W/cm². Já o LHP com parede interna de 0,3 mm de espessura não conseguiu operar satisfatoriamente, possivelmente devido a uma pressão capilar menor que a necessária. Para estudar a influência do fluido de trabalho nos tubos de calor em circuito ultrafinos, água é selecionada como fluido alternativo, na tentativa de melhorar o bombeamento capilar. Porém, a água não apresenta uma melhoria no desempenho térmico, não caracterizando uma boa solução. O modelo teórico proposto pode prever os parâmetros da ferramenta de projeto de tubos de calor em loop com diâmetro hidráulico maior que 1 mm, como: temperaturas, resistências térmicas, quedas de pressão, taxa de calor por condução do evaporador para linha de líquido e comprimentos de condensadores monofásicos e bifásicos. O dispositivo de transferência de calor proposto mostra-se atraente para aplicação no resfriamento de eletrônicos, como smartphones, devido as principais características alcançadas nesta pesquisa: um evaporador com área pequena de 1 cm², dissipação de 2 W/cm² até 9 W/cm² por convecção natural a ar, operação com temperaturas abaixo de 100 ºC e espessuras menores que 1,6 mm. No entanto, o dispositivo de transferência de calor não funciona contra a orientação da gravidade.

Considerações finais

Este trabalho apresenta discussões relevantes sobre a miniaturização de tubos de calor em circuito, revelando dispositivos com espessuras inferiores a 1,6 mm. Tais resultados contribuem para o resfriamento de aparelhos eletrônicos compactos, como os smartphones.

Palavras-chave: Tubos de calor plano em circuito ultrafinos. Desempenho térmico. União por difusão de UTLHP.

ABSTRACT

Flat loop heat pipes work with phase change of a working fluid to transfer high heat fluxes, making them suitable for electronic applications, such as smartphones. In this dissertation, a manufacturing process for ultra-thin flat loop heat pipes with thicknesses below 1.6 mm is proposed, preserving the efficiency of commonly used heat transfer devices. Loop heat pipes with 1.6, 1.2 and 0.9 mm thick are manufactured using sintering and diffusion bonding technology. The heat transfer devices have a porous structure of copper powder, located inside the evaporator, which provides the necessary driving force for the working fluid circulation. A secondary structure located in the liquid line, which consist with the same properties of the located in the evaporator, is used to ensure that the condensed fluid returns to the heated side. A workbench is developed to evaluate the thermal performance of the heat pipe, which consists of simulating the cooling of a processor chip, typical electronic application for the present devices, which are tested subjected to natural convection with air at an ambient temperature of 24 ± 1 ºC. They are tested in horizontal, vertical (assisted by gravity) and vertical inverted (against gravity) inclinations. Two different working fluids are analyzed: ethanol and distilled water. A theoretical modeling, based on equivalent thermal circuits, energy and mass balance and pressure drop, is proposed as a design tool to predict the thermal performance of the designed device. The applied manufacturing method causes little deformation in the entire loop heat pipe. Experimental results show that the liquid line wick structure is essential for the circulation of the working fluid. The experimental data confirm that, by reducing the thickness, the thermal performance of the heat pipes decreases, due to among others, the reasons: greater heat transfer by conduction and smaller confinement of the working fluid. The ultra-thin loop heat pipe with greater thickness, 1.6 mm, has the lowest thermal resistance of 0.20 ºC/W, transferring 8 W/cm². Reducing the thickness by 50%, the thermal performance worsens approximately three times. In addition, the theoretical model proves to be a promising method for designing and predicting the flat loot heat pipe operation.

Keywords: Ultra-thin flat loop heat pipe. Thermal performance. Diffusion bonding of UTLHP.

FIGURES

TABLES

LIST OF ABREVIATIONS AND ACRONYMS

EES™	*Engineering Equation Solver*™
LabTUCAL	Heat pipe Laboratory (*Laboratório de Tubos de Calor*)
LEPTEN	Laboratory of Energy Conversion Engineering and Energy Technology (*Laboratórios de Engenharia de Processos de Conversão e Tecnologia de Energia*)
LHP	Loop heat pipe
UTLHP	Ultra-thin loop heat pipe
PTFE	Polytetrafluoroethylene
UFSC	Federal University of Santa Catarina(*Universidade Federal de Santa Catarina*)

SYMBOLS

Latins

A	Area	[m^2]
a	Chance value	[-]
Bo	Bond number	[-]
c_p	Specific heat	[J/kg°C]
D	Smallest channel dimension	[m]
d	Diameter	[m]
E	Freidel parameter	[-]
F	Freidel parameter	[-]
f	Friction factor	[-]
Fr	Froude number	[-]
FR	Filling Ratio	[%]
g	Gravity acceleration	[m/s^2]
G	Mass velocity	[kg/m^2 s]
H	Freidel parameter	[-]
h	Heat transfer coefficient	[W/m^2 °C]
h_{lv}	Latent heat of vaporization	[J/kg]
I	Current	[A]
K	Permeability	[m^2]
k	Thermal conductivity	[W/m °C]
L	Length	[m]
M	Merit number	[-]
$\dot{m}$	Mass flow rate	[kg/s]
n	Number	[-]
Nu	Nusselt number	[-]
p	Perimeter	[m]
P	Pressure	[Pa]
Pr	Prandtl number	[-]
q	Heat transfer rate	[W]
q''	Heat flux	[W/ m^2]

r	Radius	[m]
R	Thermal resistance	[°C/W]
Ra	Rayleigh number	[m]
Ra^*	Modified Rayleigh number	[m]
Re	Reynolds number	[-]
u	Uncertainty	[-]
U	Voltage	[V]
v	Velocity	[m/s]
T	Temperature	[°C]
t	t-student	[-]
V	Volume	[m^3]
W	Width	[m]
We	Weber number	[-]
X	Martinelli parameter	[-]
z	Z direction	[m]

Greeks

α	Thermal diffusivity	[m^2/s]
β	Coefficient of thermal expansion	[1/K]
Δ	Difference	[-]
δ	Thickness	[m]
ε	Porosity	[m]
ζ	Roughness	[-]
ξ	Half-inclined angle	[º]
θ	Contact angle	[º]
κ	Surface area ratio	[-]
μ	Dynamic viscosity	[Pa.s]
υ	Kinematic viscosity	[m^2/s]
Ω	Chen parameter	[-]
ρ	Specific mass	[kg/m^3]
σ	Surface tension	[N/m]
φ	Channel aspect ratio	[-]

ϕ	Phase	[-]
Γ	Aspect ratio	[-]
χ	Vapor quality	[%]

Subscripts

ac	Active zone
amb	Ambient
air	Air property
avg	Average
b	Barrier
c	Condenser
cap	Capillary
case	Case material
ch	Channel
co	Combined
cs	Cross-section
e	External
eff	Effective
eq	Equivalent
ev	Evaporator
ew	Evaporator wick
h	Hydraulic
hl	Heat leak
i	Internal
in	Input
iso	Isolation
l	Liquid
lhp	Loop heat pipe
ll	Liquid line
ln	Longitudinal
lo	Liquid only
loss	Loss

llw	Liquid line wick
m	Mixture
o	Outlet
p	Pore
s	Solid
sat	Saturation
sc	Sub-cooling
sm	Screen mesh
sp	Sphere
sup	Superfial
t	Total
tr	Transversal
v	Vapor
vo	Vapor only
vg	Vapor groove
vl	Vapor line
w	Wick
wall	Wall
wire	Wire
wf	Working fluid
1ϕ	Single-phase
2ϕ	Two-phase

CONTENTS

1 INTRODUCTION

In the past years, the industry technology development allowed the production of ultra-thin and compact electronics, as portable projectors, tablets and smartphones. This progress increased the internal heat generation in these systems, due to the chip processor size reduction, rising its density and the higher processing velocity (CHEN et al., 2016). Therefore, issues concerning the thermal management have become essential in several industrial applications. The increase of electronic density can be predicted by the empirical Moore's law which described that the number of transistors in a dense integrated circuit might double at every two years (MOORE, 1998). Still, these devices undergo high temperature gradients because of the high heat fluxes and the non-uniformity of the heat dissipation sources in the equipment (CHEN et al., 2016). Despite many efforts made to improve the traditional cooling systems, electronics can reach high temperatures, restricting the electronics life expectancy. Figure 1 illustrates the power consumption from thermal design power (TDP) of Snapdragons chip processors for mobile phones along the years. In this application, the heat flux input increases along the years and might achieve huge values, such as 14 W/cm².

Figure 1 – Power consumption – thermal design power (TDP) of Snapdragon chip processors for mobile phones.

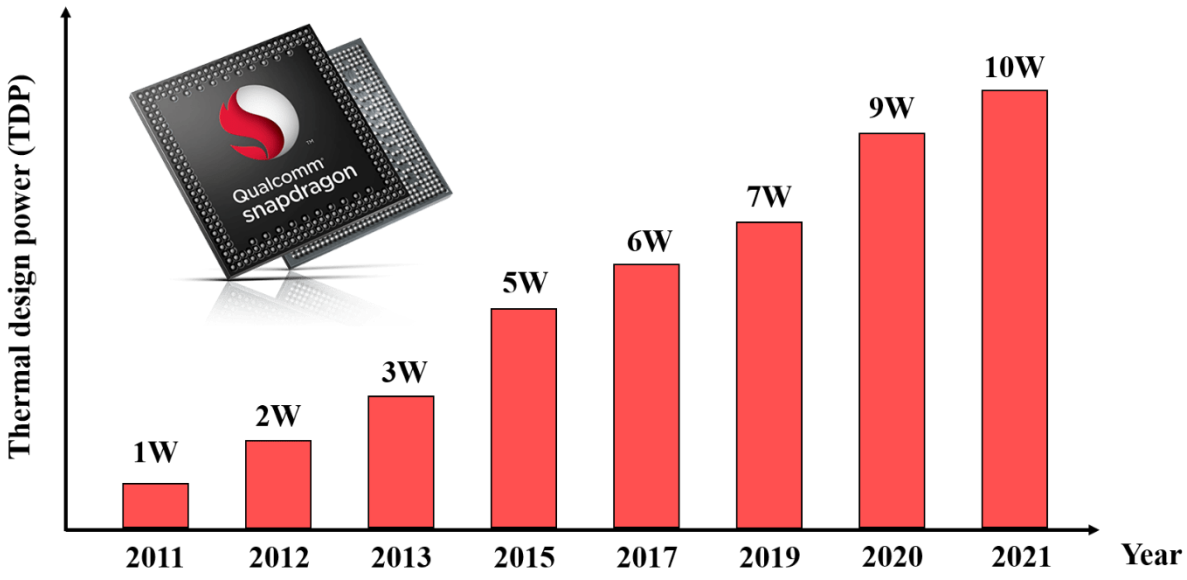

Source: (WIKICHIP, 2021a)

The development of more efficient and compact cooling solutions become a major industrial concern. According to Agostini et al. (2007), high heat fluxes can be dissipated through competing technologies such as: microchannel single-phase flow or two-phase flow,

porous media flow, and jet impingement cooling. Using porous media with single-phase and two-phase flow are the best combination to remove high heat fluxes in compact components. Heat pipes consist of a simple passive cooling system which uses working fluid phase change to transfer heat from a heated side to a heat sink. A porous media provides a capillary pumping, for the working fluid circulation. These devices can be applied in gravity or microgravity environments, in many areas as: industrial, electronic, aerospace, telecommunication and others, as shown in Figure 2. Besides conventional heat pipes, loop heat pipes (LHP) have been extensive researched due to some advantages: it can transport heat through short and long distances, has high flexibility and its operation is not affected by the gravitational field (CHEN et al., 2016).

Figure 2 – Possible applications for thermal management with ultra-thin loop heat pipes.

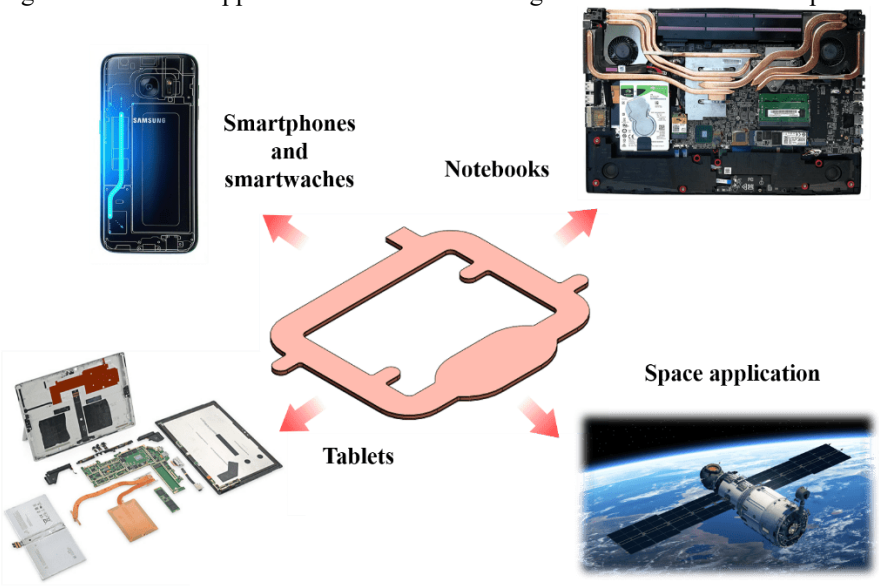

Source: (MSI, 2021); (TECHJUICE, 2021); (HOTHARDWARE, 2021)

Technologies involving heat pipes and related ultra-thin devices can represent a significant advance in the area of phase-change phenomena. Loop heat pipes with thin thickness present a challenge in the manufacturing process and thermal performance due to several problems. For example, the increase of the heat conduction (parasitic heat transfer rate) and deformation in the fabrication procedure. These problems affect the miniaturization process of these components, causing difficulties in the development of thin mobile phones with faster processing speed. Figure 3 shows that, despite the cooling systems has advanced, the smartphones failed to reduce its thickness, due to the presence of the heat dissipation devices.

Therefore, it is clear that effective heat transfer devices with thin thickness still require developments.

Figure 3 – Mobile phones thickness from technology succession of Iphones.

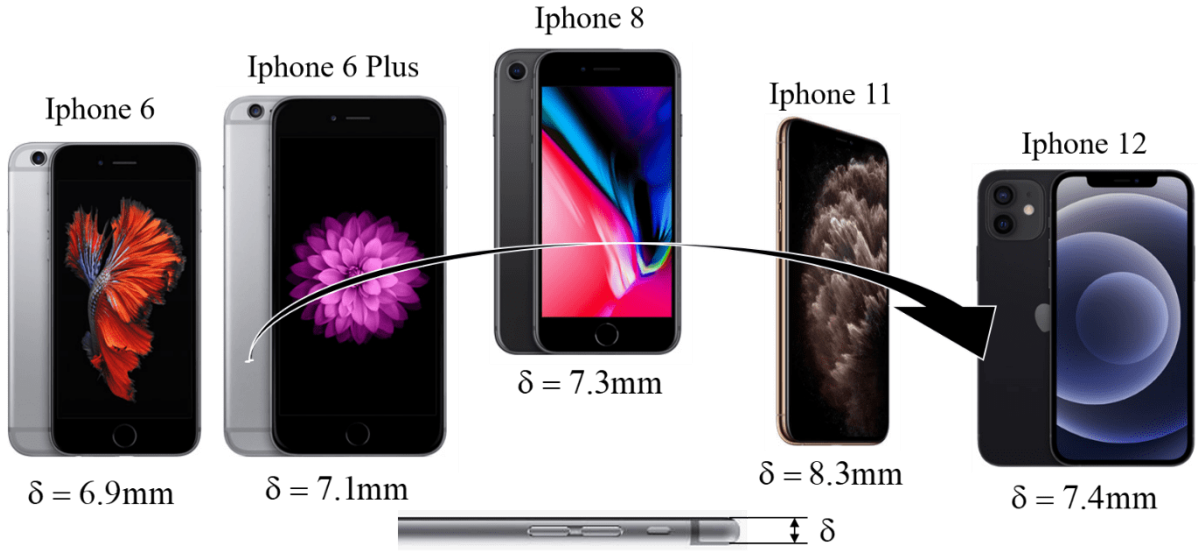

Source: (APPLE, 2021)

The literature theoretical and experimental investigations highlight the complexity of physical process required for the operation of ultra-thin loop heat pipes (UTLHPs), due to the phase change phenomena that happen inside the device. Despite the literature detailed analyses, several physical mechanisms that drive UTLHP are still not fully understood and need further investigations.

In the present work, it is intended: to concentrate efforts on the development of ultra-thin loop heat pipes, to improve the theoretical models to be used for the design of these heat transfer devices, to conform the theoretical results with experimental data. In this context, an analysis of the UTLHP thermal performance reducing its thickness will be carried out. Finally, the manufacturing process of the UTLHP and wick structure is presented, where different diffusion bonding and sintered process are applied.

1.1 OBJECTIVES

The main objective of this study is to develop technology that would result in thermally efficient miniaturized ultra-thin flat loop heat pipes. The research pursues an effective

fabrication technique of the device and foresees an analytical model for its design to validate with experimental data.

1.1.1 Specific objectives

To achieve the general objective proposed, the following specific objectives are outlined:

- To design of the geometry of ultra-thin loop heat pipes;
- To manufacture of UTLHPs with different wall thickness using novel manufacturing methods, including diffusion bonding and sintering processes;
- To determine the critical problems caused by the miniaturization of UTLHP;
- To perform experimental tests in order to analyze the thermal performance of the UTLHPs with different working fluids, applying power input cycle with distinct orientations;
- To develop an analytical model to be implemented as a design tool for UTLHP, using mass, momentum, and energy balance equations;
- To analyze and validate the proposed analytical model against experimental data, which predicts the major affecting parameters for the performance of UTLHPs, such as operating temperature, parasitic heat transfer rate and condenser length.

1.2 DISSERTATION ORGANIZATION

Disregarding the introduction and conclusion sections, this dissertation is organized as follows:

- In Chapter 2, an extensive bibliographic review is conducted, to establish the state of the art and to identify recent works regarding experimental results, numerical simulations, theoretical model developments and fabrication procedures of ultra-thin loop heat pipes.
- Chapter 3 presents the theoretical aspects of the present work. The physical mechanisms needed for understanding the UTLHP operation are discussed,

describing the functioning and properties of every component that constitutes the device. The most influential parameters regarding heat transfer are identified.

- Chapter 4 introduces the manufacturing process used for the fabrication of the proposed UTLHP. Furthermore, the section details the experimental procedure adopted.
- Chapter 5 proposes the theoretical model, developed to predict the thermal performance of the UTLHP, which encompasses: simple energy and mass balance equations, the equivalent thermal resistances circuit and the pressure loss equations.
- Chapter 6 provides the validation of the present model by comparison with data, obtained from the experimental work developed. Experimental and theoretical results are also discussed.

2 LITERATURE REVIEW

In this section, some recent and important works from the literature are presented to support this study, highlighting the development of flat loop heat pipes, their characteristics, manufacturing procedures, experimental results, conclusions and recommendations for future works.

Most of the loop heat pipes studied in the literature are made of cylindrical tubes, due to the easier fabrication processes. Recently, the need for compact devices, with mall thickness, has led to the development of flat loop heat pipes. In these devices, the evaporator geometry is flat, requiring new manufacturing process, resulting in very thin devices, sometimes with less than 1 mm of thickness.

In order to improve the thermal performance of flat loop heat pipes, Kiseev et al. (2010) carried out experiments to investigate the influence of geometric parameters, including thicknesses, configuration and size of the vapor grooves, for different materials and working fluids. They made loop heat pipes of titanium and sintered nickel, in addition to monel structures and bronze. Also, grooves with a rectangular, trapezoidal and triangular section were analyzed. The optimal wick structure regarding the thermal efficiency of the device, had pore thickness varying between 5 and 7 mm, with porosity of 55-65%. The experimental tests conducted by these authors showed that the heat transfer of flat evaporator can be intensified by making a correct choice of the vapor grooves configuration. The optimum ratio between the total cross section area of vapor grooves and the evaporator active area was around 0.4 – 0.5. Besides, decreasing the width and the distance between the vapor grooves intensified the thermal performance, increasing the heat transfer coefficient.

Li et al. (2016) carried out experiments on a loop heat pipe with an ultra-thin flat evaporator (1 mm). It was manufactured with three different wick structure configurations (metallic or sintered copper mesh, bilateral circular groove and mesh groove). Filling ratio was a parameter also analyzed. The flat geometry was obtained by compressing a cylindrical tube. Deionized water was used as the working fluid with an optimal filling ratio of approximately 70%. Through microscopy, they concluded that the fabrication process caused severe deformations in the structure. Tests were performed increasing the heat input in the evaporator and the main operating limit found was the capillary one.

A ultra-thin loop heat pipe, with 1.2 mm thick flat evaporator, and vapor line, liquid line, and condenser with a 1.0 mm thickness, was studied by Zhou et al. (2016), as shown in

the Figure 4. Excluding the evaporator, the manufacturing process consisted of compressing pure copper tubing with an internal and external diameter of 3.5 and 4.0 mm, respectively. Using the assistance of a flattening mill, a flattened tube with 1.0 mm thick was obtained. In the evaporator, a primary capillary wick structure, of 0.8 mm thick, was incorporated by sintering process over the upper and lower copper sheets, each with 0.2 mm of thickness, resulting a loop heat pipe of 1.2 mm thick. This wick structure consisted of 10 sintered layers 500 copper wire mesh with a porosity of 65.2%. To guarantee the return of working fluid back to the evaporator at low heat loads, the liquid line also holds a secondary wick structure of 0.43 mm thick, made of 4 layers of 150 copper wire mesh with a porosity of 61.2%, which is connected to the primary wick. The evaporator of their experimental set-up presented an active area of 15 mm x 9 mm, in contact with a ceramic heater. Nine thermocouples were employed to measure the UTLHP temperature distribution and the ambient temperature, as shown in Figure 4b. The device was tested in three orientations (horizontal, vertical – assisted by gravity, vertical – against gravity), to study the effects of the gravitational field its operating performance. All tests were conducted under air natural convection at an ambient temperature of $24 \pm 1\,°C$. Figure 5a shows the transient behavior of the UTLHP in the horizontal orientation with a heat load of 2 W. After about 600 seconds, the device approached a steady-state condition. Besides, the evaporator region showed very close temperatures (thermocouples 101, 102, 109, 103 and 105). The UTLHP started to work at 2 W of heat load, as observed when the condenser temperature (106) is larger than the evaporator inlet temperature (109). The heat conducted from the evaporator to the liquid line makes the liquid line (108) and condenser outlet temperatures (107) nearly close to each other.

Figure 4 - Design, dimensions and locations of nine thermocouples on the UTLHP.

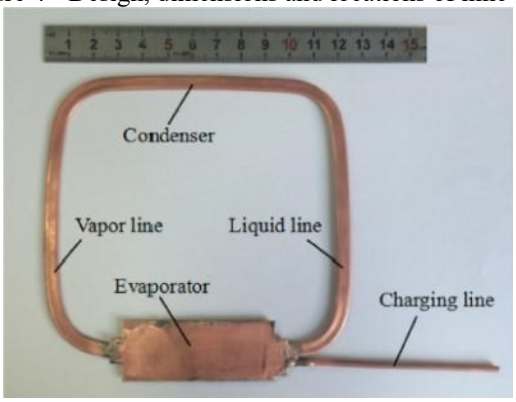

a) Design of the UTLHP and its dimensions.
Source: (ZHOU et al., 2016)

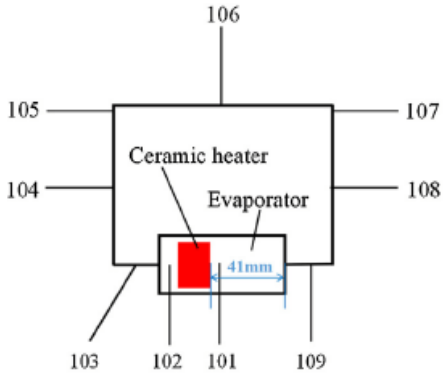

b) The locations of the nine thermocouples.

Figure 5 - Temperature values in horizontal orientation with a heat load of 2 W and the thermal resistance of UTLHP.

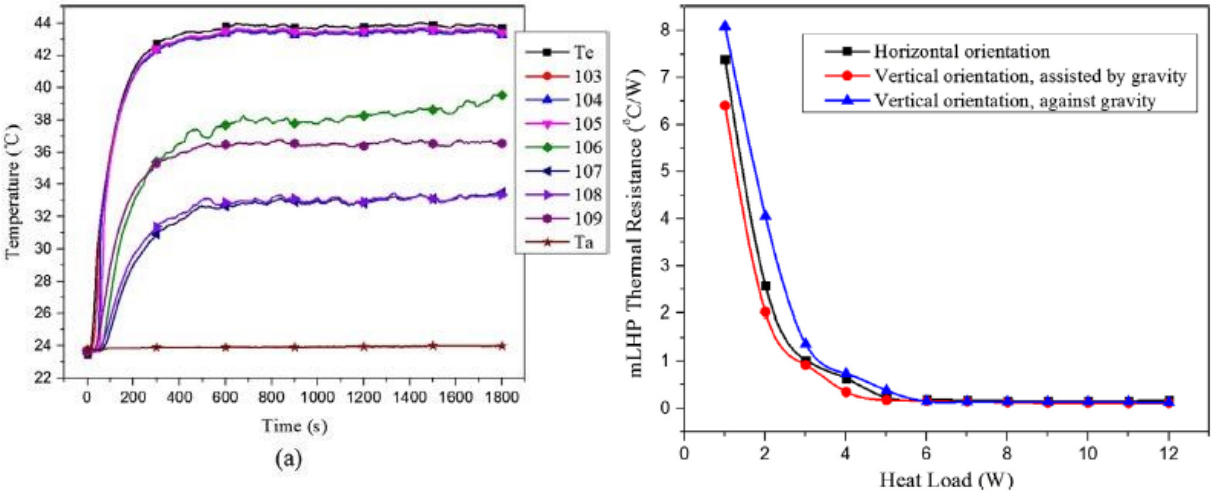

a) The temperature values of the UTLHP in the horizontal orientation during startup with a heat load of 2 W.

b) Heat load dependence of the UTLHP thermal resistance.

Source: (ZHOU et al., 2016)

Still regarding the work of Zhou et al. (2016), in all orientations tested, the UTLHP thermal resistance initially decreased rapidly, until proximally 5 W of power input. After that, the thermal resistances maintained at a constant level. The minimum value of 0.111 °C/W was achieved in the vertical orientation assisted by gravity at 11 W. At low heat loads, the thermal resistance was larger probably because the small vapor mass flow rate. This result indicated that only a portion of the condenser are occupied with working fluid in phase conditions. As the mass flow rate increases by rising the heat load, the R_{mLHP} proportionally reduces.

The work proposed by Zhou et al. (2017) investigated the efficiency of loop heat pipe with an 0.8 mm thick evaporator, manufactured by compressing a 2 mm cylinder. For the capillary pumping, they used a wick structure made of sintered copper. Water as the working fluid used. Experiments were carried out with heat inputs varying from 2.5 W to 5 W, with successive increases of 0.5 W. The results showed that the filling ratio affects the temperature uniformity of the LHP. The authors demonstrated that the optimal filling ratio is obtained when the wick structure is saturated with liquid. This charging ratio provided a temperature difference between the evaporator and condenser of 3.7 ºC and a thermal resistance of 0.29 K/W. Finally, they concluded that thermal resistance increases with increasing the heat load applied before the working fluid dries out.

Shioga et al. (2020) presented a new cooling system for thermal management of electronic devices using an ultra-thin loop heat pipe. The device was designed with an

evaporator of 0.6 mm in thickness, and a total dimension of 58 mm and 107 mm for width and length, respectively. The evaporator was constructed obtained by chemical-etching of four copper sheets of 0.1 mm, which were aligned and externally covered with no etched copper sheets. The resulting stack is diffusion bonded. The etches of the four internal layers, in the shape of through holes of 0.2 mm of diameter, piled in staggered position, provided the capillary structure. The two external sheets also enclose the channels for the working fluid flow. Figure 6 shows all layers of the flat loop heat pipe. The thermal performance of the flat LHP was evaluated by measuring the temperature through twelve K-type thermocouples. A 15 x 15 mm copper heating block in contact with only one face of the evaporator, provided the heat input. To improve the cooling capacity of the device, the condenser is larger, made of a 3 mm thick copper plate (100 x 65 mm). All tests were performed under natural air convection and room temperature between 22 °C and 23 °C.

Figure 6 - Photographs of surface layer, inner layer and evaporator section of an ultra-thin LHP.

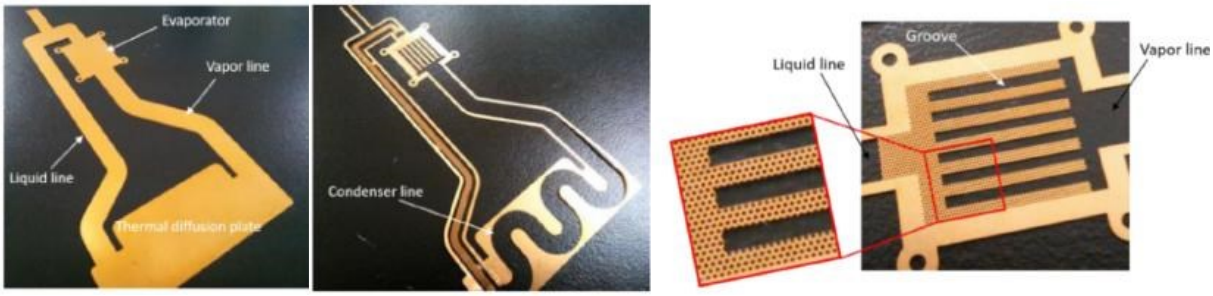

a) Suface layer b) Inner layer c) Evaporator section
Source: (SHIOGA et al., 2020)

Figure 7 - Operating temperature and input power dependence of the thermal resistance of the LHP.

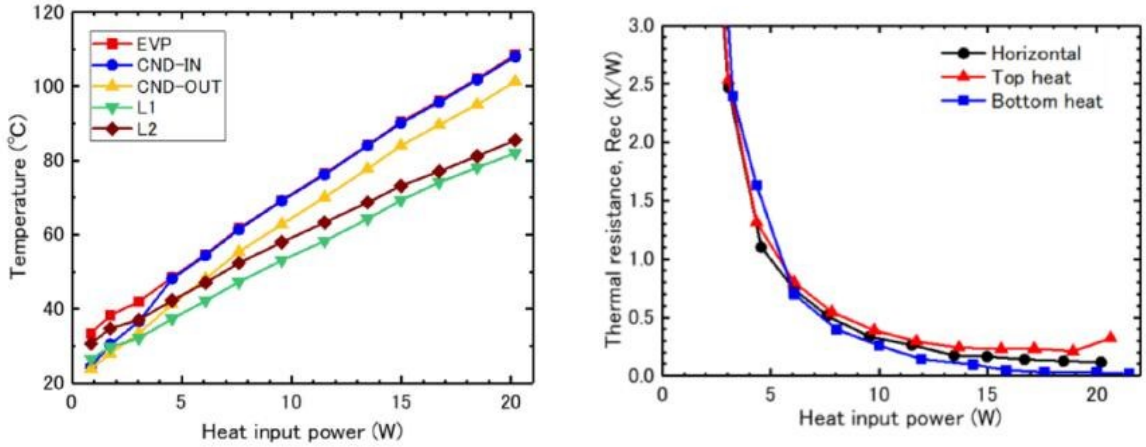

a) Temperature of the flat LHP operating in a horizontal orientation.
Source: (SHIOGA et al., 2020)

b) Input power dependence of the thermal resistance in three orientations.

Still according to Shioga et al. (2020), the heat input for the evaporator section can be expressed by the following equation:

$$q_{in} = q_{ev} - q_{ev,ll} \quad (1)$$

where q_{ev} is the amount of heat used in the evaporation of the working fluid and $q_{ev,ll}$ is the heat leak, i.e., the heat lost by conduction from the evaporator to the liquid line. Figure 7(a) indicates that the heat leak is considerable if the heat input is less than 5 W, i.e., the temperature of the evaporator inlet (L2) is larger than the temperature of the condenser outlet (CND-OUT). This means that for larger values, as 6 W, the parasitic heat is suppressed by the phase-change phenomenon and the LHP starts to work satisfactorily. These authors found a thermal resistance of 0.11 ºC/W between the evaporator and the condenser, for a power input of 20 W. At this power level, the operating orientation (horizontal or vertical, top and bottom mode) does not affect the flat LHP, as shown in the Figure 7(b). Besides that, the researchers concluded that heat leak was 10% or less compared to the heat load applied.

To summarize the important works mentioned, Table 1 presents the configurations and materials used in these studies.

Table 1 - Comparison of configurations and materials used in literature works.

Authors	Material	Thickness [mm]	Fluid	Manufacture	Capillary structure	Chamber structure
Kissev, Vlassov and Muraoka (2010)	Copper	-	Acetone and water	-	Sintered mesh and cellular structures	Nickel, titanium, bronze and monel
Li et al. (2016)	Copper	1.0	Water	Compression	Metallic powder and sintered mesh	Copper
Zhou, Li and Lv (2016)	Copper	1.2	Water	Compression	Sintered mesh	-
Zhou et al. (2017)	Copper	0.8	Water	Compression	Sintered foam mesh	Copper
Shioga, Mizuno and Nagano (2020)	Copper	1.0	Water	Chemical-etching and diffusion bonding process	Copper sheets with holes	-

Source: Prepared by the author.

Tang et al. (2018) presented a study on applications and advances in the miniaturization of ultra-thin loop heat pipes with flat evaporators. In addition, they analyze manufacturing procedures and used wick structures, discussing the technology challenges to be faced. They concluded that the limiting factors for the dissemination of this technology are related to the low pumping capacity of the capillary structures and difficulties regarding their fabrication, especially concerning the joining processes, resulting in high cost low efficient devices. Therefore, they recommended as future work: optimization of the internal structure in order to reduce the effect of its thickness on the heat transfer, development of flexible tubes (usually polymers) and improvement in the joining methods to minimize the mechanical deformations that reduce the device life expectancy.

2.1 CONCLUSIONS

Based on the literature review just presented, it is clear that the industry faces problems to make thin heat transfer devices feasible for real applications, especially concerning their wick structure, which usually limits their thermal performance. More specifically, the following problems, to be addressed in the present work, are to be solved:

- Improvement of the fabrication process of flat loop heat pipes in order to avoid the usual deformations observed.
- Decreasing of heat leakages by conduction through the device, which reduces the thermal performance of thin loop heat pipes, a consequence of its miniaturization.
- Development of a better thermal performance wick structure.
- Precise characterization of porous media (careful measurement of their properties).

3 OPERATIONAL PRINCIPLES OF LHPS

In this chapter, the theoretical concepts related to the operational principles of loop heat pipes are presented and discussed. Aspects such as: detailed description of loop heat pipe geometry (classification and comparison with conventional heat pipes), operational principles, loop heat pipe components, thermodynamic cycles, description of components, operating limits and working fluid selection, are briefly discussed.

3.1 PHASE CHANGE DEVICES

Heat transfer devices that involve the phase change of a working fluid have excellent heat transport characteristics. They are able to transfer passively a huge amount of heat, between a source and a sink. The source, some times of small dimensions, can be, for instance, electronic chips from a CPU processor of mobile phones, tablets, smartwatches or notebooks. The larger devices can be applied in the industry, for heat management of a baking oven, for example. Heat can be removed from the condenser by several mechanisms, including: natural air convection, forced air convection (use of fans), or water cooling (use of pumps).

One of the first applications of two-phase devices are related to thermosyphons, which, when large, are able to transfer high amount of heat, by using of gravity as the driving force. In 1876, an array of thermosyphons were used in baking ovens to transfer heat from the firebrick to baking chambers. This invention was registered by the Perkins Family in the United Kingdom in the beginning of the twentieth century (FAGHRI, 2014).

Differently from the thermosyphon, heat pipes are able to transfer heat in non-gravity fields. The internal wick structure provides capillary force, which guarantees the fluid circulation from the evaporator to the condenser. For this reason, heat pipes are a successful technology used in aircraft and aerospace field.

The first concept of heat pipe was introduced in 1944 by Gaugler for a refrigeration problem of the General Motors Corporation in the U.S. Furthermore, in 1962, Trefethen tried to use this device in the space program. However, only in 1964 , after the work of Grover at the Los Alamos Scientific Laboratories in New Mexico, heat pipes started to be disseminated as an efficient heat transfer and thermal control solution for a wide range of applications (FAGHRI, 2014).

Three are the major components of heat pipes: sealed container of metal (copper and stainless steel, for instance), wick structure and working fluid. Generally, they are divided into three major sections: evaporator, adiabatic and condenser, as shown in Figure 8. Due to the vacuum in the container before filling, the working fluid reaches its saturated condition at the device temperature. Therefore, the liquid present in the wick structure is saturated. Most of the heat absorbed at the evaporator section is used as latent heat, to change of phase from liquid to vapor. The formed vapor flows to the condenser direction, passing through the adiabatic section. As the saturated vapor loses (latent) heat at the condenser region, it condenses. The condensate is absorbed by the wick structure, which, by capillary forces, pumps the liquid back to the evaporator, closing the cycle.

The vapor pressure distribution along each section is very close to uniform, which make the evaporator and condenser sections, where working fluid phase change occurs to reach uniform temperature. Also, the internal temperatures between evaporator and condenser, which are actually equivalent to the saturated vapor pressure in these sections, tend to be the same. These characteristics make these devices able to transfer heat along large distances, even when the heat sink and source present small temperature differences. For small distances, the device can be light weighted and have small dimensions (BEJAN; KRAUS, 2003).

Figure 8 - Schematics of a conventional heat pipe showing the principle of operation and circulation of the working fluid.

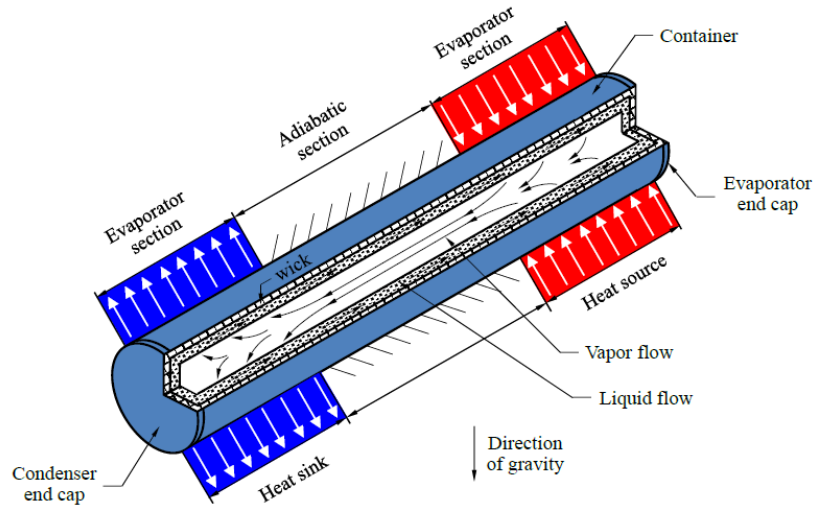

Source: (FAGHRI, 2014)

Heat pipes can operate in a wide range of temperatures, enabling different heat transfer applications. The appropriate material must be selected according to the temperature level, especially the working fluid. For electronics typical applications, large heat flux levels (such as

10^8 W/m²) can be observed in the evaporator, usually delivered in larger condenser surface areas. In this case, the devices operate as heat spreaders, where larger area can ultimately remove the heat, by natural convection and single-phase cooling systems (BEJAN; KRAUS, 2003).

Despite all advantages of heat pipes, for applications against gravity (evaporator located above the condenser) the capillary wick, located along the three major sections, might not be able to provide the necessary liquid pumping needed. In these cases, the heat transfer efficiency is abruptly decreased. To compensate this problem, additional capillary pressure could to be provided by decreasing the effective pore radius of the wick, however, this solution may increase the hydraulic resistance, which is proportional to the square of the pore radius (MAYDANIK, 2005).

3.2 LOOP HEAT PIPES

One of the motivations for the use of loop heat pipes is to overcome some disadvantage of conventional heat pipes. For that, its sections were disjointed, where the evaporator and condenser are separate through transport lines as shown in Figure 9, resulting in the "Loop Heat Pipes (LHPs)". They consist of five major components: evaporator, vapor line, condenser, liquid line and a compensation chamber. The major characteristic of LHP is the separation of the working fluid vapor and liquid phases. The capillary structure is usually located inside the evaporator. However, for small devices, wick structure can also be extended into the liquid line (liquid line wick). One great advantage of these devices is that the geometry of the evaporator can be designed separately from that of the condenser, which make them more adjustable to the application.

Figure 9 – Scheme and general view of a LHP.

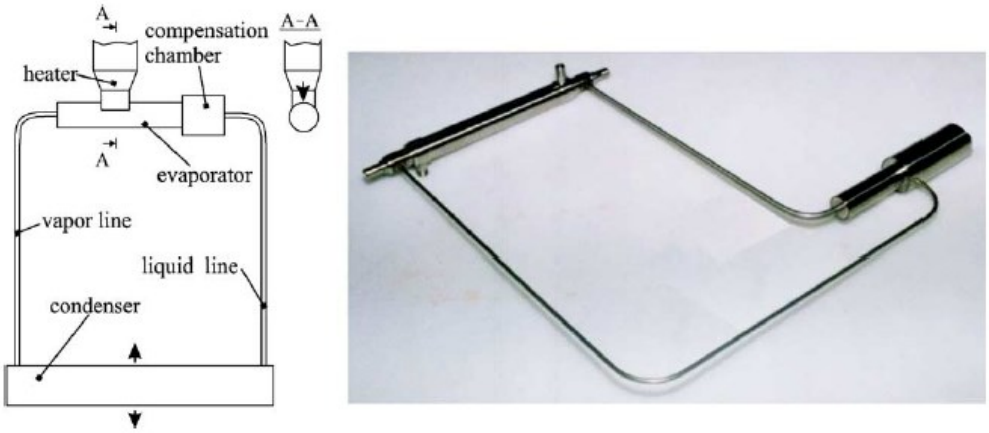

Source: (MAYDANIK, 2005)

Maydanik (2005) concludes that well-designed LHPs may present low-pressure losses related to the liquid circulation inside the capillary structure and inside the transportation sections (vapor and liquid) by selecting different porous wicks, smaller ones in the capillary pump inside the evaporator and larger pores, for other wicks.

The first report of LHP is dated in 1982 by Russian scientists from the Lavochkin Association in cooperation with the Institute of Thermal Physics (Ural Branch of the Russian Academy of Sciences), developed by Gerasimov Yu. F. with his colleagues Maidanik Yu. F. and Kiseev V. M. (GONCHAROV; BARANTSEVICH, 2005).

LHPs showed to be very convenient for aerospace applications, where high efficient heat exchangers able to operate in any orientation regarding the gravity field are required (MAYDANIK, 2005).

3.2.1 Classification of LHPs

The concept of micro heat pipes was first introduced by Cotter in 1984, who developed heat pipes for the thermal control improvement of semiconductor devices. This concept is also used for LHPs. This author points out that the micro heat pipe must be "so small that the mean curvature of the liquid-vapor interface is necessarily comparable in magnitude to the reciprocal of the hydraulic radius of the total flow channel". Mathematically, micro heat pipes must fulfill the condition (PETERSON, 1994):

$$\frac{r_{cap}}{r_h} \geq 1 \tag{2}$$

where r_{cap} is the capillary radius and r_h is the hydraulic radius of liquid flow channel ($4A_{tr}/P$). Based on this definition and according to Ma (2015), the hydraulic diameter of typical micro heat pipe ranges from 10 to 500 μm. For ultra-thin heat pipes, the hydraulic diameter must be in the order of 1 mm (CHEN et al., 2001).

On the other hand, Tang et al. (2018) classified heat pipes differently, where, for electronic applications, a flat-plate heat pipe, with less than 2 mm thickness can be called as ultra-thin heat pipes (UTHPs). In a stricter classification, Aoki et al. (2012) considered conventional heat pipes as ultra-thin if its thickness is less or equal to 1 mm.

Taking into account the fluid flow, Kandlikar (2006) classified the channels through considering its diameter, where, for non-circular channels, the minimum channel dimension is proposed to be used. Table 2 summarizes the classification of heat pipes, according to this author.

Table 2 - Classification of the channels.

Channel classification	D: Smallest channel dimension
Convention channels	> 3 mm
Minichannels	3 mm ≥ D > 200 μm
Microchannels	200 μm ≥ D > 10 μm
Transitional microchannels	10 μm ≥ D > 1 μm
Transitional nanochannels	1 μm ≥ D > 0.1 μm
Nanochannels	0.1 μm ≥ D

Source: (KANDLIKAR, 2006).

LHPs are geometrically flexible devices, which can be designed in a large variety of configurations, adjustable to their applications. Maydanik (2005) proposed a classification of LHP, according to the design of its components, temperature operation range and temperatures control system, as shown in Table 3, which was updated with new configurations shown in literature.

Table 3 - Classification of loop heat pipes.

LHP design	**LHP Dimensions**	**Evaporator shape**	**Evaporator design**
Conventional (diode)	Mini	Cylindrical	One butt-end compensation chambers
Reversible	Micro	Flat disk-shaped	Two butt-end compensation chambers
Flexible	All the rest	Flat rectangular	Coaxial
Ramified	-	-	No compensation chambers
Condenser Design	**Number of evaporators and condensers**	**Temperature range**	**Operating-temperature control**
Pipe-in-pipe	One	Cryogenic	Without active control
Flat coil	Two and more	Low-temperature	With active control
Collector	-	High-temperature	-

Source: Adapted from (MAYDANIK, 2005).

3.2.2 LHP operating principle

Loop heat pipe, despite being robust, presenting high design flexibility, able to operate in wide conditions and presenting high heat transfer capacity, can also be miniaturized.

Figure 10 illustrates the LHPs operational principles. The evaporator receives the heat, which reaches the vapor grooves by conduction. The capillary structures in the grooves is soaked with saturated liquid and evaporation starts. The formed vapor travels through the grooves and reaches the vapor line, flowing to the condenser, where heat is removed and vapor is condensed. The resulting condensate is transported through the liquid line, being subcooled before returning to the evaporator, reaching a compensation chamber, coupled to the evaporator. A wick structure connects the compensation chamber to the evaporator, to guarantee that the evaporator wick is always soaked with liquid.

Figure 10 - Scheme of the operating principle of a loop heat pipe.

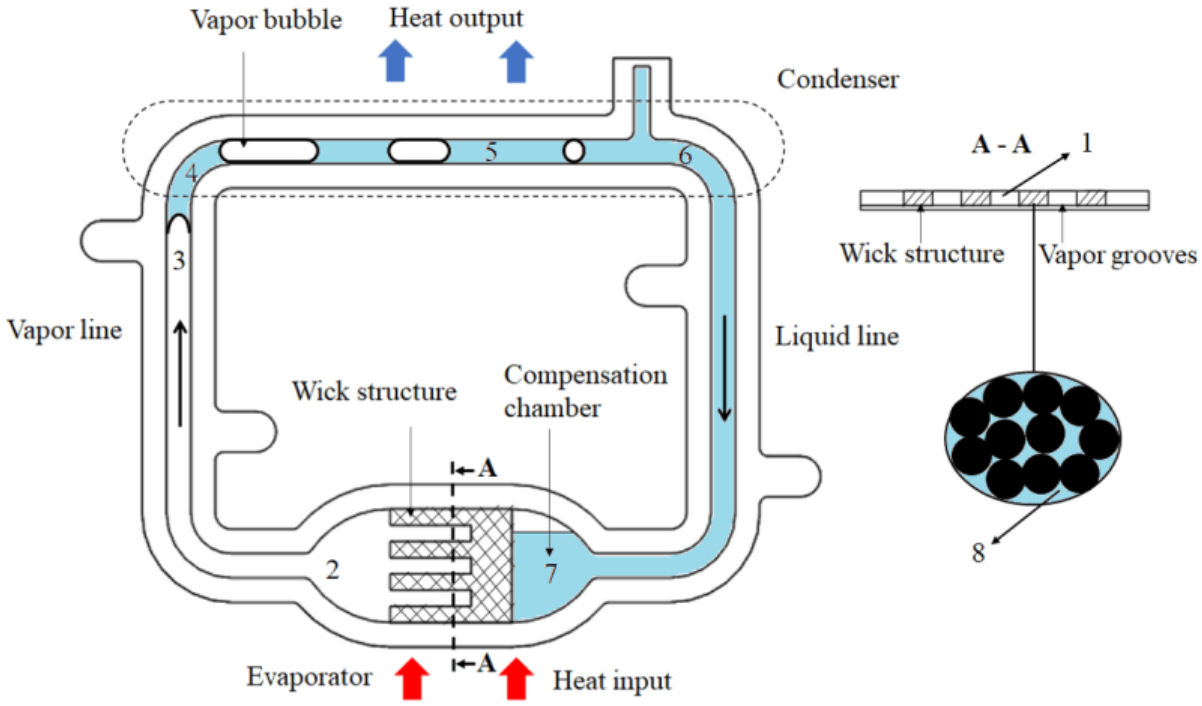

Source: Own authorship.

3.2.3 Thermodynamic cycle of an LHP

The thermodynamic processes that happen in a LHP can be presented in a pressure-temperature plot, in steady-state operation conditions, as shown in Figure 11, which numbered points are those highlighted in Figure 10. The processes are described as:

Figure 11 - Thermodynamic cycle of a LHP.

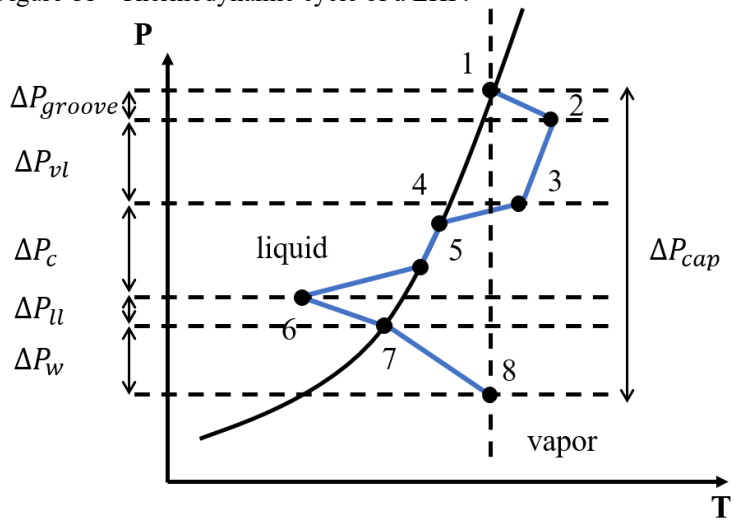

Source: Own authorship.

1 → 2 In the evaporator, superheated vapor is generated, by increasing the saturated liquid-vapor interface (1) temperature to the groove temperature, T_{groove}.

2 → 3 After evaporation occurs, vapor flows through the vapor line until the condenser. In the meanwhile, if the ambient temperature (T_{amb}) is lower than its temperature, heat is leaked to the surroundings. The pressure drops due to friction forces between the vapor and walls, ΔP_{vl}, might be large, depending on the geometry of the vapor line.

3 → 6 When vapor enters the condenser, heat is lost to the ambient by natural convection, or other cooling system, as forced air convection or water flow. The vapor is cooled down until it reaches the saturation temperature (4). The condensation continues up to some point (5), after this point it is subcooled (6) and finally leaves the condenser. The pressure drop between these points can reach large values due to the friction in the liquid-vapor interface, depending on the geometry of the liquid line.

6 → 7 The subcooled liquid flows through the liquid line until it reaches the compensation chamber. If the tube is not isolated and the ambient temperature is larger than the liquid temperature, it receives heat from the surroundings, increasing its temperature.

7 → 8 As heat enters in the evaporator, the liquid flows through the wick structure to the vapor grooves, until it reaches the liquid-vapor interface (8). At this point, the liquid achieves the saturation temperature corresponding to the local pressure.

8 → 1 The gradient pressure between the wick structure and the groove interface gives the capillary pressure delivered by the wick.

3.2.4 Operating limits

The physical phenomena within LHPs can impose limits on their operation, which impair their thermal performance or even stop their functioning. Apart from the capillary limit above mentioned, other limits are critical: boiling, capillary, sonic, viscous, overheating, and entrainment. In LHPs, these limitations have different magnitudes and characteristics compared to conventional heat pipes due to their designs (CHUANG, 2014).

3.2.4.1 Boiling limit

Excess surface temperature related to liquid saturation (overheating) can cause the fluid boiling phenomena at the solid-liquid interface. In conventional heat pipes, heat has to cross the wick structure before reaching the liquid-vapor interface, where the formation of vapor occurs. Due to the separation of liquid and vapor in LHPs, the liquid evaporation might develop at the outer surface in the evaporator wick in a more controlled process (CHUANG, 2003). The formation of bubbles inside the capillary structure of two-phase devices is very inconvenient because vapor can block the return of liquid to the evaporator, and may cause an early dry out of the working fluid (MANTELLI, 2021). According to Kaya and Goldak (2006), trapping vapor in small cavities increases the probability of boiling with less overheating. These authors also stated that improving the contact surface area and increasing the purity of the working fluid reduce the chance of this problem to occur.

Van Oost et al. (2007) stated that vapor formation inside the capillary wick cannot be avoided. For this reason, the vapor must be free to leave the wick structure to guarantee a reliable operation of LHPs. The author mentions two reasons that causes this problem: the presence of non-condensable gases (NCG) solved in the working fluid (subcooled liquid induces bubbles formation when the liquid temperature increases near to saturation conditions) and high parasitic heat transfer rate through the evaporator envelope (casing wall) to the liquid line.

3.2.4.2 Capillary limit

As already stated, the capillary structure must compensate the total pressure drops along the heat pipe during its operation, as expressed by (KU, 1999):

$$\Delta P_t = \Delta P_{vg} + \Delta P_{vl} + \Delta P_c + \Delta P_{ll} + \Delta P_{ew} + \Delta P_{llw} + \Delta P_g \quad (3)$$

where the pressure drop is: ΔP_{vg} in the evaporator grooves, ΔP_{vl} in the vapor line, ΔP_c in the condenser, ΔP_{ll} in the liquid line, ($\Delta P_{ew} + \Delta P_{llw}$) in the evaporator plus liquid line wick structure and ΔP_g is any static pressure drop due to the gravity force.

The wick radius of curvature of the meniscus in the wick structure adjusts automatically as the total pressure of the system reduces or increases, as given by the expression:

$$\Delta P_{cap} = \frac{2\sigma \cos\theta}{r_p} \quad (4)$$

where σ is the surface tension of the working fluid, r_p is the radius of curvature of the meniscus in the wick structure and the θ represents the contact angle between the liquid and the wick. The mass flow and pressure drop increase proportionally. At larger power inputs, the meniscus radius of curvature decrease to provide a larger capillary pumping, adjusted to the total pressure drop. The meniscus continues to decrease until its limit, equivalent to the effective pore radius of the wick structure. If the heat load applied requires a larger capillary pressure than the porous media can provide, the liquid cannot return to the evaporator, and the device fails. Note that component with small thickness may cause larger pressure drops when the fluid circulates (AOKI et al., 2012). To guarantee its operation, the following condition must be satisfied:

$$\Delta P_t \leq \Delta P_{cap} \quad (5)$$

3.2.4.3 Sonic limit

When heat pipes start operating (startup), the vapor velocity may reach its maximum value (sonic) and chock waves can be observed. Under these condition, compressibility effects must be taken into account (REAY; KEW, 2007). Further power levels will result in the evaporator temperature increase while the condenser temperature is not affected, which means that the overall thermal resistance increases, although the device still operates in this condition (FAGHRI, 2014).

3.2.4.4 Viscous limit

In the situation of low heat loads, the heat pipe operation temperatures may reach low values. Under this condition, the viscous forces may be larger than the pressure gradients, and the working fluid may be limited or stay stagnant, reaching the viscous limitation. Usually, this condition is observed in cryogenic applications or during startup of heat pipes from frozen states (CHUANG, 2003).

3.2.4.5 Overheating limit

Heat pipes designed for electronics cooling applications must be able to transfer large amounts of heat to ensure a threshold temperature set by the manufacturer in order to guarantee its integrity. According to Siedel (2015), the maximum operating temperature of electronic components should not exceed 100 ºC. In this way, this temperature limits the heat load applied in the heat pipe, characterizing the overheating limit.

3.2.4.6 Entrainment limit

The entrainment limit is caused by the shear force at liquid-vapor interface. It consists of liquid being entrained into the vapor in its flow towards the condenser (FAGHRI, 2014). As the vapor and liquid phases of the working fluid are separated in LHPs, this limitation is less important than in traditional heat pipes. Nevertheless, at the interface region between the vapor grooves and the evaporator wicks, it is possible that this phenomenon occurs.

3.2.5 LHP components

In this section, the elementary components of the loop heat pipes are presented, highlighting its geometries, capillary structures and working fluids.

3.2.5.1 Evaporator

The evaporator is the most important and critical component of LHP, as its design and thermal characteristics influences significantly the heat transfer capacity of the device. It

consists of an envelope case, a porous wick structure and vapor grooves. Three main geometries are found in the literature: cylindrical, flat and flat disk-shaped, as shown in the Figure 12.

Figure 12 - Evaporator designs.

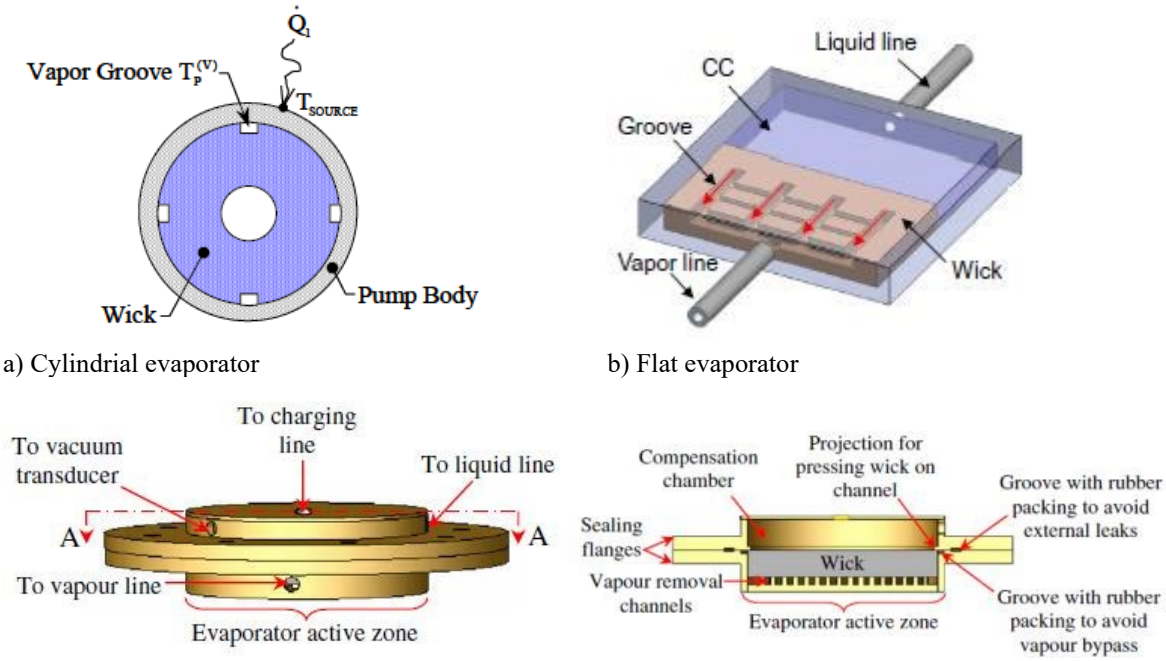

a) Cylindrial evaporator

b) Flat evaporator

c) Flat disk-shaped evaporator

Source: (FUKUSHIMA; NAGANO, 2017); (HOANG; KU, 2003); (SINGH et al., 2010a).

The shape of the first evaporator developed by the Russian scientists was cylindrical, due to manufacturing limitations (GONCHAROV; BARANTSEVICH, 2005). After that, most researches were focused in this design geometry. Recently, as the heat sources application required cooling devices with flat surfaces, such as electronic and aerospace applications, new flat surface geometries started to be considered in the past years. This is the case of the thermal management of modern electronics gadgets, as smartphones and tablets, where larger power dissipation levels are associated to a reduction of the packaging size (LAUNAY; VALLÉE, 2011).

3.2.5.2 Capillary structure

As previously seen, the operation of heat pipe requires a capillary structure, which provides the necessary pumping of the working fluid from the condenser to the evaporator, preventing, in addition, dry regions in the heat transfer device.

Eq. (4) shows that larger capillary pumping are achieved with small diameter pore of the wick structure. However, the decrease of the porous radius causes low permeability of the porous media, with increasing pressure drops.

Figure 13 shows several capillary structures, commonly found in heat pipes. According to Mantelli (2021), usually, for electronics applications, homogeneous structures are preferred, such as screens (e) and sintered metallic powder media (f).

Figure 13 - Types of common capillary structures: (a) comprise tube (b) rectangular groove (c) triangular groove (d) parallel wires (e) wire screens (f) sintered metal powder.

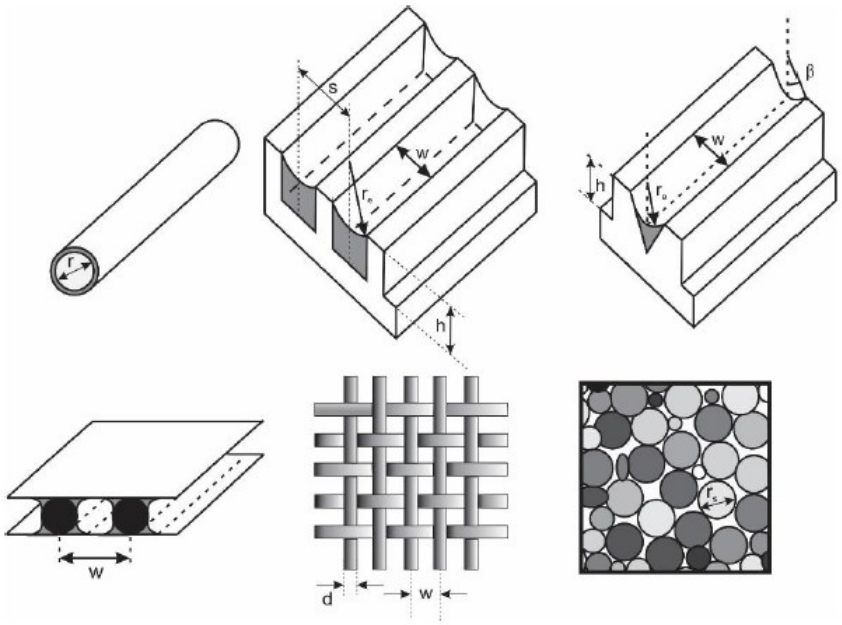

Source: Adapted from (MANTELLI, 2021).

To compare different porous media, the literature suggests the use of the equivalent effective radius concept, where the maximum pumping capacity of the wick is attributed to this wick capillary radius. Chi (1976) proposes the effective radius for several wick structures as shown in Table 4. Generally, for steady-state operation conditions and considering a perfect wetting conditions between fluid and case material (cos θ = 1), Eq. 4 can be used for to relate the effective radius with the resulting capillary pressure by the expression:

$$\Delta P_{cap} = \frac{2\sigma}{r_{eff}} \tag{6}$$

Table 4 - Pore radius of the wick for several wick structures.

Structure	r_{eff}	Data
Circular cylinder (artery or tunnel wick)	r	r = radius of liquid flow passage
Rectangular groove	W	W = groove width
Triangular groove	$W / \cos\xi$	W = groove width ξ = half-included angle
Parallel wires	W	W = wire spacing
Wire screens	$(W + d_{wire}) / 2 = 1 / 2n_{sm}$	W = wire spacing d_{wire} = wire diameter n_{sm} = screen mesh number
Packed spheres	$0.41r_{sp}$	r_{sp} = sphere radius

Source: (CHI, 1976).

In order to fabricate loop heat pipes with high thermal performance and thin thickness, greater care should be given to the capillary structure design. Aoki et al. (2012) recommended a capillary structure formed by metallic mesh or sintered metal to overcome the miniaturization problem. These authors reported that ultra-thin tubes should transfer a maximum power input of approximately 20 W, as shown in Figure 14.

Figure 14 - Dependence on the maximum heat transfer rate with the thickness of the heat pipe.

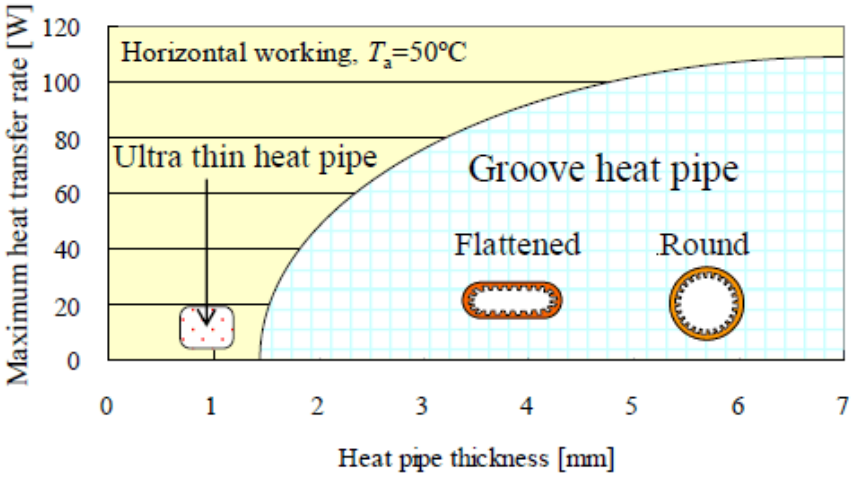

Source: (AOKI et al., 2012).

It should be noted that the evaporator thickness reduction is directly related to the wick thickness reduction. Besides, this reduction increases the parasitic heat flow though the casing material, from the evaporator to the compensation chamber or liquid line. The optimization of the wick structure (improvement of the heat transfer capacity) might be accomplished by combining the parameters: wick material, porosity, permeability and effective thermal conductivity, as is discussed in the sequence.

Several works in the literature suggest the use of different wick material for loop heat pipe as plastic, ceramic and sintered metal powder. Plastic has the advantage of reducing the heat leak from the wick structure to the compensation chamber and/or liquid line due to its low thermal conductivity. However, the porosity of this material is significantly low and the working temperature range is also low because of its maximum tolerable temperature. For high heat fluxes, dry-out might occur and so, case materials with higher thermal conductive are recommended (YAKOMASKIN et al., 2011).

P. D'entremont and Ochterbeck (2005) studied the performance of two ceramic wicks, iron oxide and silicon oxide, applied inside the evaporator of a capillary pumped loop (CPL) and a LHP. The authors show advantages against the plastic material, as they may support higher temperatures and heat fluxes. Its thermal conductivity is lower compared to metals, but higher than plastic. Its porosity can be lower as 33% for the iron oxide and 57% for the silicon oxide. They concluded that ceramics are, actually, good for LHP applications. In electronics cooling, non-metal wick structure with low thermal conductivity can provide a lower heat leak, allowing the design of ultra-thin loop heat pipes (SINGH et al., 2010b).

The sintered metal powder is the most used material in heat pipes. Its usual effective pore radius is of the order of 2 μm, they present high porosity (55-75%) and the permeability ranges between 10^{-12} to 10^{-13} m^2 (HOANG et al., 2003). The usual metal powder used for sintering power wicks are: copper, stainless steel, nickel and titanium. Singh et al. (2009a) developed and tested ultra-thin loop heat pipe with different types of copper and nickel wick structures. The authors demonstrated that the copper wick showed superior thermal performance than the nickel wick. However, the parasitic heat from the evaporator to the compensation chamber or liquid line are larger for copper wicks.

The wick porosity is defined as the ratio between the volume occupied by the solid material and the total volume of the capillary structure. Chen et al. (2001) studied the effect of porosity with different sintered copper powder wicks in ultra-thin heat pipes. They concluded that the porosity has large influence on the maximum heat transfer rate: a slight increase in the porosity as (10%, for instance) can double the heat transfer ability of the wick structure. Taking a powder material, the parameters: time, temperature, pressure and geometry of the powder particles, can be selected in order in order to obtain different porosities of the wick structure (FLOREZ et al., 2014).

The permeability is the parameter that measures the ability of a liquid to be transported through a porous medium, when subjected to a pre-defined pressure difference (FLÓREZ

MERA et al., 2017). As this parameter is directly proportional to the sample thickness, the miniaturization has a negative impact in the wick transportation capacity. For LHP applications, the wick permeability has to be high to ensure a good liquid flow through the porous media, not causing high pressure drops. To calculate the permeability for a specific difference of pressure, the Darcy law is applied (REAY; KEW, 2007):

$$K_w = \frac{\dot{m}\mu_l \delta_w}{\rho_l A_w \Delta P_w} \tag{7}$$

where $\dot{m}$ is the mass flow rate, μ_l and ρ_l is the dynamic viscosity and density of the liquid, respectively, δ_w represents the wick thickness, A_w is the flow cross-sectional area and ΔP_w consists of the capillary pressure across the wick.

The pore diameter is an important design parameter to specify the flow characteristics of the wick. Its value influences the capillary radius of curvature, porosity and permeability. As already commented, small pore sizes provide higher capillary pressure and may guarantee the fluid flow along the LHP, even against the gravity. On the other hand, decreasing the porous diameter, the fluid flow pressure drop rises proportionally, in the limit causing porosity obstruction.

Singh et al. (2009) studied the effect of pore size with two samples. The authors concluded that small pore radius provides a better thermal performance for UTLHP, reducing the vapor temperature by approximately 12%. Besides, their small pore diameter wicks were able to block the vapor, avoiding vapor to flow from the evaporator to the compensation chamber, a very undesirable situation. Their results also showed that biporous wicks (use of two characteristic pore sizes) are able to greatly improve the thermal efficiency of the LPH, by 12% when compared to the monoporous wick. They used small pore wicks to provide a path to the liquid flow and larger pore wicks for the vapor flow.

The wick effective thermal conductivity is a parameter of great interest to LHP design, as it can determine the heat spreading velocity from the evaporator envelope to the evaporation zone. It also establishes the heat leak (conduction of parasitic heat) from the evaporator and wick structure to the compensation chamber or liquid line. There are a huge number of correlations that can be used to predict the effective thermal conductivity. This property depends on the material, geometry parameter, porosity, the mean pore diameter and the pore size distribution. Florez et al. (2013) proposed a model for the prediction of this parameter

formed by sintering powder metal over flat surfaces based on heat transfer phenomenological aspects and uses the mean diameter of the spheres (powder particles).

As a part of the optimization of the LHP wick structure, the heat transfer between the evaporator wall and the evaporation zone (vapor grooves) must be improved, the formed vapor must be isolated from the liquid line or compensation chamber and the parasitic heat must be decreased as much as possible. According to Siedel (2015) the vapor channels or vapor grooves has two main functions: to provide a thermal path to the conductive heat transfer from the evaporator envelope to the liquid-vapor interface and to guarantee that the vapor reaches the vapor line.

The main studies of wick structures are for loop heat pipes with cylindrical evaporators (KISEEV et al., 2010) (SINGH et al., 2014) (CHOI et al., 2013). However, the first flat evaporator was patented in 1975 to overcome heat sources that require cooling with flat surface (MAYDANIK et al., 2014). Since then, some researchers as Zhang et al. (2012) evaluated LHP with flat evaporator and different vapor grooves as shown in Figure 15. The authors concluded that the heat transfer coefficient of the evaporator with vapor groove inside the wick (i) is higher than inside the wall envelope (ii). Their model predicted an optimum ratio of height and width ($\alpha = H_v / W_v$) for the vapor groove as 1, concerning its thermal performance. For the wick width parameter ($\beta = (W_w - W_v) / W_v$), the recommendation varies from 0.5 to 1, the smaller is this parameter, the lower is the wick temperature.

Figure 15 – Flat evaporator with different vapor groove.

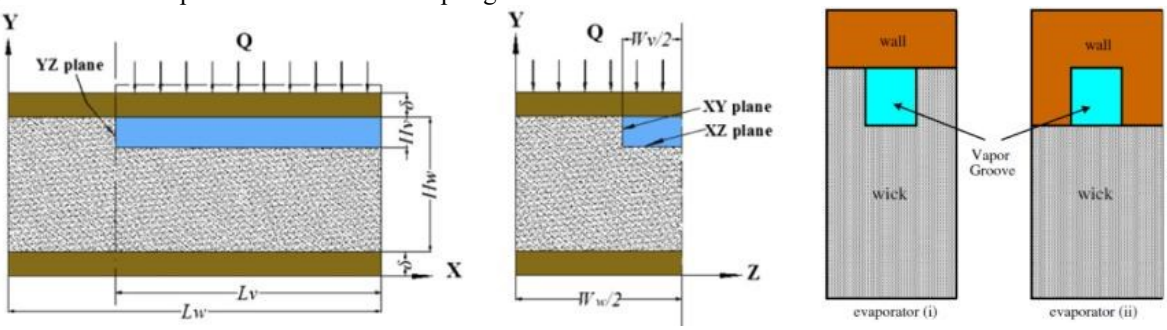

Source: (ZHANG et al., 2012).

The compensation chamber (or reservoir) is an important component of the LHP. Its major function is to maintain the evaporator wick always saturated with liquid to prevent early dry-out. Usually, the reservoir internal volume is a little larger than the combined volume of the vapor line and the condenser (HOANG et al., 2003).

In LHPs, the compensation chamber (CC) is an integral part of the evaporator. If the conduction of heat from the evaporator to the CC is considerable, vapor can be formed in the CC, which may tend to flow through the liquid line, blocking the device and avoiding the startup, especially under low heat loads (KU, 1999). This is a huge problem for miniaturized devices particularly for in ultra-thin loop heat pipes. It is quite important to remember that electronics applications require that the LHP starts-up with low heat inputs, such as 2 W. For this reason, one solution could be the removal of the CC.

The vapor and liquid channels are the transport lines, that connect the evaporator to the condenser. According to Launay and Vallée (2011), some requirements must be applied for selecting their geometries:

- The wall thickness must be dimensioned taking into consideration the material to be applied and the necessary pressure.
- The transport line length is defined by the heat source and the heat sink position.
- The cross-section area of the liquid and vapor channels are adjustable parameters, as larger areas provide lower pressure drops, while devices with small channels are smaller and more flexible.

If the vapor transport lines are not sufficiently thermally isolated from the surroundings, it may work as a condenser. Siedel et al. (2013) concluded that vapor lines may supply all the condensation before the liquid enters the condenser, being subcooled along the condenser.

The second most critical component of the LHP is the condenser. Its function is to remove the heat received from the evaporator. The heat transfer in the condenser consists of the working fluid condensation, conduction through the heat sink envelope and walls, convective heat transfer dissipated (air, liquid, radiation, depending on the cooling system). Some of these condensers, found in the literature are shown in the Table 5 (LAUNAY; VALLÉE, 2011).

Table 5 - Classification of the condenser elements.

Condensation cross-section	Thermal link	Modes of external heat transfer
Circular	Plate heat exchanger	Air forced convection
Annular	Finned heat exchanger	Air natural convection
	Tube-in-tube heat exchanger	Liquid forced convection
		Radiative heat transfer

Source: (LAUNAY; VALLÉE, 2011)

Maydanik and Vershinin (2009) compared the effect of air and water cooling of UTLHP condensers. They concluded that the heat transfer capacity and the thermal resistance of the device is limited by condenser cooling conditions, being the major governing parameter for the heat transfer capacity of the condenser. For this reason, the geometry of the condenser is over-sized to transfer the maximum heat with lower thermal resistance (LAUNAY et al., 2008).

Based on this conclusion, one can say that the cooling method is the major limitation to actual application of LHPs. For example, for mobile electronics, the condenser is under natural convection without any active cooling system, limiting the transportation of heat from this device (ZHOU et al., 2016).

The working fluid has the task of transferring latent heat from the evaporator do the condenser. According to Siedel (2015), the working fluid selection must fulfill some criteria as:

- The operating temperature and pressure ranges must be considered in the mechanical design of the device, to avoid mechanical deformations.
- The triple point temperature of the working fluid must be lower than the lowest operation temperature level.
- Fluids with a large latent heat of vaporization should be value to obtain higher energy transfer rates and lower pressure drop with low mass flow rates.
- The liquid surface tension should be high enough to provide the necessary capillary pressure.
- The density of the vapor must be high in order to reduce its velocity and pressure drop along the device.
- The fluid must be chemically stable, non-corrosive and pure, preventing the generation of non-condensable gases (NCG) during the LHP operation.

The chemical compatibility between the working fluid, capillary structure and the envelope material must be also respected in order to avoid the formation of non-condensable gases that would block some regions of the LHP, jeopardizing its operation. Mishkinis et al. (2010) collected working fluid/material compatibility data from several works in the literature, reproduced in Figure 16. The compatibility parameters depend on many factors such as cleanliness, fluid purity, quality of the tube manufacturing process and others.

Figure 16 - Chemical compatibility between working fluid, capillary structure and wrapping material by several authors in the literature.

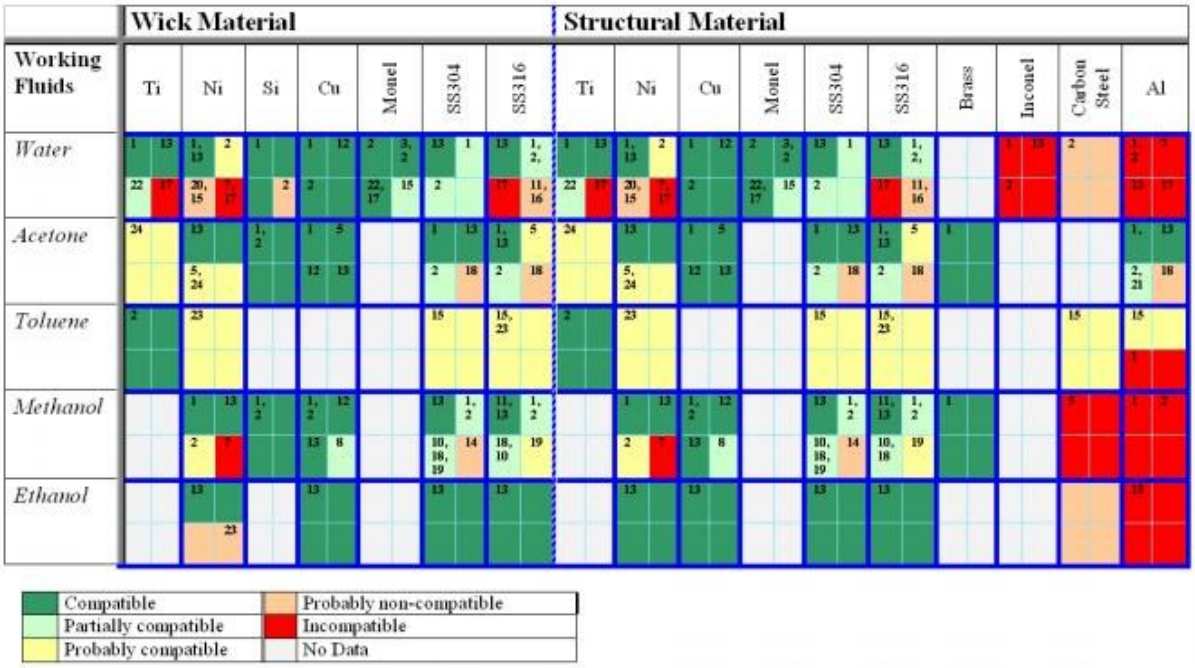

Source: (MISHKINIS et al., 2010)

Non-condensable gases can be produced by other factors, especially those involving manufacturing process (envelope cleaning) and impurities within the working fluid. (KU, 1999).

Choosing the best working fluid for each device is not a simple task. To help with the fluid selection, Reay and Kew (2007) developed a parameter that they denominated as the merit number, which represents the maximum heat transfer capacity of the working fluid, to a specific operating temperature. This criterion is expressed as:

$$M = \frac{\rho_l \sigma h_{lv}}{\mu_l} \tag{8}$$

where h_{lv} is the latent heat of vaporization of the working fluid. Figure 17 shows the merit number behavior as a function of the operating temperature, for several working fluids found in the literature.

Figure 17 – Merit number for commonly used heat pipe workind fluids.

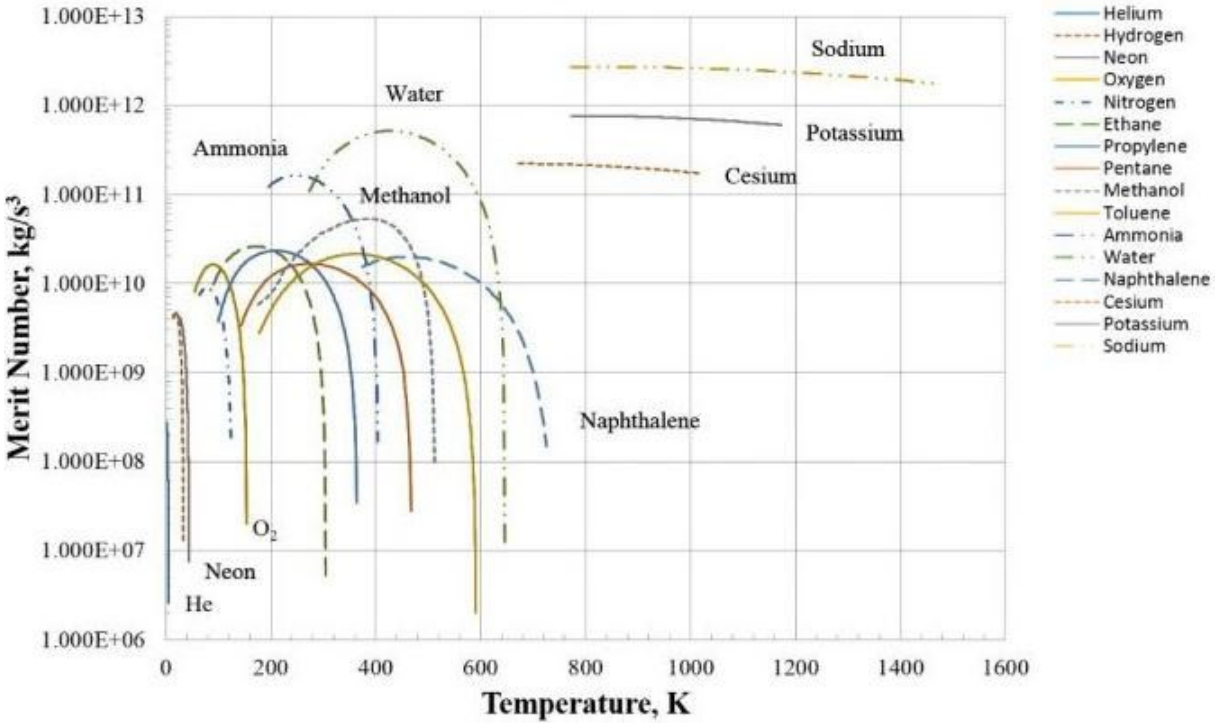

Source: (ACT, 2020).

From Figure 17, it is very clear why water is the most used working fluid in heat pipes. Its heat transfer capacity is approximately ten times larger than other usual fluids, except liquid metals.

4 MANUFACTURING AND EXPERIMENTAL PROCEDURE

Once the components of the loop heat pipe are defined, the manufacturing technique must be selected. This section presents the manufacturing procedure used, including sintering and diffusion bonding. The experimental set-up and test procedure adopted in order to analyze the thermal performance of the UTLHP and resulting experimental uncertainties are also shown.

As mentioned, the studied UTLHP was designed for the thermal management of electronics, especially for smartphones. Table 6 presents the overall dimensions of Apple's smartphone during its development in the past years. One should note that the smallest mobile phone width is 67 mm. It is also notable that, despite the industry work to produce more compact and thin mobiles, the new features added to the device are making them thicker in the past smartphone generations. The problem in obtaining ultra-thin smartphones is mostly related to the difficulty in removing the heat from the processors.

Table 6 - Apple smartphone dimensions through its development.

Smartphone	Dimensions	Release year
Iphone 6	138.1 x 67 x 6.9 mm	2014
Iphone 6 Plus	158.1 x 77.8 x 7.1 mm	2014
Iphone 8	138.4 x 67.3 x 7.3 mm	2017
Iphone 11	150.9 x 75x7 x 8.3 mm	2019
Iphone 12	146.7 x 71.5 x 7.4 mm	2020

Souce: (APPLE, 2021).

4.1 MANUFACTURING

Figure 18 shows the external and internal view of the proposed UTLHP. It is composed mainly of seven components: evaporator, evaporator wick structure, vapor line, condenser, liquid line, liquid line wick structure and a tube line for charging the working fluid. The UTLHP is designed to remove heat from chip processors of smartphones and tablets. The fabrication method was established to produce a very thin LHP, avoiding the deformations that would reduce the thermal performance of loop heat pipes and its lifespan (Tang et al., 2018). This work UTLHP was manufactured through sintering and diffusion bonding process.

Figure 18 – The prototype of the flat UTLHP (a) external view (b) internal view.

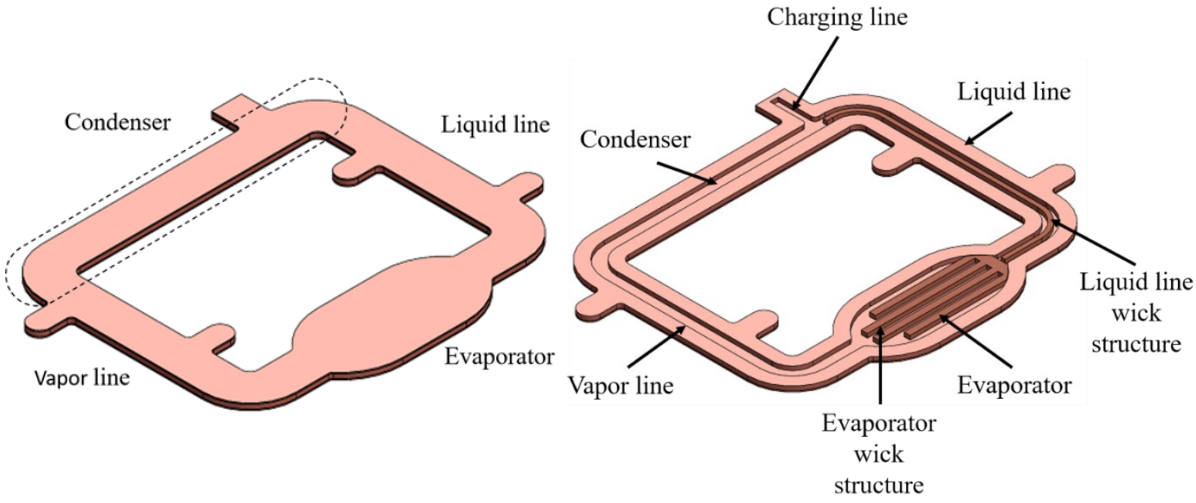

Source: Own authorship.

Four ultra-thin flat loop heat pipes were fabricated with three copper sheets in sandwich arrangement: two external closing sheets of 0.3 mm of thickness and a slotted inner layer sheet, of 0.3, 0.5 or 1.0 mm thick. The internal plate thickness represents the height of the working fluid channels, which are formed by their slots (see Figure 19). Water jet cutting technique is used to produce these complex geometries (FLOW, 2021). Figure 19 shows the copper sheets components of the UTLHP after the cutting process.

Figure 19 – Components of the loop heat pipe.

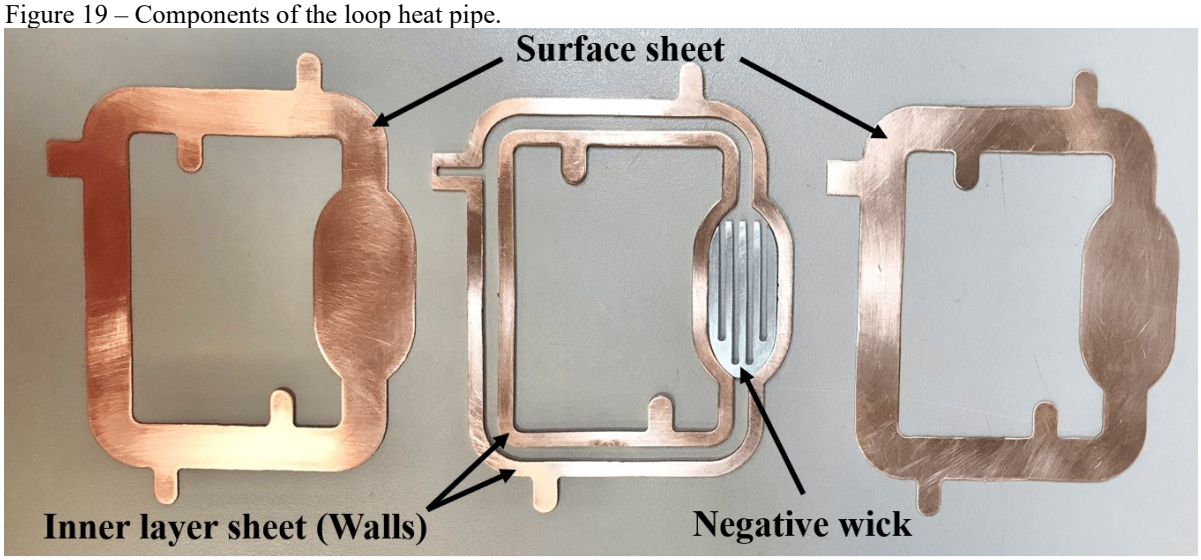

Source: Own authorship.

As shown in Table 6, besides the wall difference, the first UTLHP tested is composed of only one wick structure, located in the evaporator, i.e., no capillary structure is inserted in

the liquid line. Theoretically, the capillary force developed at the liquid-vapor interface in the evaporator wick structure is sufficient to pump the fluid from the condenser to the evaporator, completing full circulation. In the other three devices, a liquid line wick structure is provided. Actually, the evaporator and liquid line porous media are made of the same material (sintered cooper powder) and have similar properties, but different thickness, according to thickness of the internal plate used. Table 7 summarize the design characteristics of the proposed UTLHPs.

Table 7 – Design characteristics of the mini loop heat pipes studied.

Loop heat pipe	Inner Layer Sheet - δ_{wall} (mm)	Porous media	Liquid line wick structure
A	1.0	Sintered copper	No
B	1.0	Sintered copper	Yes
C	0.5	Sintered copper	Yes
D	0.3	Sintered copper	Yes

Source: Own authorship.

The maximum external dimensions of the constructed UTLHP are 76x60 mm. Their evaporators hold five vapor grooves (channels) of 1.3 mm width, used to remove the vapor formed in the evaporator direct to the vapor line. The evaporator wick structure consists of four branches in teeth format, with 1.5 mm of width each. A vapor barrier is employed to guarantee that vapor does not flow back to the liquid line and consists of the same sintered copper powder, with approximately 2.6 mm of length. The liquid line wick structure follows the liquid line geometry and is located in its center (in the transversal direction), holding a width of 1 mm, which leaves a passage of 1 mm in each side. The designed prototype does not include the compensation chamber, as in conventional loop heat pipes, to avoid heat leaks and to save space in electronic applications. As mentioned, the only variable parameter of the tested UTLHPs are the inner layer sheet (δ_{wall}) and the wick structure thicknesses, which are actually related. Figure 20 shows all dimensions of the devices.

Figure 20 – Schematics of the UTLHP with its dimensions. All dimensions are in mm.

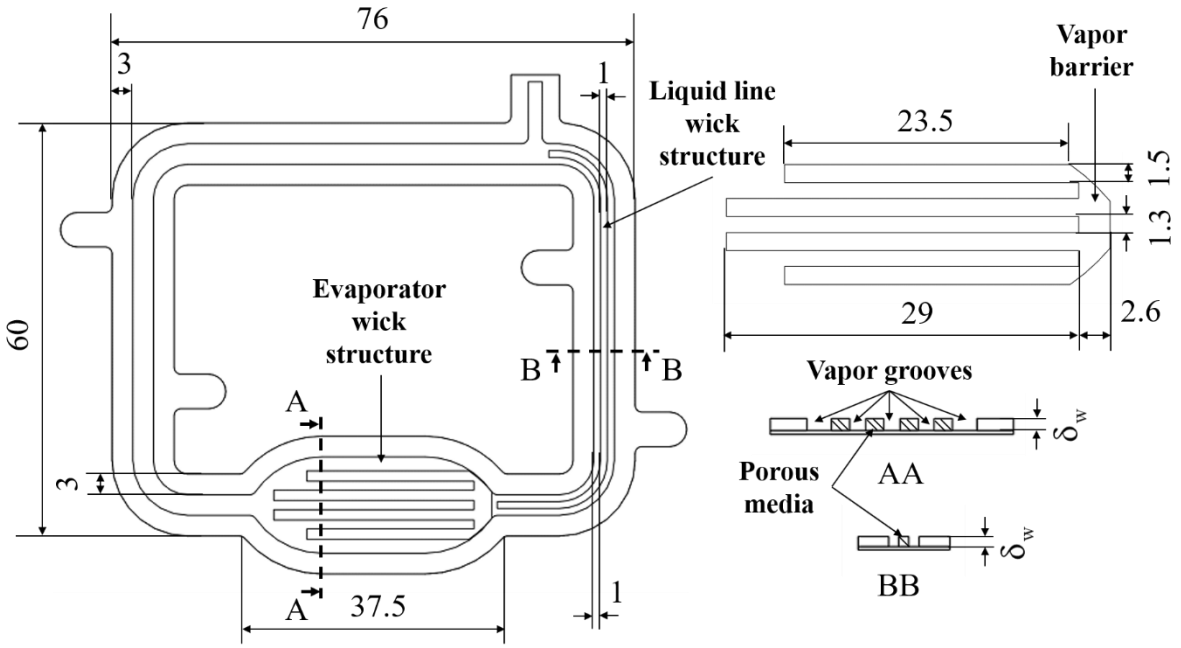

Source: Own authorship.

Table 8 lists the main parameters of the ultra-thin flat loop heat pipe components. Ethanol and distilled water were selected as the working fluids, based on startup considerations, heat transfer characteristics and physic-chemical compatibility with cooper, the material used for the plate and porous media powder.

Table 8 - The main specifications of the ultra-thin loop heat pipe.

UTLHP	Overall size	Dimensions (mm)
Evaporator	Size (LxW)	37.5 x 20
	Heating area (LxW)	10 x 10
Evaporator wick	Overall dimensions (LxW)	23.5 x 1.5 / 29 x 1.5
Liquid line wick	Size (LxW)	70.49 x 1
Vapor line	Channel size (LxW)	79.17 x 3
Liquid line	Channel size (LxW)	79.17 x 3
Condenser	Channel size (LxW)	46 x 3
Working fluids	Ethanol and distilled water	

Source: Own authorship.

4.1.1 Sintering

Sintering is defined by the thermal treatment of metallic powder particles resulting in a coherent, predominantly solid structure, via mass transport events that often occur on the atomic scale (GERMAN, 1996).

According to Exner and Arzt (1990), the essential difference between porous and dense solid bodies of the same material and identical mass is, from an energetic point of view, the excess of free energy due to broken atomic bonds at the surfaces of the porous material. Figure 21 shows microscopic pictures of the sintering process of spherical copper particles at 1300 K for one hour (left) and eight hours (right).

Figure 21 – Sintering process of spherical copper particles at 1300 K for one hour (left) and eight hours (right). 150x.

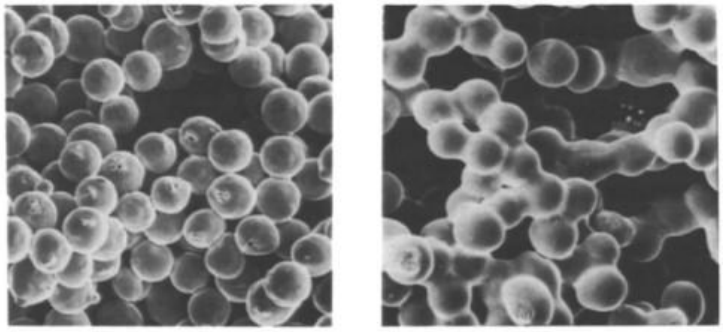

Souce: (EXNER; ARZT, 1990).

Typically, particles smaller than 1 mm size, such as spheres, cubes, wires, flakes, disks, snowflakes or others tend to bond (sintering) when heated to a relatively high temperature, usually 70% to 90% below the absolute melting temperature (REAY; KEW, 2007). The porosity of the sintered material can be controlled by pressure application (GERMAN, 1996). Other parameters also influence the final properties of the sintered material, such as: time, temperature, size of particle and atmosphere and depend on the material to be sintered. The control of the atmosphere is important in order to avoid the oxidation. Some inert atmosphere can be used: methane, butane, propane, dissociated ammonia, controlled mixture of nitrogen and hydrogen and pure hydrogen (LENEL, 1980).

In the present study, the wick structure of the capillary pump (evaporator) was formed by sintering copper powder, in a non-assisted pressure process carried out in a *JUNG*^{TM} Furnace, Model 1513, which reaches a maximum power of 8.5 kW and temperatures of 1300 ºC. Figure 22 summarizes the sintering process employed. Initially, the equipment (see Figure 23) raises the temperature up to 875 ºC in 4980 seconds, where it holds for 3600 seconds. After that, natural convection air cooling takes place, until the device reaches a temperature close to the ambient temperature, around 25 ºC.

Figure 22 - Sintering and diffusion bonding temperature with time conditions.

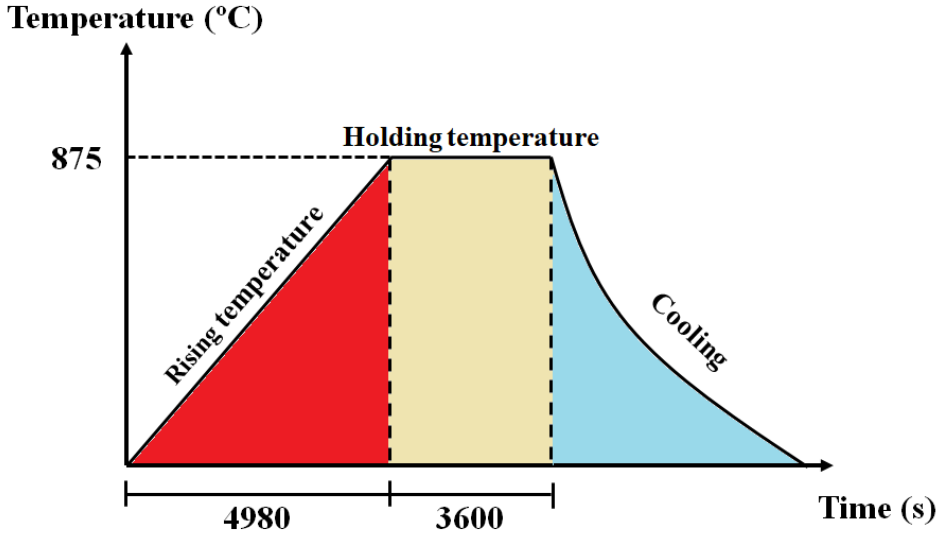

Source: Own authorship.

The quality (particles diameter and circularly factor) of the cooper powder to be used must be carefully controlled, so that the resulting wick has the desired properties, such as: porosity, effective thermal conductivity, permeability and porous radio. Previous wicks were fabricated by Mera (2016) at the Heat Pipe Laboratory at UFSC, resulting in a wick structure with the properties shown in Table 9. Exactly the same copper powder and sintering procedure was adopted in the present work, so the Table 9 parameters are assumed in the present work. For more information and details about the porous media see (MERA, 2016).

Table 9 - Properties of the copper sintered porous media.

Properties	Powder C
Particle average diameter [µm]	49.72
Porosity [%]	53.46±3.87
Permeability [m²]	$1.99 \times 10^{-12} \pm 1.02$
Effective porous radio [µm]	21.04±2.2

Source: (MERA, 2016).

The effective thermal conductivity was calculated with the following equation (PETERSON, 1994); (REAY; KEW, 2007):

$$k_{eff} = k_s \left[\frac{2 + (k_l / k_s) - 2\varepsilon(1 - k_l / k_s)}{2 + k_l / k_s + \varepsilon(1 - k_l / k_s)} \right] \quad (9)$$

where, ε represents the porosity, k_{eff} is the effective thermal conductivity, and k_s and k_l are the thermal conductivity of the solid and liquid, respectively.

Basically, the shape of the wick structure in the evaporator and liquid line was obtained by spreading loose copper powder over a negative piece of stainless steel, as shown in Figure 19. Stainless steel was selected to ensure that the copper powder will not bond to the stainless steel at the molecular level, during the copper powder sintering process. After sintering, the negative is removed and the wick structure has formed the required geometry.

The alignment of the water-machined cut plates is essential for the success of the fabrication of the LPH. For that, four some metallic protuberances (here denominated as “ears”) are provided along the device, as one can see in Figure 18 and in Figure 19.

The following steps were used for the fabrication of the desired wick structures. First, all sheets and support pieces are intensively cleaned by screwing, brushing and soaking into a pure acetone solution, to ensure good joining process. Second, spot-welding process, using the Spot Welder Messer Griesheim of *PECO WIDERSTANDS-SCHWEIBTECHNIK*^{TM} , as shown in the Figure 23(a) is realized over the “ears” to join the base plate with the internal plate. Third, the negative wick structure is inserted and fourth, the copper powder is deposited. After that, the whole apparatus is put in the oven, for the sintering of the copper power, according to the heating/cooling steps shown in Figure 22.

Figure 23 - Machines used in the manufacturing process: (a) Spot welder and (b) Furnace.

(a) (b)
Source: Own authorship.

Figure 24 shows the resulting wick structures for the four LHP samples fabricated and tested in this work.

Figure 24 - Sintered porous media for each wall thickness.

$\delta_{wall} = 0.3mm$ $\delta_{wall} = 0.5mm$ $\delta_{wall} = 1.0mm$

Source: Own authorship.

4.1.2 Diffusion bonding

A manufacturing process used for fabrication of different models of heat pipes is the diffusion bonding. Figure 25 presents a schematic of this process, which consists in diffusion of metallic surfaces at solid state in contact, under the action of high pressure and high temperature, during a determined period of time. Polishing the surfaces to be joined is very important in order to guarantee the quality of the fabricated device. Unlike other joining processes, it preserves the microscopic structure at the interface. Despite that, thermal gradients must be avoided in the devices joined by diffusion bonding, to prevent deformation and stress at the interfaces (RUSNALDY, 2001).

Figure 25 - Manufacturing process through diffusion bonding: formation mechanisms at the interface. (a) localized plastic deformation; (b) filling in remaining voids and (c) interfacial movement of grain outlines.

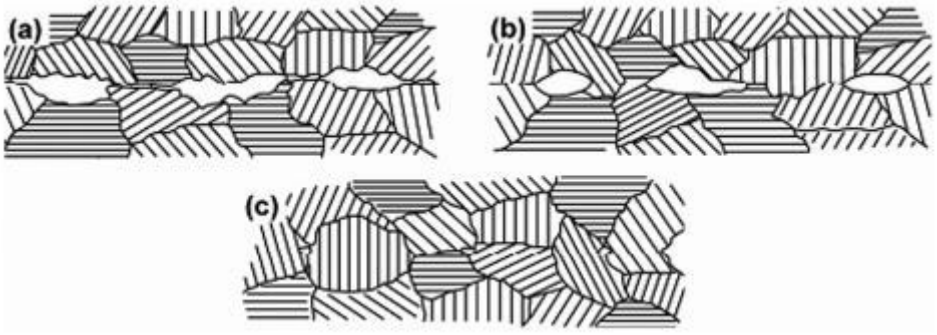

Source: (MORTEAN et al., 2016).

This manufacturing method has some advantages, as mentioned by Rusnaldy (2001), such as maintenance of properties and microstructures similar to the bulk material after joining, so that the joined pieces can be thinner and with less weight. In addition, it is expected that the formed parts have minimal deformation. Besides, the major advantage is the possibility of

making several joint simultaneously. On the other hand, as disadvantages it is observed: the equipment (ovens) necessary to carry out the process are expensive, the manufacturing time (using a thermal cycle) is longer than those observed in conventional processes and, finally, greater care should be taken during the preparation of the surfaces.

Betancur-Arboleda et al. (2020) used the diffusion bonding process to fabricate flat pulsating heat pipes with square and circular channels. The authors concluded that the square channel showed large deformations, while circular ones revealed less visible, as shown in Figure 26. Their results indicate that fabricating devices with square channels must be carefully analyzed.

Figure 26 – Square and circular cross-sectional deformation due to the diffusion bonding process.

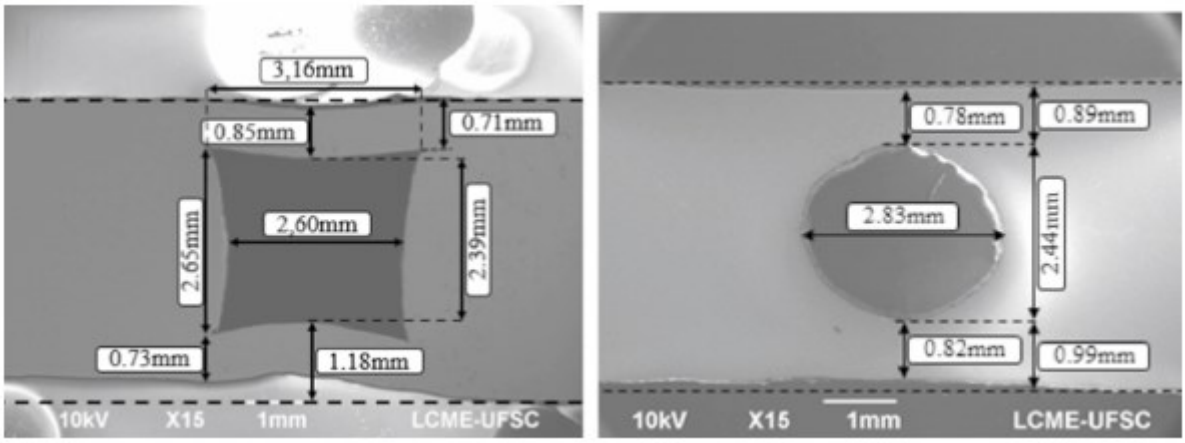

Source: (BETANCUR-ARBOLEDA et al., 2020).

As mentioned, diffusion bonding was used in the fabrication of the ultra-thin flat loop heat pipe in the present work. Using this process, all the LHP components, that is, evaporator, condenser and working fluid channels, are produced at once, in a single process. Therefore, the pressure must be evenly distributed along the device. Two stainless steel plates, with very similar geometry of the LHP internal plate (external dimensions approximately 0.5 mm larger), were manufactured using the same water-cutting process mentioned before, and were located above and below the pile (see Figure 27) in order to guarantee uniform pressures along the UTLHP, even if a slight non-alignment of the sheets may occur. Besides that, these additional plates reduce the chance of any deformation inside the square channels. The stainless-steel plate at the evaporator region was fabricated with no holes in order to certify a good attachment between the wick structure and both external cooper surface sheets, avoiding gaps where vapor could leak and return back to the liquid line. Again, spot welding at the “ears” are used to join

the plates. The final step consists of inserting a charging line of copper (umbilical) for working fluid loading.

Figure 27 – Exploded view of the difussion bonding process employed.

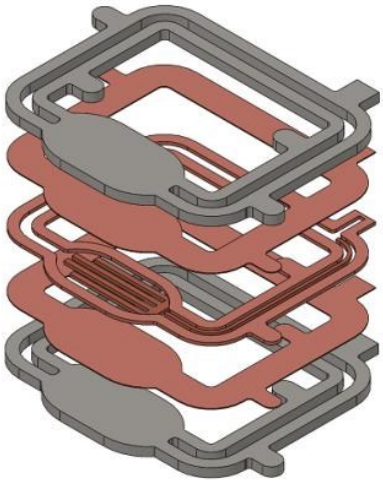

Source: Own authorship.

In addition to the stainless-steel plates, a stainless-steel matrix was fabricated, to apply, by controlled torque on thirteen M10 screws, the desired pressure for diffusing bonding, as shown in Figure 28. Each screw can hold 130 N.m, without deforming.

Figure 28 - Assembly process with the UTLHP and its matrix.

Source: Own authorship.

Figure 29 shows the resulting devices, demonstrating that the diffusion bonding process caused small deformations along the entire ultra-thin loop heat pipe.

Figure 29 - Results of the UTLHP after diffusion bonding process.

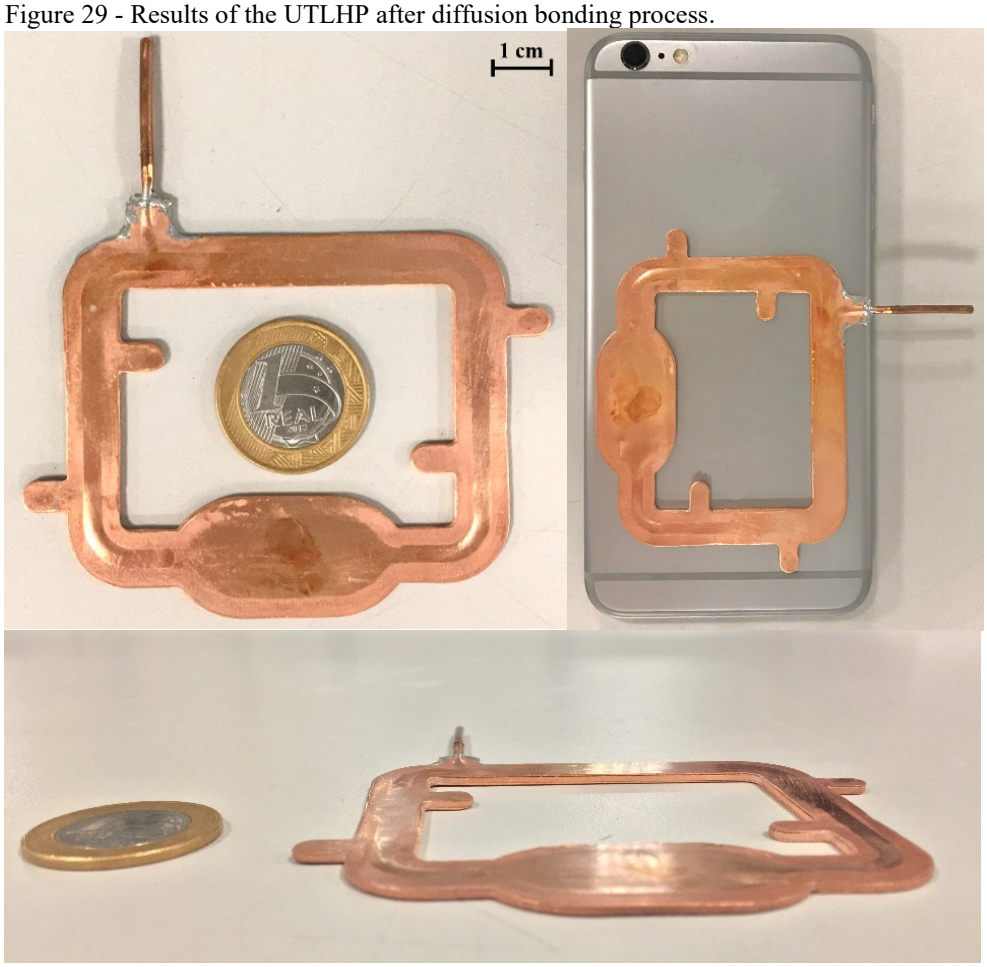

Source: Own authorship.

Sealing is also an important fabrication concern. For this reason, the diffusion bonding must be successful, ensuring a molecular joining of the copper sheets. To certify the sealing, after fabrication, a leak test is executed with the *PFEIFFER VACCUM*^{TM}, model ASM340. All the UTLHP passed in the leakage tests.

After concluding the manufacturing process, a cleaning procedure was employed. Pure acetone and isopropyl alcohol are separably inserted, two times, to remove any oils, metal filings or other substances that could produce non-condensable gases.

4.2 EXPERIMENTAL PROCEDURE

In order to evaluate the thermal performance of UTLHP, several tests were carried out. The experimental procedure to evaluate the operation of UTLHP consisted basically of three steps: remove any working fluid inside the device using a cleaning pump and evacuate with a vacuum pump (see Figure 30), charge the UTLHP with the desired fluid volume and connect

to the experimental set-up. An experimental test bench was specifically designed for this procedure, as shown in the schematics of Figure 31(a).

The experimental set-up is simple. Heat is delivered in the evaporator by an electrical heater and the condenser is cooled by natural convection. A data acquisition system (DAQ-NI^{TM} SCXI-1000) collects the data information (thermocouple temperature and power input readings) that are stored and processed on a computer.

Figure 30 - Vacuum pumps used in cleaning process: (a) Nel liquid and (b) Turbomolecular station.

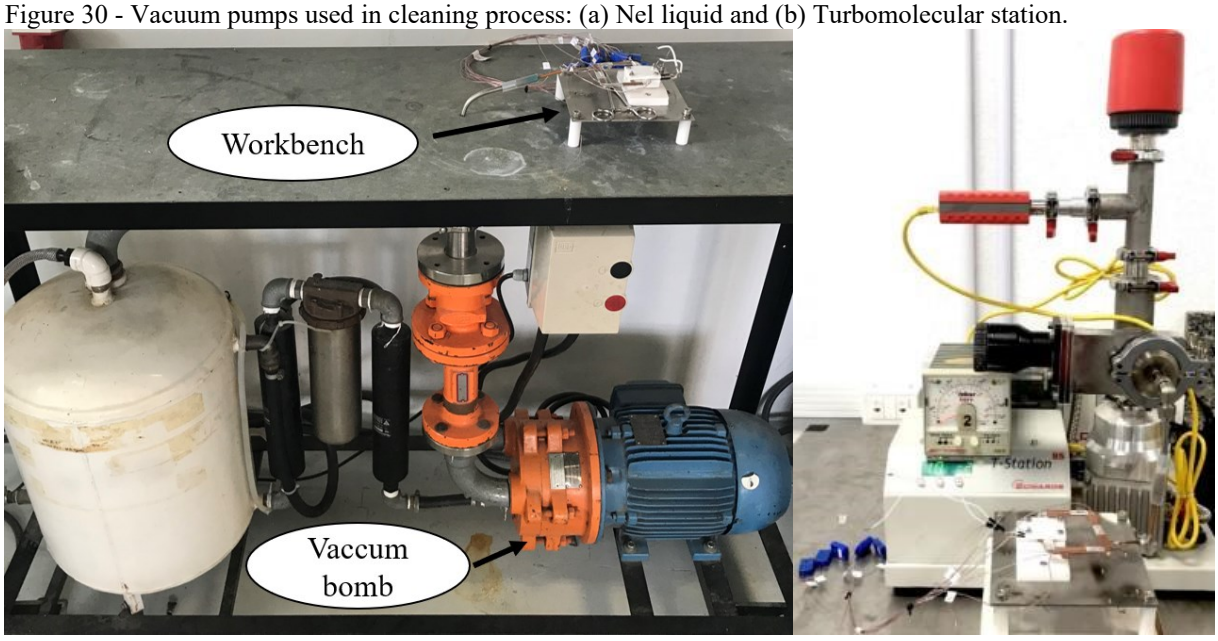

(a) (b)

Source: Own authorship.

Seven T-type thermocouples from Omega Engineering^{TM} are used to measure temperature in specific points of the UTLHP thermal behavior, fixed on the outer surface by a thermosensitive adhesive strip Kapton^{TM} and a metallic adhesive tape. Thermocouple T_1 is located on the heating surface of the evaporator. Thermocouple T_2 represents the evaporator outlet. Thermocouples T_3, T_4, and T_5 are distributed in the inlet, middle region and outlet of the condenser section, respectively. Finally, the thermocouple T_6 is located at the evaporator inlet. In addition, a thermocouple T_{amb} measure the ambient temperature.

Figure 31 – Experimental apparatus: (a) Schematic of the experimental set-up and (b) thermocouples distribution.

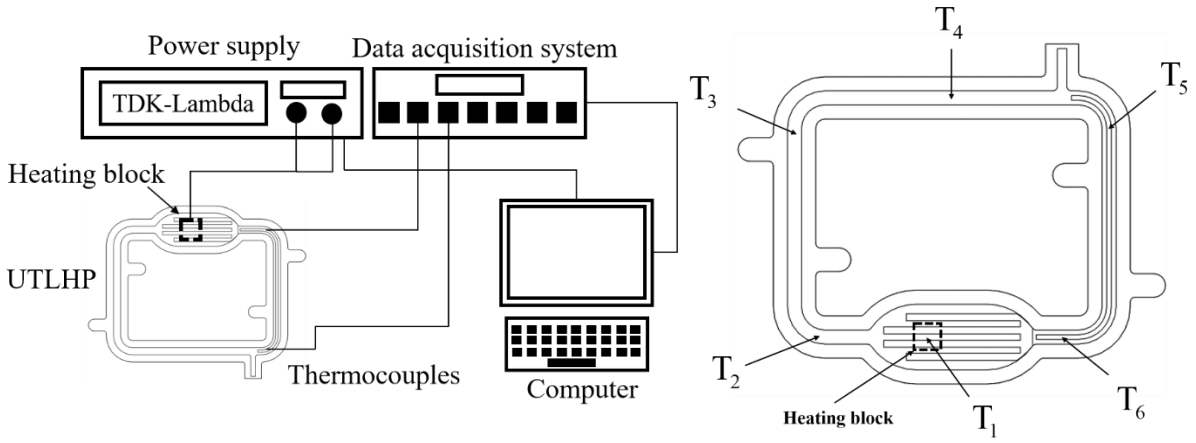

Source: Own authorship.

To justify the design of the heating system (heating area and power input), remembering that present UTLHP devices are being designed especially for smartphones, Table 10 shows some typical dimensions and power dissipations (maximum heat transfer rate - TDP) of actual gadgets and chips processors. From this information, a heating area of 100mm², average for a chip size, and power inputs varying from 6W to 10W, showed to be representative.

The heating system consisted of a copper block with one cartridge electrical resistor (3.2 mm of diameter and 25 mm of length) connected to a power source (TDK-Lambda).

Table 10 - Dimensions and thermal design power of chip processor.

Chip processor	Chipset size	Thermal design power (TDP)
Snapdragon 855	73.27mm² (8.48mm x8x64mm)	10W
Kirin 990 5G+	113.31mm² (10.68mm x 10.61mm)	6W
A12X Bionic	122mm²	6W
A14 Bionic	88mm²	6W
Exynos 9820	127mm²	9W

Souce: (WIKICHIP, 2021b)

In order to prevent heat leakages, the evaporator section was isolated with a 5 mm thick Polytetrafluoroethylene (PTFE polymer) with thermal conductivity of 0.25 W/m.K. Figure 32 shows a photograph of the UTLHP test configuration in the horizontal position with the thermocouples and insulation.

Figure 32 - Photograph of the UTLHP workbench in the horizontal position.

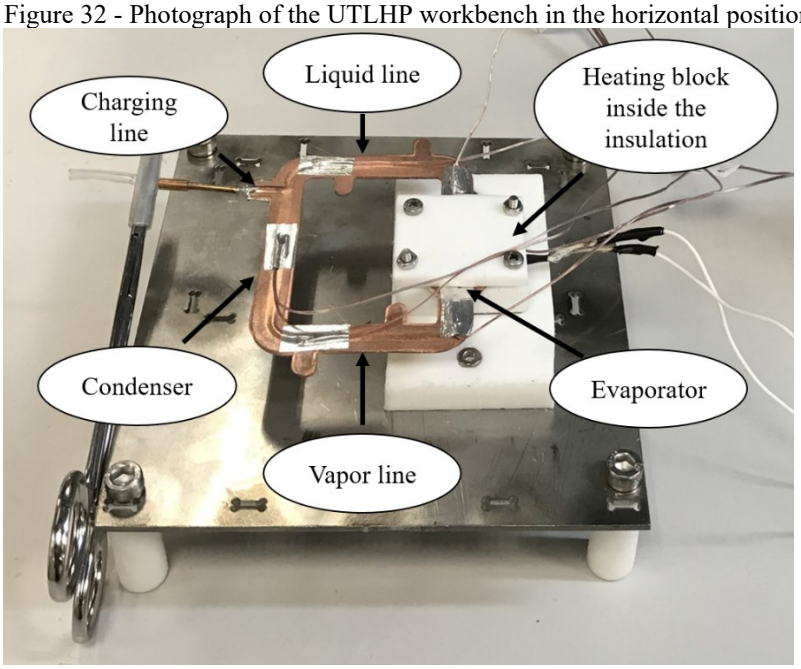

Source: Own authorship.

Each UTLHP was tested with several filling ratio (FR), to determine the volume that provides the optimum thermal performance. This parameter can be calculated as:

$$FR = \frac{V_l}{V_t} \times 100\% \tag{10}$$

where V_l is the working fluid volume inserted in the UTLHP and V_t is the total void volume of the device, which is represented by the sum of the following volumes:

$$V_t = V_c + V_{ll} + V_{vl} + V_{ev} + \varepsilon V_{ew} + \varepsilon V_{llw} \tag{11}$$

where V_c stands for condenser, V_{ll} to the liquid line, V_{vl} to the vapor line, V_{ev} to the evaporator and V_{ew} and V_{llw} for the void fraction of evaporator and liquid line wick structures. Table 11 shows the total volume for the four UTLHP tested.

Table 11 – The total inlet volume of each UTLHP.

UTLHP	Total volume (ml)
A	0.87
B	0.82
C	0.50
D	0.19

Source: Own authorship.

For each filling ratio, the apparatus is experimented in the horizontal, gravity-assisted and against gravity (against the gravity force) orientations, as shown in Figure 33. The temperature of the ambient that provided the natural convection heat removal, remained proximally at 24 ± 1 °C. For each test, power inputs from 0.5 W to 1.0 W, then increasing by 1 W were applied, and kept for 1200 s (when the steady state conditions were reached), until the evaporator temperature reaches a maximum value of 100 ºC. This temperature level was thought based on the application, to guarantee the safe operating temperature of the electronic components.

Figure 33 – Experimental orientations tested.

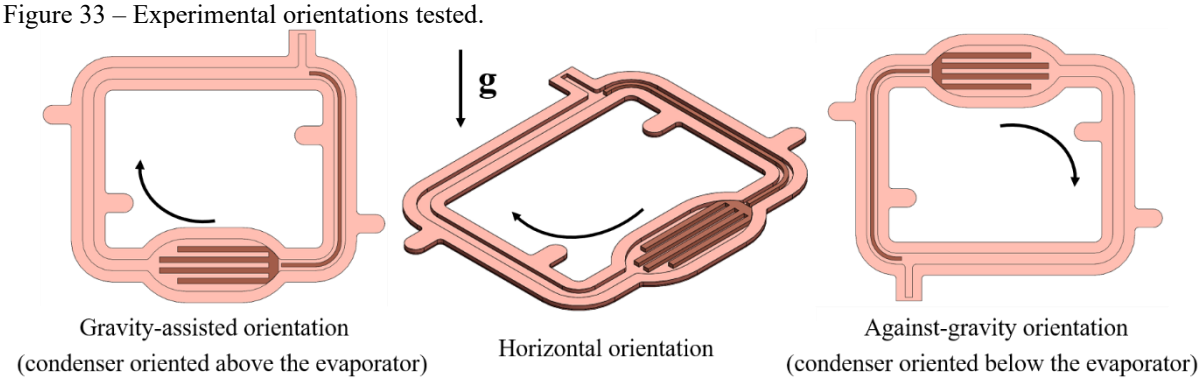

Source: Own authorship.

4.3 THERMAL PERFORMANCE ANALYSIS

The thermal resistance concept is used to analize the steady-state operating performance of an UTLHP. The lowest is the thermal resistance, the larger the heat transfer capacity and more isothermal the UTLHP can be. The thermal resistance of UTLHP (R_{lhp}) can be calculated as:

$$R_{lhp} = \frac{T_{ev} - T_c}{q} \tag{12}$$

where, T_{ev} is the external temperature of the evaporator, T_c is the average temperature of the condenser active zone and q is the total heat load applied in the evaporator section, which is provided by a power source. The evaporator (R_{ev}) and condenser (R_c) thermal resistances can also be measured, using the expressions:

$$R_{ev} = \frac{T_{ev} - T_v}{q} \tag{13}$$

$$R_c = \frac{T_v - T_c}{q} \tag{14}$$

here, T_v is the vapor temperature, here considered as the evaporator outlet temperature (ZHOU et al., 2016).

Many authors define the LHP temperature operation as the vapor temperature (CHERNYSHEVA et al., 2007). Chen et al. (2006) however, proposed the use of the evaporator maximum temperature as the operating temperature. KU (1999) considers that the compensation chamber (CC) temperature represents the LHP, but this resercher was questioned by Ambirajan et al. (2012), who affirmed that the CC temperature might not be a good representation of this temperature, as it can be influenced, both by the cold liquid returning from the condenser and by the heat leak from the evaporator envelope to the compensation chamber. For aerospace and electronic cooling applications, the maximum overall temperature of the device, (T_{ev}), is more adequate to represent the operation temperature, due to the strict temperature limitation of the electronic components to be cooled.

5 UTLHP THEORETICAL MODEL

This chapter presents the development of an analytical model to be implemented as a design tool for UTLHPs. The steady state model is based on energy balance equations, thermal resistance circuits and pressure drops analyses. The model is able to predict the thermal performance of the UTLHP and provides the operating and condenser temperatures, thermal resistances, heat leakage estimation and the necessary condenser length. Gravity is not taken into account in the model.

5.1 UTLHP MODEL

A theoretical model is proposed to predict the thermal performance of an UTLHP at steady-state conditions, for a given heat input, wick properties and surrounding temperature. As mentioned, the vapor line and liquid line of the LHP are not isolated. The cooling method is natural convection, similar configuration to electronics application. The vapor and liquid transport lines are considered as parts of the condenser. For modelling purposes, the UTLHP is divided into three control volumes (evaporator, two-phase region and single-phase region). For each zone, mass, momentum, and energy balance equations are applied, as shown in Figure 34.

The proposed model is based on the study developed by Ramasamy et al. (2018), which was applied to a UTLHP, subjected to water cooling in the condenser. As the present heat transfer device rejects heat to the environment by air natural convection, some corrections are necessary to be used in the present problem, as discussed along the chapter.

The following assumptions are made in the present work:

- The UTLHP system achieves steady state conditions for any heat input.
- The UTLHP has only two components: evaporator and condenser, i.e., the vapor and liquid lines are assumed as part of the condenser.
- The flow of the working fluid along the entire system is considered incompressible.
- Vapor and air are considered as ideal gas.
- Ambient temperature is constant.
- Thermophysical properties are evaluated at the working fluid saturation state.
- The working fluid enters the evaporator through the evaporator wick as saturated liquid.

- The vapor in the evaporator and condenser is not overheated and the superheating process is ignored.
- Part of the heat input in the evaporator spreads by conduction through the liquid line and evaporator wick of the UTLHP. This heat is considered parasitic heat and does not participate in the evaporation of the working fluid. However, this heat transfer rate is rejected by the condenser in the single-phase region.

Figure 34 - Energy balance in (a) Control volume I (b) Control volume II and (c) Control volume III.

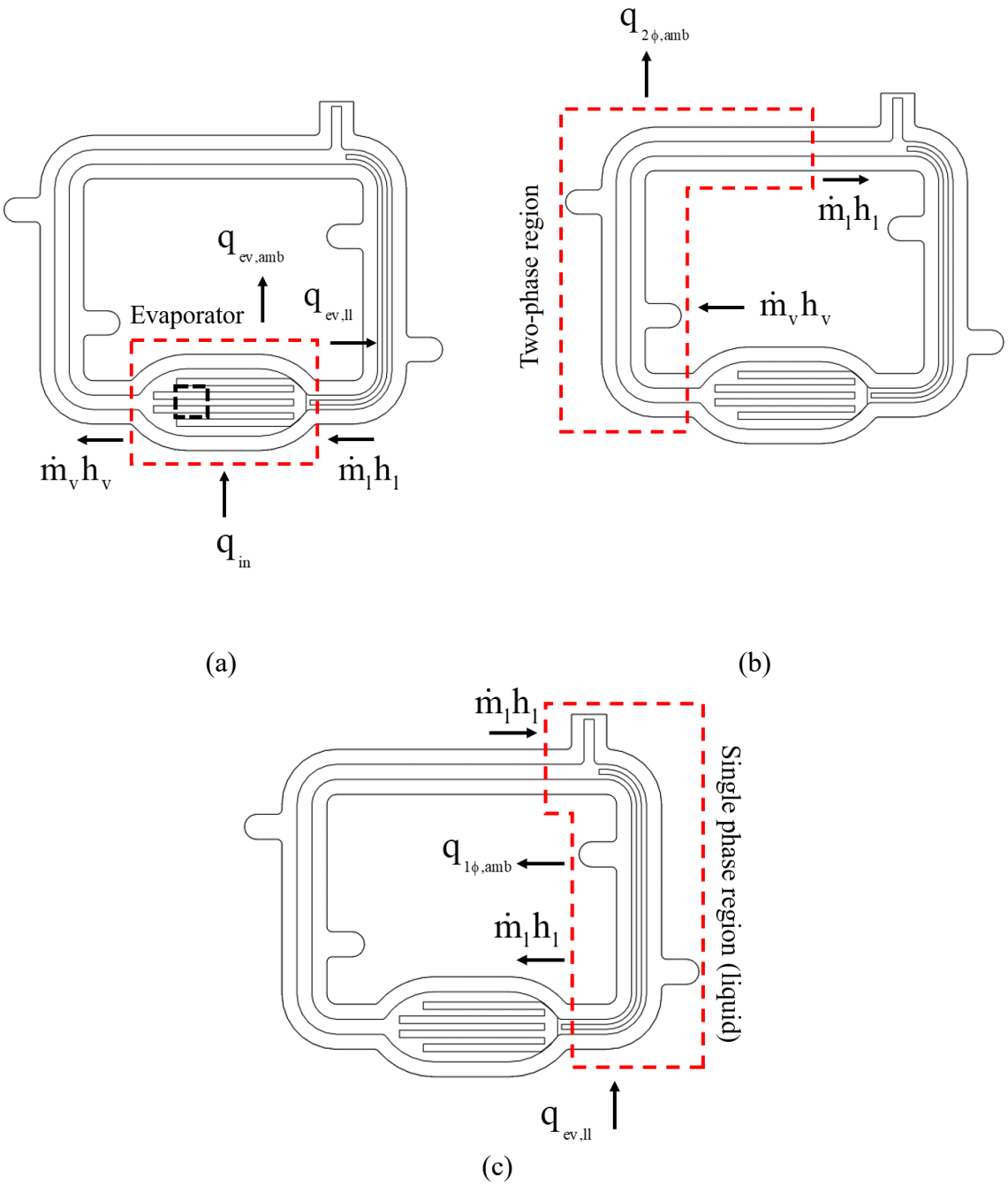

Souce: Own authorship.

5.1.1 Energy balance

Under steady-state, the energy balance of the system is zero, i.e., net heat input is equal to the net heat output for all control volumes. Control volume I (a) (see Figure 34(a)) represents the evaporator of the UTLHP. Considering the evaporator wick saturated with liquid, all the net heat absorbed by the working fluid, is used to generate vapor, which leaves the evaporator as saturated vapor. From the total heat delivered in the evaporator, the leakage along the evaporator wick and liquid line casing materials has a large impact on the thermal performance and must be considered in this energy balance. Despite being isolated, heat is also lost to the surrounding ambient. In this model, for simplicity, all heat losses (which does not participate in the evaporation) are considered concentrated in the evaporator. From the Figure 34(a), the energy balance applied to the control volume I provides:

$$\dot{m}_{wf} h_{lv} = q_{in,eff} - q_{ev,ll} \tag{15}$$

where, $\dot{m}_{wf}$ is the mass flow rate, h_{lv} represents the latent heat of vaporization, $q_{in,eff}$ is the effective heat input (= $q_{in} - q_{loss,amb}$) and $q_{ev,ll}$ is the heat leak from the evaporator to the liquid line.

Control volume II constitutes the two-phase region of the condenser. Since the UTLHP operates only under air natural convection, the vapor line and liquid line are considered as a part of the condenser, which can be divided into two regions: two-phase and one-phase flows.

From Figure 34(b), applying energy and mass balance for the two-phase region of the condenser results in:

$$\dot{m}_{wf} h_{lv} = q_{2\phi,amb} \tag{16}$$

where, $q_{2\phi,amb}$ is the heat transfer rate due to the condensation phenomenon (two-phase region).

Control volume III consists of the single-phase region of the condenser. The liquid enters in this section as saturated liquid and continues to reject heat to the surrounding ambient, getting sub-cooled. Before reaches the liquid line outlet, the working fluid receives the heat leak by conduction from the evaporator ($q_{ev,ll}$) and enters in the evaporator as saturated liquid. Therefore, it is considered that this region dissipates only the heat lost though the casing and

the wick structure. Based on Figure 34, equating net energy input and the net energy output, one has:

$$q_{ev,ll} = q_{l\phi,amb} \tag{17}$$

here, $q_{l\phi,amb}$ is the heat transfer rate of the liquid flowing. Finally, rearranging Equations (15), (16), and (17) gives:

$$q_{2\phi,amb} = q_{in,eff} - q_{ev.ll} \tag{18}$$

5.1.2 Evaporator heat leak

As previously mentioned, a fraction of total heat input leaks from evaporator to the liquid line by heat conduction through the case material, wick structure and sensible heat, absorbed by the liquid in evaporator-liquid line system, as shown in Figure 35(a). This heat leak is driven by the temperature difference observed across the evaporator wick and the liquid line (condenser outlet), which also includes the difference between the operating temperature (evaporator) and liquid inlet temperature. This heat transfer path can be represented by the resistance network, shown in Figure 35(b), composed by the association of the following thermal resistances:

Figure 35 – Schematic of evaporator and thermal resistance circuit of heat leak.

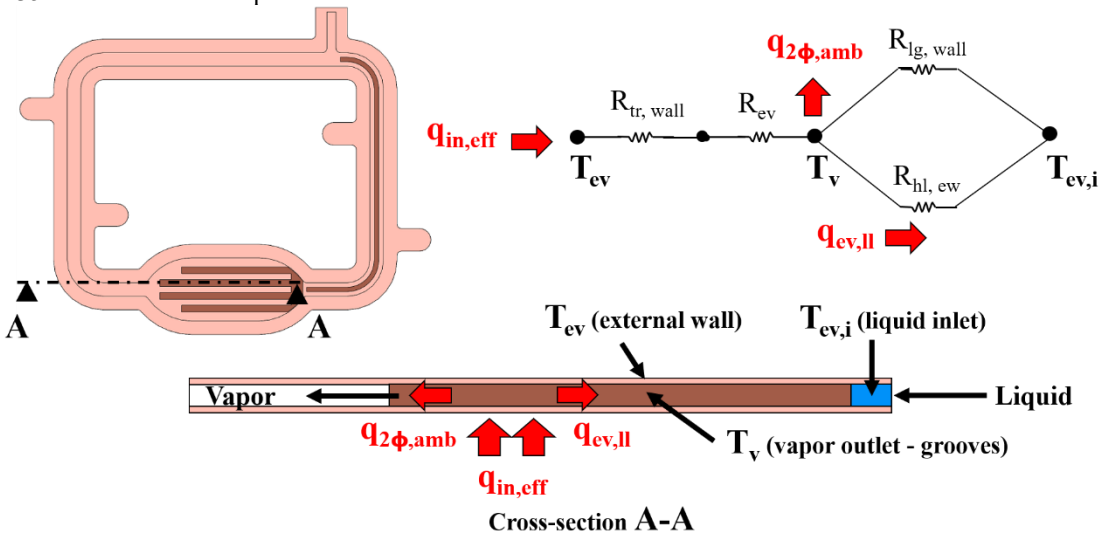

Souce: Own authorship.

$$R_{ev} = \frac{1}{h_{ev} A_{ac}} \tag{19}$$

$$R_{tr,wall} = \frac{\delta_{wall}}{k_{case} A_{ac}} \tag{20}$$

$$R_{hl,ew} = \frac{L_{case}}{k_{eff} A_{cs,ew}} \tag{21}$$

$$R_{lg,wall} = \frac{L_{case}}{k_{case} A_{cs,case}} \tag{22}$$

where, R_{ev} is the evaporator thermal resistance, which is given by the boiling heat transfer coefficient (h_{ev}) and the heat input active area (A_{ac}).; $R_{tr,wall}$ is the conduction thermal resistance through the wall of thickness (δ_{wall}), given by the case material thermal conductivity (k_{case}); $R_{hl,1w}$ represents the thermal resistance of the heat leak from the evaporator wick to the liquid line, given by case characteristic length (L_{case}), wick effective thermal conductivity (k_{eff}) and the cross-section area of the evaporator wick ($A_{cs,ew}$), and $R_{lg,wall}$ is the longitudinal conduction thermal resistance through the wall, passing over its cross-section area ($A_{cs,case}$).

The heat leak effective thermal resistance ($R_{ev,ev}$) can be computed from the resistance network presented in Figure 35 as:

$$q_{ev,ll} = \frac{\Delta T_w}{R_{eq,ev}} \tag{23}$$

$$q_{ev,ll} = \frac{T_v - T_{ev,i}}{\left(\frac{1}{R_{hl,1w}} + \frac{1}{R_{lg,wall}} \right)^{-1}} \tag{24}$$

here, T_v is the vapor temperature in the evaporator section and $T_{ev,in}$ is the evaporator inlet temperature. To ensure the presence of working within the UTLHP during startup, there must be an unbalance of temperatures (and consequently pressures) between the liquid-vapor interface in the evaporation zone and liquid line. This condition can be obtained from the thermodynamic cycle and is represented as follows:

$$\Delta T_w = T_v - T_{ev,in} = \left(\frac{\partial T}{\partial P} \right)_{sat} \left(\Delta P_t - \Delta P_{ev} \right) \tag{25}$$

where ΔP_t represents the total pressure drop of the UTLHP and ΔP_{ev} is the pressure drop due to the liquid in the evaporator wick and vapor grooves. The expression $\left(\frac{\partial T}{\partial P}\right)_{sat}$, at a reference temperature, applied to liquid-vapor saturation line, is an important thermophysical characteristic of the working fluid, and can be predicted using the Clausius-Clayperon equation:

$$\left(\frac{\partial T}{\partial P}\right)_{sat} = \frac{T_v\left(\upsilon_v - \upsilon_l\right)}{h_{lv}} \tag{26}$$

where the working fluid properties υ_v and υ_l are the specific volume of the vapor and liquid, respectively.

The relation between the vapor and evaporator temperatures in the evaporator region (see Figure 35) is given by the effective heat input and the equivalent resistance (serie) of R_{ev} and $R_{tr,wall}$.

$$T_v = T_{ev} - q_{in,eff}\left(R_{ev} + R_{tr,wall}\right) \tag{27}$$

5.1.3 Ambient interaction

Considering surrounding air natural convection as the cooling mechanism, available correlations are applied in the model. Actually, the only component that should exchange heat energy with the ambient around is the condenser, as thermal insulation is used over the device. However, heat is still lost to the surroundings and is predicted considering the ratio of the temperature difference between fluid and surrounding and the insulator effective thermal resistance.

5.1.3.1 Evaporator – surrounding heat transfer

The heat transfer between the evaporator and the surrounding ambient is expressed as:

$$q_{ev,amb} = \frac{T_{ev} - T_{amb}}{R_{wall,iso} + R_{amb,iso}} \tag{28}$$

$$R_{wall,iso} = \frac{\delta_{iso}}{k_{iso} A_{sup,iso}} \tag{29}$$

$$R_{amb,iso} = \frac{1}{h_{iso} A_{sup,iso}} \tag{30}$$

where $R_{wall,iso}$ represents the isolate wall thermal resistance, which is determined by the isolation wall thickness (δ_{wall}), isolation thermal conductivity (k_{iso}) and the isolation superficial area ($A_{sup,iso}$); $R_{amb,iso}$ represents the heat energy exchange from the insulation to surrounding ambient, being given by external heat transfer coefficient (h_{iso}) over the external insulation area. This convection coefficient is determined from the following parameters (INCROPERA et al., 2008), for flat plates:

$$Ra_{iso} = \frac{g\beta_{air}\left(T_{ev} - T_{amb}\right)L_{iso}^{\ 3}}{\nu_{air}\alpha_{air}} \tag{31}$$

here, L_{iso} is the isolation characteristic length, which is given by the ratio between the insulation perimeter (p) and the insulation surface area, expressed as:

$$L_{iso} = \frac{A_{sup,iso}}{p} \tag{32}$$

The Nusselt number for a heated surface from above and the heat transfer coefficient are calculated by the following expressions (INCROPERA et al., 2008):

$$Nu_{iso} = 0.54\left(Ra_{iso}\right)^{1/4} \qquad 10^4 \le Ra_{iso} \le 10^7 \tag{33}$$

$$h_{iso} = \frac{Nu_{iso} k_{air}}{L_{iso}} \tag{34}$$

5.1.3.2 Condenser – surrounding heat transfer

The most important parameter for electronic application is the operating temperature, in the present work assumed as the evaporator temperature (see discussions in the last chapter),

which is almost equal to the vapor temperature, as the thermal resistances R_{ev} and $R_{tr,wall}$ are small (approximately 0.025 ºC/W), i.e., $T_{ev} \approx T_v$.

The working fluid flowing in the condenser channel exchanges heat with the surrounding ambient and two major regions can be accounted for: two-phase and single-phase. The heat transfer between the condenser and the surrounding ambient in the two-phase region is modelled as:

$$q_{2\phi,amb} = \frac{T_v - T_{amb}}{R_{2\phi,amb}} \tag{35}$$

where $R_{2\phi,amb}$ is the equivalent thermal resistance between two-phase (condensation) fluid and the ambient air, which includes the wall conduction and natural convection over the outer surface area, from this specific region. As this region is governed by the two-phase change phenomena, its temperature is almost constant and is represented by the vapor temperature (T_v), as shown in Figure 36. The $R_{2\phi,amb}$ resistance is given by:

$$R_{2\phi,amb} = \frac{1}{h_{c,i} A_{2\phi,i}} + R_{w,2\phi} + \frac{1}{h_o A_{2\phi,e}} \tag{36}$$

here, $h_{c,i}$ is the condensation heat transfer coefficient, h_o is the external natural convection heat transfer coefficient, while $A_{2\phi,i}$ and $A_{2\phi,e}$ represent the two-phase internal and external areas, respectively. Figure 36 shows the thermal resistance path along one of the walls. The net effective resistance of the wall conduction is given by the parallel sum of the thermal resistances of upper and lower flat plane walls, which are equal in this case, resulting in:

$$R_{wall,2\phi} = \left(\frac{2}{R_{wall,1,2\phi}} + \frac{2}{R_{wall,3,2\phi}} \right)^{-1} \tag{37}$$

where, each thermal resistance of conduction is given by:

$$R_{wall,1,2\phi} = R_{wall,2,2\phi} = \frac{W_{wall}}{k_{case} L_{2\phi} \delta_{wall}} \tag{38}$$

$$R_{wall,3,2\phi} = R_{wall,4,2\phi} = \frac{\delta_{wall}}{k_{case} L_{2\phi} W_{ch}} \tag{39}$$

Figure 36 – Heat transfer interation of the two-phase region with surrounding.

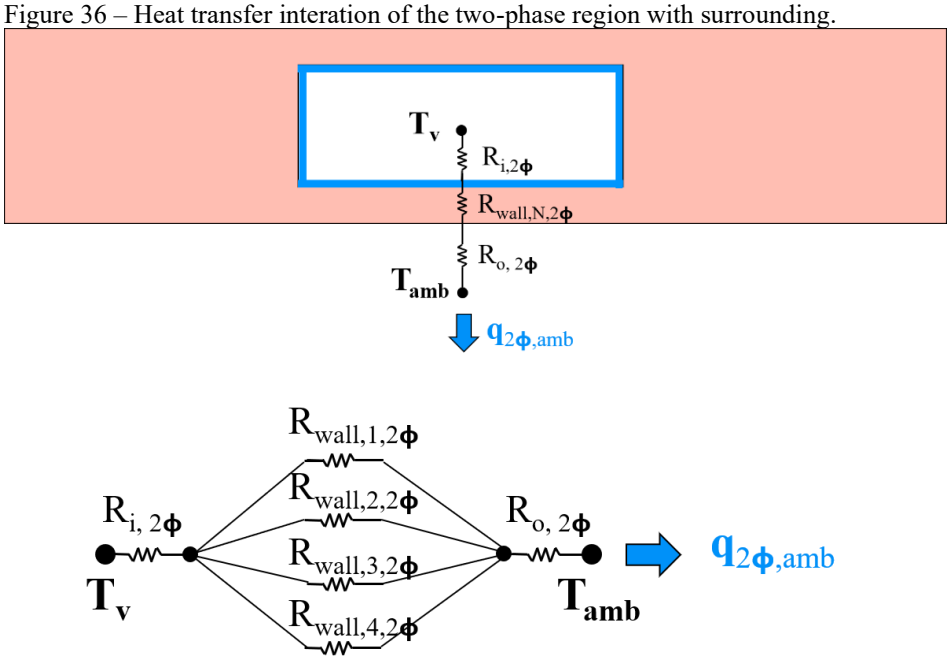

Souce: Own authorship.

As shown in Figure 37, the heat interaction with the ambient in the single-phase region is determined by:

$$q_{1\phi,amb} = \frac{T_{1\phi,avg} - T_{amb}}{R_{1\phi,amb}} \tag{40}$$

where $T_{1\phi,avg}$ is the average between the single-phase temperature (considered the same of the vapor temperature) and the evaporator inlet temperature, given by:

$$T_{1\phi,avg} = \frac{T_v + T_{ev,i}}{2} \tag{41}$$

The effective thermal resistance of the single-phase region (R1ϕ,amb) is the combination of the internal convection due to liquid flow, wall conduction, and free air convection. This zone assumes the same lumped system for the two-phase region, however, embracing the liquid flow convection instead of the condensation phenomena, i.e.:

$$R_{1\phi,amb} = \frac{1}{h_{l,i} A_{1\phi,i}} + R_{wall,1\phi} + \frac{1}{h_o A_{1\phi,e}} \tag{42}$$

here, $h_{l,i}$ is the internal liquid flow heat transfer coefficient, and $A_{1\phi,i}$ and $A_{1\phi,e}$ are the single-phase region internal and external areas, respectively. Each conduction thermal resistances are given by:

$$R_{wall,1,1\phi} = R_{wall,2,1\phi} = \frac{W_{wall}}{k_{case} L_{1\phi} \delta_{wall}} \tag{43}$$

$$R_{wall,3,1\phi} = R_{wall,4,1\phi} = \frac{\delta_{wall}}{k_{case} L_{1\phi} W_{ch}} \tag{44}$$

Figure 37 – Heat transfer interation of the single-phase region with surrounding.

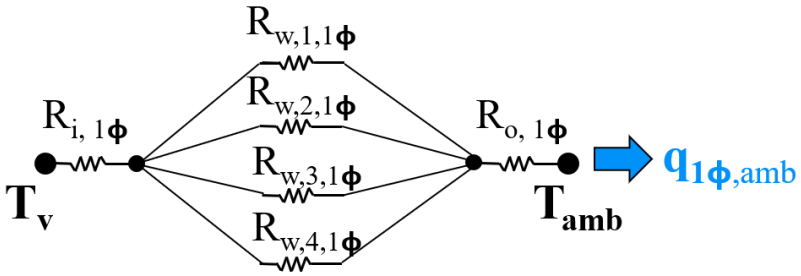

Souce: Own authorship.

5.1.4 Hydrodynamic model

As seen in Equation (25) the pressure drop is an important parameter for the determination of the heat transfer of the device. The total pressure drop (ΔP_t) in the UTLHP is determined by the sum of: the pressure drops in the evaporator (including the vapor grooves - ΔP_{vg} - and the saturated liquid in the evaporator wick), the two-phase region of condenser ($\Delta P_{2\phi}$) and the single-phase region of condenser (including the supercooled and liquid line wick flows - $\Delta P_{1\phi}$). Therefore, the overall pressure drop is given by:

$$\Delta P_t = \Delta P_{ev} + \Delta P_{2\phi} + \Delta P_{1\phi} \tag{45}$$

The pressure drop in the evaporator occurs mainly in the vapor grooves. The vapor is continuously generated along the groove and so its mass velocity increases linearly, reaching its maximum value at the channel outlet, as shown in (BAI et al., 2009):

$$v_{vg} = \frac{\dot{m}_{wf}}{n_{vg} \rho_v \delta_{wall} W_{vg}} \tag{46}$$

where n_{vg} is the number of vapor grooves, ρ_v is the vapor specific mass and W_{vg} is the vapor grooves width. In order to determine the Reynolds number, the following expressions for the hydraulic diameter of each vapor groove and Reynolds number are:

$$d_{h,vg} = \frac{2\delta_{wall} W_{vg}}{\delta_{wall} + W_{vg}} \tag{47}$$

$$Re_{vg} = \frac{\rho_v v_{vg} d_{h,vg}}{\mu_v} \tag{48}$$

The pressure drop in the vapor channel can be expressed by the following equation:

$$\Delta P_{vg} = \frac{f_{vg} L_{vg}}{2\rho_v d_{h,vg}} \left[\frac{\dot{m}_{wf}}{A_{vg}} \right] \tag{49}$$

where A_{vg} is the vapor grooves cross-section area and f_{vg} is the friction factor, calculated by the following equation (WHITE, 2011):

$$f_{vg} = \begin{cases} 64 / Re_{vg} & Re_{vg} \leq 2000 \\ 0.032 & 2000 < Re_{vg} < 9150 \\ 0.316\, Re_{vg}^{-0.25} & Re_{vg} \geq 9150 \end{cases} \tag{50}$$

The calculated Re_{vg} achieved a maximum value of 144. As the applied heat load is low, the vapor flows predominantly in the laminar regime, i.e., $Re_{vg} \leq 2000$.

Saturated liquid flows through the porous media of the evaporator and of liquid line, causing additional frictional pressure drops. According to the Darcy's law, the pressure drop due to liquid flow along the wick structures can be determined as (FAGHRI, 2014):

$$\Delta P_{ew} = \frac{\dot{m}_{wf} \mu_l \delta_{wall}}{\rho_l A_{cs,ew} K_w} \tag{51}$$

$$\Delta P_b = \frac{\dot{m}_{wf} \mu_l \delta_{wall}}{\rho_l A_{cs,b} K_w} \tag{52}$$

where ΔP_{ew} is the pressure drop of each line of the evaporator wick, ΔP_b is the pressure drop of the evaporator wick barrier and $A_{cs,b}$ is the cross-section area of the evaporator wick barrier.

Once the mass flow can circulate through two different paths, evaporator and vapor grooves, the concept of hydraulic resistance (R_h) is used, and expressed as follows:

$$R_h = \frac{\Delta P}{\dot{m}_{wf}} \tag{53}$$

Figure 38 presents the net hydraulic system in the evaporator, where the pressure drops are determined by the parallel combination of the expressions given by Eq. (49) and Eq. (51), which are combined in series with Eq. (52), resulting in:

$$\Delta P_{ev} = \dot{m}_{wf}\left[\left(\frac{5}{R_{h,vg}} + \frac{4}{R_{h,ew}}\right)^{-1} + R_{h,b}\right] \tag{54}$$

Figure 38 – Evaporator hydraluic system.

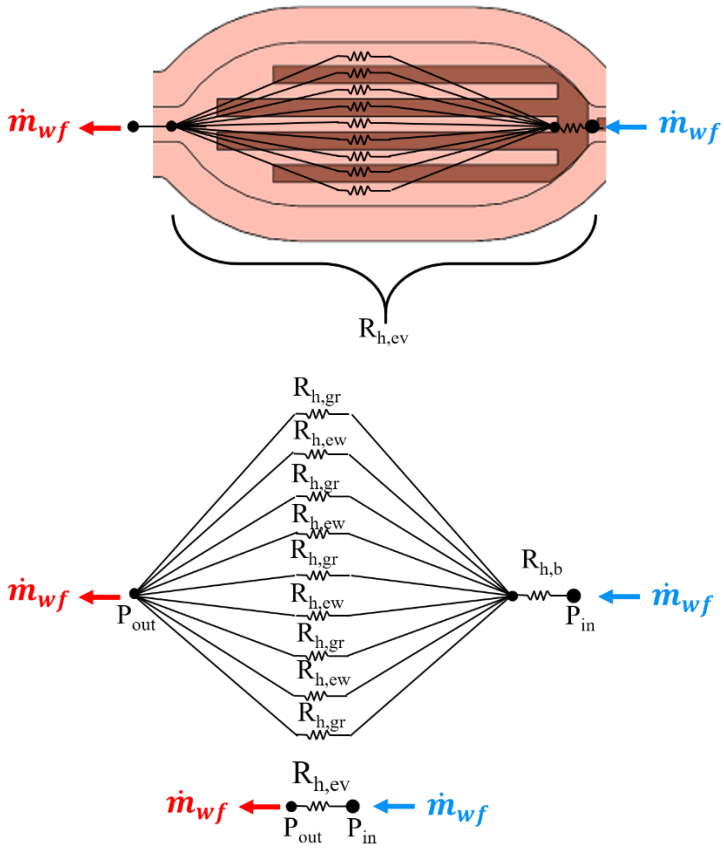

Souce: Own authorship.

5.1.4.1 Two-phase pressure drops

Two-phase phenomena occurring inside microchannels are highly complex to predict its pressure drop. Different correlations stand in the literature with huge errors as large as 30%. As this parameter affect the present model, the calculation of the two-phase region pressure gives by four correlations to obtain fewer errors.

Pressure drops along channels can be calculated using Lockhart and Martinelli's (1949) correlation, only carrying the specific geometry or flow conditions. This correlation basis on adiabatic flow with water and others fluids along with a hydraulic diameter of 1.5 to 26 mm (KANDLIKAR, 2006b). The authors predict the slip between the phases with the Martinelli parameter (X), defined as:

$$X = \left[\frac{(dP/dz)_l}{(dP/dz)_v} \right]^{1/2} \tag{55}$$

where $(dP/dz)_l$ and $(dP/dz)_v$ corresponds to the pressure drop of the liquid and vapor flow in the channel, respectively. These pressure gradients are expressed as follow:

$$\left(\frac{dP}{dz}\right)_l = \frac{f_l G^2 (1-\bar{\chi})^2}{2 d_{h,i} \rho_l} \tag{56}$$

$$\left(\frac{dP}{dz}\right)_v = \frac{f_v G^2 \bar{\chi}^2}{2 d_{h,i} \rho_v} \tag{57}$$

The two-phase pressure gradient is given by:

$$\Delta P_{2\phi} = \phi_l^{\,2} \left(\frac{dP}{dz}\right)_l L_{2\phi} \tag{58}$$

here, the two-phase multiplier (ϕ_l^2) is defined as:

$$\phi_l^{\,2} = 1 + \frac{C}{X} + \frac{1}{X^2}; \qquad C = \begin{cases} & \text{Liquid} & \text{Vapor} \\ 20 & \text{Turbulent} & \text{Turbulent} \\ 12 & \text{La min ar} & \text{Turbulent} \\ 10 & \text{Turbulent} & \text{La min ar} \\ 5 & \text{La min ar} & \text{La min ar} \end{cases} \tag{59}$$

Another classical correlation to predict the two-phase pressure drop was developed by Friedel (1978). The experimental tests employed channels with hydraulic diameter higher than 1 mm with adiabatic flow in the horizontal orientation. Furthermore, the surface tension effects were included (KANDLIKAR, 2006b). The resulting two-phase multiplier is calculated as follows:

$$\phi_{lo}^{\ 2} = E + \frac{3.24FH}{Fr^{0.045}We^{0.035}} \tag{60}$$

where the parameters E, F and H are evaluated as follows:

$$E = (1-\overline{\chi})^2 + \overline{\chi}^2 \frac{\rho_l f_{vo}}{\rho_v f_{lo}} \tag{61}$$

$$F = \overline{\chi}^{0.78}(1-\overline{\chi})^{0.24} \tag{62}$$

$$H = \left(\frac{\rho_l}{\rho_v}\right)^{0.91}\left(\frac{\mu_v}{\mu_l}\right)^{0.19}\left(1-\frac{\mu_v}{\mu_l}\right)^{0.7} \tag{63}$$

where the f_{vo} and f_{lo} are the single-phase friction factors flowing alone, which can be calculated using the Churchill (1977) correlation with the respective Reynolds number (Re_{vo} and Re_{lo}) as:

$$f = 9\left[\left(\frac{8}{Re}\right)^{12} + \left\{\left[2.457\ln\left(\frac{1}{\left(\frac{7}{Re}\right)^{0.9} + 0.27\zeta/d_{h,i}}\right)\right]^{16} + \left(\frac{37530}{Re}\right)^{16}\right\}^{-1.5}\right]^{1/12} \tag{64}$$

where ζ is the tube roughness. It is assumed a smooth tube, that is, $\zeta = 0$. Reynolds number of liquid and vapor flowing alone is defined as:

$$Re_{lo} = \frac{Gd_{h,i}}{\mu_l} \qquad Re_{vo} = \frac{Gd_{h,i}}{\mu_v} \tag{65}$$

The Froude and Weber numbers are given by:

$$Fr = \frac{G^2}{g d_{h,i} \rho_{TP}^{\ 2}} \tag{66}$$

$$We = \frac{G^2 D}{\rho_{TP} \sigma} \tag{67}$$

where ρ_{TP} is the two-phase mixture density calculated as follows:

$$\rho_{TP} = \left(\frac{\overline{\chi}}{\rho_v} + \frac{1-\overline{\chi}}{\rho_l} \right)^{-1} \tag{68}$$

Finally, the two-phase pressure drop is determined by:

$$\Delta P_{2\phi} = \phi_{lo}^{\ 2} \left(\frac{dP}{dz} \right)_{lo} L_{2\phi} \tag{69}$$

where $(dP/dz)_{lo}$ corresponds to the single-phase pressure gradient of the liquid flowing alone, which is calculated as follows:

$$\left(\frac{dP}{dz} \right)_{lo} = \frac{f_{lo} G^2}{2 d_{h,i} \rho_l} \tag{70}$$

Chen attempted to account for the influence of the surface tension in a channel with a hydraulic diameter less than 10 mm for fluids as air and water. It was modified the homogenous flow model by including the Bond number and the Weber number to take into account the surface tension and mass flux effect (KANDLIKAR, 2006b):

$$\Delta P_{2\phi} = \left. \frac{dP}{dz} \right|_{Friedel} L_{2\phi} \Omega; \quad \Omega = \begin{cases} \dfrac{0.0333\, Re_{lo}^{\ 0.45}}{Re_v^{\ 0.09} (1 + 0.4 \exp(-Bo))} & Bo < 2.5 \\ \dfrac{We^{0.2}}{2.5 + 0.06 Bo} & Bo \geq 2.5 \end{cases} \tag{71}$$

where the Weber number and the Bond number are defined as follows:

$$We = \frac{G^2 d_{h,i}}{\sigma \rho_m} \tag{72}$$

$$Bo = g(\rho_l - \rho_v)\left(\frac{(d_{h,i}/2)^2}{\sigma}\right) \tag{73}$$

where ρ_m is the mixture density.

The two-phase flow pressure drops in the condenser line can be modelled with the Yang and Webb (1996b) correlation. These authors measured the pressure drops in rectangular tubes with low hydraulic diameter as 0.4 mm. They adjusted the mass flux concept, proposing an equivalent mass velocity parameter, as follows (KANDLIKAR, 2006b):

$$G_{eq} = G\left[\left(1-\overline{\chi}\right) + \overline{\chi}\left(\frac{\rho_l}{\rho_v}\right)^{1/2}\right] \tag{74}$$

where ρ_v and ρ_l are the specific mass of vapor and liquid, respectively, χ is the vapor quality and G represents the mass flux, given by:

$$G = \frac{\dot{m}_{wf}}{A_{c,i}} \tag{75}$$

The equivalent Reynolds number for the two-phase flow is given by the following expression:

$$Re_{eq} = \frac{G_{eq} d_{h,i}}{\mu_l} \tag{76}$$

Finally, the two-phase pressure drop is calculated as:

$$\Delta P_{2\phi} = f\frac{Re_{eq}^2 \mu_l^{\,2} 4L_{2\phi}}{2\rho_l d_{h,i}^{\,3}} \tag{77}$$

where $d_{h,i}$ is the inlet hydraulic diameter, $L_{2\phi}$ is the two-phase region length and f is the shear friction factor of the two-phase flow, given by:

$$f = 498.3\,Re_{eq}^{-1.074} \tag{78}$$

As the average vapor quality is not known, it is assumed that this parameter increases linearly in the two-phase region, i.e., leaves the evaporator as only vapor ($\chi = 1$) and reaches the single-phase region as liquid ($\chi = 0$). This variation behavior between these two points is due to the uniform heat flux, and consequently the condensation rate is uniform along the condenser length, that is (MILANEZ; MANTELLI, 2010):

$$\chi = 1 - \frac{z}{L_{2\phi}} \tag{79}$$

where z corresponds the direction of the working fluid flow. In order to obtain the average vapor quality, Eq. (79) is integrated along the direction z from 0 to $L_{2\phi}$:

$$\bar{\chi} = \frac{1}{L_{2\phi}} \int_0^{L_{2\phi}} \chi dz \tag{80}$$

5.1.4.2 Single-phase pressure drop

The pressure drop due to the liquid single-phase flow is totalized as the net pressure losses in the condenser tube (ΔP_l) and in the liquid line wick (ΔP_{llw}):

$$\Delta P_{1\phi} = \Delta P_l + \Delta P_{llw} \tag{81}$$

The pressure drop caused by the single-phase liquid flow region is due to frictional resistance produced by the channel walls. The pressure drops of liquid flowing alone is given by the Darcy-Weisbach equation for a laminar flow:

$$\Delta P_l = \frac{128 \dot{m}_{wf} \mu_l L_{1\phi}}{\pi \rho_l d_{h,i}^{\ 4}} \tag{82}$$

where the single-phase region length is expressed as $L_{1\phi} = L_c - L_{2\phi}$. The pressure drop in the liquid line wick is given by:

$$\Delta P_{llw} = \frac{\dot{m}_{wf}\mu_l\delta_{wall}}{\rho_l A_{cs,llw} K_w} \tag{83}$$

where $A_{tr,llw}$ represents the cross-section area of the evaporator wick and K_w is the wick permeability.

Figure 39 presents a schematics of the net hydraulic system in the single-phase region governed by Eq. (82) and Eq. (83), in parallel, gives:

$$\Delta P_{1\phi} = \dot{m}_{wf}\left(\frac{2}{R_{h,l}} + \frac{1}{R_{h,llw}}\right)^{-1} \tag{84}$$

Figure 39 – Single-phase region hydraluic system.

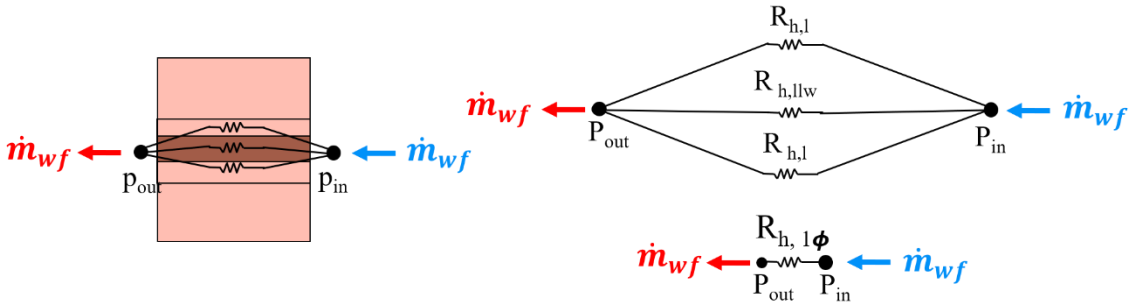

Souce: Own authorship.

5.1.5 Determination of the heat transfer coefficients

For the present UTLHP, the evaporation and the condensation heat transfer coefficients are determined from the experimental data following classical definitions (ZHOU et al., 2016):

$$h_{c,i} = \frac{q_{in,eff}}{A_{c,i}(T_v - T_{ev,i})} \tag{85}$$

$$h_{ev} = \frac{q_{in,eff} - q_{ev,ll}}{A_{ac}(T_{ev} - T_v)} \tag{86}$$

where T_v is the vapor temperature, which may be approximately defined as the evaporator outlet temperature, given by thermocouple T_2. T_{ev} and $T_{ev,i}$ are the outer surface temperatures measured by thermocouples T_1 and T_6, respectively.

5.1.5.1 Internal liquid flow heat transfer coefficient

Liquid flowing along the condenser line exchanges heat with the wall and, consequently, with the surrounds. In this theoretical model, it is assumed that the condenser length is long enough to produce a fully developed laminar flow inside the channel. The Nusselt number in this regime is constant and depends on the channel geometry and the wall heat transfer boundary conditions. For rectangular microchannels, this parameter is based on the channel aspect ratio $\varphi = \delta_{wall}/W_{ch}$. Considering constant circumferential wall temperature and uniform axial heat flux, the Nusselt number is given by (KANDLIKAR, 2006b):

$$Nu_{l,i} = 8.235(1 - 2.0421\varphi + 3.0853\varphi^2 - 2.4765\varphi^3 + 1.0578\varphi^4 - 0.1861\varphi^5) \quad (87)$$

In order to calculate the internal liquid flow heat transfer coefficient, the following equation is applied:

$$h_{l,i} = \frac{Nu_{l,i} k_l}{d_{h,i}} \quad (88)$$

5.1.5.2 External convection heat transfer coefficient

An important parameter that may limit the maximum heat input supported by UTLHP is the cooling method. For air natural convection, the heat transfer coefficient from horizontal rectangular ducts can be calculated by the Nusselt Number definition, expressed as:

$$h_o = \frac{Nu_c k_{air}}{L_{c,e}} \quad (89)$$

where k_{air} is the air thermal conductivity and $L_{c,e}$ represents the condenser external characteristic length, given by the sum of the total external thickness and condenser width ($L_{c,e} = \delta_e + W_c$).

Ali (2007) proposed a correlation for the averaged Nusselt number at laminar regime as function of the aspect ratio, surface area ratio and modified Reynolds number. At laminar regime ($\kappa \geq 100$ and $1x10^6 \leq Ra_c^* \leq 7x10^6$), one has:

$$Nu_c = 33633.84\left(Ra_c^*\right)^{-0.241} \kappa^{-0.860}\Gamma^{0.0779} \tag{90}$$

where the aspect ratio is expressed as $\Gamma = \delta_e/W_c$ and the surface area ratio is the rate between external surface and the cross-section external areas of condenser ($\kappa = A_{c,e}/A_{cs}$). The modified Reynolds number is determined by the expression:

$$Ra_c^* = \frac{g\beta_{air}(q_{in,eff}/A_{c,e})L_{c,e}^{\ 4}}{\nu_{air}\alpha_{air}k_{air}} \tag{91}$$

where, g is the gravity acceleration, and β_{air}, ν_{air}, and α_{air} are the coefficient of thermal expansion, kinematic viscosity and thermal diffusivity of air, respectively.

5.1.6 Solution procedure

In order to solve the proposed theoretical model, the equation system formed by Equations (18), (24), (25), (35) and (40) is calculated with input variables such as: UTLHP dimensions, wick properties, heat input and the average heat transfer coefficients, previously calculated by correlation or experimentally. The average heat transfer exchange between evaporator and the surrounding ambient is calculated from Equation (28). Then, an initial guess for the saturation temperature (T_{sat}) is defined and the initial mass flow is determined as follow:

$$\dot{m}_i = \frac{q_{in,eff}}{h_{lv}} \tag{92}$$

With the initial values for the temperatures, heat transfer rates, pressure drops, and single-phase and two-phase lengths, the first convergence criteria is verified, $T_{sat} - T_v \leq 0.01$. If the difference between these temperatures is larger, a new value for T_{sat} is used as $T_{sat} = T_v$. After these values matches, the mass flow is calculated as follows:

$$\dot{m}_{wf} = \frac{q_{in,eff} - q_{ev,ll}}{h_{lv}} \tag{93}$$

With the new mass flow, the second convergence criteria is verified:

$$\frac{|\dot{m}_{wf} - \dot{m}_i|}{\dot{m}_i} \leq 0.001 \tag{94}$$

If the difference between the two mass flows is larger, the new value is used to calculate all parameters, until both criteria are validated, as shown in the flowchart of Figure 40. The proposed theoretical model is executed using the EES^{TM} (Engineering Equation Solver) and the graph are plotted with Origin^{TM}.

Figure 40 – Flowchart for solving the proposed theoretical model.

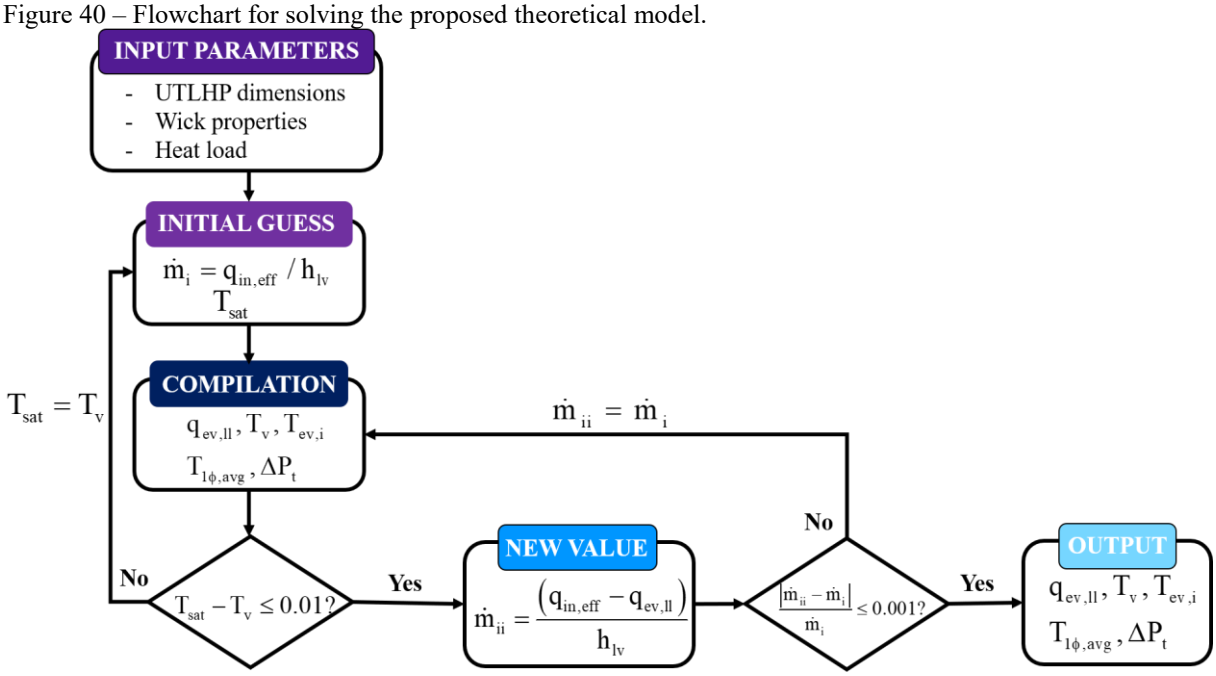

Souce: Own authorship.

The model results are validated against experimental data. Operating, condenser and inlet evaporator temperatures, heat transfer rates, and single-phase and two-phase lengths are analyzed and discussed in the next chapter. Table 12 presents the summary of areas used in the UTLHP theoretical model.

Table 12 – Summary of areas used in the model.

Symbol	Name	Description
A_{ac}	Heat input active area	$= W_{ac} \times L_{ac}$
$A_{cs,b}$	Cross-section area of the evaporator wick barrier	$= W_b \times \delta_{wall}$
$A_{cs,ew}$	Cross-section area of the evaporator wick	$= W_{tr,ew} \times \delta_{wall}$
$A_{cs,llw}$	Cross-section area of the liquid line wick	$= W_{tr,llw} \times \delta_{wall}$
$A_{cs,case}$	Cross-section area of the case	$= W_{case} \times \delta_{case}$
$A_{tr,ev}$	Evaporator transversal area	$= W_{ev} \times \delta_{wall}$
$A_{c,e}$	Condenser external area	$= 2 \times (W_{case} + \delta_{case} + \delta_{wall}) \times L_c$
$A_{c,i}$	Condenser internal area	$= 2 \times (W_{ch} + \delta_{wall}) \times L_c$
A_{vg}	Vapor grooves transversal area	$= W_{vg} \times \delta_{wall}$
A_{cs}	Cross-section external area of the condenser	$= W_{case} \times (\delta_{case} + \delta_{wall})$
$A_{sup,iso}$	Isolation superficial area	$= W_{iso} \times L_{iso}$
$A_{2\phi,i}$	Two-phase internal area	$= 2 \times (W_{ch} + \delta_{wall}) \times L_{2\phi}$
$A_{2\phi,e}$	Two-phase external area	$= 2 \times (W_{case} + \delta_{case} + \delta_{wall}) \times L_{2\phi}$
$A_{1\phi,i}$	Single-phase region internal area	$= 2 \times (W_{ch} + \delta_{wall}) \times L_{1\phi}$
$A_{1\phi,e}$	Single-phase region external area	$= 2 \times (W_{case} + \delta_{case} + \delta_{wall}) \times L_{1\phi}$

Souce: Own authorship.

6 RESULTS AND DISCUSSIONS

In this section, experimental results of the proposed UTLHP operation are presented and discussed in details. The thermal performance of each device and influence of its characteristics is debated. Besides, the validation and analysis of the theoretical model are shown.

6.1 INFLUENCE OF LIQUID LINE WICK STRUCTURE

In general, when the heat load applied to the evaporator is large, LHP may startup easily. Differently, the startup at low heat input is more difficult. Besides, usually thin heat transfer devices show larger heat leakages from the evaporator to the liquid line. To understand these holdbacks, the influence of the wick structure inserted in the liquid line is analyzed.

6.1.1 Influence of the wick structure in the liquid line

A minimum pressure difference across the evaporator wick is required for the startup, i.e., the complete circulation of the working fluid in the UTLHP. Actually, the startup can be considered the most important aspect for thermal performance evaluation.

Figure 41(a) shows the measured temperatures (see Figure 31 for thermocouple numbering) during the tentative startup process of the UTLHP - A with ethanol (FR of 30%) and without wick structure at the liquid line, in the horizontal orientation. At each power step, after approximately 1200 s, one can see that all the UTLHP temperatures stabilize, approaching to steady-state conditions. However, as the power input increases the temperature difference between the evaporator and condenser regions also increase, especially the evaporator, which shows clear overshoots, showing that the device did not startup. The attempts to startup are observed from the temperature oscillations.

Figure 41(b) presents the transient temperatures for the same conditions as Figure 41(a), but with the device operating in gravity-assisted operation. The heat transfer device requires a heat input of 2 W to startup that is, the condenser temperature (T_4) gets higher than T_6, showing that vapor flow reached the condenser. This proceeding occurs approximately at 2500 s, after stable operation condition is achieved (no apparent temperature variation). No obvious temperature oscillations are observed. In these curves, one can observe that the evaporator inlet temperature (T_6) is higher than the condenser outlet temperature (T_5). This is mainly due to the heat conduction leakage from the evaporator to the liquid line. At 3 W, the two-phase change phenomenon clearly overcomes the heat leak (temperature T_5 overpass T_6)

and the UTLHP operates successfully until 8 W, when the temperature limitation of 100 ºC for electronics applications is reached.

Figure 41 – UTLHP - A (FR=30%) thermal behavior with ethanol in: (a) horizontal orientation (b) gravity-assisted orientation.

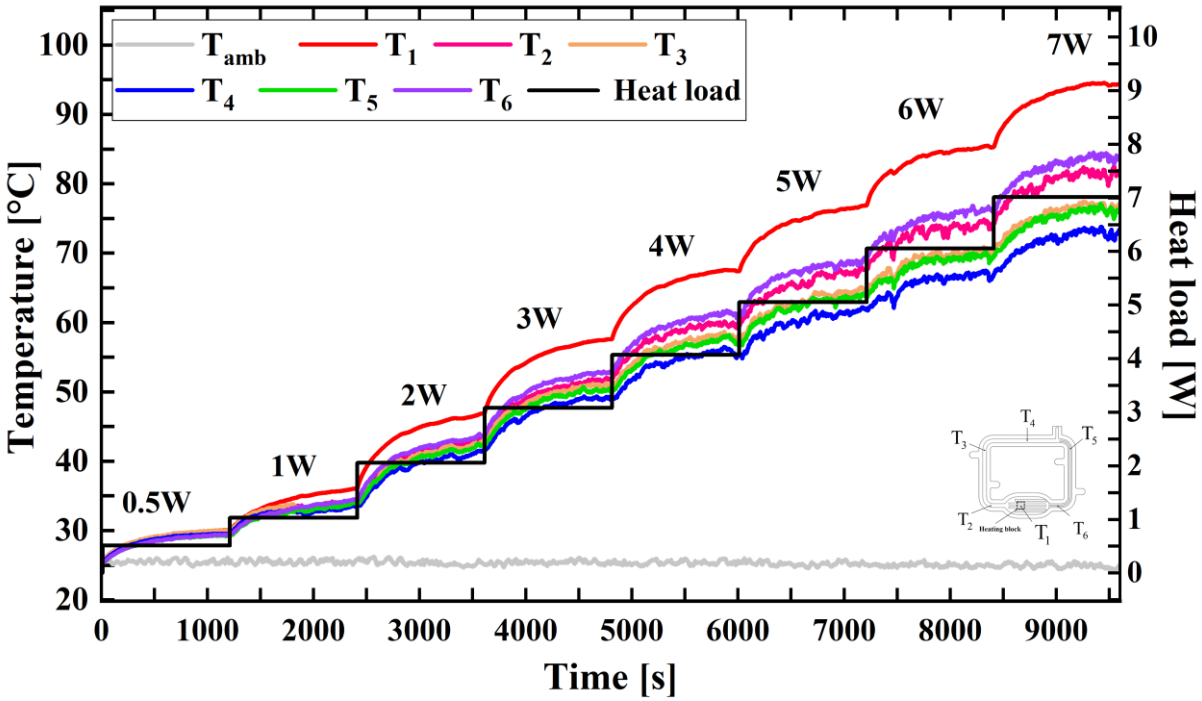

(a)

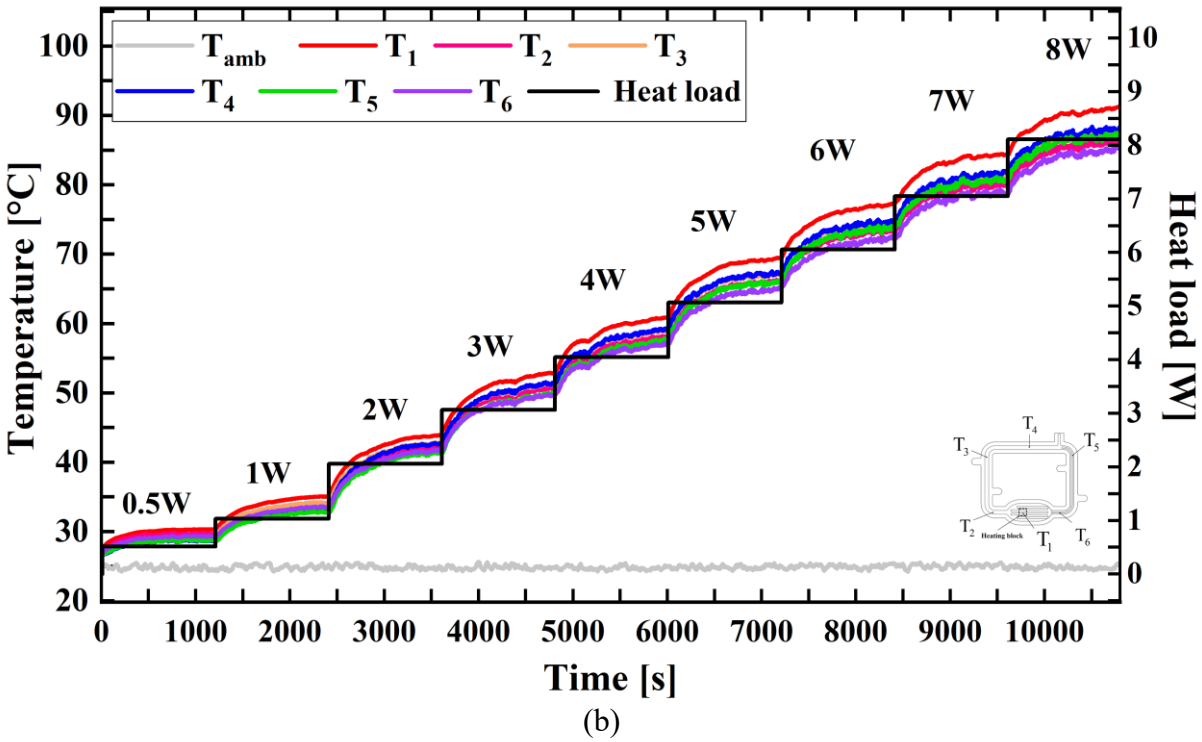

(b)

Souce: Own authorship.

Figure 42(a) shows the measured temperatures for UTLHP - B with ethanol in the horizontal orientation, for several power levels. The major difference comparing to Figure 41(a) is the presence of the wick structure in the liquid line. One can see that, at 2 W and approximately 3100 s, the device starts to operate in conditions similar to that of Figure 41 (b), i.e., the UTLHP with no wick at the liquid line, but with the aid of gravity. As noticed, the wick structure of the liquid line provides the necessary capillary pressure to allow the device to startup in the horizontal orientation without gravity assistance. Despite this improvement, at 3 W, the evaporation and condensation phenomena overcome the heat leakage by conduction, and the evaporator, liquid line, and condenser temperatures (T1, T2, T3, and T4) show values close to each other, showing good heat transfer capability. Furthermore, the wicked liquid line temperatures (T5 and T6) are lower, showing sub-cooled conditions, as expected. The observed fluctuations are related to the two-phase phenomena or caused by variations in the air natural convection.

Figure 42(b) illustrate the transient temperature values during the startup process for the same device of Figure 42(a), but operating in gravity-assisted orientation. Similarly, to Figure 42(a), the UTLHP starts to operate at 2 W and shows very similar behavior. However, in the horizontal orientation, the device is able to transfer a maximum value of 8 W, but with gravity assistance, it can transfer 9 W before reaching 100 ºC.

Figure 42 - UTLHP - B (FR=30%) thermal behavior with ethanol in: (a) horizontal orientation (b) gravity-assisted orientation.

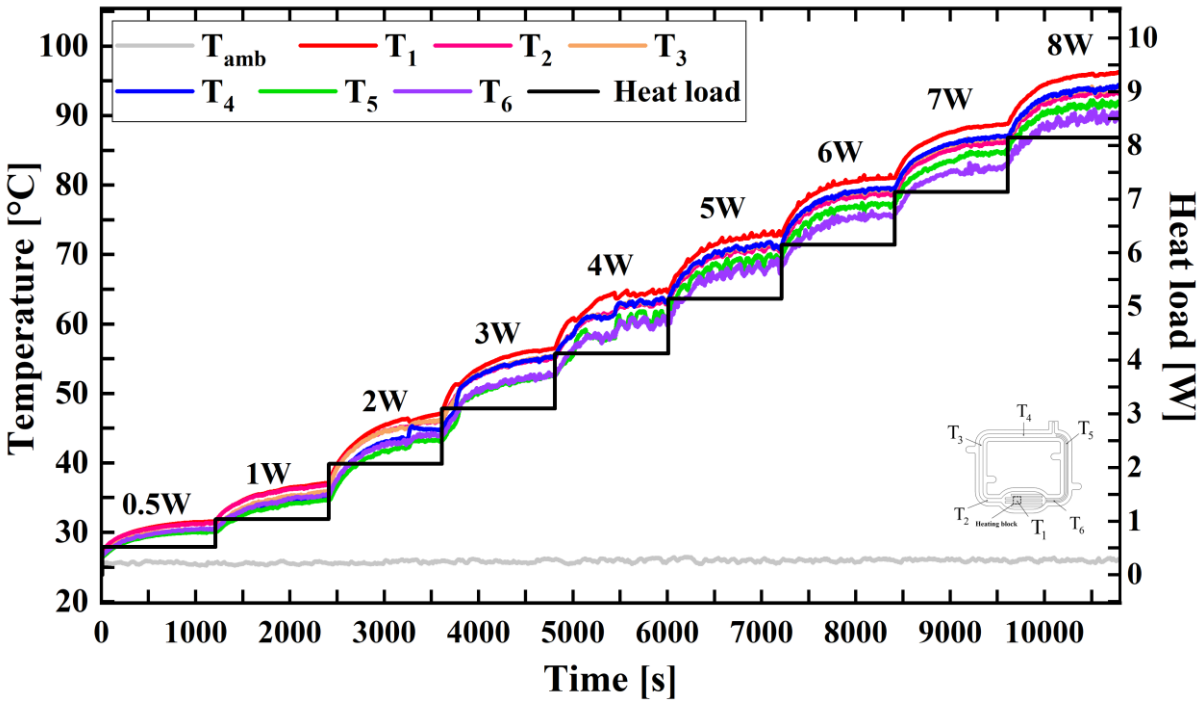

(a)

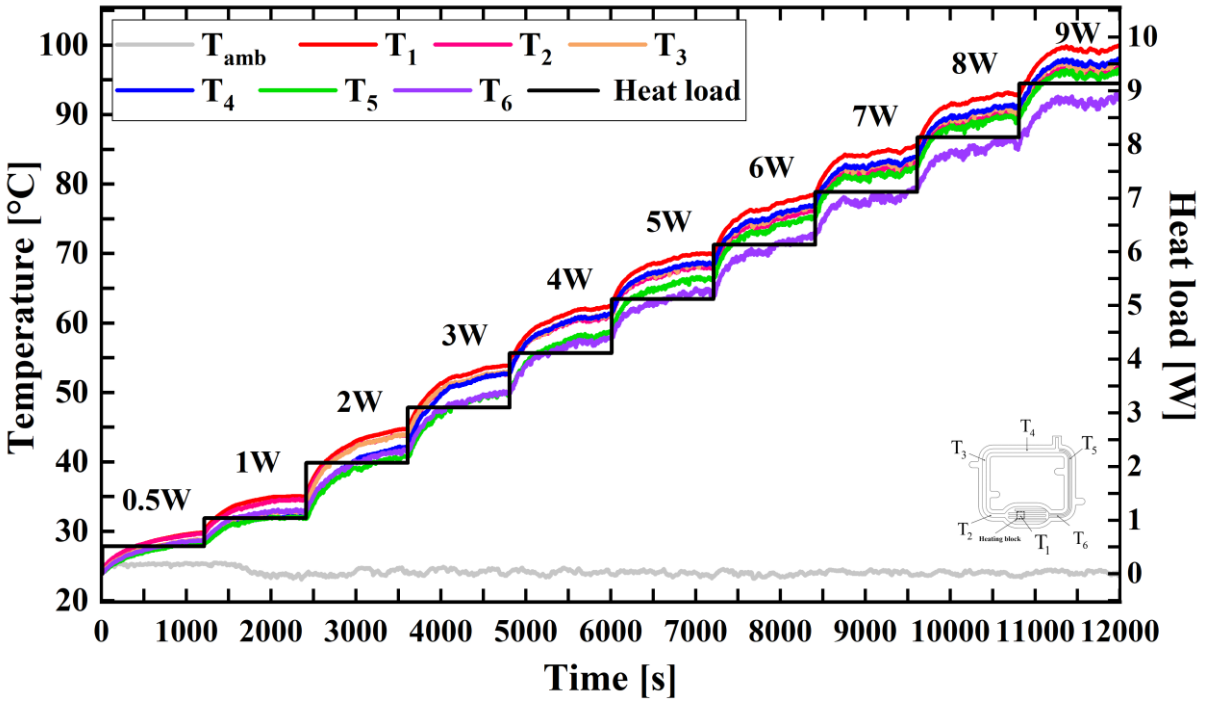

(b)

Souce: Own authorship.

6.1.2 Steady-state operation

In order to highlight the influence of gravity in the thermal behavior of the UTLHP, the total thermal resistance as a function of the heat input power, for the device with FR30% of ethanol, in horizontal and gravity-assisted positions, for UTLHP - A (a) and UTLHP - B (b) (the same devices which data are shown in Figures 41 and 42), are shown in Figure 43.

As Figure 43(a) illustrates, increasing the heat input from 0.5 W to 8 W, in the horizontal orientation, the thermal resistance of the UTLHP without wick structure in the liquid line increases, quickly, for the first power inputs, but tending to constant levels at higher power inputs. The increase of thermal resistance at lower power input can be explained by the larger heat conduction back from the evaporator to the liquid line through the case, as the device does not work as a heat pipe, i.e., it does not starts-up, as already observed from Figure 41(a). In the gravity-assisted orientation, the thermal resistance decreased sharply from power inputs of 0.5 W to 2 W, as result from the startup. After the device starts to operate, this parameter decreased slowly, reaching the lowest value of 0.40 ºC/W, at 8 W.

Figure 43(b) shows the thermal resistances obtained for UTLHP - B (similar to the UTLHP - A, but with wick structure at the liquid line). One can see that this device operates in both orientations successfully. As for the gravity-assisted oriented LHP (Figure 43(a)), for the

first power input levels, the thermal resistance decreases rapidly and, above 4 W, it remains at an almost constant level as the heat power increases. The minimum thermal resistance achieved is 0.24 ºC/W at 8 W and 0.22 ºC/W at 9 W, for the horizontal and gravity-assisted orientations, respectively.

Figure 43 - Thermal resistance of FR30% with ethanol in the horizontal and gravity-assisted orientation for (a) UTLHP -A and (b) UTLHP - B.

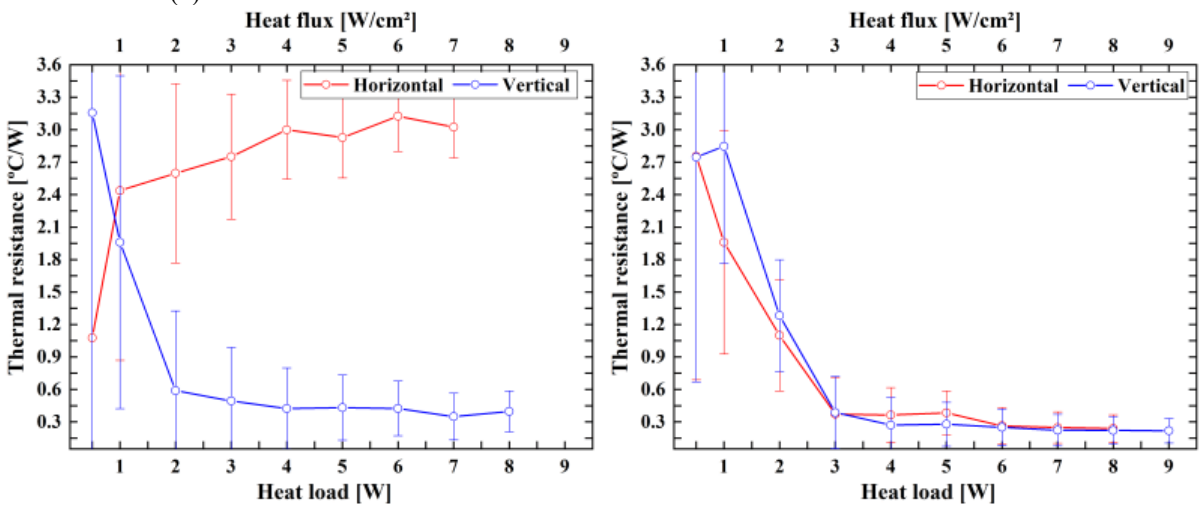

Souce: Own authorship.

6.2 INFLUENCE OF FILLING RATIO

The filling ratio is an important parameter which might influence the thermal performance of UTLHP. In order to verify the influence of this parameter, Figure 44 shows the thermal resistance of UTLHP - A (no wick structure at the liquid line) with ethanol as a function of heat input, for several working fluid filling ratios. Figure 44(a) shows the data for the horizontal operation conditions, while Figure 44(b) is for the gravity-assisted orientation. From Figure 44(a), one can see that, even varying the volume of working fluid (charging ratio), the startup in the horizontal orientation does not happen. As the startup was observed for this orientation in Figure 41(b), one can conclude that a wick structure in the liquid line is necessary in order to startup. Besides, the wick structure in the liquid line may cause greater confinement in the internal channel, which guarantees that the liquid line and condenser are always wet.

From Figure 44(b), with UTLHP - A in gravity-assisted orientation, one can see that the thermal resistance decreases quickly with increasing heat inputs, for filling ratios of 22% and 30%, with startup occurring at the first power input level tested. However, for FR of 40%, the thermal resistance decrease is smaller, and the startup is late. For power input levels larger than 4 W, all the devices tend to work similarly and the thermal resistance remains at a constant

level, even with the increasing the heat input power. A minimum value of 0.37 ºC/W is achieved at 8 W.

Figure 44 - Thermal resistance of UTLHP - A with ethanol for different values of filling ratio in: (a) horizontal orientation (b) gravity-assisted orientation.

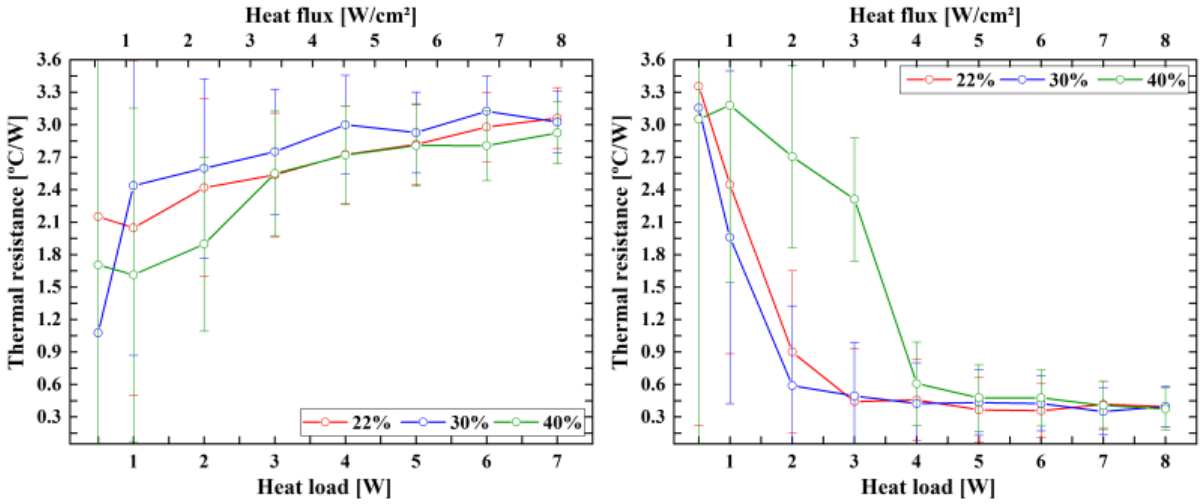

Souce: Own authorship.

Figure 45 shows the thermal resistance as a function of the filling ratio with ethanol at heat input of 6 W in the horizontal orientation for UTLHP - B and UTLHP - C (the difference between these LHPs is the internal plate thickness, which is 1mm in the first and 0,5 mm in the second). One can see that the total internal volume affects directly the thermal performance of the device. For the thicker device, the lowest thermal resistance is observed for the best ethanol filling ratio between 30% and 40%. For the thinner device, the best results were obtained with the filling ratio of approximately 40%.

Figure 45 – Influence of the filling ratio with ethanol at 6W and horizontal orientation for (a) UTLHP - B and (b) UTLHP - C.

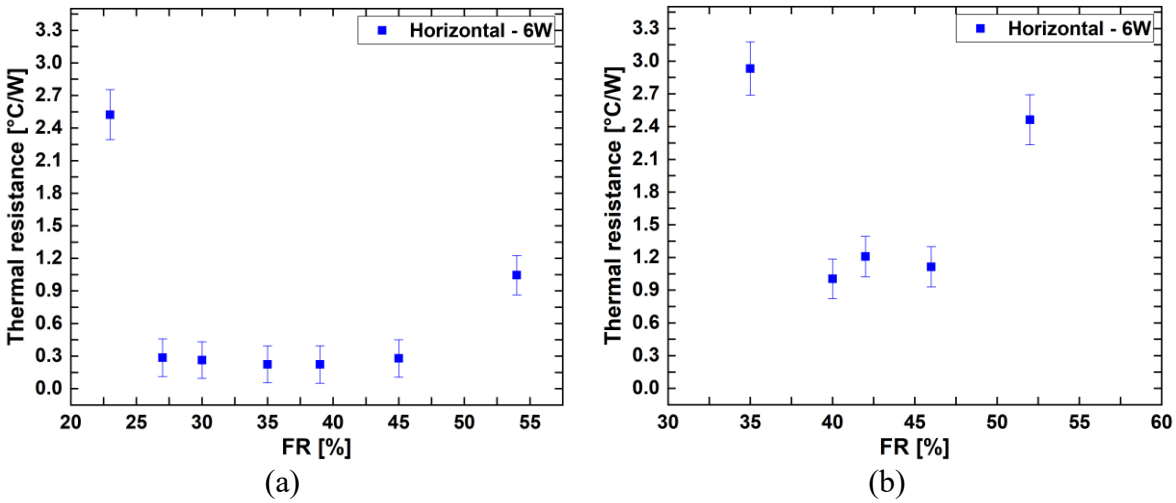

Souce: Own authorship.

6.3 INFLUENCE OF UTLHP THICKNESS

In order to understand the influence of miniaturization on the startup behavior and on the thermal performance in steady-state operation, data obtained in this study is presented and analyzed. All figures in this section are related to UTLHP with ethanol and a filling ratio of 40%.

Figure 46 shows the transient temperature behavior for several power input levels of UTLHP - B (internal plate 1 mm thick, with wick structure in the liquid line) in horizontal orientation. The data provides no indication of evaporator temperature overshoot. At 2 W and approximately 3200 s, it is observed that the vapor reaches the condenser region (T_3 and T_4). At the same time, sub-cooled liquid enters the evaporator, decreasing its temperature. The two-phase change phenomena overcome the heat transfer conduction from the evaporator to the liquid line only at 3 W. The UTLHP operates with heat input power up to 8 W, when it reaches almost 100 ºC. Besides, thermocouples T_1, T_2, T_3 and T_4 (evaporator and vapor line) are nearly equivalent at 3-5 W, when the UTLHP achieves its best thermal performance. At 6 W, the temperatures of the condenser get different from the other readings, presumably because most of the condenser length is fulfilled with vapor.

Figure 46 - UTLHP - B (FR=40%) thermal behavior with ethanol in the horizontal orientation.

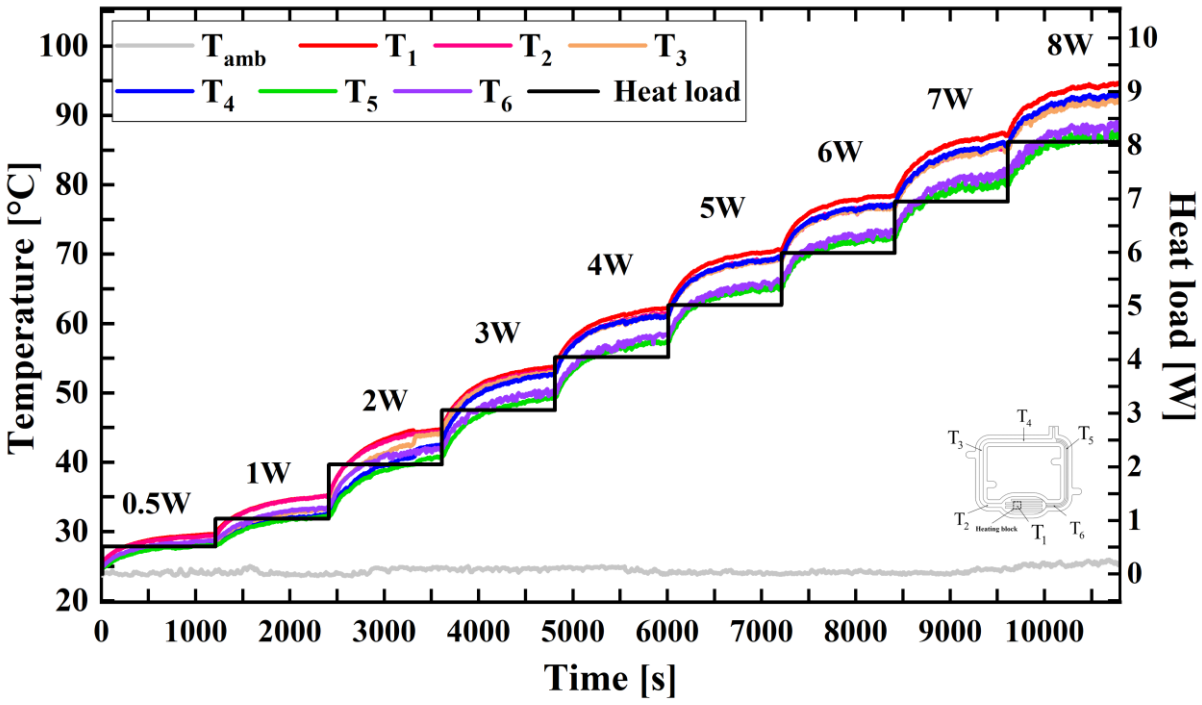

Souce: Own authorship.

Figure 47 presents the temperature readings for UTLHP - C (same configuration as Figure 46, with thinner internal plate of 0.5mm thick) in the horizontal orientation, for several power input levels. It is apparent that the startup occurs at 2 W, at approximately 3000 s. At 3 W, the evaporator (T_1), evaporator outlet (T_2), condenser inlet (T_3) and condenser (T_4) temperatures are very close. The temperature behavior of UTLHP - C is similarly to that of UTLHP - B up to 6 W. At 7 W, the thinner UTLHP failed to operate, probably because the condenser was fulfilled with vapor and the two-phase phenomena could no longer occur, i.e., the condenser length was not enough. Besides that, with vapor along the entire condenser, the pressure drop drastically increases, and the wick structure could no longer provide the necessary capillary pressure. For this reason, an evaporator temperature overshoot is observed (at 7 W). Because of the thickness reduction in 0.5 mm (50%), heat leakage from evaporator to the liquid line increases, resulting in higher values of evaporator inlet temperature (the condenser outlet temperature T_5 is lower than T_6).

Figure 47 - UTLHP - C (FR=40%) thermal behavior with ethanol in the horizontal orientation.

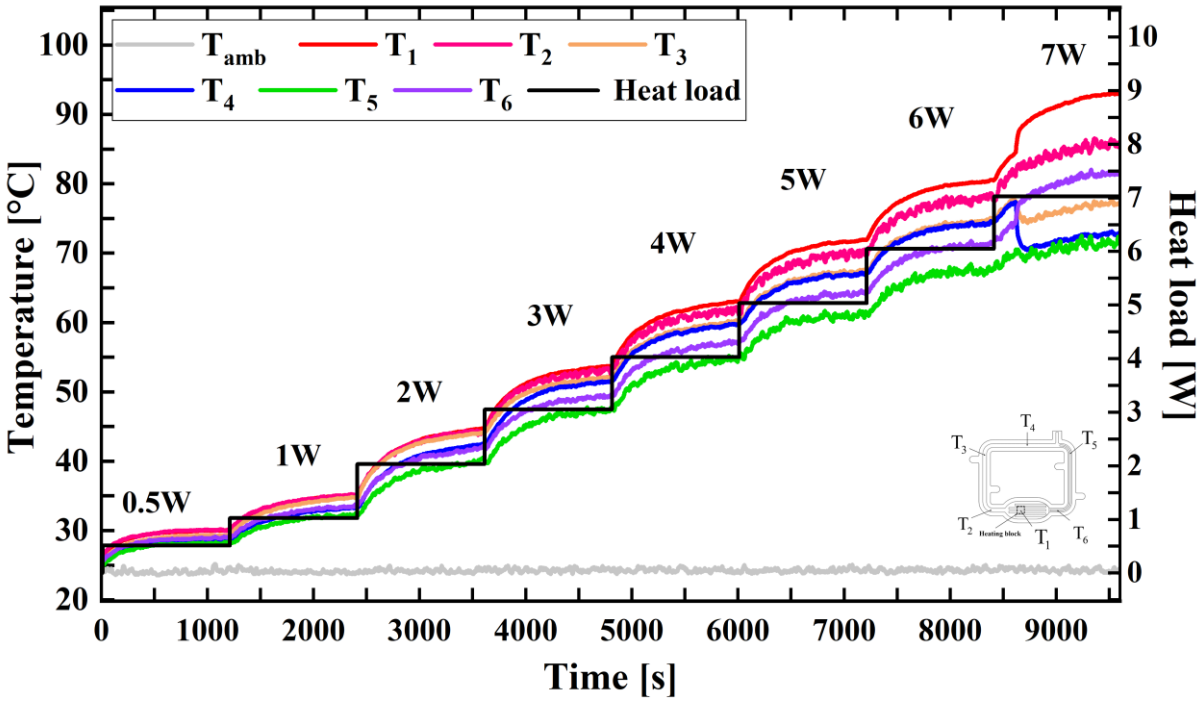

Souce: Own authorship.

Figure 48 illustrates the transient temperature values of UTLHP - D (the inner plate has 0.3 mm of thickness) in the horizontal orientation. The data indicates the evaporator temperature overshoot for all heat input applied, showing that the device does not startup. Because of the new thickness reduction to 0.3 mm (40% from UTLHP - C), the confinement

and the minimum pressure drop difference are larger. In this case, the wick could not provide the heat input power required to produce larger capillary pressure, so the liquid is not up to reach the evaporator, causing the device failure.

Equation (6) shows two possible solutions to increase the capillary pressure: to select other working fluid with larger surface tension or to select a different wick structure, which provides a smaller effective pore radius. Note that these solutions applied at the same time are not a good option: the increase of the surface tension, the fluid meniscus requires a larger driving force to circulate in the UTLHP and the decrease of the radius of curvature, the pressure drop provided by the wick structure is larger, and the working fluid might not move.

Another possible solution regarding the parasite heat would be the change of the wick material, selecting one with low wick effective thermal conductivity. This option would reduce the heat leak from the evaporator to the liquid line through the evaporator wick structure, and so higher heat loads can be applied. Likewise, the thermal conductivity of the casing should take into consideration for similar reasons. This option should be used with care because, on the condenser side, heat exchange with the environment may be less effective.

Figure 48 - UTLHP - D (FR=40%) thermal behavior with ethanol in the horizontal orientation.

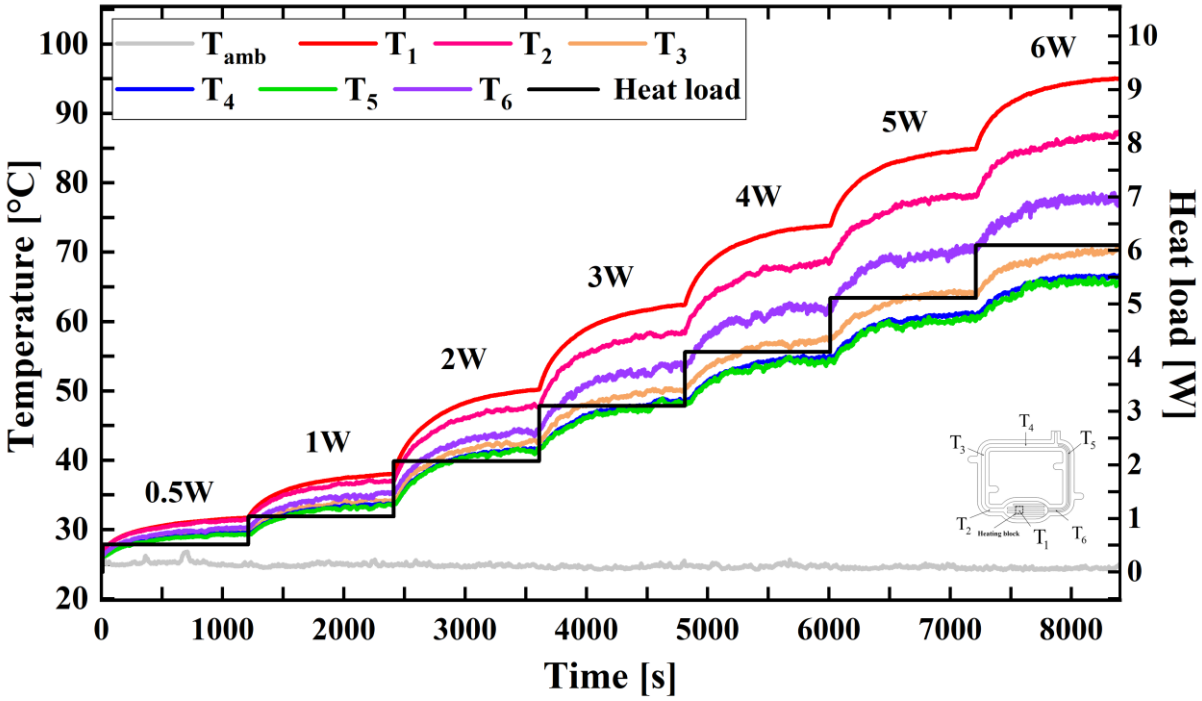

Souce: Own authorship.

Note that the experimental data showed above are the most important ones. A large number of tests were executed, varying the filling ratio for every ultra-thin loop heat pipe.

APPENDIX A – Additional experimental results show all the other experimental procedures tested.

6.3.1 Combination of thickness and filling ratio influences

Figure 49 shows the thermal resistance of UTLHP - B as a function of the applied heat load for several filling ratios and three orientations. In the horizontal and gravity-assisted orientations, for almost all filling ratios, the thermal resistance initially decreases rapidly. Above 4 W, it remains practically constant with increasing heat input level, achieving a minimum value of 0.20 ºC/W at 8 W and 0.20 ºC/W at 9 W, both for FR39%, in the horizontal and the vertical operation, respectively. It is also evident that the thermal resistance in the horizontal orientation is slight lower that in the gravity-assisted operation, specially at 3 W. Zhou, Li and Lv (2016) mentioned that this difference could be due to the presence of a larger volume working fluid in the liquid phase in the evaporator, for the gravity assisted orientation, resulting in larger liquid film thickness in the evaporator. Besides, the UTLHP had a slight better thermal performance in the gravity-assisted orientation for 9 W, probably because the air natural convection is more effective with the condenser vertically oriented. At low values of heat input, the mass flow rate of vapor is small. Consequently, only a fraction of the condenser length is used for condensation. As the applied heat load increases, the mass flow rate intensifies, and the vapor occupies a larger fraction of the condenser, achieving the best thermal performance (decreasing the thermal resistance). It is apparent that for the two extreme filling ratios tested, the UTLHP could not operate as well as for the other filling rations in the horizontal orientation: at a low filling ratio (23%), the internal channel has not enough working fluid and could not startup, while, for larger filling ratio (54%), the UTLHP could have only a late startup. In the gravity-assisted orientation, the heat transfer device has better thermal performance in these filling ratios (54% and 23%) than in the horizontal position but worse than the rest of the tested filling ratios.

The against-gravity orientation is the most difficult operation one for UTLHPs, as the working fluid needs to circulate against gravity. Therefore, the wick structure has to provide the needed capillary pressure to overcome gravity forces. Figure 49(c) illustrate the UTLHP operating is this orientation. It can be noticed that the heat transfer device could not startup and liquid is not able to return to the evaporator.

From this analysis, one can say that the orientation does not affect the UTLHP operation in gravity-assisted and horizontal orientations, but it does affect deeply when the device operated against gravity. In order to solve this problem, it is necessary to provide a larger capillary pressure, changing either the working fluid or wick structure.

Figure 49 - Thermal resistance of UTLHP - B with ethanol at different filling ratio in: (a) horizontal orientation (b) gravity-assisted orientation (c) against-gravity orientation.

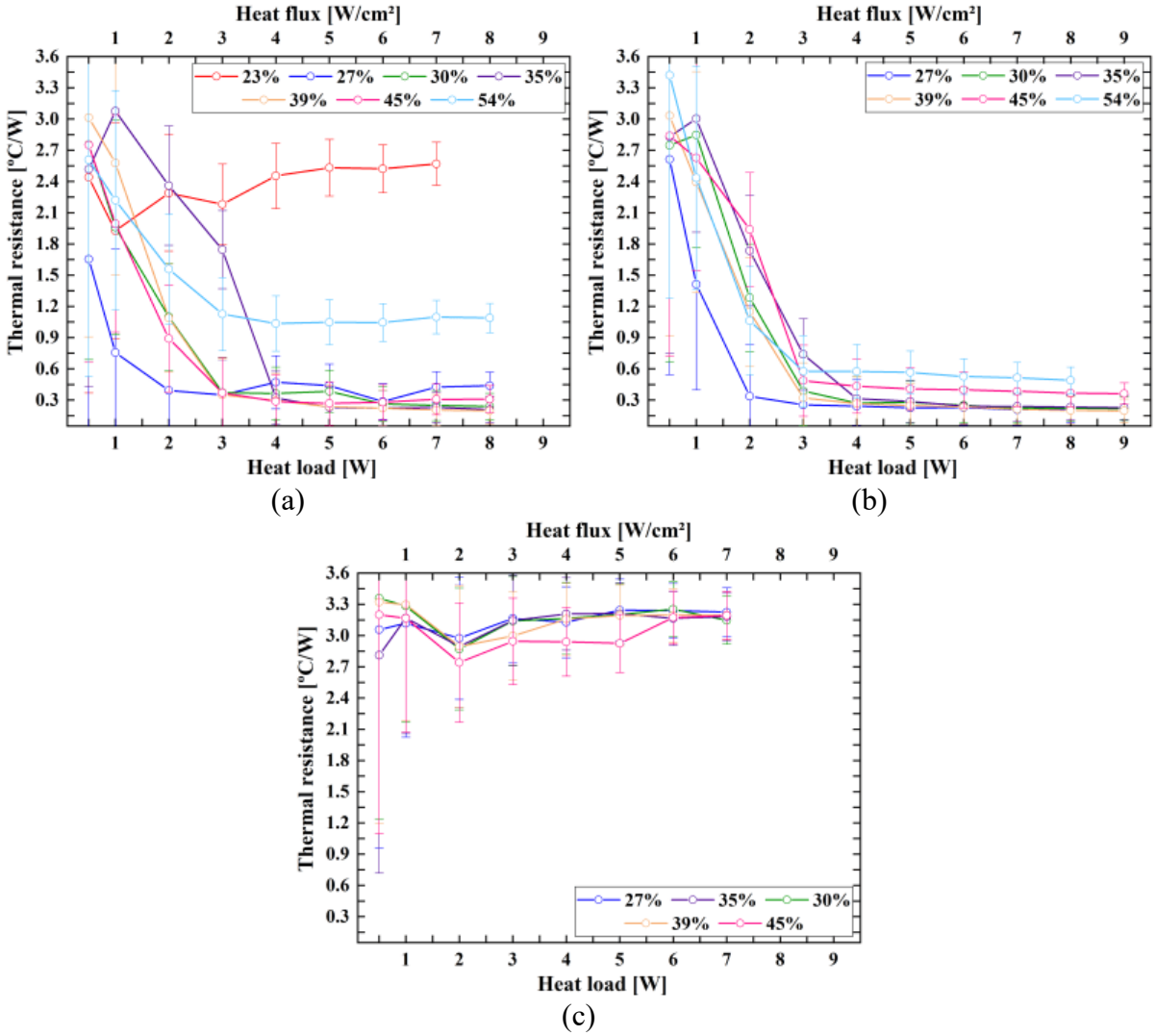

Souce: Own authorship.

Figure 50 illustrate the thermal resistance of UTLHP - C (inner layer 0.5 mm thick) as a function of increasing heat loads, in all tested orientations. In the horizontal and gravity-assisted orientations, (a) and (b), respectively, the thermal resistance decreases quickly with the power input and then stays at almost constant levels, similarly to the observations of UTLHP - B. In this case, the lowest thermal resistance values of 0.72 ºC/W is achieved at 3 W in the horizontal orientation and 1.00 ºC/W at 8 W in the gravity-assisted orientation. Compared to

the previous (and thicker) heat transfer device, the thermal resistance is approximately eight times larger, considering the best thermal performance of each UTLHP. With against-gravity operation, after 6 W, the UTLHP failed to operate, as observed by the increase in the thermal resistance. On the other hand, in the gravity-assisted orientation, UTLHP - C can operate at all tested heat inputs, up to 9 W. As happened with UTLHP - B, the device charged with two extreme filling ratios (35% and 52%) did not behave as for the other ratios. Again, in the gravity-assisted orientation, the UTLHP can stand larger values of heat input, due to the air natural convection. Lastly, as shown in Figure 50(c), in against-gravity orientation, the heat transfer device is not able to operate, as occurs with UTLHP - B, for the same reasons mentioned before.

Figure 50 - Thermal resistance of UTLHP - C with ethanol at different filling ratio in: (a) horizontal orientation (b) gravity-assisted orientation (c) against-gravity orientation.

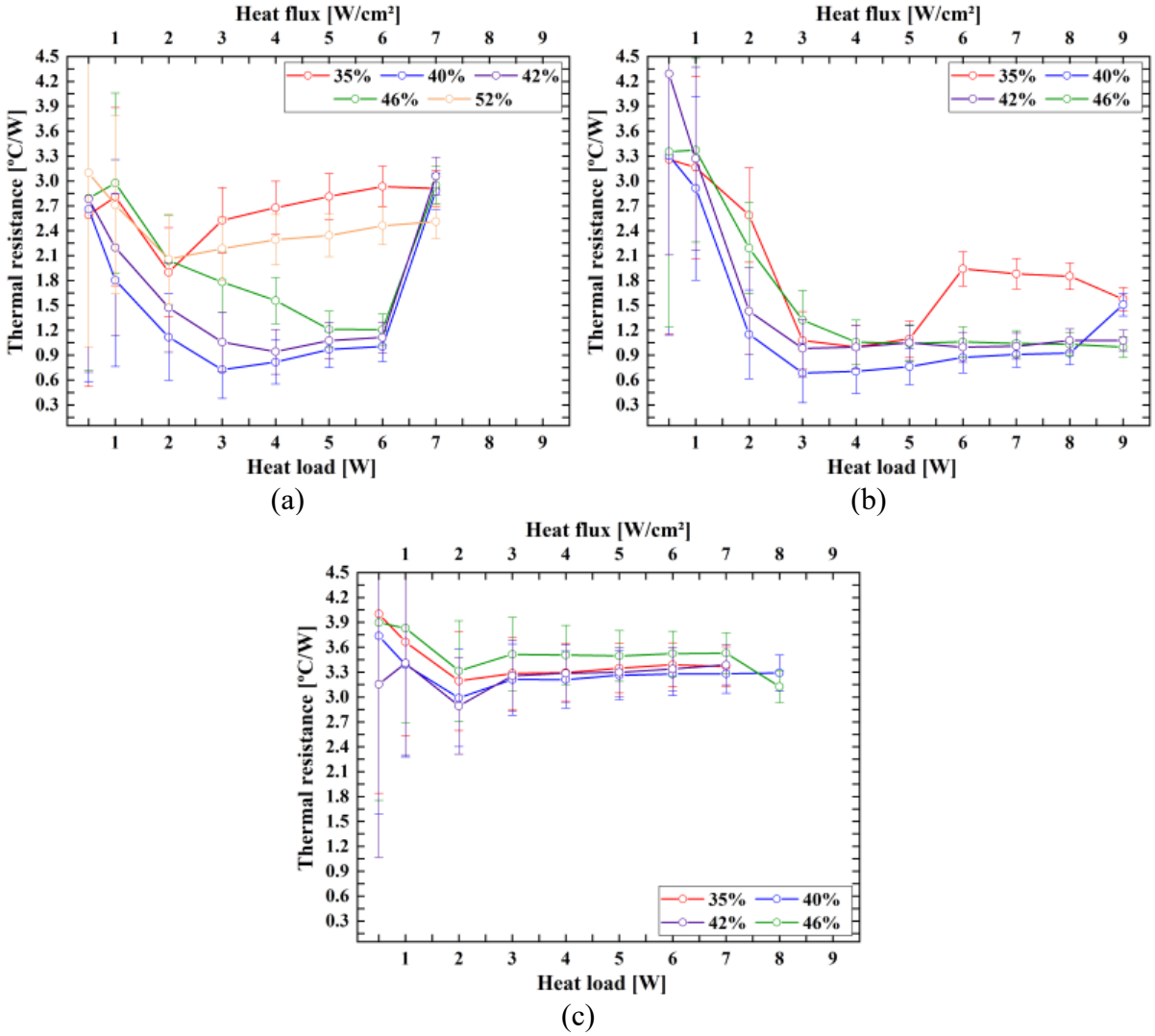

Souce: Own authorship.

Figure 51 shows the thermal resistance of UTLHP - D (the thinner tested device) as a function of the heat power input, for filling ratio of 40% and horizontal orientation. This thickness reduction of 0.2 mm causes the heat transfer device failure at any heat load applied, as showed by the thermal resistance for power levels, which remains at 4.5 ºC/W, transferring heat only by the conduction through the case material. The wick structure cannot provide the capillary pressure necessary to circulate the working fluid.

Figure 51 - Thermal resistance of UTLHP - D (FR=40%) with ethanol in the horizontal orientation.

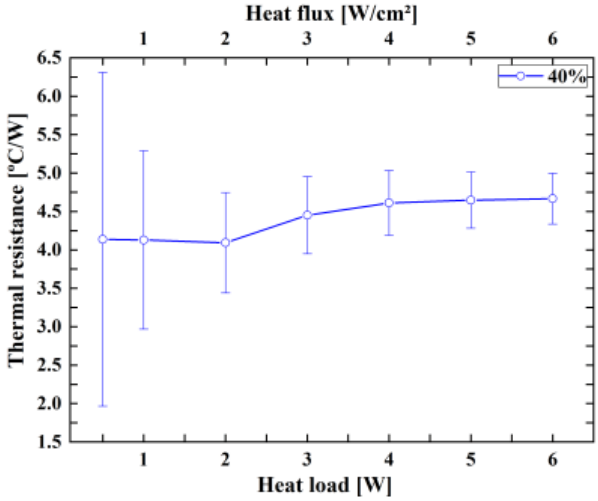

Souce: Own authorship.

6.4 INFLUENCE OF THE WORKING FLUID

As mentioned before, one possible solution to obtain larger capillary pressure is by selecting working fluids that are more adequate. For this reason, a study was performed by replacing ethanol with water, which has three times larger surface tension.

Figure 52 shows the thermal resistance as a function of the filling ratio at a heat input of 5 W in the horizontal orientation, for UTLHP - B filled with water, for variable filling ratios. The behavior of the UTLHP thermal resistance is very dependent on the fluid volume. The filling ratio of 30% indicates the most favorable thermal performance, being taken as the best filling ratio tested considering the effective heat transfer capability of the device.

Figure 52 - Influence of the filling ratio at 5W in the horizontal orientation for UTLHP - B with water.

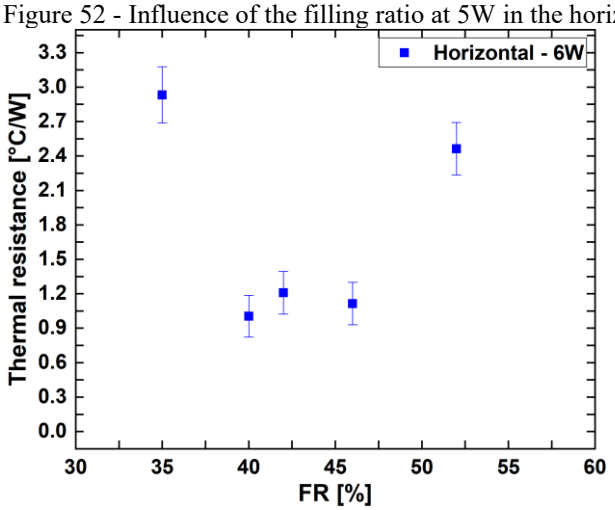

Souce: Own authorship.

The temperature readings as a function of time for the several power steps, for the UTLHP - B in the horizontal orientation, filled with FR30% of water, is shown in Figure 53(a). The data provides no indication of evaporator temperature overshoot. Compared to the heat transfer device with ethanol, it is apparent that the UTLHP with water has a startup process delayed from 2 to 3 W, achieving the same maximum heat input of 8 W. The temperatures of evaporator outlet (T_2), condenser inlet (T_3) and condenser (T_4) are very close, but further from the evaporator temperature (T_1), showing worse thermal performance than that of the device with ethanol. After 5 W, one can see that the two-phase change phenomena overcome the heat transfer conduction through the evaporator to the liquid line, i.e., T_5 reaches higher values then T_6.

Figure 53(b) shows the data from the same device operating in gravity-assisted operation. It is observed that the startup is delayed from 3 W to 5 W, happening at approximately 6500 s. At this time, the evaporator temperature decreased as the condenser temperature increased, reaching almost the same level, showing that the two-phase heat transportation overcomes the heat lost by conduction through the case material and evaporator wick. Besides, the heat transfer device did operate until 9 W, which is larger than the value of 8W in the horizontal orientation, probably because air natural convection vertically oriented is larger than in the horizontal position. Compared with Figure 53(a), the water configuration presented lower evaporator and higher condenser temperatures, at the same heat input. It can be noticed that vapor flows to the condenser more easily in the vertical orientation due to the assistance of the gravity, differently from the heat transfer device with ethanol. Figure 53(c) presents the same UTLHP - B configuration operating in the against-gravity orientation.

Analogous to the heat transfer device with ethanol, the UTLHP did not startup, even with the increasing capillary pressure of the wick structure due to the water. A possible explanation is caused by the low porosity of the wick structure (53%), which provides large pressure drops for liquid flowing in the porous media. Still, changing to water, the surface tension increases three times, which is worse in the finned pore radius.

Figure 53 – UTLHP - B (FR=30%) thermal behavior with water in: (a) horizontal orientation (b) gravity-assisted orientation (c) against-gravity orientation.

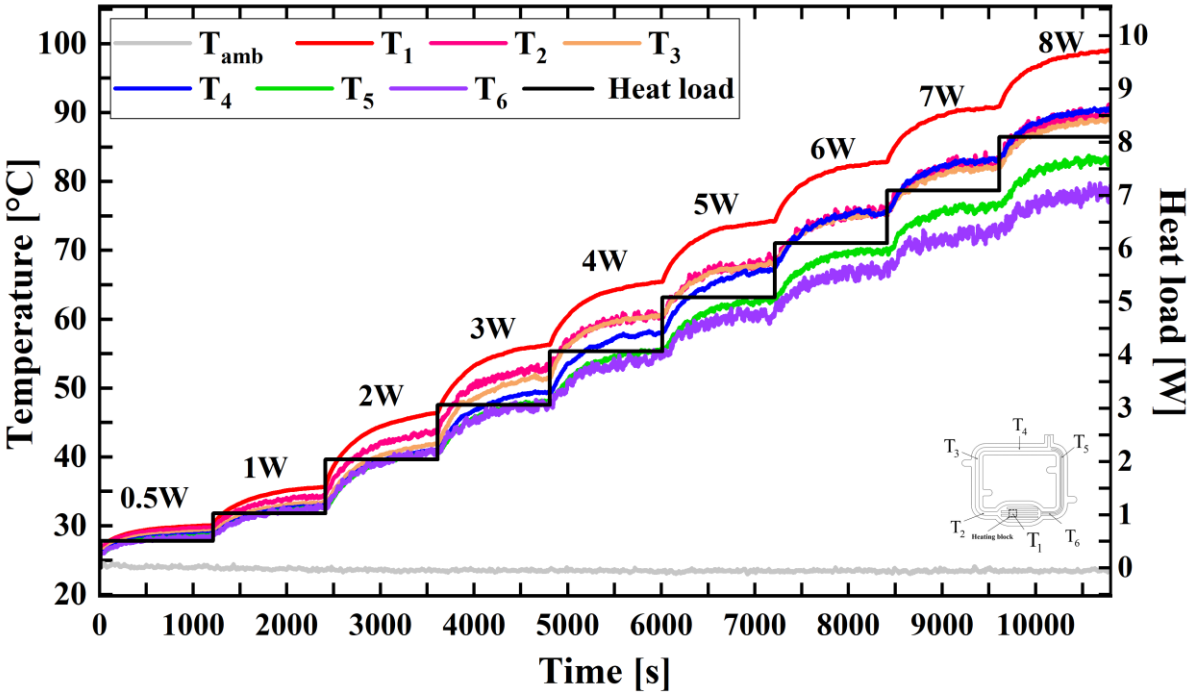

(a)

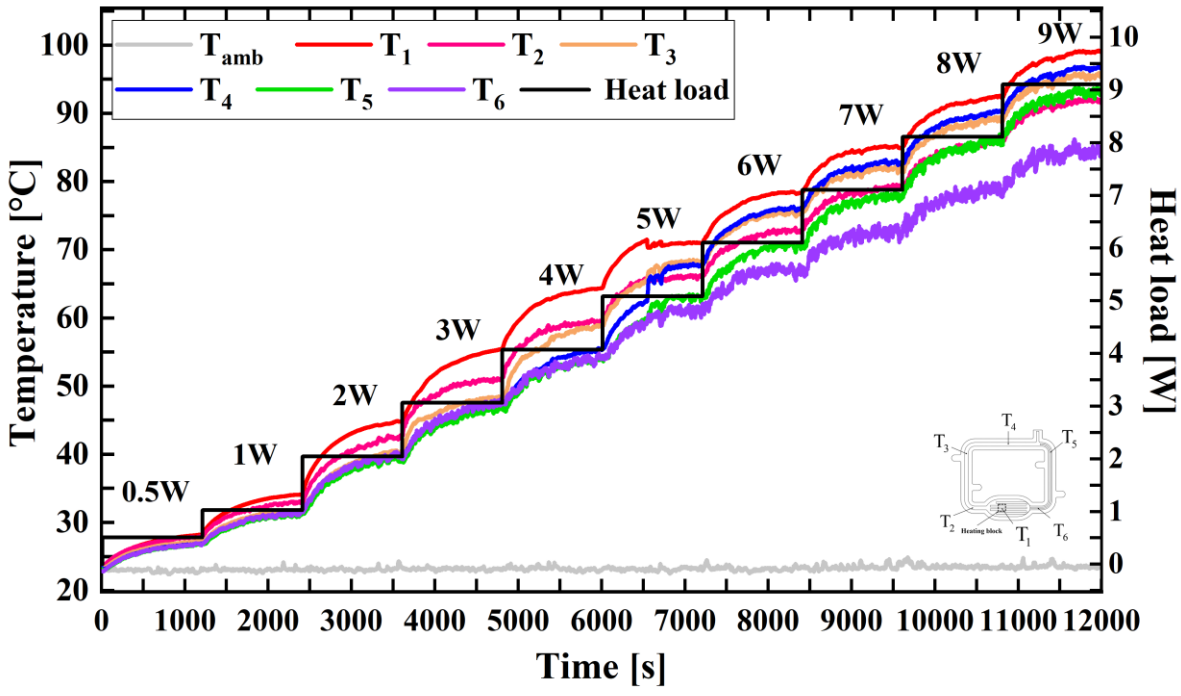

(b)

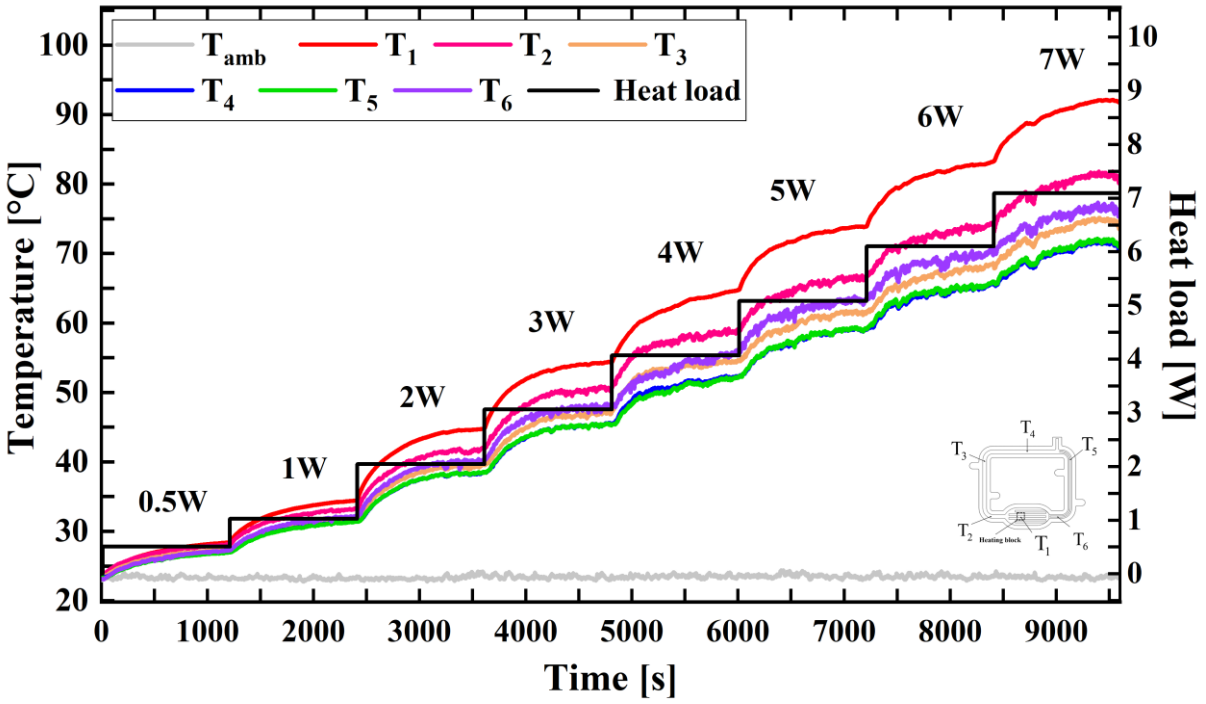

(c)

Souce: Own authorship.

The thermal resistances of UTLHP – B with water as a function of the heat inputs, at different filling ratios, in the horizontal, gravity-assisted and against gravity orientations, are shown in Figure 54. Differently from the heat transfer device with ethanol, it is apparent that the UTLHP is influenced by its orientation. In the horizontal position with a filling ratio above 25%, the UTLHP does startup, reaching a minimum thermal resistance value of 1.05 ºC/W at FR30% and 8 W, yielding the best thermal performance. For larger values of filling ratio, the device decreases its heat transfer capability. In the vertical operation, the UTLHP shows better thermal performance, as shown by the thermal resistance values. With gravity assistance, the device is able to startup in all tested filling ratios, yielding a lowest thermal resistance of 0.26 ºC/W at 9 W and FR30%, almost eight time less compared to the horizontal orientation. As expected, using water as the working fluid, the gravity influences the thermal performance of the device. Lastly, in against gravity orientation, the UTLHP is not able to operate, due to the same reasons previously mentioned.

Figure 54 - Thermal resistance of UTLHP - C with water at different filling ratio in: (a) horizontal orientation (b) gravity-assisted orientation (c) against gravity orientation.

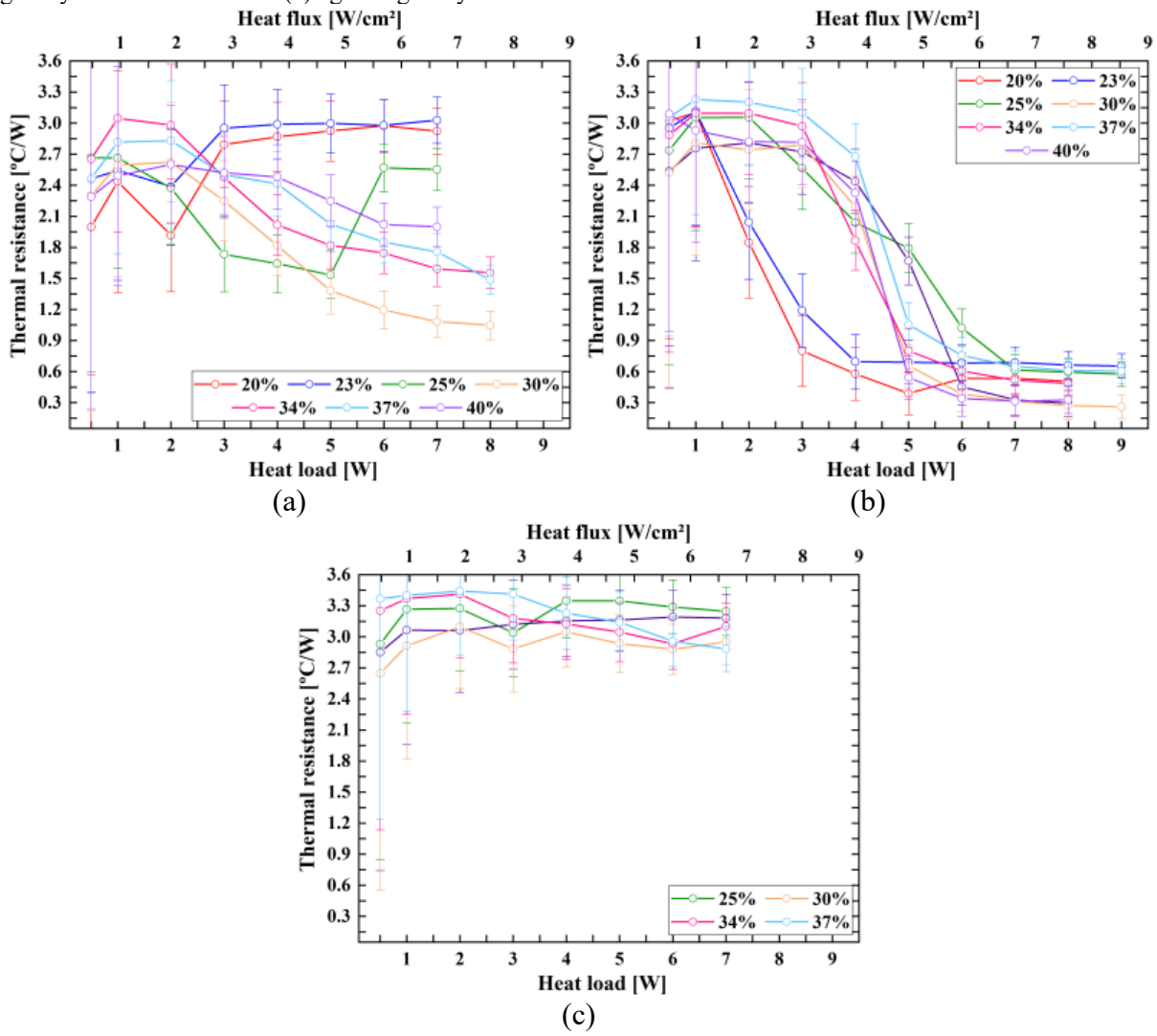

Souce: Own authorship.

Figure 55 presents the transient temperature readings for UTLHP - C with inner plate thickness of 0.5 mm, operating in the horizontal orientation. The working fluid used is water, with filling ratio of 60%. As mentioned, the objective of changing ethanol to water is to increase the capillary pressure in order to improve the thermal performance of the heat transfer device, which could be able to operate in any orientation, even against gravity. From Figure 55, it is apparent that the strategy of changing the working fluid is not effective. 60% is the only filling ratio that could circulate liquid by convection inside the device, but is not enough to cause the phase change, that characterizes the startup, when as expected, the condenser temperature (T_4) is lower than the evaporator inlet temperature (T_6).

From these results, it can be noticed that the best option to get better thermal performance and overcome the problems of miniaturization is through the wick structure

improvement, i.e., it should be proposed a porous media with higher porosity to operate with water.

Figure 55 - UTLHP - C (FR=60%) thermal behavior with water in the horizontal orientation.

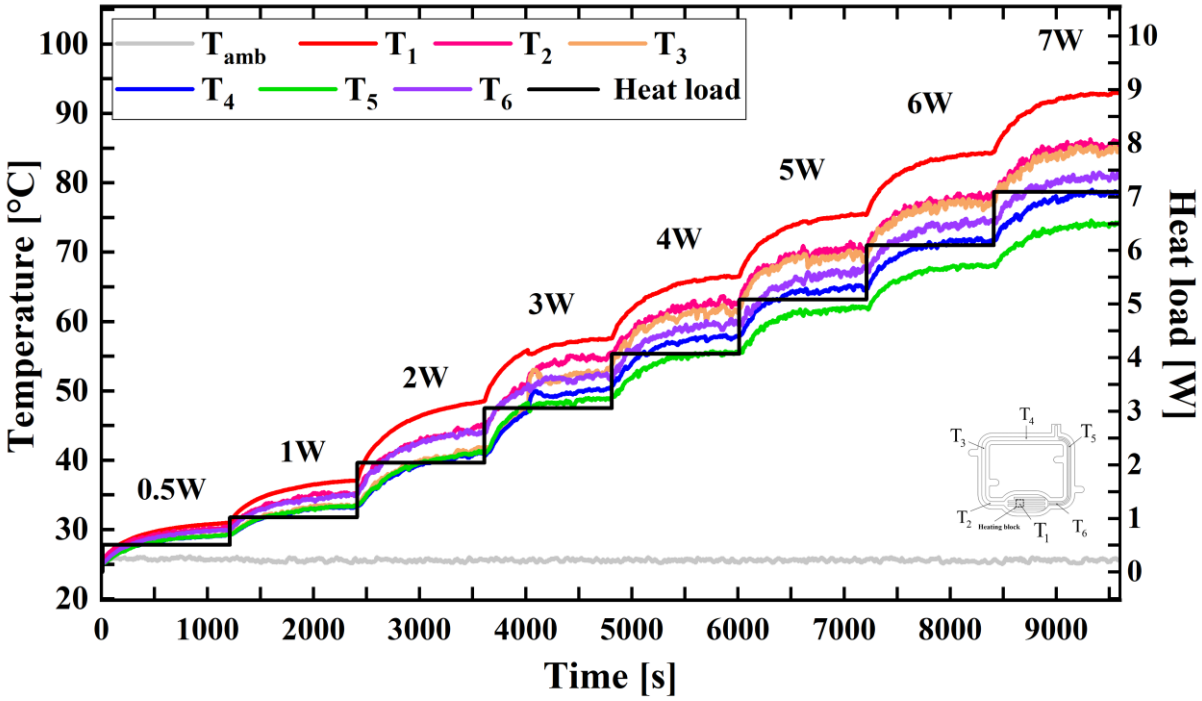

Souce: Own authorship.

6.5 VALIDATION OF THE THEORETICAL MODEL

In this section, the theoretical model results are compared with the experimental data from the UTLHP – B and UTLHP – C with ethanol as the working fluid, and with a filling ratio of 40%.

As already observed, the pressure drop is an input information for the overall thermal resistance model and this parameter was obtained from literature models. Figure 56 shows the total capillary pressure drops, for the UTLHP – B and UTLHP – C, that the wick structure can deliver. It also shows the total pressure drops expected due to the fluid movement along with the device, using several theoretical models from the literature. The UTLHP – B is thicker than the UTLHP-C and therefore smaller pressure drops are expected, as the graph shows. It is noticed that there is a huge discrepancy among the correlations of Lockhart and Martinelli, Freidel, Yang and Webb, and Chen. These correlations were used along with the present model.

For the UTLHP - B, the Freidel correlation showed better pressure drop results, with the predicted values always below the capillary limit of the wick structure, showing that the

device is able to work. Although Chen's correlation was developed for microchannels (hydraulic diameter less than 10 mm), it showed too small pressure gradients, not physically expected for very thin devices. The same can be said for Lockhart and Martinelli correlation. However, Young and Webb correlation over predicts the pressure drops, unfeasible for the system operation. Friedel correlation predicts that, for UTLHP – B with 4 W of heat load, the pressure drop almost reaches the capillary limit (proximally 75%).

For the UTLHP - C with the reduction of 0.5 mm in the loop heat pipe total thickness, resulting in a hydraulic diameter reduction from 1.5 mm to 0.8 mm, the Friedel correlation shows higher pressure drops than the capillary wick is able to provide. Also, all tested correlations for the heat transfer device with reduced thickness in 0.5 m shows poor results. The Freidel correlation predicts good results only up to 1 W for the UTLHP – C, after which level the device theoretically would be capable of functioning. However, the tests showed it operated up to 6 W. This means that the proposed theoretical model fails to predict loop heat pipes with less than 1 mm of hydraulic diameters, such as UTLHP – C and UTLHP – D. Thus, the Freidel correlation was used in the proposed theoretical model for the UTLHP - B (hydraulic diameter of 1.5 mm). Another explanation for this poorer comparison with data is that the tested loop heat pipes actually worked with less heat input than used in the model, i.e., the heat losses can be higher than predicted, mainly due to the uncertainties associated to the measurement of the heat transfer rates.

Figure 56 – Two-phase region pressure drops for (a) UTLHP – B and (b) UTLHP – C.

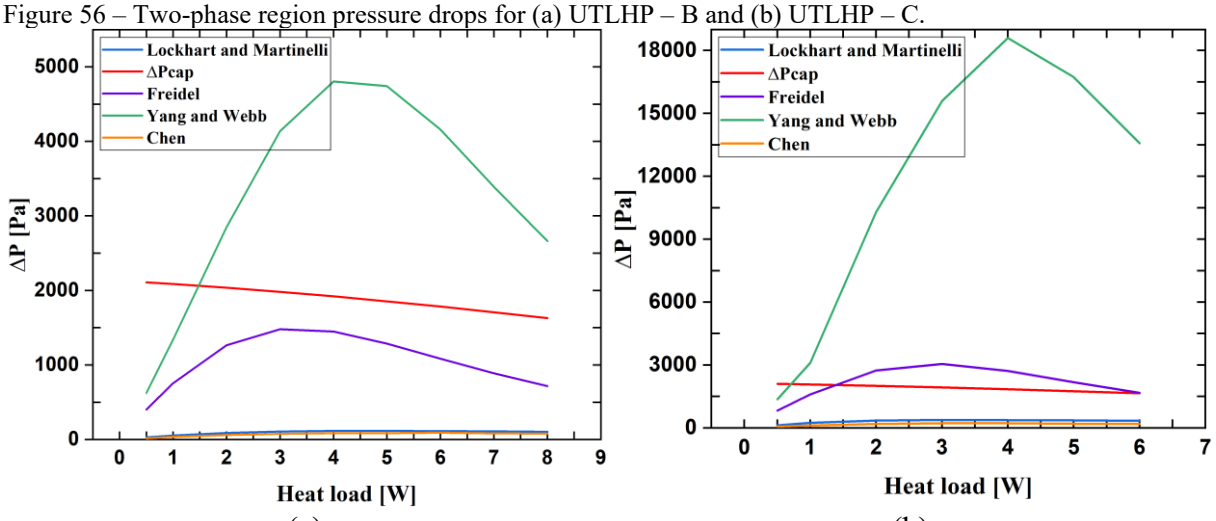

Souce: Own authorship.

Figure 57 shows the steady-state temperatures of the evaporator, the evaporator inlet and the condenser for the proposed UTLHP - B in the horizontal orientation, as function of the

heat load. The full lines and the dot points represent the analytical and the experimental results, respectively. It is apparent that the theoretical lines show three very similar theoretical temperature curves, which are in good agreement with data. Figure 57 illustrates that, for UTLHP – B, the experimental condenser temperatures (which are assumed as the average temperatures of the single-phase region, $T_{1\phi,avg}$) and evaporator temperatures (T_{ev}) are very close, while the differences between theory and data for the evaporator temperatures ($T_{ev,i}$) increase as the heat input increases. The difference between the theoretical $\widehat{T}$ (ºC) and experimental temperature T_i is calculated as $\left|\widehat{T} - T_i\right| / T_i$, resulting in: 16.15%, 14.31% and 12.82% for the evaporator, condenser and evaporator inlet temperatures, respectively. These values can be considered small considering the complexity of the physical phenomena involved. Nevertheless, the discrepancy of these results can be explained by the use of an average and constant heat transfer coefficients (h_{ev} and $h_{c,i}$) and by the uncertainties of the pressure drops theoretical predictions, which can be quite high, as this parameter could not be measured directly, due to the geometry of the sensor, usually too large for the size of the device. If variable parameters with temperature were used, the theoretical predictions could be better.

However, the good comparison clearly demonstrated that the model developed in this work can be used to evaluate the thermal performance of UTLHP with hydraulic diameters larger than 1 mm.

Figure 57 - Temperatures comparison from the experimental results and the theoretical model of UTLHP - B. E – Experimental. M – Model.

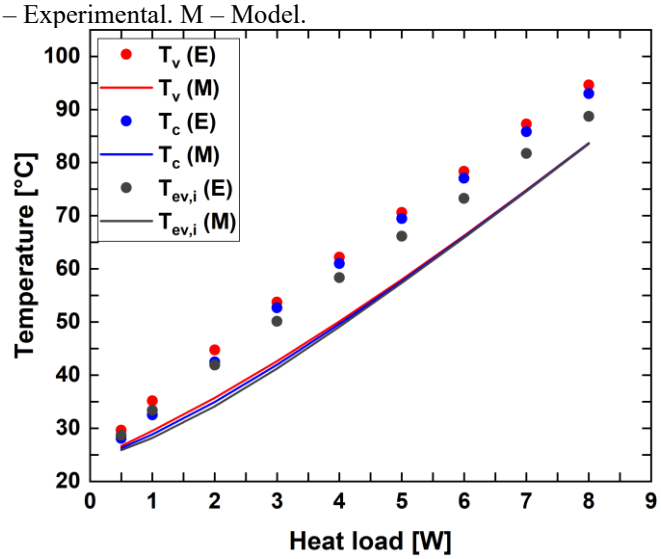

Souce: Own authorship.

The theoretical and experimental thermal resistances are also compared. The thermal resistance is also evaluated only for UTLHP - B. The resulting plots with the theoretical curves

and the experimental data as a function of the heat load are shown in Figure 58. The theoretical model under-predicts all the data points, being worse for lower power inputs, and with the difference tending to be constant as the heat load increases, after around 3 W. The average deviation of this parameter is 71.82%. This error is mainly caused because of the initial power inputs and the temperature accumulation error. However, above 3W, this difference drops to 54.35%

Figure 58 – Thermal resistance comparison between the experimental results and the theoretical model for the UTLHP - B.

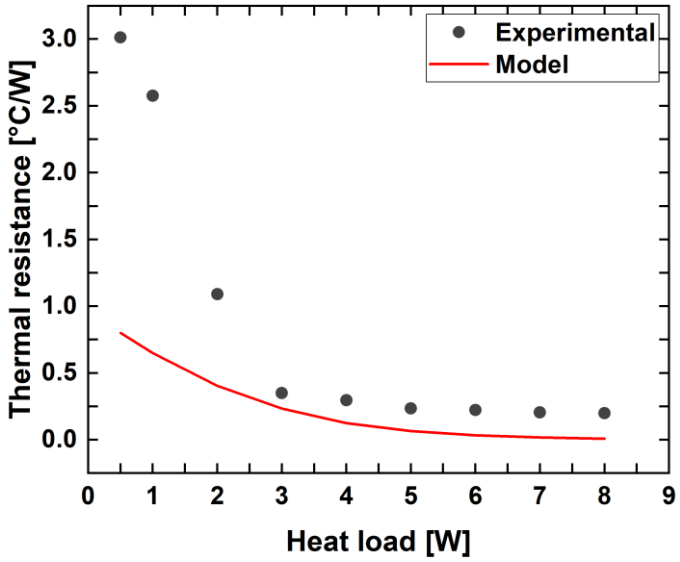

Souce: Own authorship.

The proposed theoretical model can also predict the heat leak by conduction through the case material from the evaporator to the liquid line. Figure 59 shows the heat leak comparison between the data and the analytical results, for UTLHP - B. The data indicates good agreement only up to 2 W. Above this heat input, the difference between these results is much larger. As Equation (25) shows, the increase of the total pressure drop causes larger increases in the temperature difference between T_v and $T_{ev,I}$, increasing the heat leak. The discrepancy in these results is due to the uncertainty of predicting the pressure drop, mainly in the two-phase region, which can be high as ±40% (KANDLIKAR, 2006b).

Figure 59 – Heat leak comparison from the experimental data and the theoretical model for the UTLHP – B.

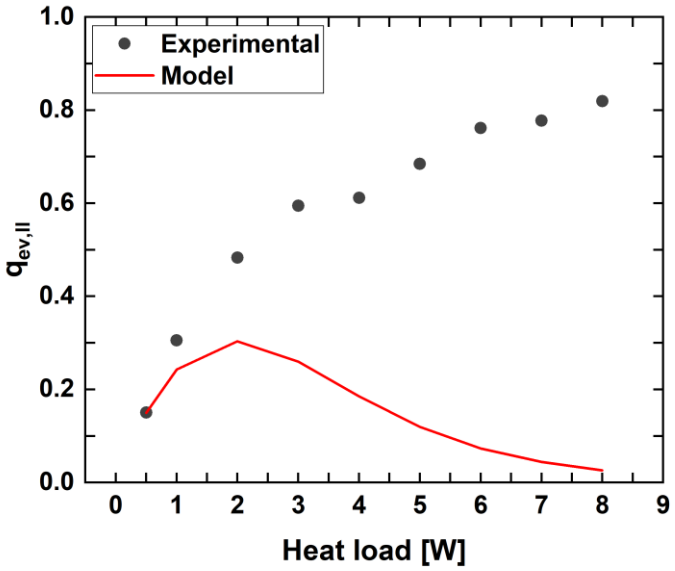

Souce: Own authorship.

Figure 60 presents the ratio between the theoretical total pressure drop in the internal channels and the capillary force provided by the wick structure, for the UTLHP - B prototype, in the horizontal orientation. This ratio should be smaller than one for the device to work. It is shown that the pressure drops gradually increase with the increasing heat input, up to 4 W. Above this point, pressure drops slowly decrease. This figure helps understanding the discrepancy between the proposed model and the data, which is also attributed to the calculation of the pressure drop and the average working fluid quality data, that takes into account the vapor volume in the device.

Besides the discrepancy caused by the pressure gradient due to large errors obtained from the correlation used in the literature, the total pressure drop decrease above 4 W of power input, as shown in Figure 60, this discrepancy can be caused by the hypothesis of the linear quality variation along the two-phase region of the condenser. The quality is also difficult to predict, increasing with the heat transfer rate applied. As the power input levels increases, the vapor may reach the liquid line wick structure, close to the evaporator inlet. If the vapor phase completes the entire condenser, which has lower convection heat transfer coefficients, the natural convection cooling effect in the condenser regions may fail, and the heat dissipation in the condenser is no longer effective.

Figure 60 – Pressure balance according to the theoretical model for the UTLHP – B.

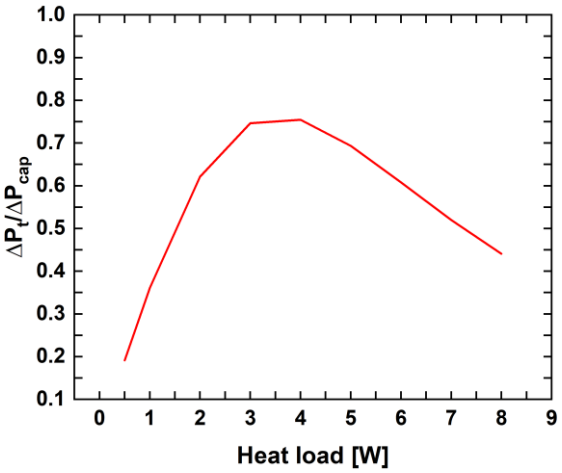

Souce: Own authorship.

The last parameter to be determined is the necessary condenser length for both single and two-phase change flow phenomena. Actually, the condenser length is a limiting parameter for the operation of UTLHP. Figure 61 shows the condenser length ratio, $L_{1\phi}/L_c$ and $L_{2\phi}/L_c$, according to the theoretical model in the horizontal orientation. As expected, for UTLHP - B, at low values of heat load applied, the single-phase flow ($L_{1\phi}$) and two-phase change ($L_{2\phi}$) lengths are nearly the same. Above 1 W, the condensation region length increases with increasing heat inputs, reaching almost the total condenser length at 8 W. This result shows that, at 4 W, condition where the theoretical model starts to fail, the two-phase condenser length estimated is around 95% of the total condenser length, confirming the good agreement between the results until this point. The fulfillment of the condenser with vapor will cause the condenser failure. For this reason, the theoretical model can only show good agreement with data only up to 4 W, as, after this point, the results are not reliable.

Figure 61 - Condenser length according to the theoretical model for the UTLHP - B.

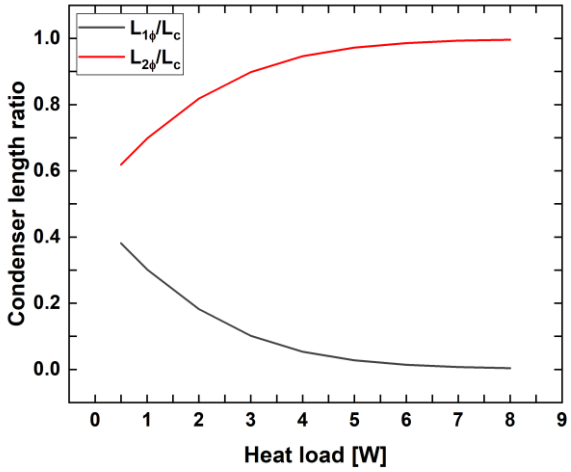

Souce: Own authorship.

7 CONCLUSIONS

This dissertation focused on the study of miniaturization of flat loop heat pipes, aiming to electronics applications. Based on the literature review, three lines of action were adopted in the present study. First, the development of a new fabrication methodology, aiming the reduction of the common deformations mentioned. Second, a parametric study involving the construction and tests of several UTLHPs, in which the influence of the following parameters was accessed: wall thickness, filling ratio, operation mode, heat input and working fluid. Third, a theoretical model is proposed, taking into account the geometry and the thermophysical properties of the UTLHP in order to obtain a design tool for this UTLHP and help in the analysis of the data.

The present work provides the following main contributions for the state of the art:

- It was demonstrated that the diffusion bonding is a convenient fabrication method, as it causes few deformations along the heat transfer device.
- A capillary structure in the liquid line is necessary in order to improve the working fluid pumping capacity for the device working in horizontal orientation. However, in vertical operation, both heat transfer device works similarly, both achieving a minimum thermal resistance of 0.22 ºC/W.
- The experimental results show that the total volume of working fluid inside the heat transfer device affects directly its thermal performance. The best filling ratio configurations for the heat transfer device of 1.6 mm thick with ethanol varied between 30% and 40%, and for water the best filling ratio was 30%. The same device, but with 1.2 mm thick and ethanol, demonstrated better thermal performance at 40% of filling ratio.
- As expected, the data confirms that reducing the thickness of heat pipes, its thermal performance reduces, due to the higher heat leaks by heat conduction and larger working fluid confinement. The ultra-thin loop heat pipe, with 1.6 mm of thickness, shows smaller values of evaporator inlet temperature compared to the device with 1.2 mm of thickness. Still, this last heat transfer device presents a condenser outlet temperature lower than the evaporator inlet

temperature, showing that the two-phase heat transfer mechanism did not overcome the heat conduction through the casing material (heat leakages).

- In the horizontal orientation, the ultra-thin loop heat pipe with ethanol and 1.6 mm of total thickness can startup and overcome the heat leak at 2 W and 3 W. A minimum thermal resistance value of 0.20 ºC/W was achieved at 8 W. Reducing the wall thickness by 50%, i.e., 0.5 mm thick, the heat transfer device failed to operate at 7 W, probably because the condenser area was not enough. For this device, the lowest thermal resistance value of 0.72 ºC/W was achieved at 3 W. for the 0.3 mm thick inner plate device, the heat transfer device could not operate, presumably because the heat input power requires higher capillary pressure than the wick could provide. Using ethanol, the gravity influence in the horizontal orientation is not large, but in the against gravity orientation the wick structure is not able to overcome the gravity force.
- To study the influence of the working fluid in the ultra-thin loop heat pipes, water was selected as an alternative fluid, due to its parameters that theoretically would improve the capillary pressure. It was demonstrated that water and probably any other fluid, might not be a good solution. The heat transfer device of 1.6 mm thick with water, worked but with a worse thermal performance, reaching a minimum thermal resistance value of 1.05 ºC/W in the horizontal orientation. Besides, the device with water showed to be influenced by gravity. Maintaining the low porosity of the wick structure (53%) with increasing the surface tension of the working fluid can be an explanation.
- The proposed theoretical model was able to predict: temperatures, thermal resistances, pressure drops, heat leaks, and single and two-phase condenser lengths. Freidel's correlation showed better results compared to other correlations. The discrepancies found may be explained by three major factors: the use of average and constant heat transfer coefficients (h_{ev} and $h_{c,i,}$); the uncertainties associated with the heat transfer rate measurements; the large error of the pressure drop predictions. Despite that, it was demonstrated that the proposed theoretical model can predict the design tool parameters of loop heat pipes with hydraulic diameter larger than 1 mm.
- The proposed heat transfer device showed to be attractive for electronic application, as smartphones. The following requirements were achieved: a heat

source with small area as 1 cm², dissipation from 2 W up to 9 W by air natural convection, operated with temperatures below 100 ºC and thicknesses less than 1.6 mm. However, the heat transfer device failed to work in against gravity orientation.

As demonstrated in this work, the heat and mass transfer mechanisms in ultra-thin loop heat pipes are highly complex and is being recently much investigated by researches around the world, especially for electronics applications. The present study does not claim to solve and explain all problems regarding the operation of this heat transfer device. Therefore, in order to continue the investigation, some ideas for future works are suggested below:

- To design an enhanced wick, which would improve the thermal performance of the heat transfer device. Different wick structures should be tested, with higher porosity, from 60 to 75%. A less conductive porous structure and chemically compatible with the working fluid would be good in order to reduce the heat transfer conduction through the evaporator and liquid line wick. Furthermore, it is essential to properly characterize the properties of the porous wick in order to provide reliable experimental data for comparison with theoretical models.
- In order to improve the available capillary pressure, the liquid line wick structure could be replaced by some solid fiber, which may provide the confinement level in the liquid channel of the same order of the configuration without this wick structure.
- The experimental setup should be tested with various configurations, such as new with vapor grooves designs, a more efficient condenser and more adequate transport lines.
- Further studies regarding the pressure drops of two-phase change in the condenser should be undertaken, mainly for channels with hydraulic diameter less than 1 mm. Pressure measurements should be performed in order to enable better choice of pressure drop correlations for the theoretical model or to propose a novel correlation for microchannels.

REFERENCES

ACT. **MERIT NUMBER AND FLUID SELECTION**. Disponível em: <https://www.1-act.com/merit-number-and-fluid-selection/>. Acesso em: 24 dec. 2020.

AGOSTINI, B. et al. State of the art of high heat flux cooling technologies. **Heat Transfer Engineering**, v. 28, n. 4, p. 258–281, 2007.

ALBERTAZZI, G. J. A.; SOUSA, A. R. **Fundamentos de Metrologia: Científica e Industrial**. 1º edição ed. Barueri: Editora Manole Ltda., 2008.

ALI, M. E. Natural convection heat transfer from horizontal rectangular ducts. **Journal of Heat Transfer**, v. 129, n. 9, p. 1195–1202, 2007.

AMBIRAJAN, A. et al. Loop heat pipes: A review of fundamentals, operation, and design. **Heat Transfer Engineering**, v. 33, n. 4–5, p. 387–405, 2012.

AOKI, H.; IKEDA, M.; KIMURA, Y. Ultra Thin Heat Pipe and Its Application. **Frontiers in Heat Pipes**, v. 2, n. 4, p. 2–6, 2012.

APPLE. **Iphone compare**. Disponível em: <https://www.apple.com/br/iphone/compare/>.

BAI, L. et al. Mathematical modeling of steady-state operation of a loop heat pipe. **Applied Thermal Engineering**, v. 29, n. 13, p. 2643–2654, 2009.

BEJAN, A.; KRAUS, A. D. **Heat Transfer Handbook**. Hoboken, New Jersey: John Wiley & Sons, Inc., 2003.

BETANCUR-ARBOLEDA, L. et al. Diffusion-bonded pulsating heat pipes: fabrication study and new channel proposal. **Journal of the Brazilian Society of Mechanical Sciences and Engineering**, v. 42, n. 9, p. 1–17, 2020.

CHEN, X. et al. A review of small heat pipes for electronics. **Applied Thermal Engineering**, v. 96, p. 1–17, 2016.

CHEN, Y. et al. Steady-state and transient performance of a miniature loop heat pipe. **International Journal of Thermal Sciences**, v. 45, n. 11, p. 1084–1090, 2006.

CHEN, Y. M.; WU, S. C.; CHU, C. I. Thermal performance of sintered miniature heat pipes. **Heat and Mass Transfer/Waerme- und Stoffuebertragung**, v. 37, n. 6, p. 611–616, 2001.

CHERNYSHEVA, M. A.; VERSHININ, S. V.; MAYDANIK, Y. F. Operating temperature and distribution of a working fluid in LHP. **International Journal of Heat and Mass Transfer**, v. 50, n. 13–14, p. 2704–2713, 2007.

CHI, S. W. **Heat pipe theory and practice: A sourcebook (Series in thermal and fluids engineering)**. [s.l.] Hemisphere Pub. Corp, 1976.

CHOI, J. et al. Interface engineering to enhance thermal contact conductance of evaporators in miniature loop heat pipe systems. **Applied Thermal Engineering**, v. 60, n. 1–2, p. 371–378, 2013.

CHUANG, P.-Y. A. An improved steady-state model of loop heat pipe based on experimental and theorical analyses. v. 1, n. December, p. 271, 2003.

CHUANG, P. A. An Improved Steady-State Model of Loop Heat Pipe Based on Experimental and Theoretical Analyses The Pennsylvania State University The Graduate School Department of Mechanical and Nuclear Engineering AN IMPROVED STEADY-STATE MODEL OF LOOP HEAT PIPES BASED . n. December, 2014.

EXNER, H. E.; ARZT, E. Sintering Processes. In: **Sintering Key Papers**. Dordrecht: Springer Netherlands, 1990. p. 157–184.

FAGHRI, A. Heat Pipes: Review, Opportunities and Challenges. **Frontiers in Heat Pipes**, v. 5, n. 1, 2014.

FLOREZ, J. P. M. et al. Powder Geometry based models for sintered media porosity and effective thermal conductivity. **Journal of Thermophysics and Heat Transfer**, v. 28, n. 3, p. 507–517, 2014.

FLOREZ, J. P. M.; MANTELLI, M. B. H.; NUERNBERG, G. G. V. Effective thermal conductivity of sintered porous media: Model and experimental validation. **International Journal of Heat and Mass Transfer**, v. 66, p. 868–878, 2013.

FLÓREZ MERA, J. P.; CHIAMULERA, M. E.; MANTELLI, M. B. H. Permeability model of sintered porous media: analysis and experiments. **Heat and Mass Transfer/Waerme- und Stoffuebertragung**, v. 53, n. 11, p. 3277–3285, 2017.

FLOW. **Como o jato de água funciona**. Disponível em: <https://www.flowwaterjet.com.br/Aprender/Como-o-jato-de-agua-funciona.aspx#basics>. Acesso em: 11 jan. 2021.

FUKUSHIMA, K.; NAGANO, H. New evaporator structure for micro loop heat pipes. **International Journal of Heat and Mass Transfer**, v. 106, p. 1327–1334, 2017.

GERMAN, R. M. **Sintering Theory and Practice**. New York, NY: John Wiley & Sons, Inc., 1996.

GONCHAROV, K. A. .; BARANTSEVICH, V. L. . Experience of development of heat pipes applied in russian spacecrafts. **Orlov A.A. TAIS Ltd.**, 2005.

HOANG, T. T. et al. Miniature loop heat pipes for electronic cooling. **Advances in Electronic Packaging**, v. 2, p. 517–525, 2003.

HOANG, T. T.; KU, J. Heat and mass transfer in loop heat pipes. **Proceedings of the ASME Summer Heat Transfer Conference**, v. 2003, p. 485–493, 2003.

HOTHARDWARE. **Surface pro4 teardown highlights disposable nature of tablet pcs**. Disponível em: <https://hothardware.com/news/surface-pro-4-teardown-highlights-disposable-nature-of-tablet-pcs>. Acesso em: 21 feb. 2021.

INCROPERA, F. P.; DEWITT, D. P.; BERGMAN, T. L. **Fundamentos De Transferência De Calor E De Mass**. 6ª ed. [s.l.] LTC, 2008.

KANDLIKAR, S. G. Flow Boiling in Minichannels and Microchannels. **Heat Transfer and Fluid Flow in Minichannels and Microchannels**, p. 175–226, 2006a.

KANDLIKAR, S. G. Single-Phase Liquid Flow in Minichannels and Microchannels. **Heat Transfer and Fluid Flow in Minichannels and Microchannels**, n. 1999, p. 87–136, 2006b.

KAYA, T.; GOLDAK, J. Numerical analysis of heat and mass transfer in the capillary structure of a loop heat pipe. **International Journal of Heat and Mass Transfer**, v. 49, n. 17–18, p. 3211–3220, 2006.

KISEEV, V. M.; VLASSOV, V. V.; MURAOKA, I. Experimental optimization of capillary structures for loop heat pipes and heat switches. **Applied Thermal Engineering**, v. 30, n. 11–12, p. 1312–1319, 2010.

KU, J. Operating characteristics of loop heat pipes. **SAE Technical Papers**, 1999.

LAUNAY, S.; SARTRE, V.; BONJOUR, J. Analytical model for characterization of loop heat pipes. **Journal of Thermophysics and Heat Transfer**, v. 22, n. 4, p. 623–631, 2008.

LAUNAY, S.; VALLÉE, M. State-of-the-Art Experimental Studies on Loop Heat Pipes. **Frontiers in Heat Pipes**, v. 2, n. 1, 2011.

LENEL, F. V. **Powder Metallurgy: Principles and Applications**. Princeton, NJ: Metal Powder Industry, 1980.

LI, Y. et al. Thermal performance of ultra-thin flattened heat pipes with composite wick structure. **Applied Thermal Engineering**, v. 102, p. 487–499, 2016.

MA, H. **Oscillating Heat Pipes**. New York, NY: Springer New York, 2015.

MANTELLI, M. B. H. **Thermosyphons and Heat Pipes: Theory and Applications**.

Cham: Springer International Publishing, 2021.

MAYDANIK, Y. F. Loop heat pipes. v. 25, p. 635–657, 2005.

MAYDANIK, Y. F.; CHERNYSHEVA, M. A.; PASTUKHOV, V. G. Review: Loop heat pipes with flat evaporators. **Applied Thermal Engineering**, v. 67, n. 1–2, p. 294–307, 2014.

MAYDANIK, Y. F.; VERSHININ, S. V. Development and tests of ammonia Miniature Loop Heat Pipes with cylindrical evaporators. **Applied Thermal Engineering**, v. 29, n. 11–12, p. 2297–2301, 2009.

MERA, J. P. F. **HEAT AND MASS TRANSFER ANALYSIS OF A COPPER LOOP HEAT**. [s.l.] Universidade Federal de Santa Catarina, 2016.

MILANEZ, F.; MANTELLI, M. B. H. Heat Transfer Limit Due To Pressure Drop of a Two-Phase Loop Thermosyphon. **Heat Pipe Science and Technology, An International Journal**, v. 1, n. 3, p. 237–250, 2010.

MISHKINIS, D. et al. Development of LHP for Intermediate Temperature Range. **15th International Heat Pipe Conference**, n. APRIL 2010, 2010.

MOORE, G. E. Cramming more components onto integrated circuits (Reprinted from Electronics. **Proceedings Of The Ieee**, v. 86, n. 1, p. 82–85, 1998.

MORTEAN, M. V. V. et al. Soldagem por difusão de aços inoxidáveis para fabricação de trocadores de calor compactos. **Soldagem e Inspecao**, v. 21, n. 1, p. 103–114, 2016.

MSI. **Understanding what goes into designing an efficien laptop cooling solution**. Disponível em: <https://www.msi.com/blog/laptops-101-understanding-what-goes-into-designing-an-efficient-laptop-cooling-solution%0A>. Acesso em: 21 feb. 2021.

P. D'ENTREMONT, B.; OCHTERBECK, J. M. **Pipes and Capillary Pumped Loops**. 38th AIAA Thermophysics Conference. **Anais**...Toronto, Ontario Canada: 2005

PETERSON, G. P. **An introductin to heat pipes: Modeling, testing, and applications**. 1. ed. New York, NY: John Wiley & Sons, Inc., 1994.

RAMASAMY, N. S. et al. Miniature ammonia loop heat pipe for terrestrial applications: Experiments and modeling. **International Journal of Thermal Sciences**, v. 124, n. July 2017, p. 263–278, 2018.

REAY, D. .; KEW, P. . Heat Pipes Theory Design and Applications. **Heat Pipes (Fifth Edition)**, p. 1–8, 2007.

RUSNALDY, R. Diffusion Bonding : an Advanced of Material Process. **ROTASI**, v. 3, n. 1, p. 23–27, 2001.

SHIOGA, T.; MIZUNO, Y.; NAGANO, H. Operating characteristics of a new ultra-thin loop heat pipe. **International Journal of Heat and Mass Transfer**, v. 151, 2020.

SIEDEL, B. Analysis of heat transfer and flow patterns in a loop heat pipe : Modelling by analytical and numerical approaches and experimental observations. 2015.

SIEDEL, B.; SARTRE, V.; LEFÈVRE, F. Numerical investigation of the thermohydraulic behaviour of a complete loop heat pipe. **Applied Thermal Engineering**, v. 61, n. 2, p. 541–553, 2013.

SINGH, R. et al. Theoretical modelling of miniature loop heat pipe. **Heat and Mass Transfer/Waerme- und Stoffuebertragung**, v. 46, n. 2, p. 209–224, 2009a.

SINGH, R.; AKBARZADEH, A.; MOCHIZUKI, M. Effect of wick characteristics on the thermal performance of the miniature loop heat pipe. **Journal of Heat Transfer**, v. 131, n. 8, p. 1–10, 2009b.

SINGH, R.; AKBARZADEH, A.; MOCHIZUKI, M. International Journal of Heat and Mass Transfer Operational characteristics of the miniature loop heat pipe with non-condensable gases. **International Journal of Heat and Mass Transfer**, v. 53, n. 17–18, p. 3471–3482, 2010a.

SINGH, R.; AKBARZADEH, A.; MOCHIZUKI, M. Thermal potential of flat evaporator miniature loop heat pipes for notebook cooling. **IEEE Transactions on Components and Packaging Technologies**, v. 33, n. 1, p. 32–45, 2010b.

SINGH, R.; NGUYEN, T.; MOCHIZUKI, M. Capillary evaporator development and qualification for loop heat pipes. **Applied Thermal Engineering**, v. 63, n. 1, p. 406–418, 2014.

TANG, H. et al. Review of applications and developments of ultra-thin micro heat pipes for electronic cooling. **Applied Energy**, v. 223, n. January, p. 383–400, 2018.

TECHJUICE. **Samsung galaxy s9 note heat pipe**. Disponível em: <https://www.techjuice.pk/samsung-galaxy-s9-note-9-heat-pipes/%0A>. Acesso em: 21 feb. 2021.

VAN OOST, S. et al. Secondary wick operation principle and performance mapping in LHP and FLHP evaporators. v. 94, p. 94–103, 2007.

WHITE, F. M. **Fluid Mechanics**. [s.l.] Tata Mcgraw Hill Education, 2011.

WIKICHIP. **Snapdragon 800**. Disponível em: <https://en.wikichip.org/wiki/qualcomm/snapdragon_800/855>.

WIKICHIP. **A12x Bionic**. Disponível em: <https://en.wikichip.org/wiki/apple/ax/a12x>.

YAKOMASKIN, A. .; MORSKOY, D. N.; AFANASIEV, V. N. **Feasibility Study of Loop Heat Pipes with Flat Microchannel Evaporator and Non-Metal Wick**. International Heat Pipe Symposium. **Anais**...Taipei, Taiwan: 2011

ZHANG, X.; LI, X.; WANG, S. Three-dimensional simulation on heat transfer in the flat evaporator of miniature loop heat pipe. **International Journal of Thermal Sciences**, v. 54, p. 188–198, 2012.

ZHOU, G.; LI, J.; LV, L. An ultra-thin miniature loop heat pipe cooler for mobile electronics. **Applied Thermal Engineering**, v. 109, p. 514–523, 2016.

ZHOU, W. et al. Thermal performance of ultra-thin flattened heat pipes. **Applied Thermal Engineering**, v. 117, p. 773–781, 2017.

APPENDIX A – Additional experimental results

All others obtained experimental data are presented below:

- UTLHP - A (Working fluid: Ethanol)

Figure A1 - UTLHP - A (FR=22%) behavior during a power cycle in the (a) horizontal orientation (b) gravity-assisted orientation.

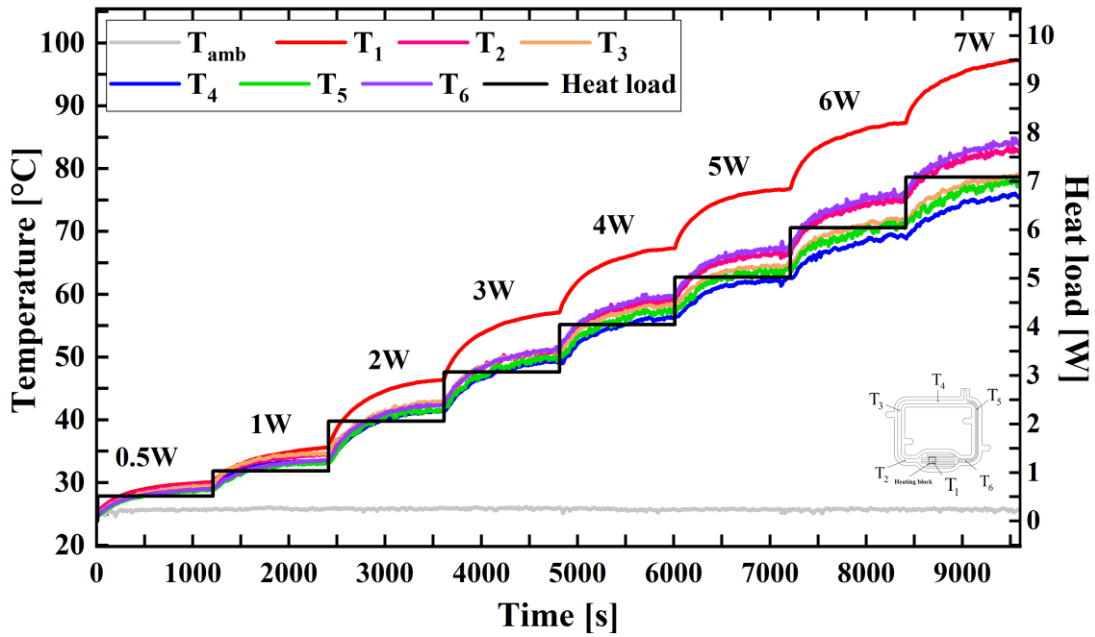

(a)

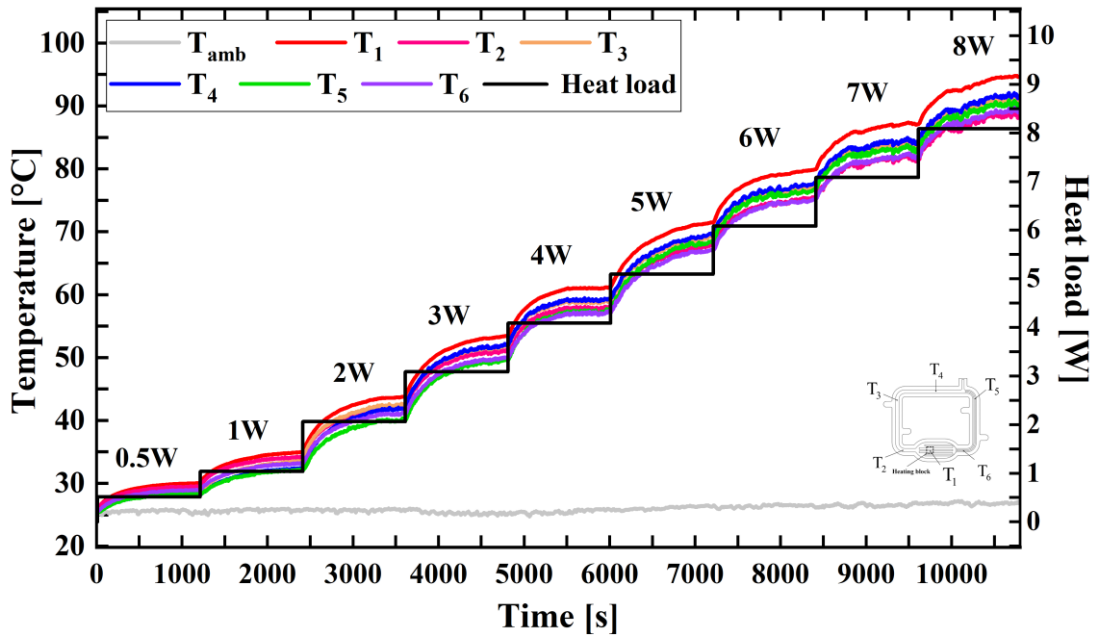

(b)

Souce: Own authorship.

Figure A2 - UTLHP - A (FR=40%) behavior during a power cycle in the (a) horizontal orientation (b) gravity-assisted orientation.

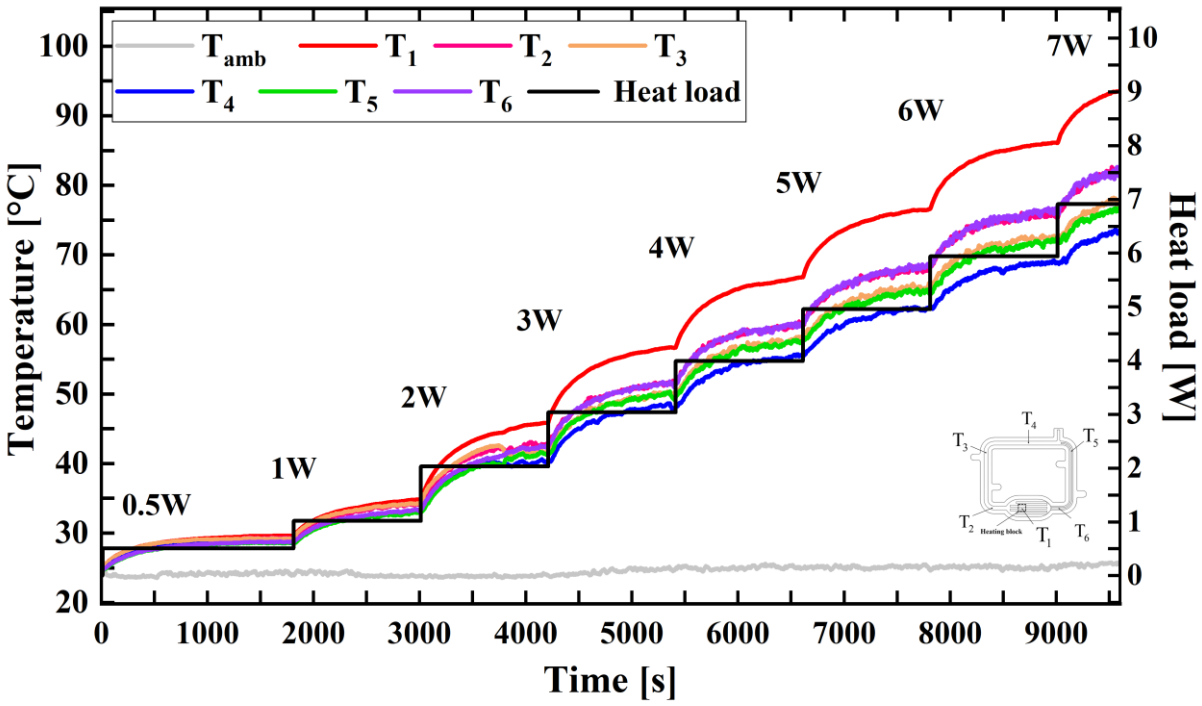

(a)

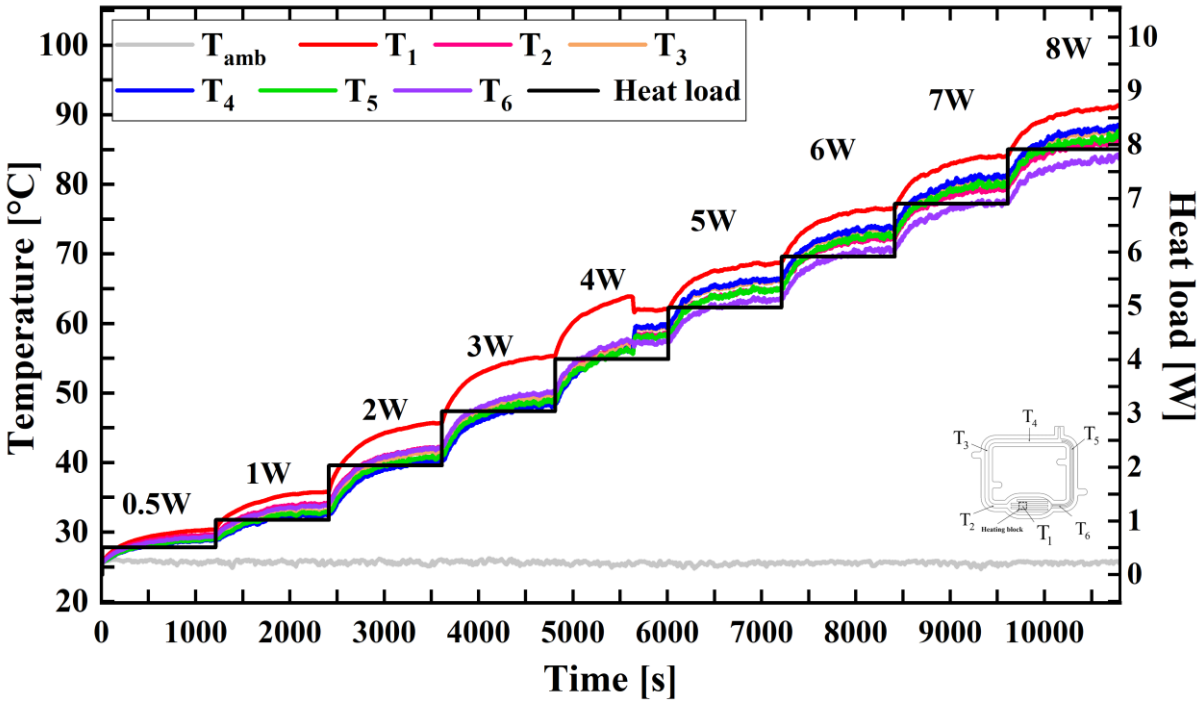

(b)

Souce: Own authorship.

- UTLHP - B (Working fluid: Ethanol)

Figure A3 - UTLHP - B (FR=23%) behavior during a power cycle in the horizontal orientation

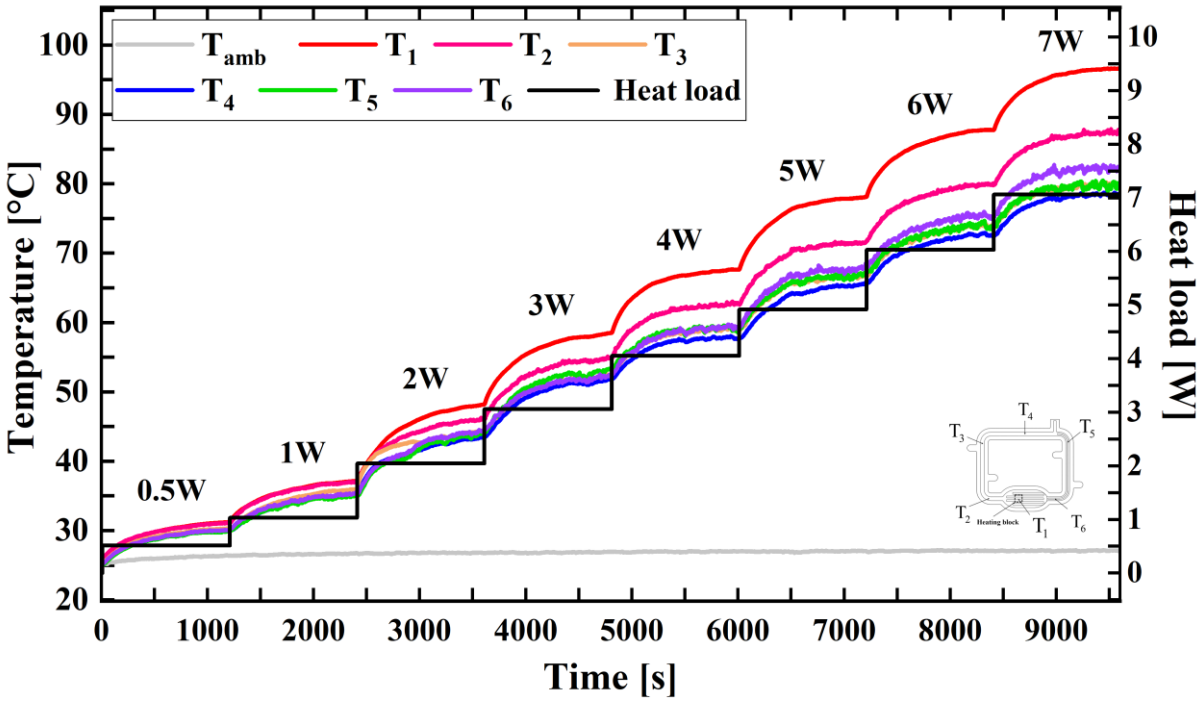

Souce: Own authorship.

Figure A4 - UTLHP - B (FR=27%) behavior during a power cycle in the (a) horizontal orientation (b) gravity-assisted orientation (c) against gravity orientation.

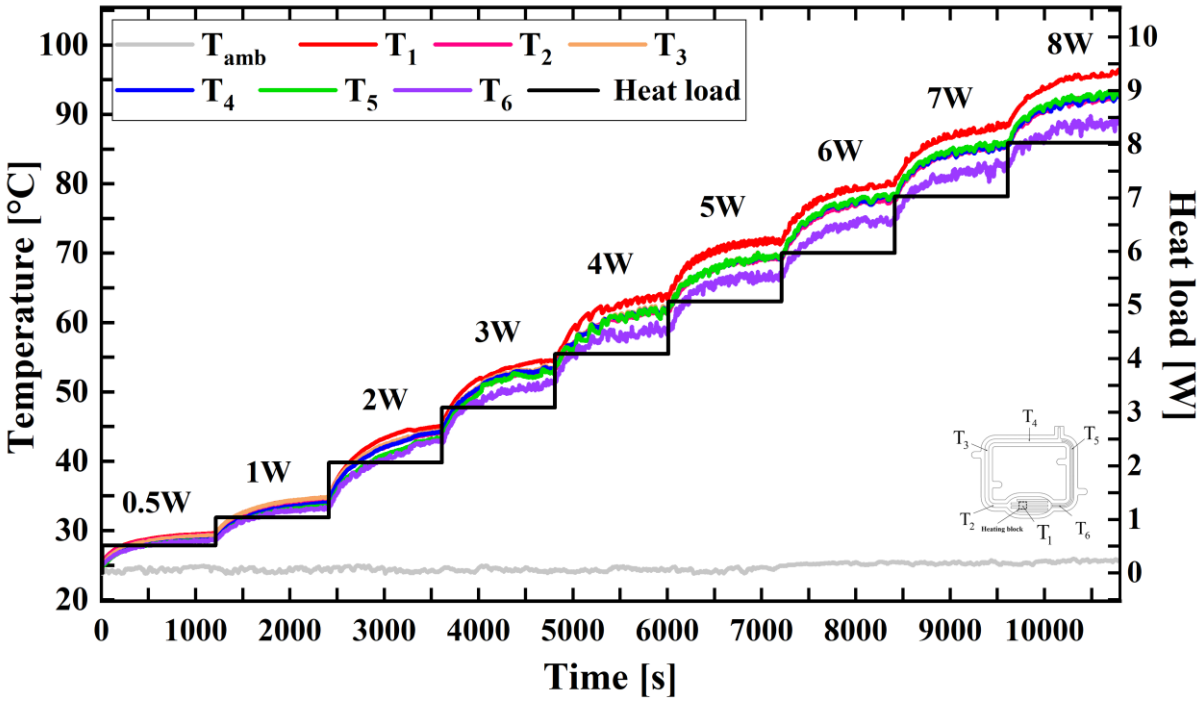

(a)

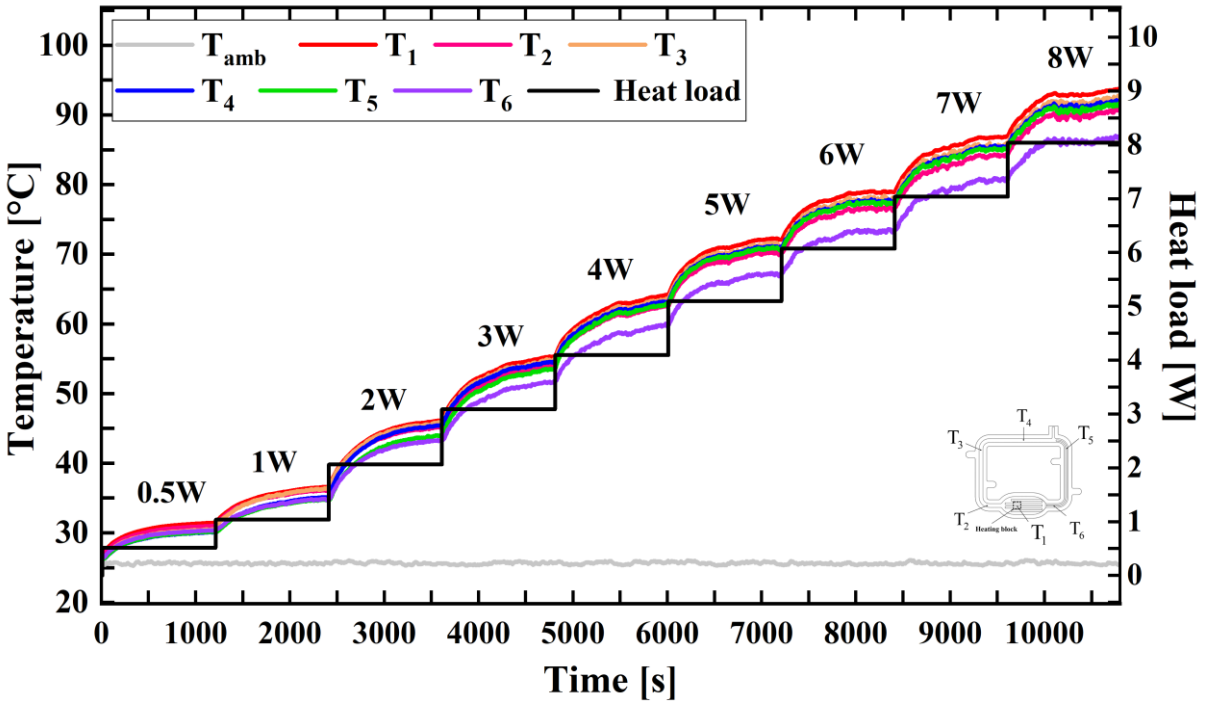

(b)

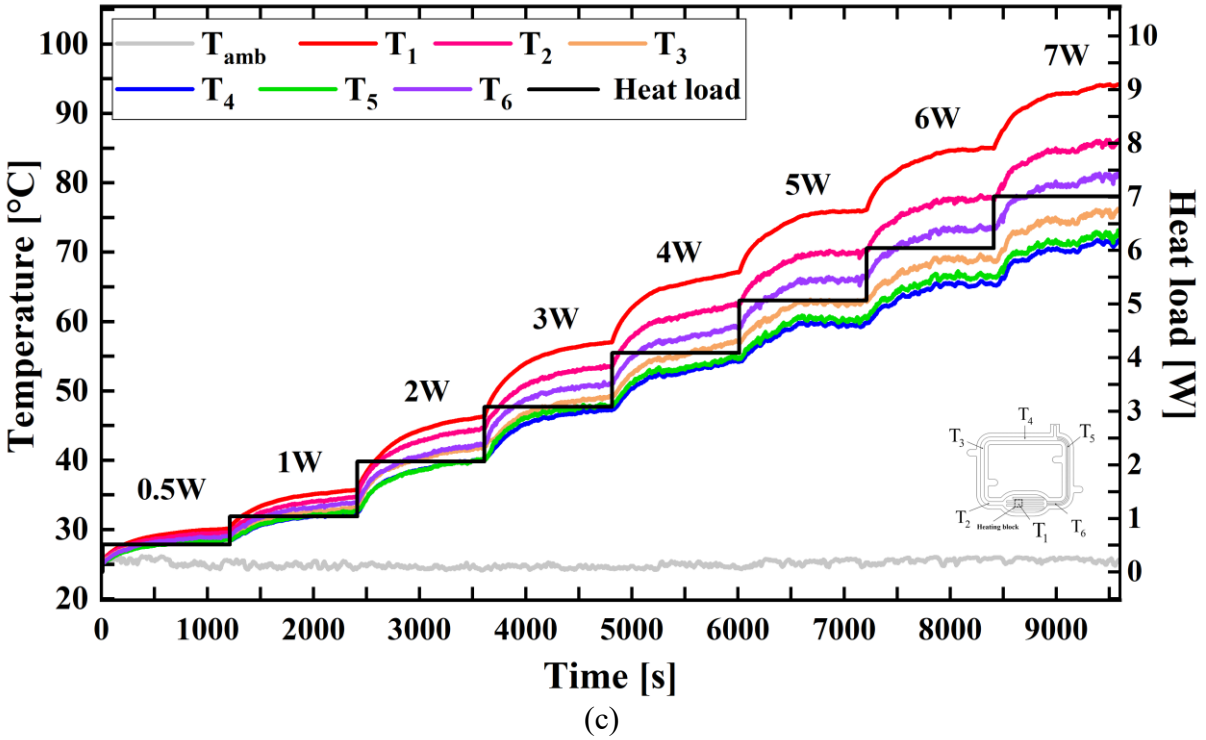

(c)

Souce: Own authorship.

Figure A5 - UTLHP - B (FR=30%) behavior during a power cycle in the against gravity orientation.

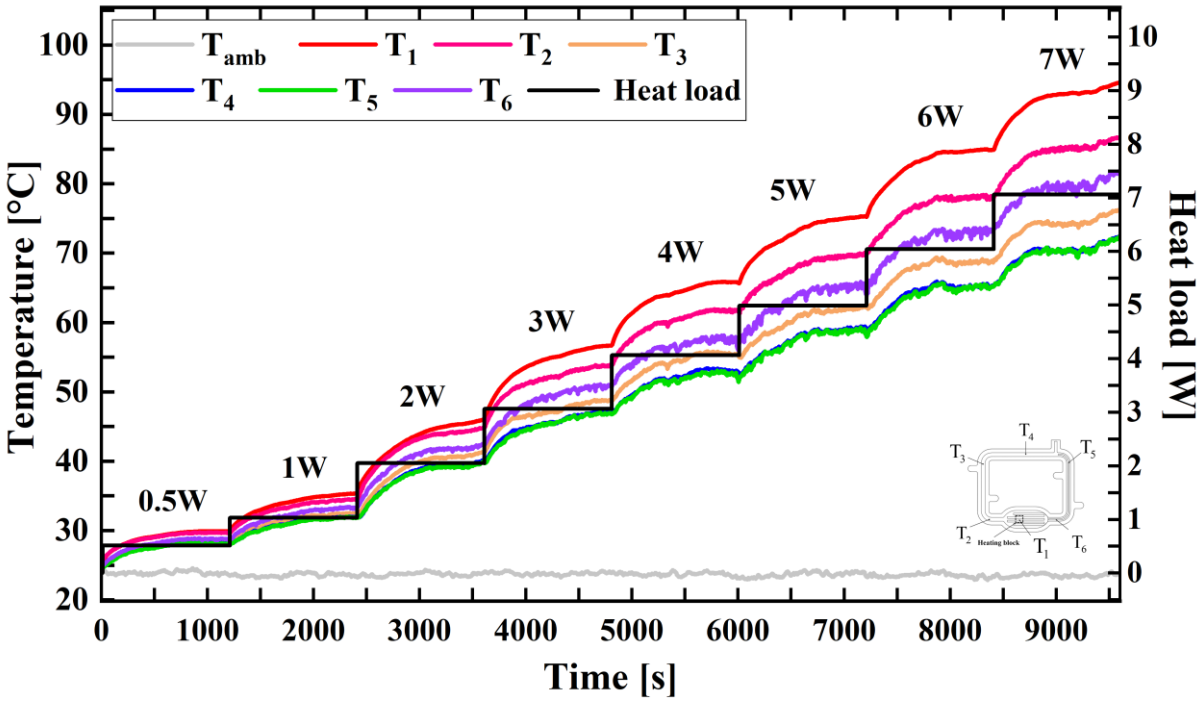

Souce: Own authorship.

Figure A6 - UTLHP - B (FR=35%) behavior during a power cycle in the (a) horizontal orientation (b) gravity-assisted orientation (c) against gravity orientation.

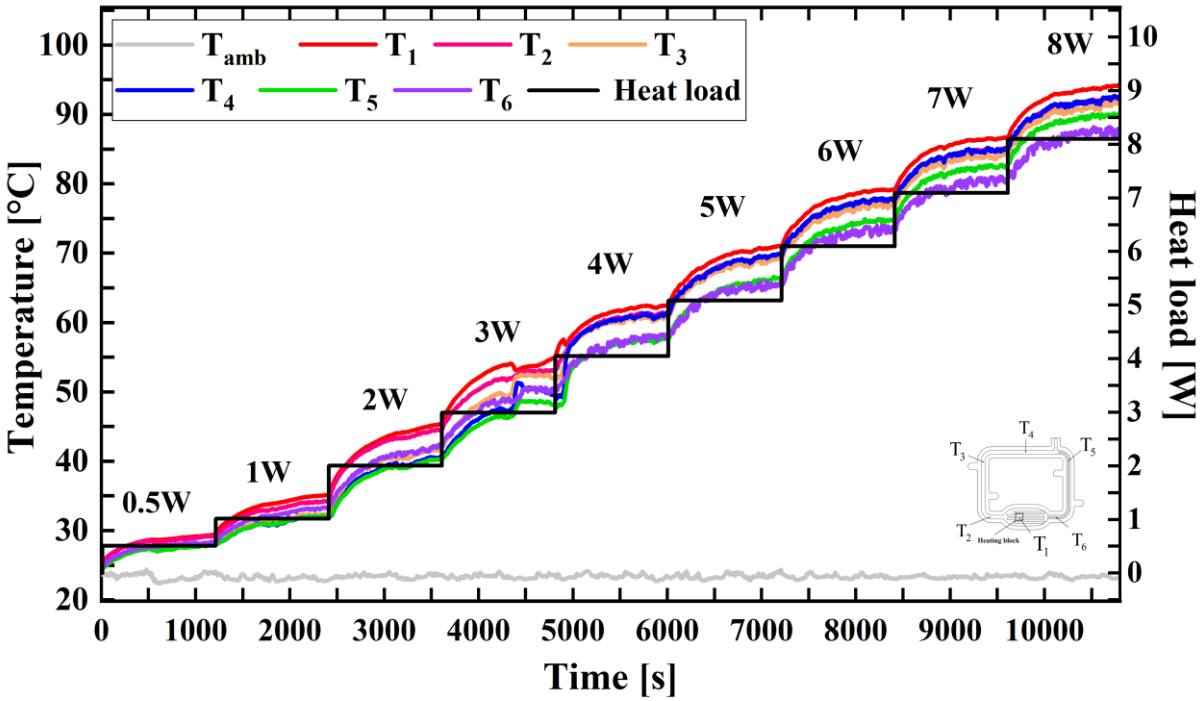

(a)

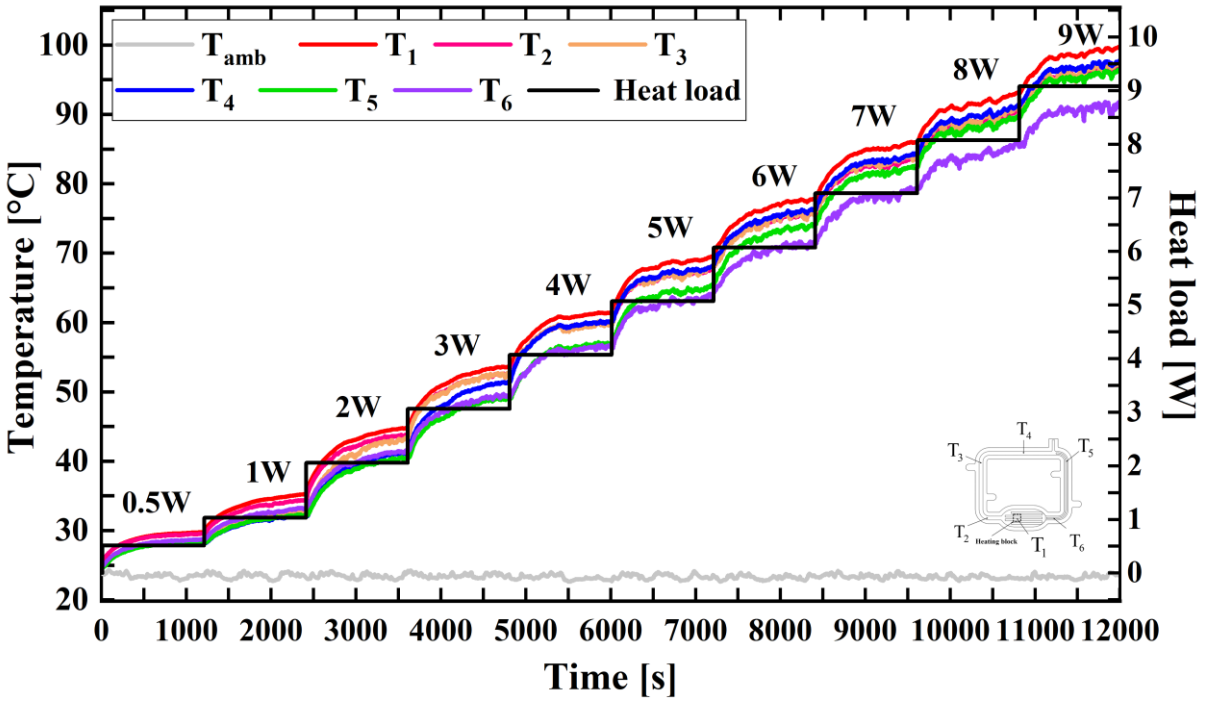

(b)

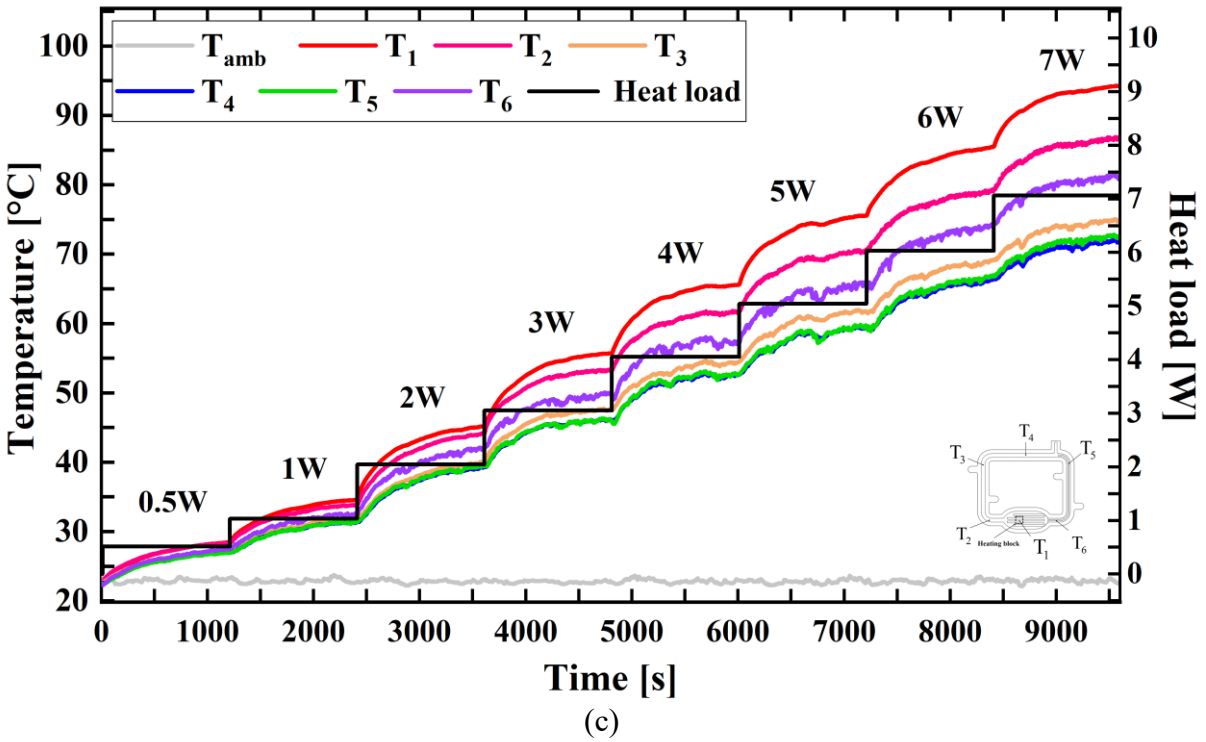

(c)

Souce: Own authorship.

Figure A7 - UTLHP - B (FR=40%) behavior during a power cycle in the (a) gravity-assisted orientation (b) against gravity orientation.

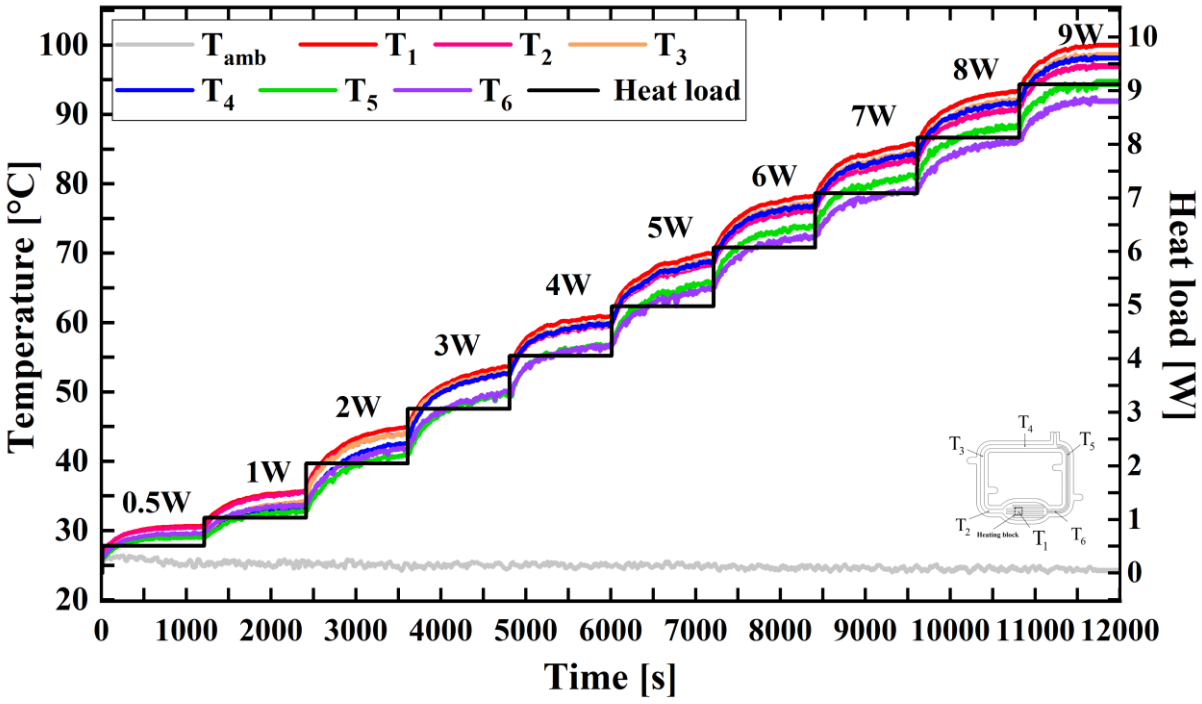

(a)

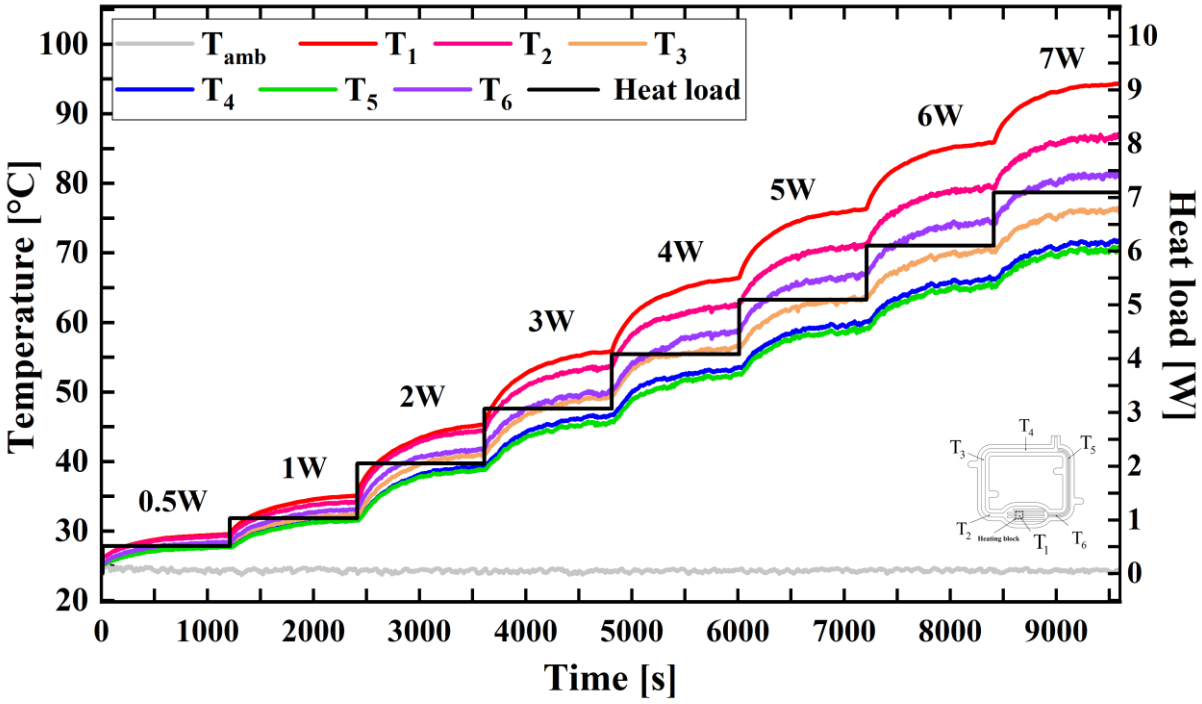

(b)

Souce: Own authorship.

Figure A8 - UTLHP - B (FR=45%) behavior during a power cycle in the (a) horizontal orientation (b) gravity-assisted orientation (c) against gravity orientation.

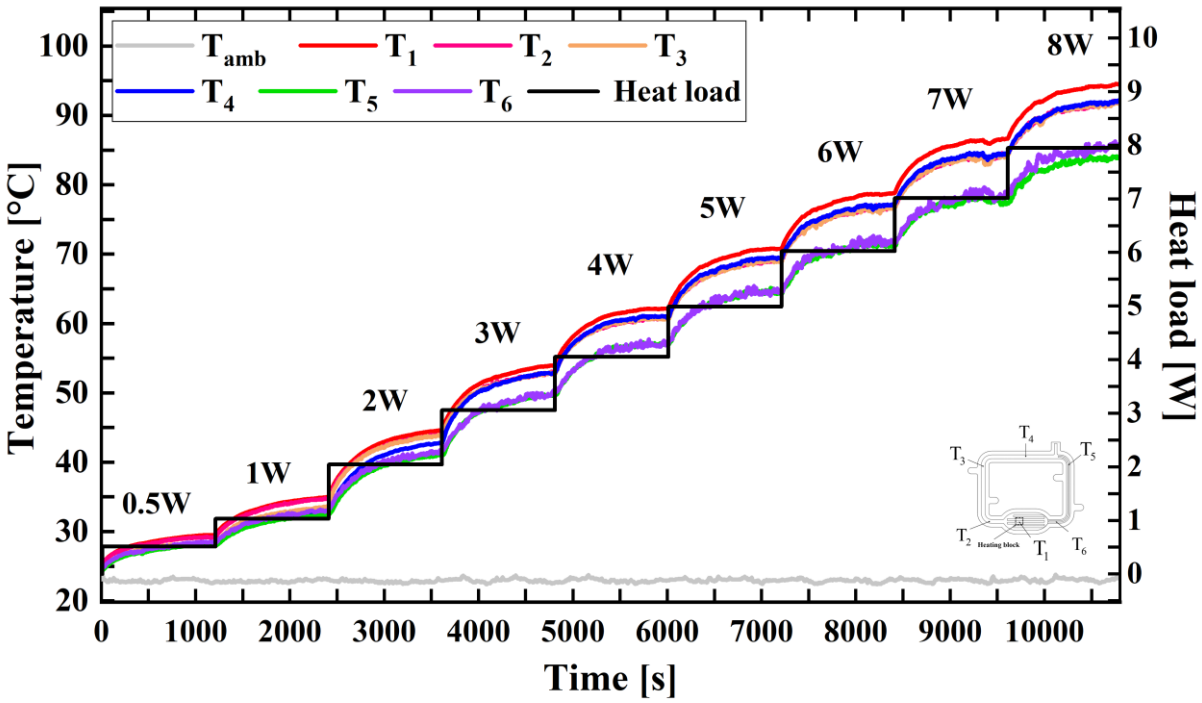

(a)

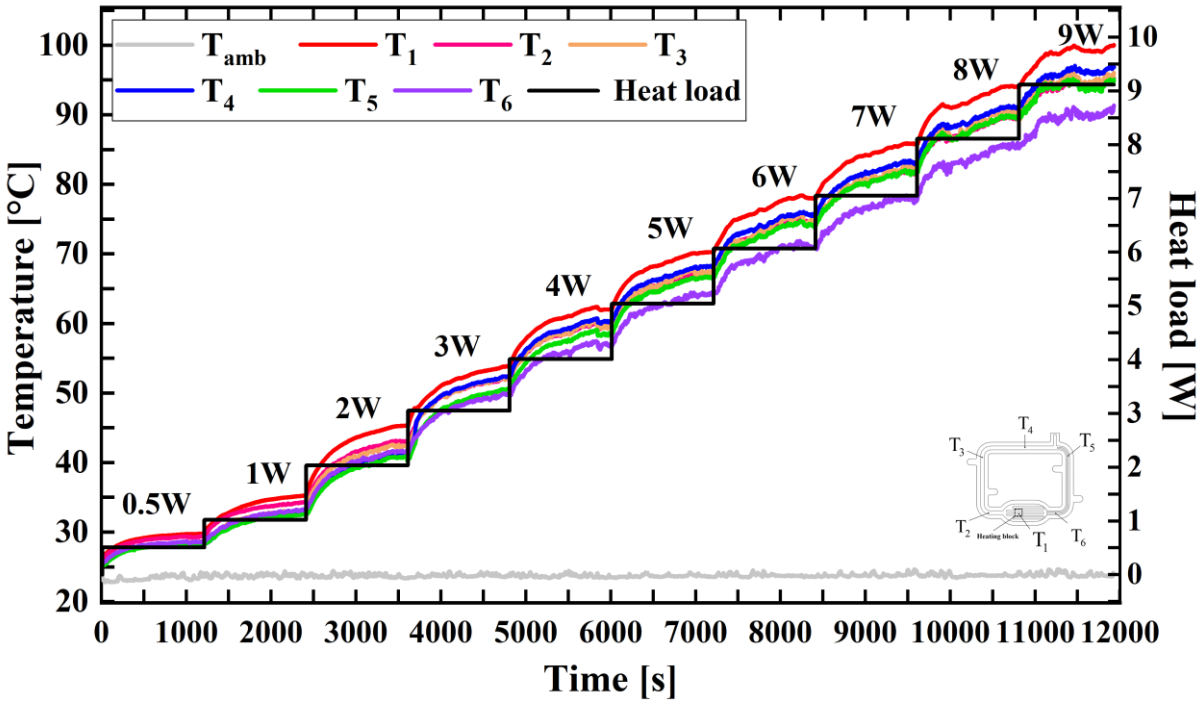

(b)

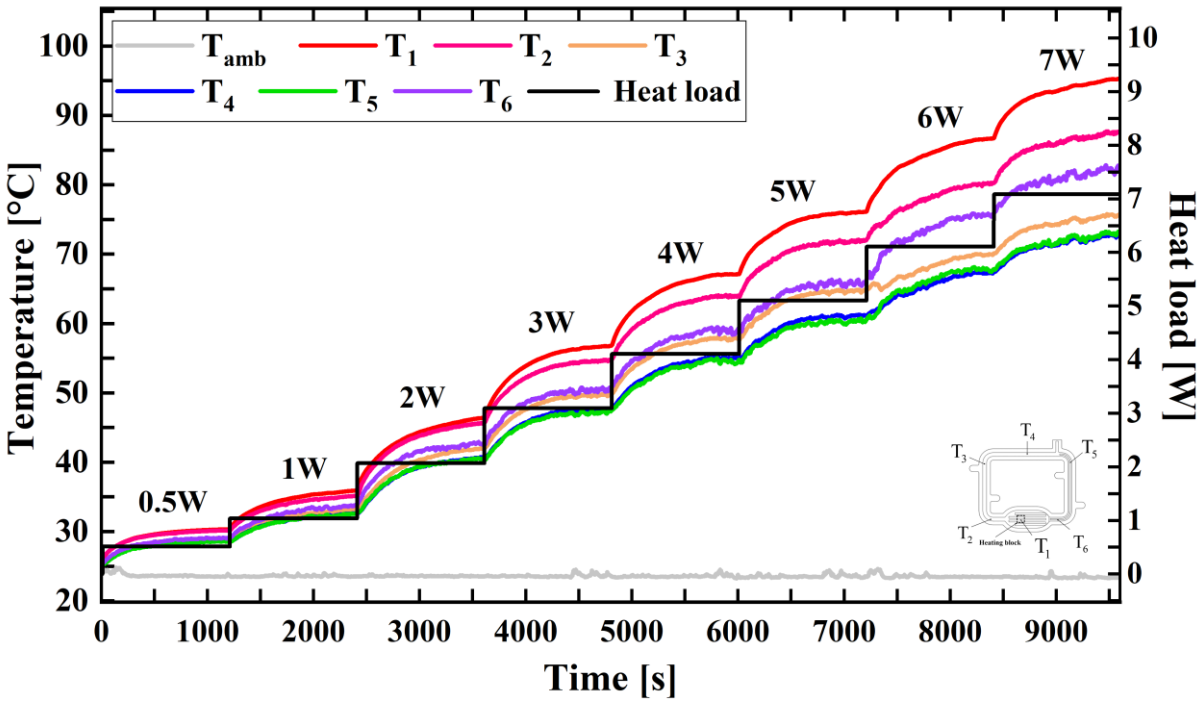

(c)

Souce: Own authorship.

Figure A9 - UTLHP - B (FR=54%) behavior during a power cycle in the (a) horizontal orientation (b) gravity-assisted orientation

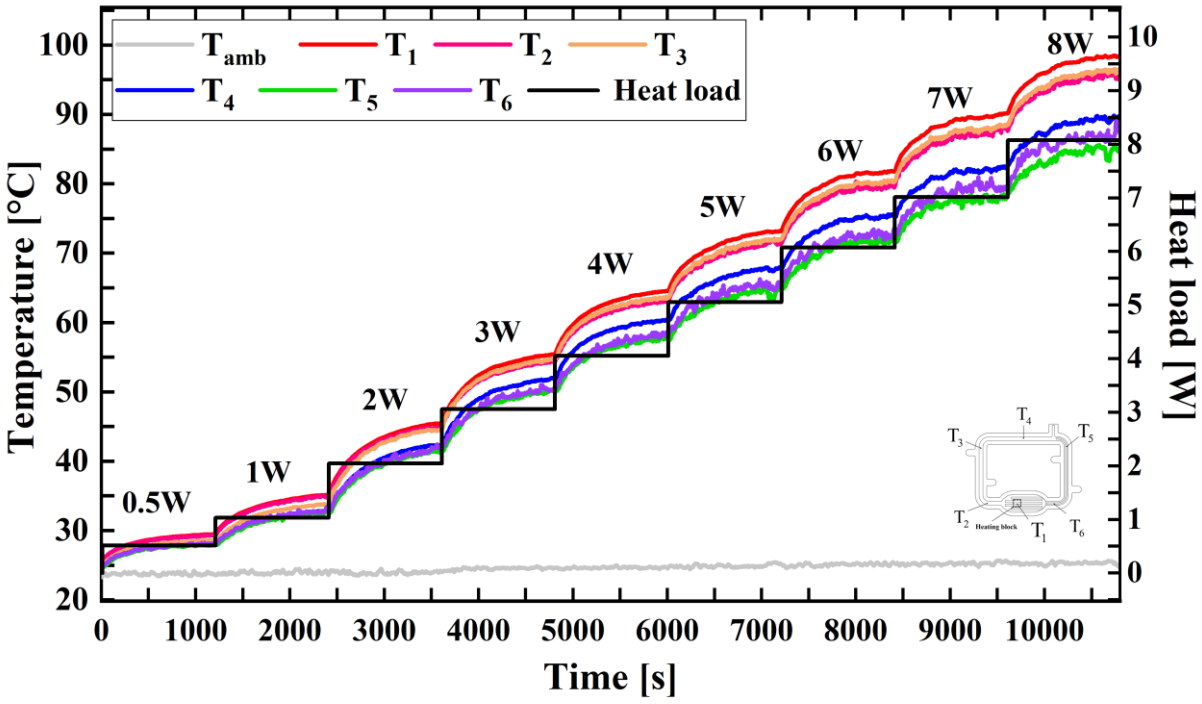

(a)

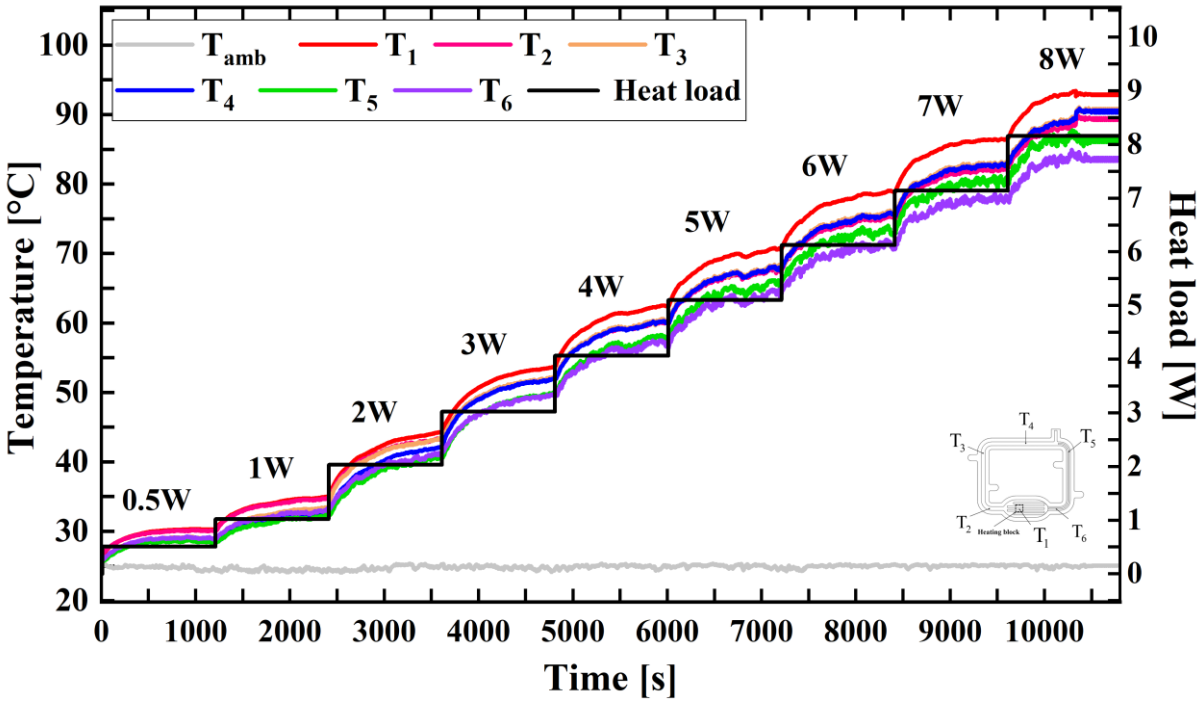

(b)

Souce: Own authorship.

- UTLHP - B (Working fluid: Water)

Figure A10 - UTLHP - B (FR=20%) behavior during a power cycle in the (a) horizontal orientation (b) gravity-assisted orientation.

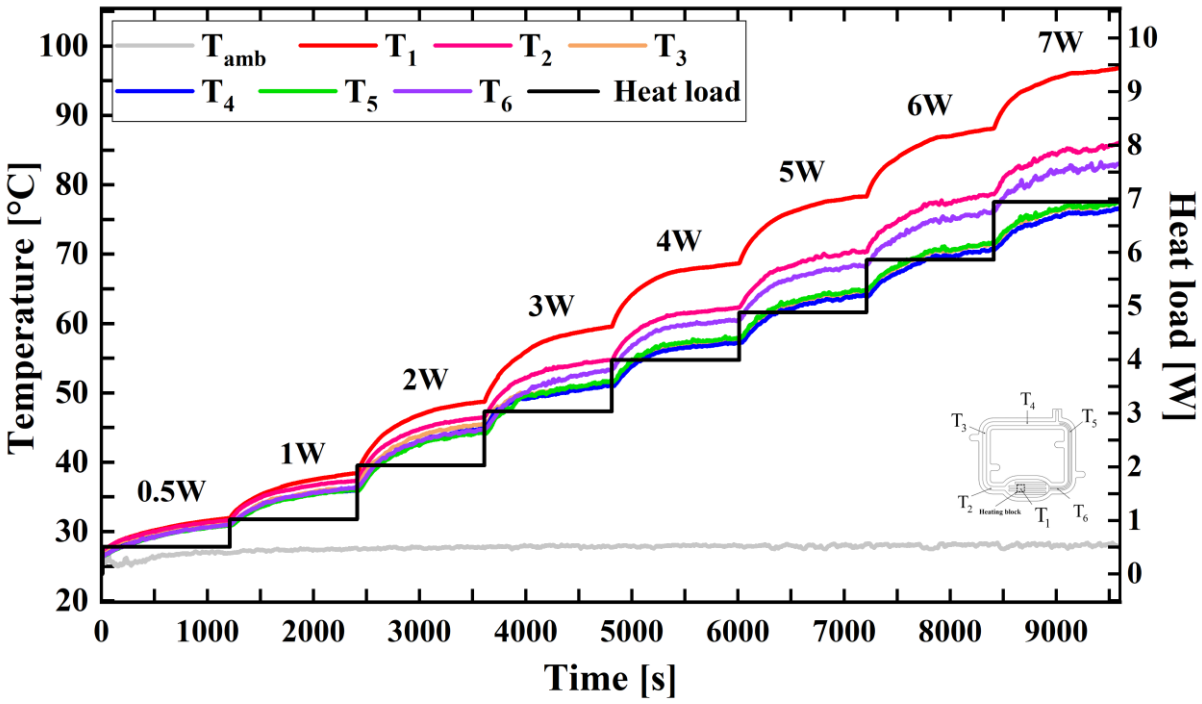

(a)

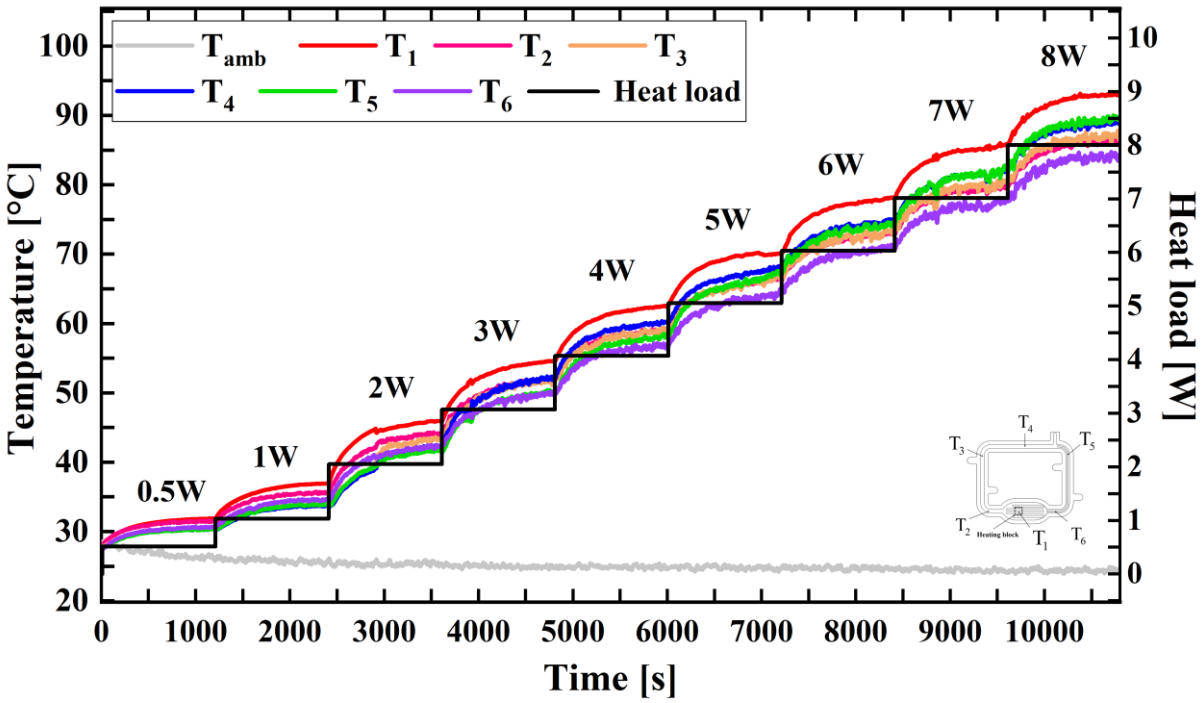

(b)

Souce: Own authorship.

Figure A11 - UTLHP - B (FR=23%) behavior during a power cycle in the (a) horizontal orientation (b) gravity-assisted orientation.

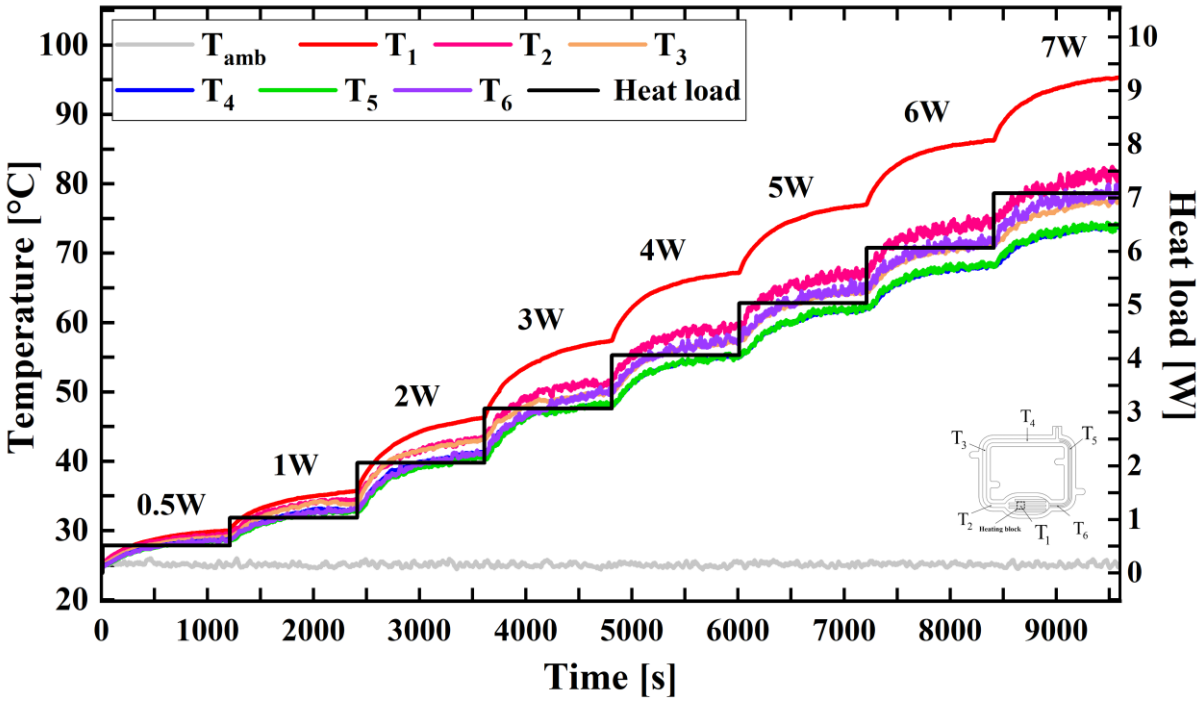

(a)

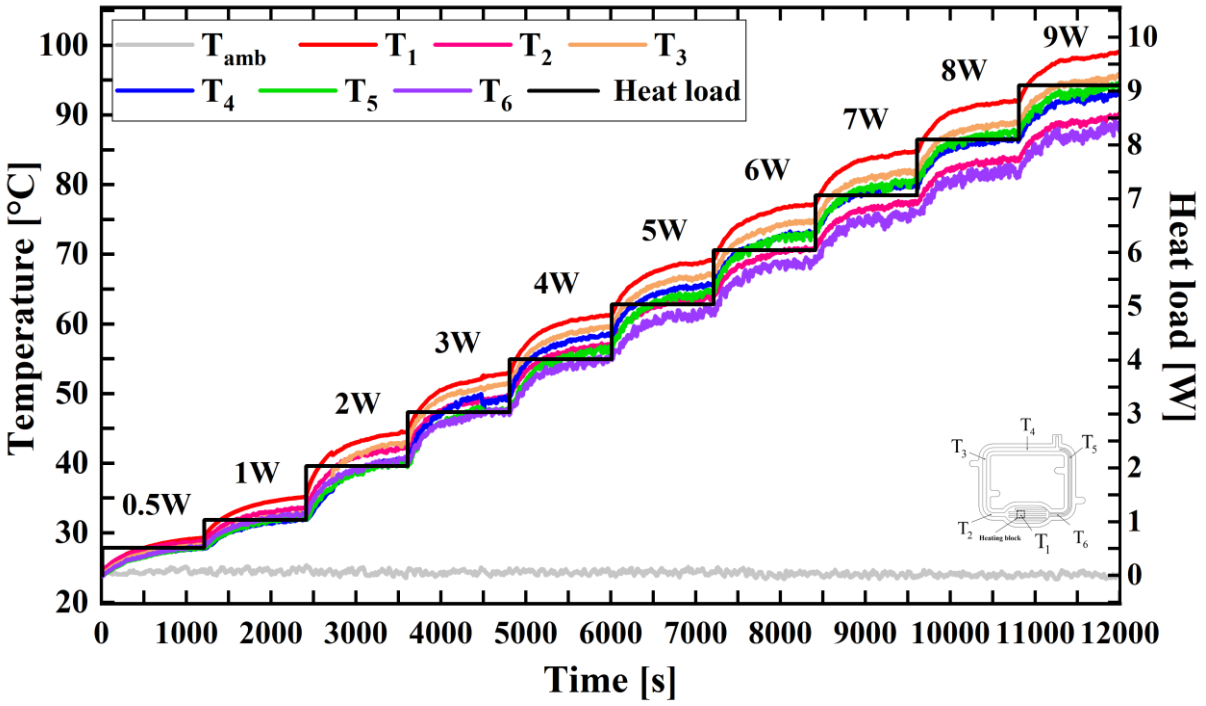

(b)

Souce: Own authorship.

Figure A12 - UTLHP - B (FR=25%) behavior during a power cycle in the (a) horizontal orientation (b) gravity-assisted orientation (c) against gravity orientation.

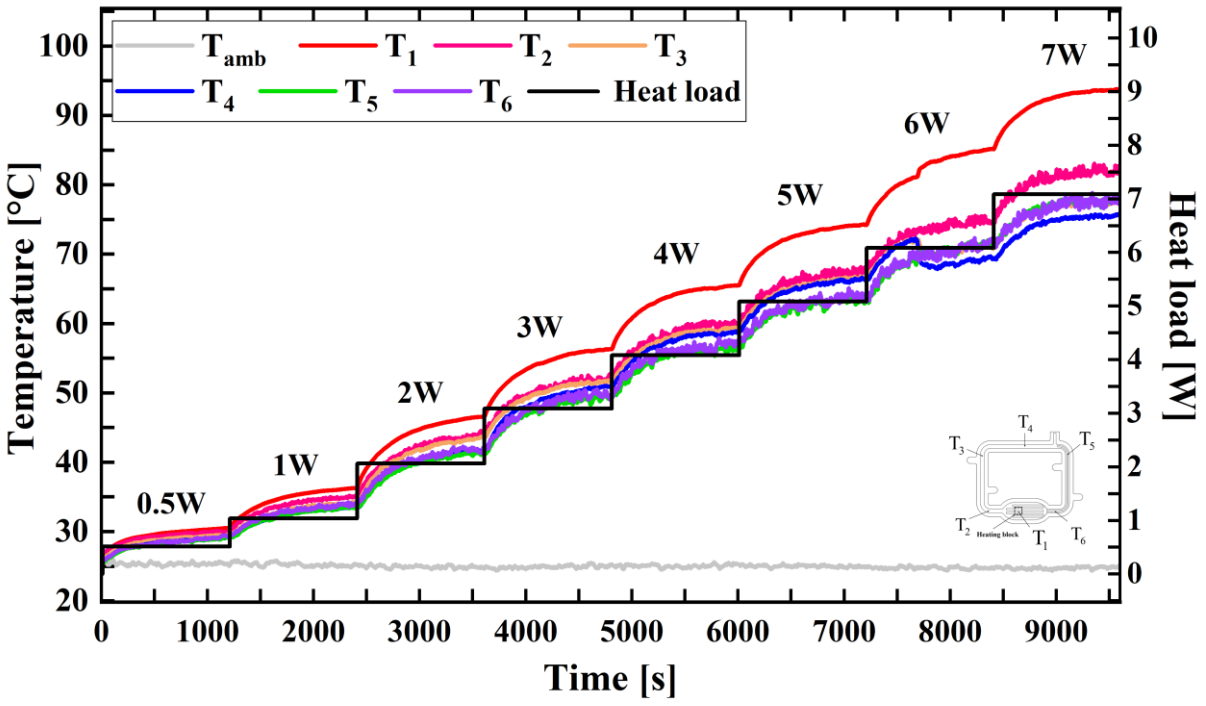

(a)

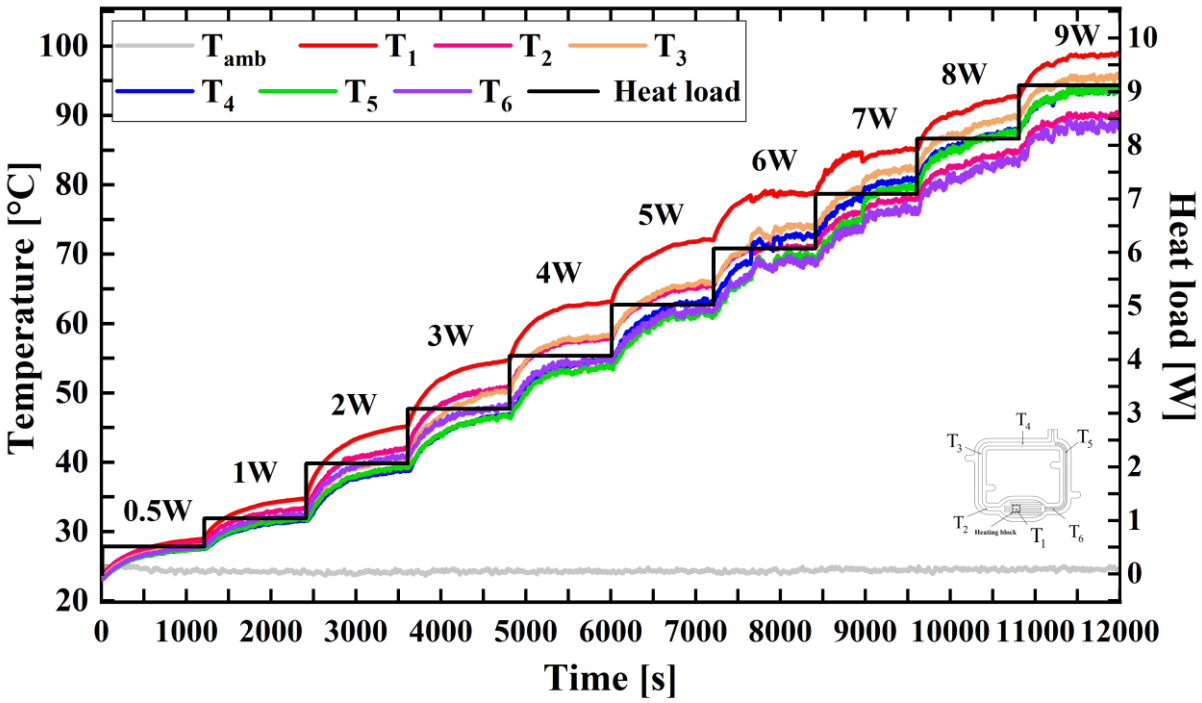

(b)

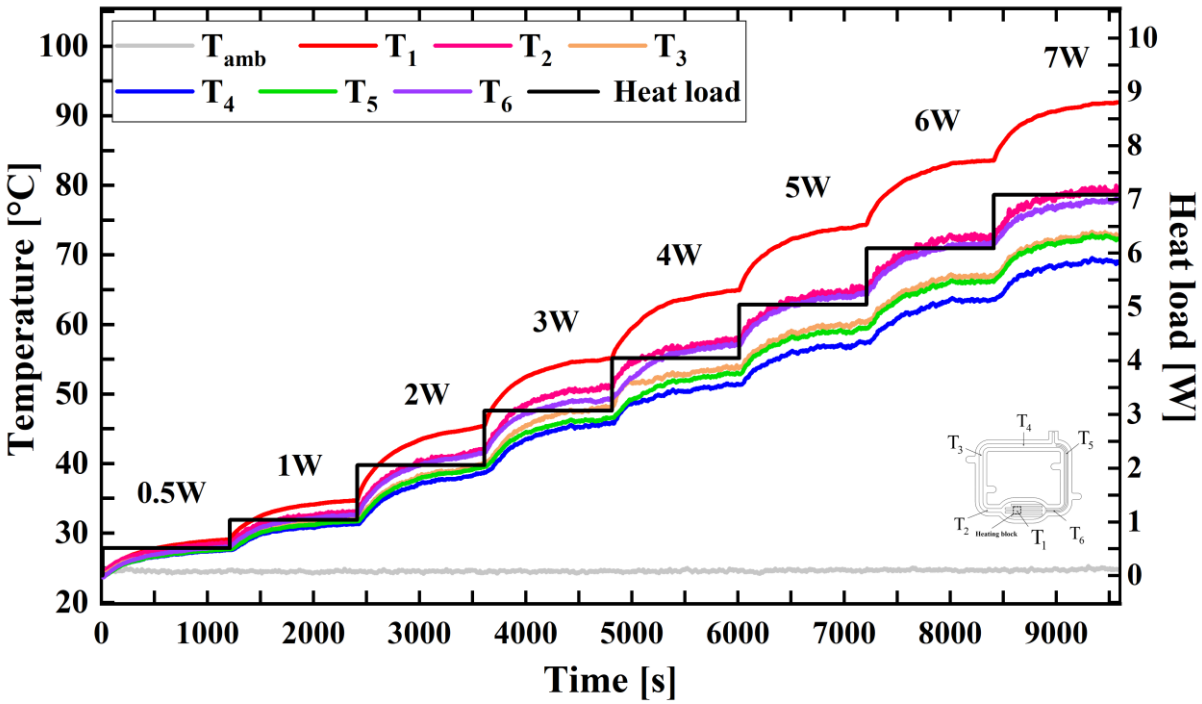

(c)

Souce: Own authorship.

Figure A13 - UTLHP - B (FR=28%) behavior during a power cycle in the (a) horizontal orientation (b) gravity-assisted orientation (c) against gravity orientation.

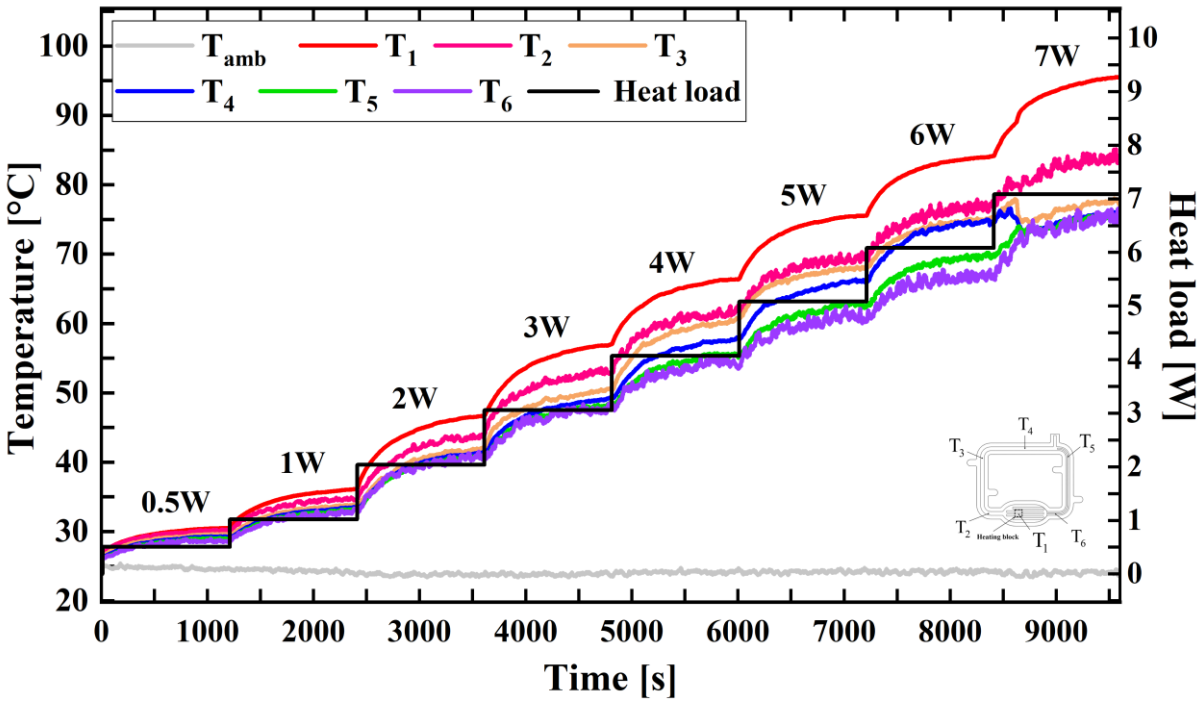

(a)

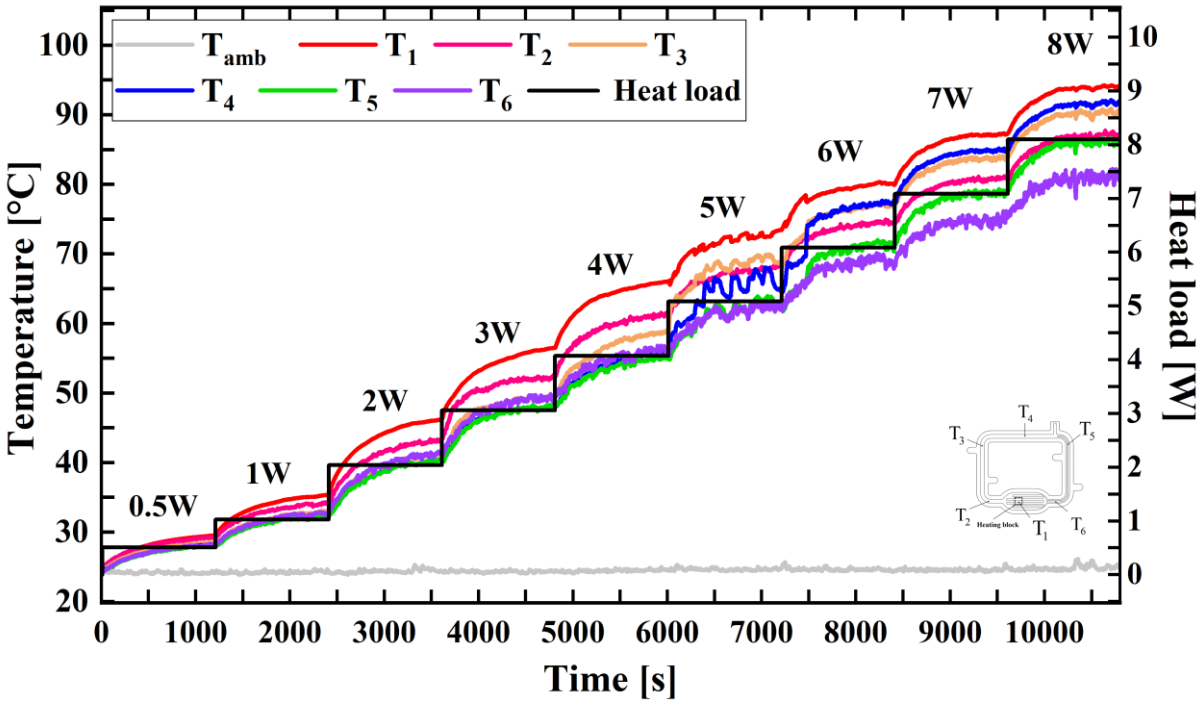

(b)

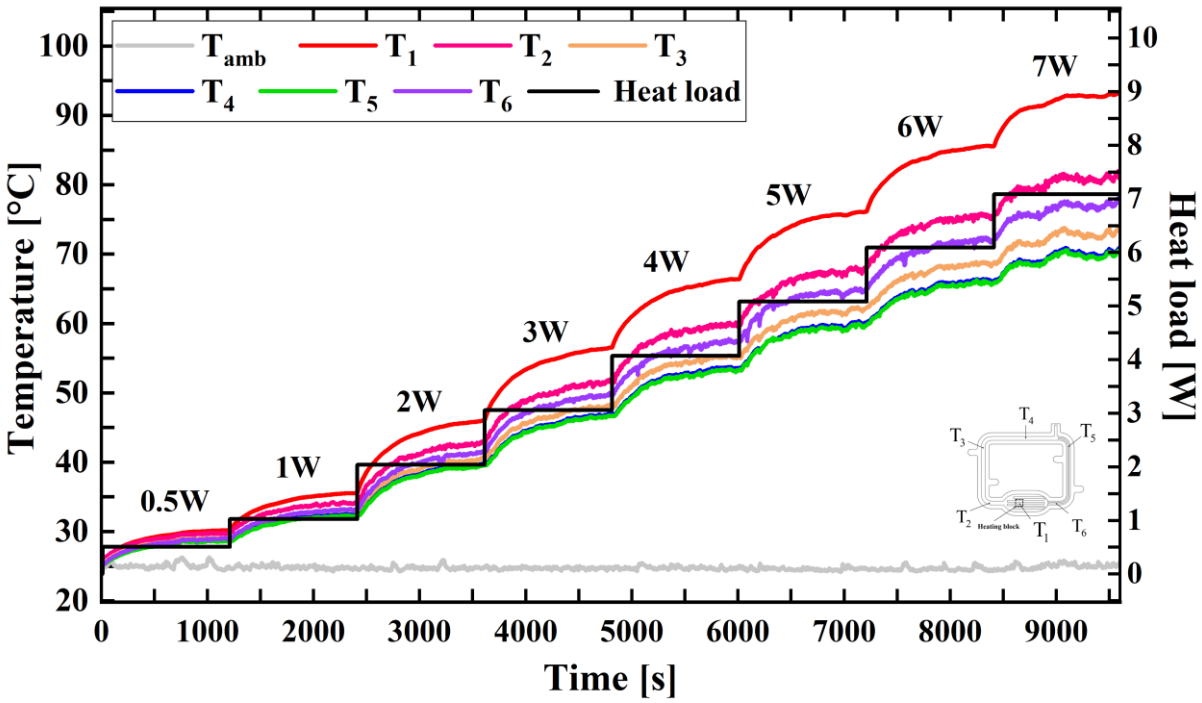

(c)

Souce: Own authorship.

Figure A14 - UTLHP - B (FR=34%) behavior during a power cycle in the (a) horizontal orientation (b) gravity-assisted orientation (c) against gravity orientation.

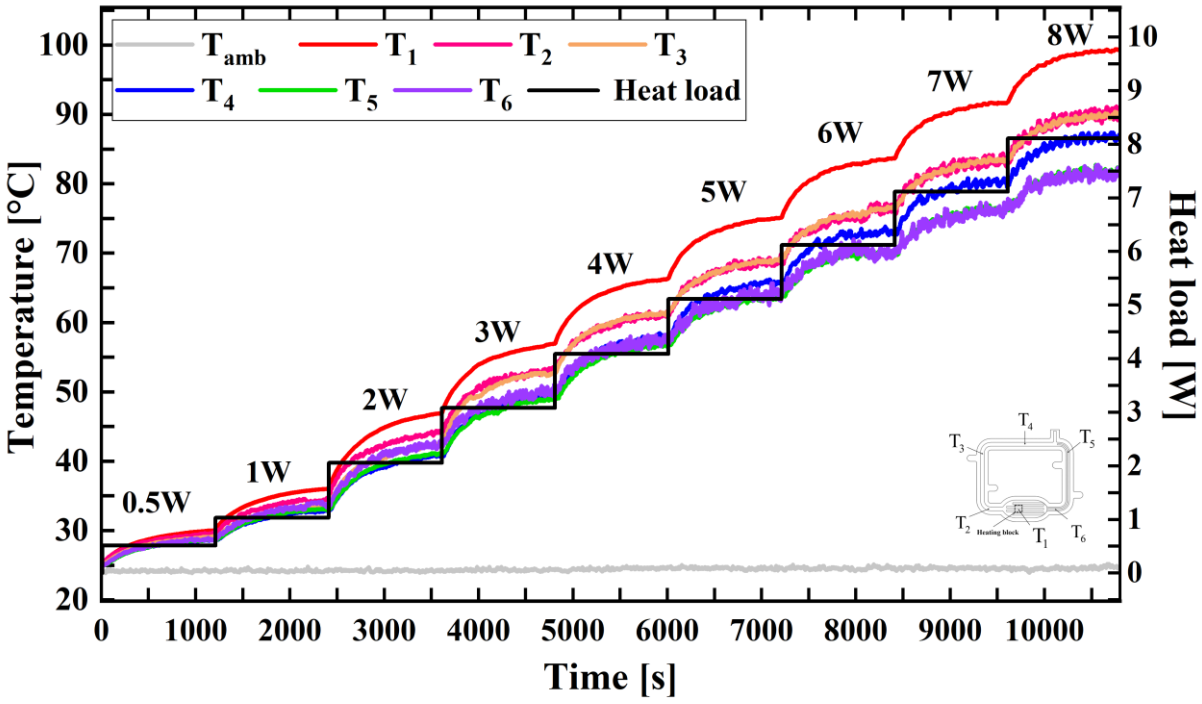

(a)

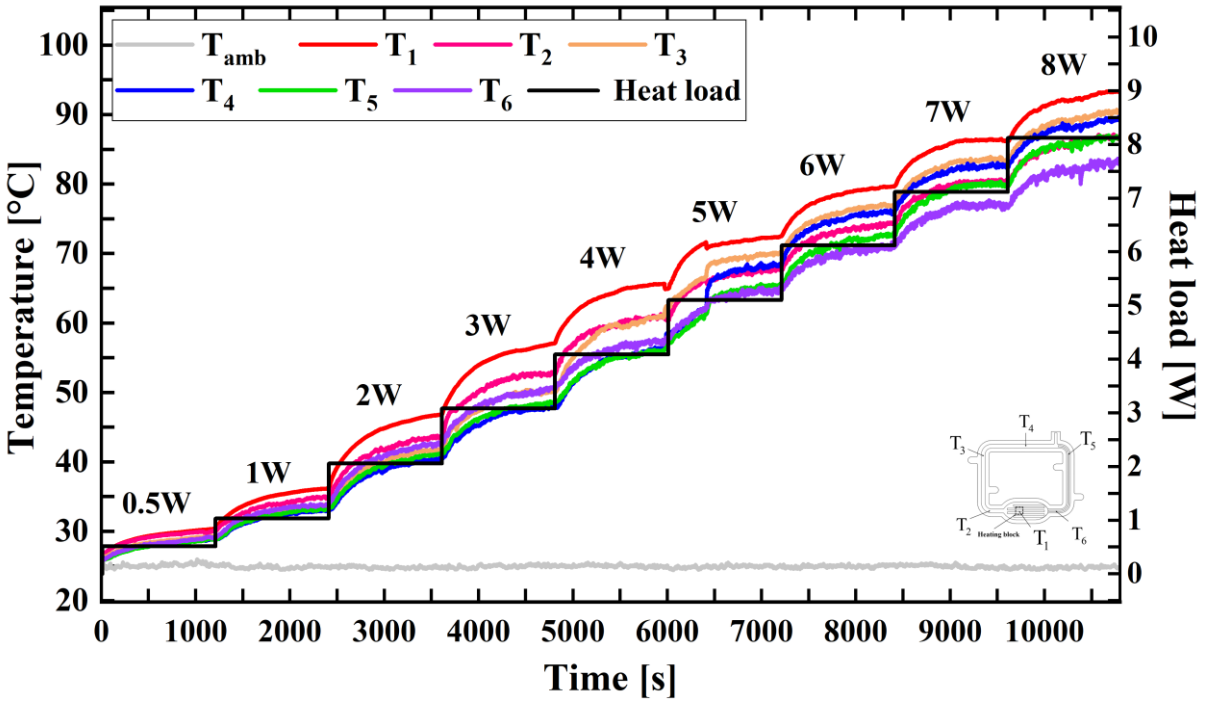

(b)

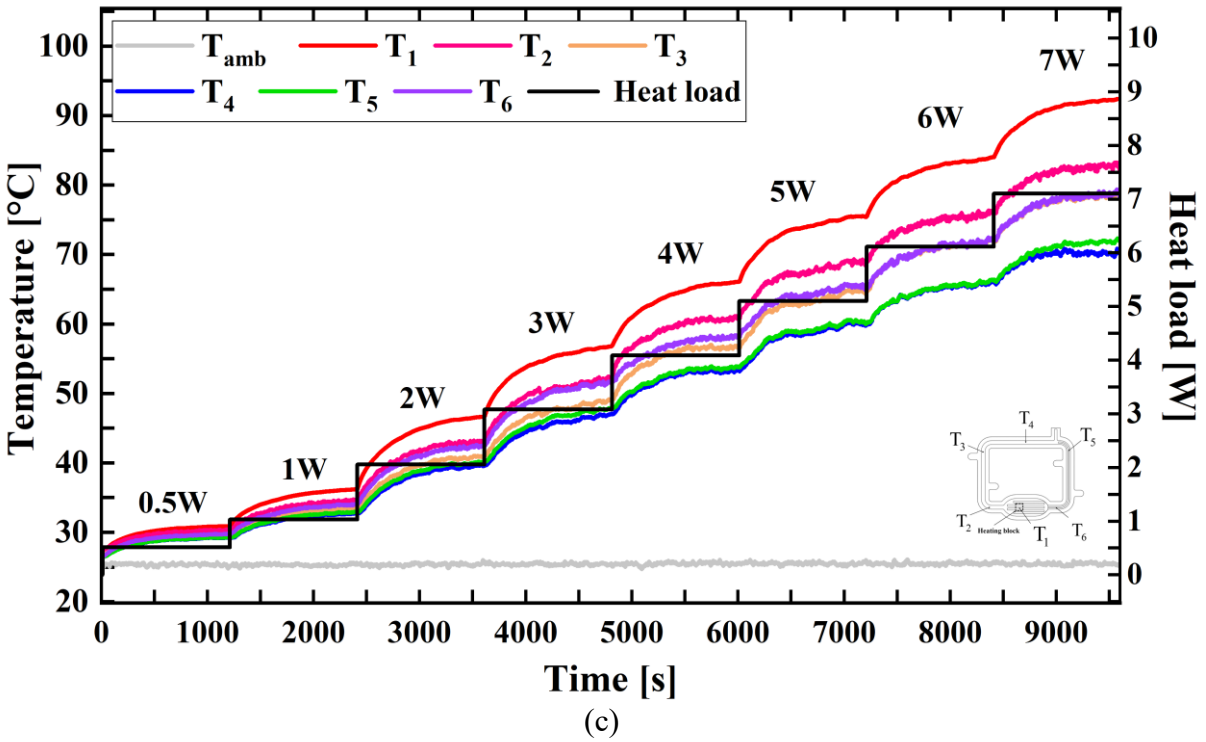

(c)

Souce: Own authorship.

Figure A15 - UTLHP - B (FR=37%) behavior during a power cycle in the (a) horizontal orientation (b) gravity-assisted orientation (c) against gravity orientation.

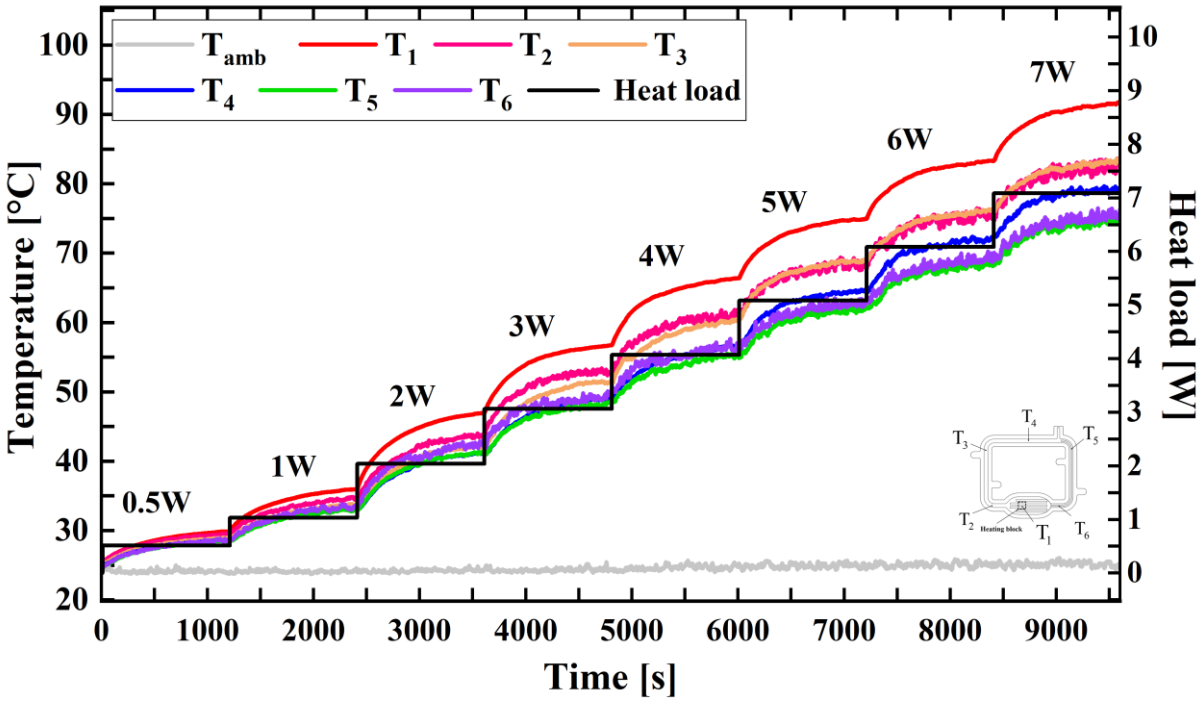

(a)

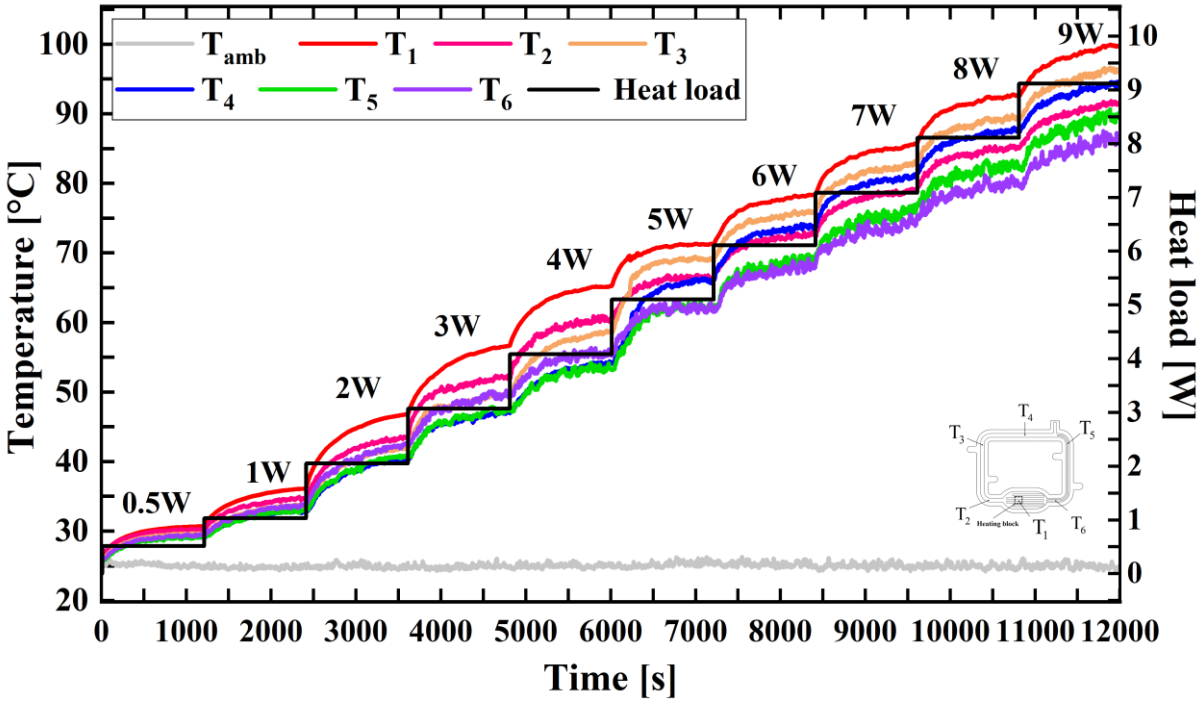

(b)

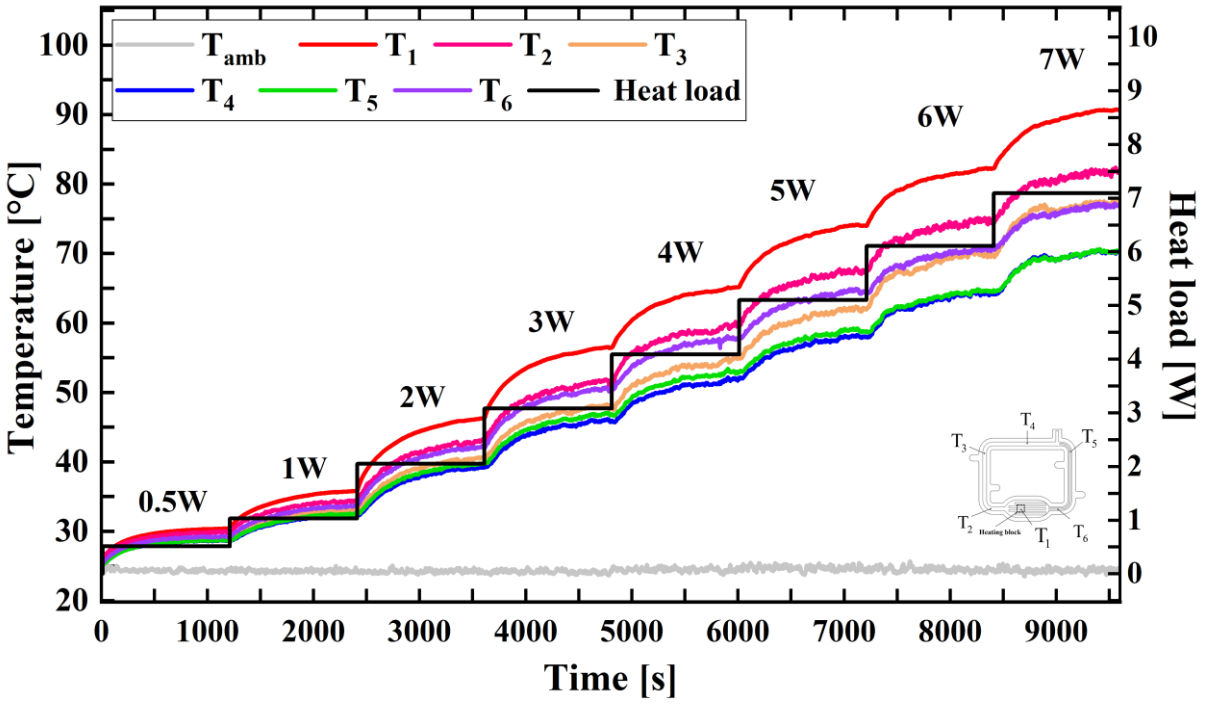

(c)

Souce: Own authorship.

Figure A16 - UTLHP - B (FR=40%) behavior during a power cycle in the (a) horizontal orientation (b) gravity-assisted orientation.

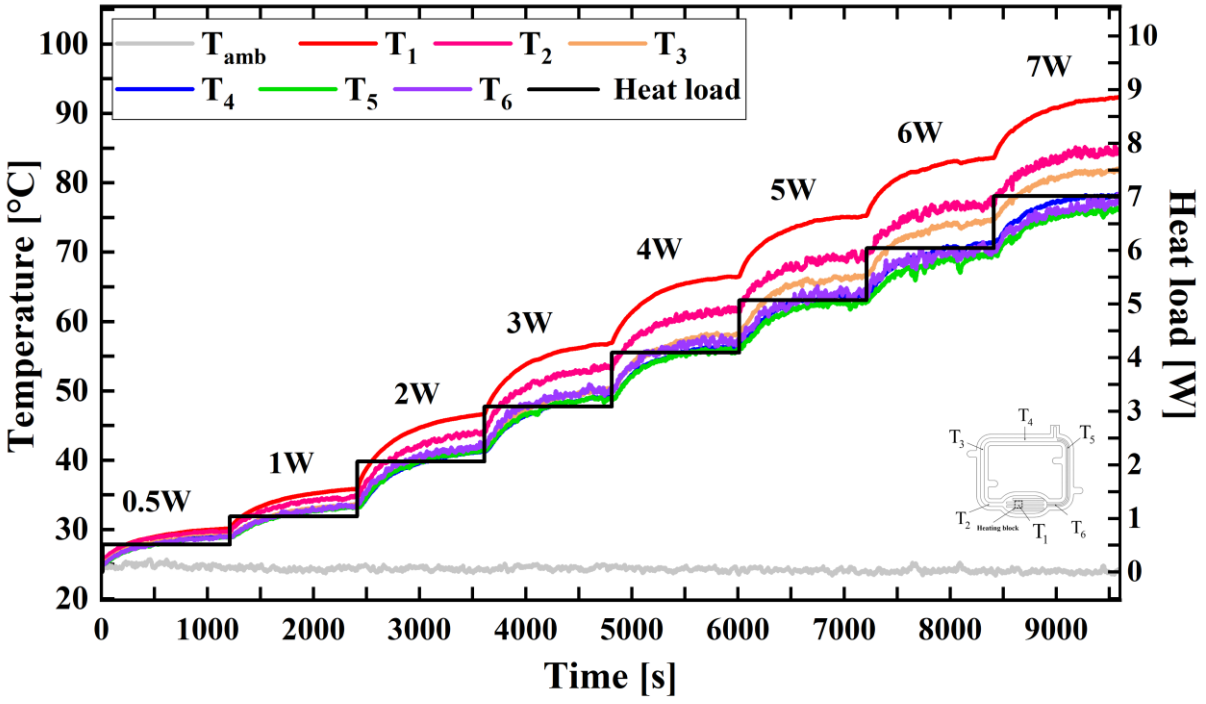

(a)

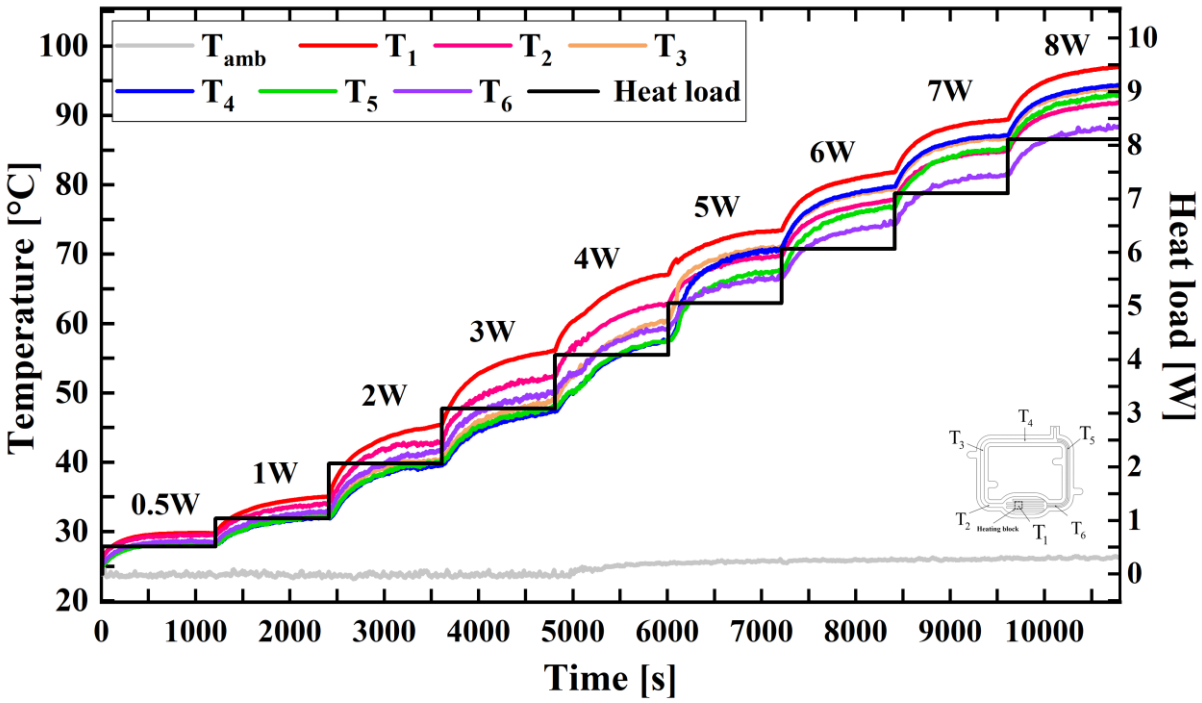

(b)

Souce: Own authorship.

- UTLHP - C (Working fluid: Ethanol)

Figure A17 - UTLHP - C (FR=35%) behavior during a power cycle in the (a) horizontal orientation (b) gravity-assisted orientation (c) against gravity orientation.

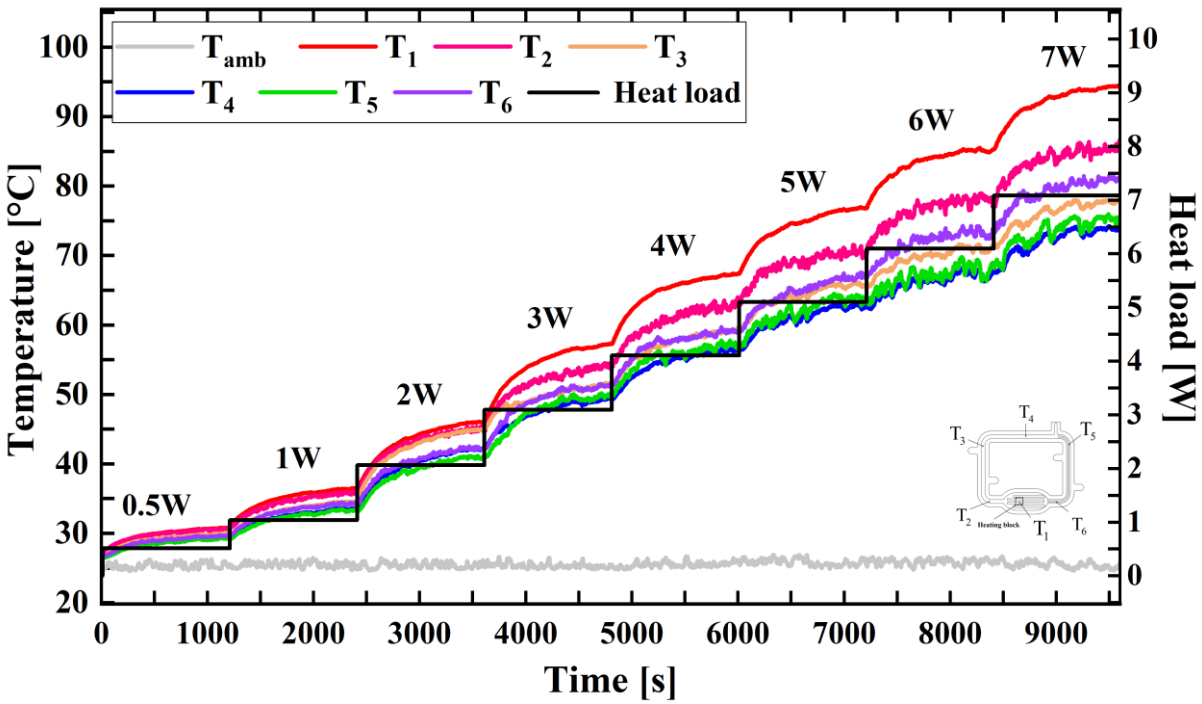

(a)

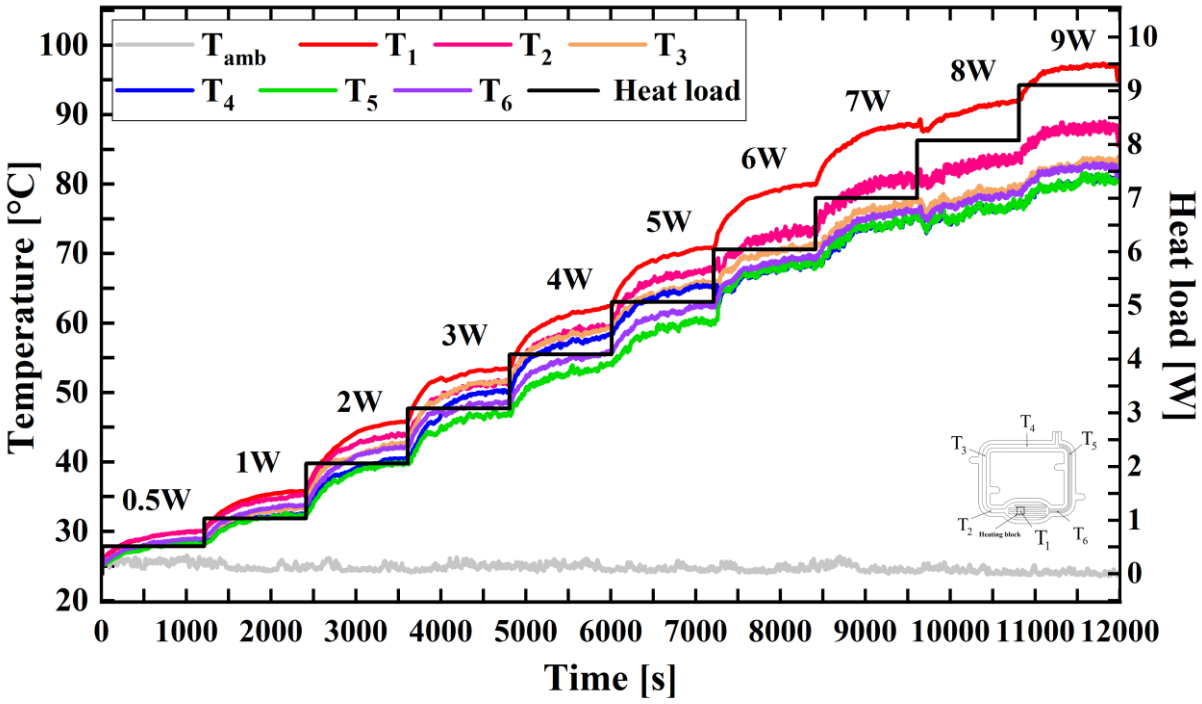

(b)

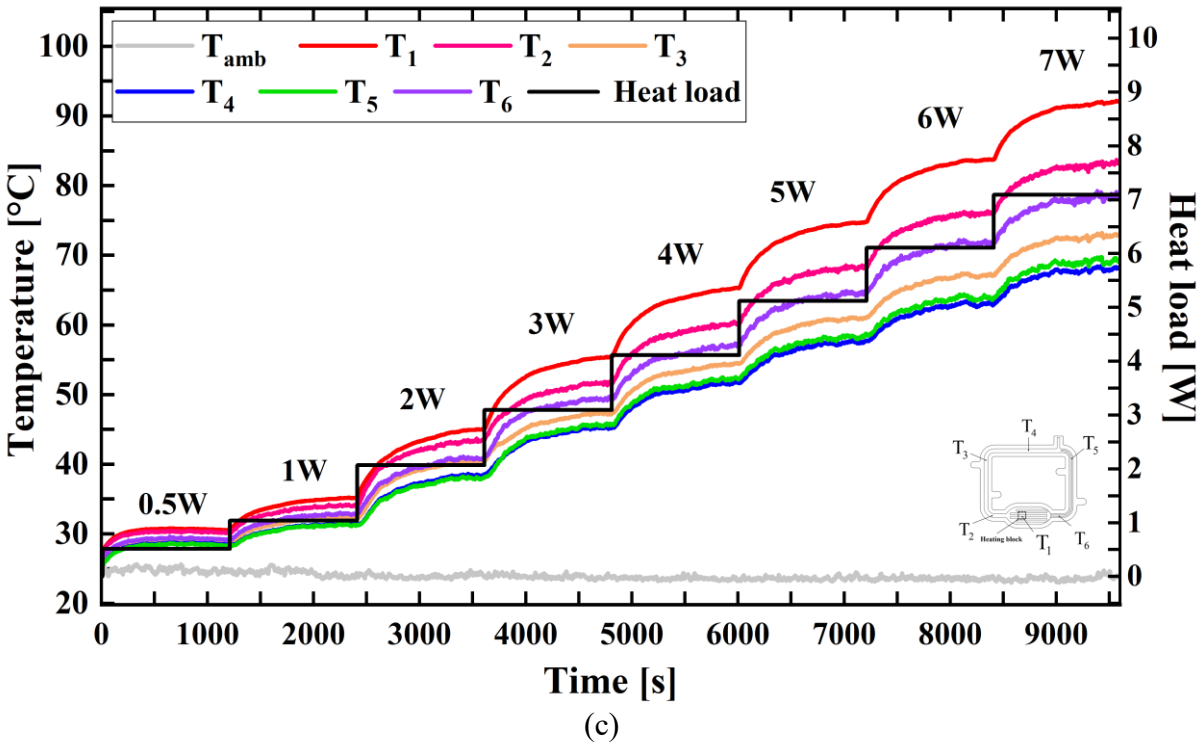

(c)

Souce: Own authorship.

Figure A18 - UTLHP - C (FR=40%) behavior during a power cycle in the (a) gravity-assisted orientation (b) against gravity orientation.

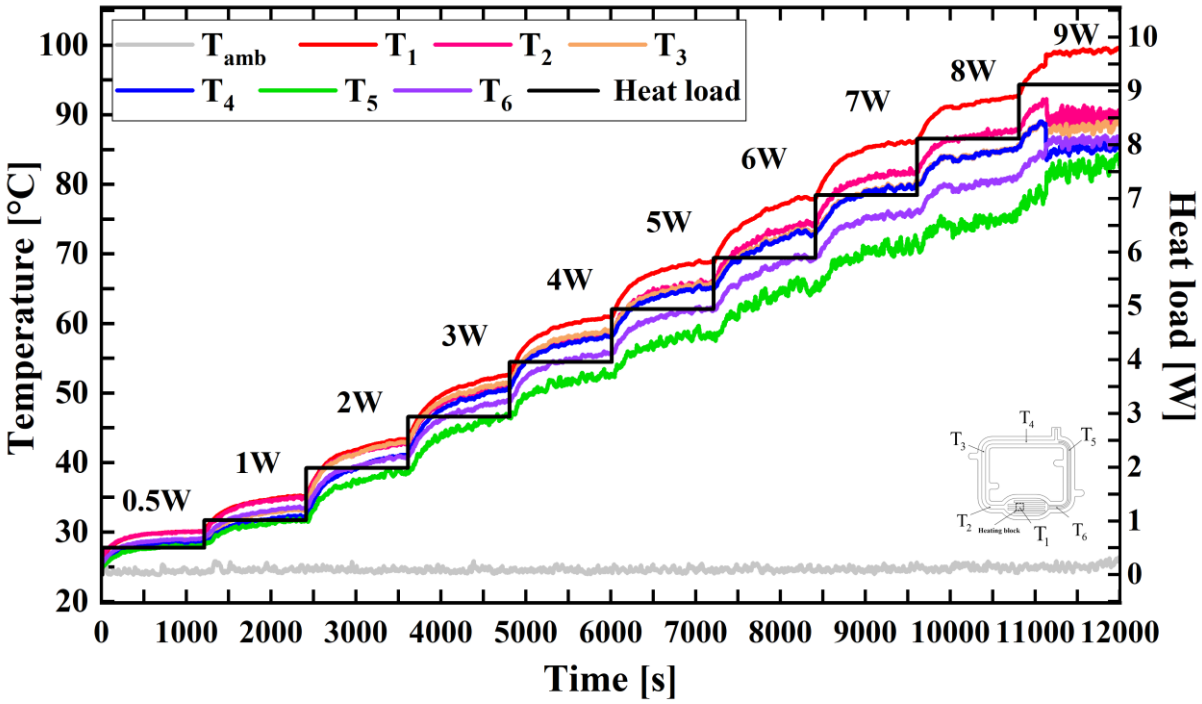

(a)

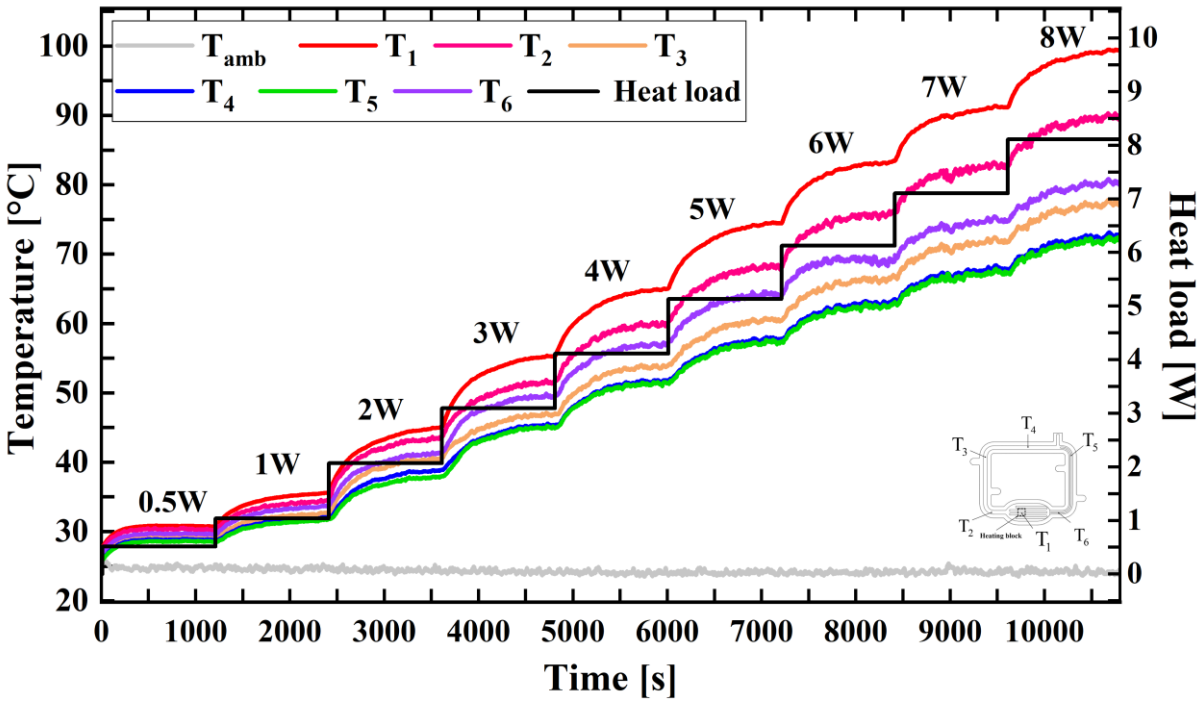

(b)

Souce: Own authorship.

Figure A19 - UTLHP - C (FR=42%) behavior during a power cycle in the (a) horizontal orientation (b) gravity-assisted orientation (c) against gravity orientation.

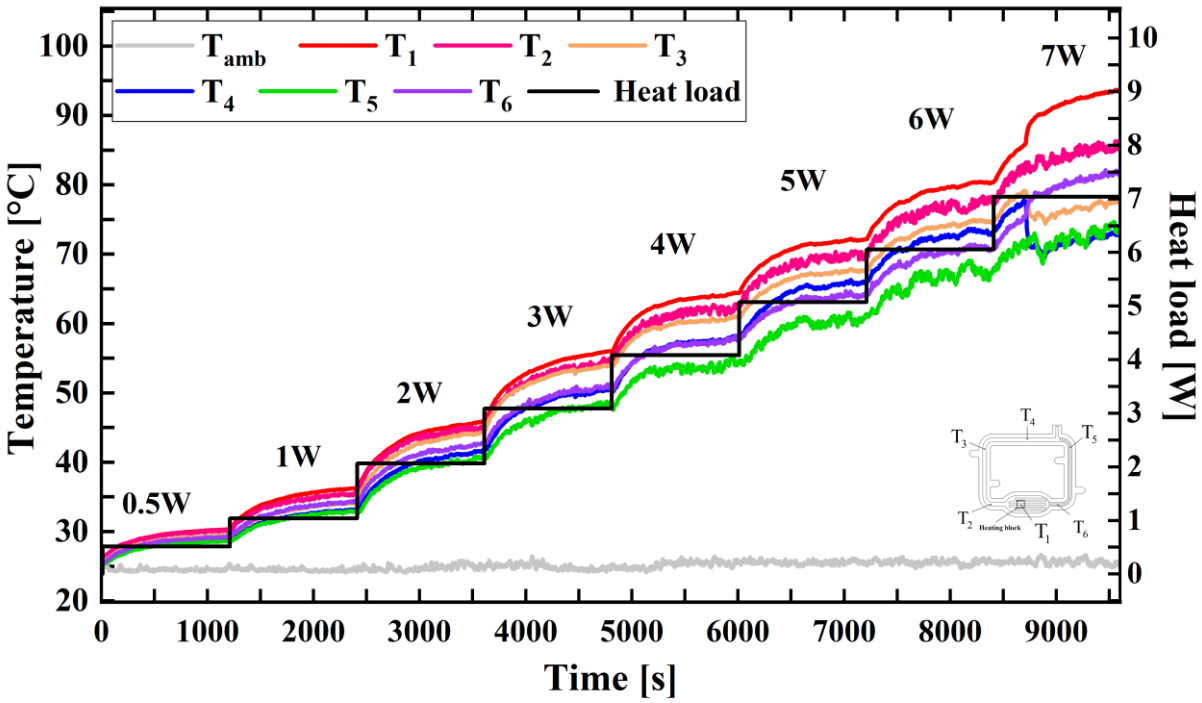

(a)

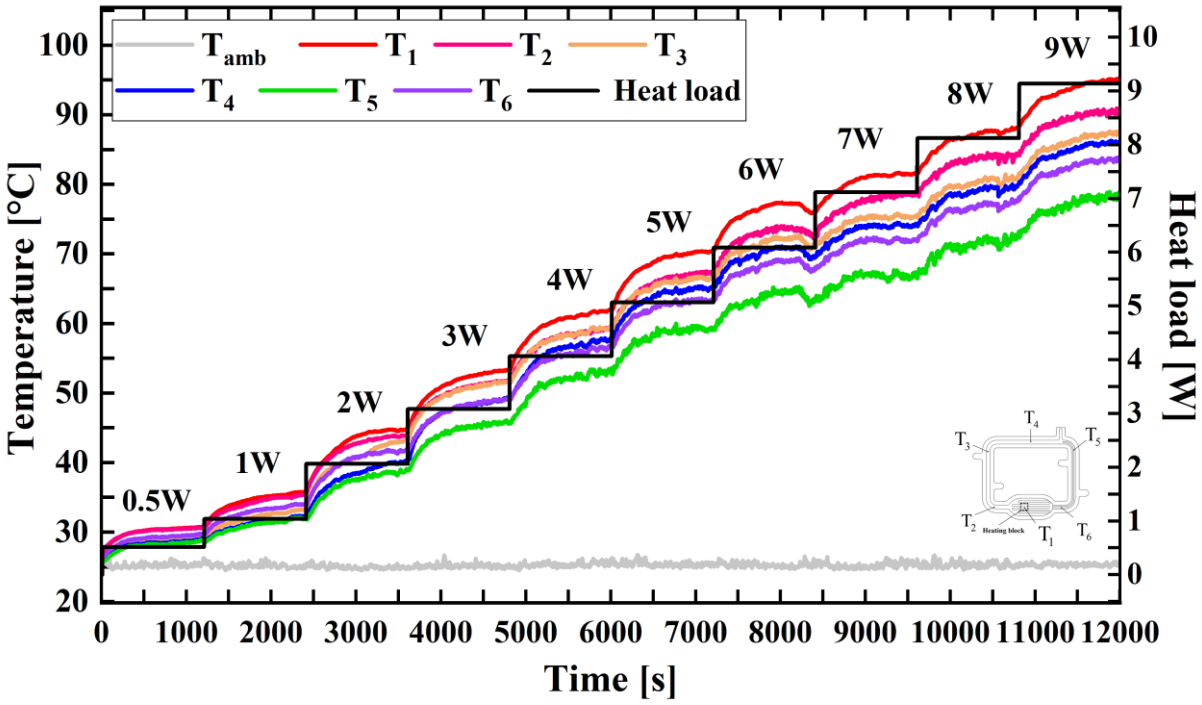

(b)

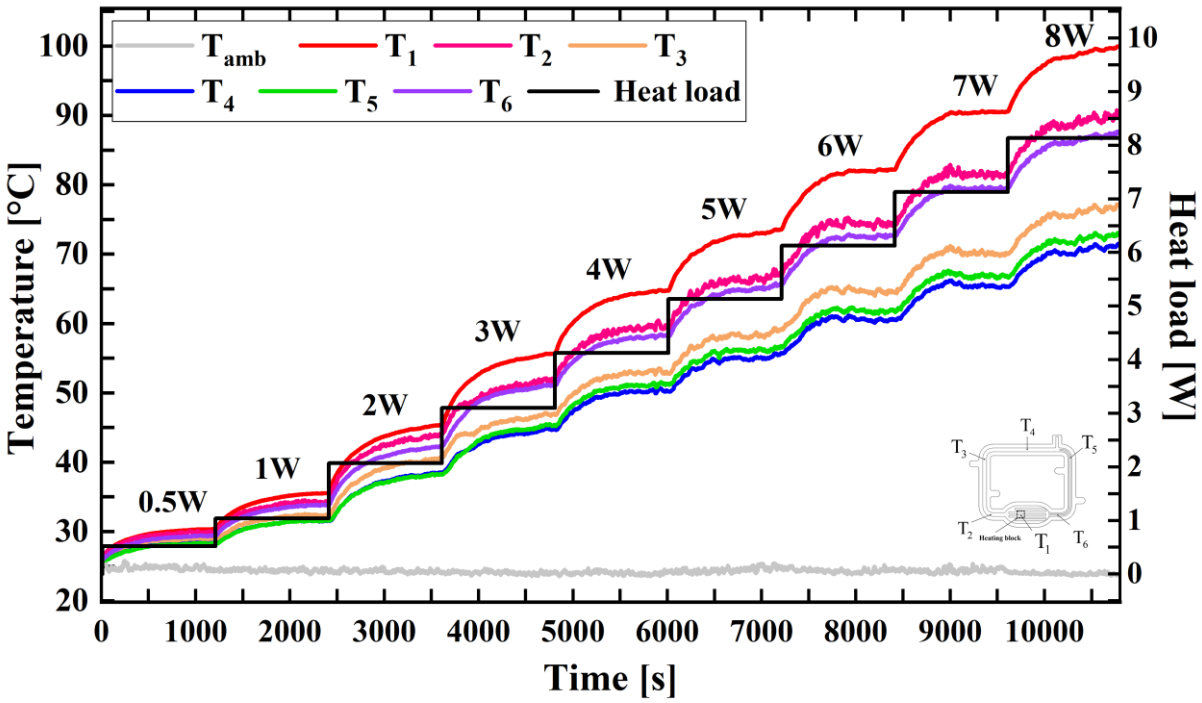

(c)

Souce: Own authorship.

Figure A20 - UTLHP - C (FR=46%) behavior during a power cycle in the (a) horizontal orientation (b) gravity-assisted orientation (c) against gravity orientation.

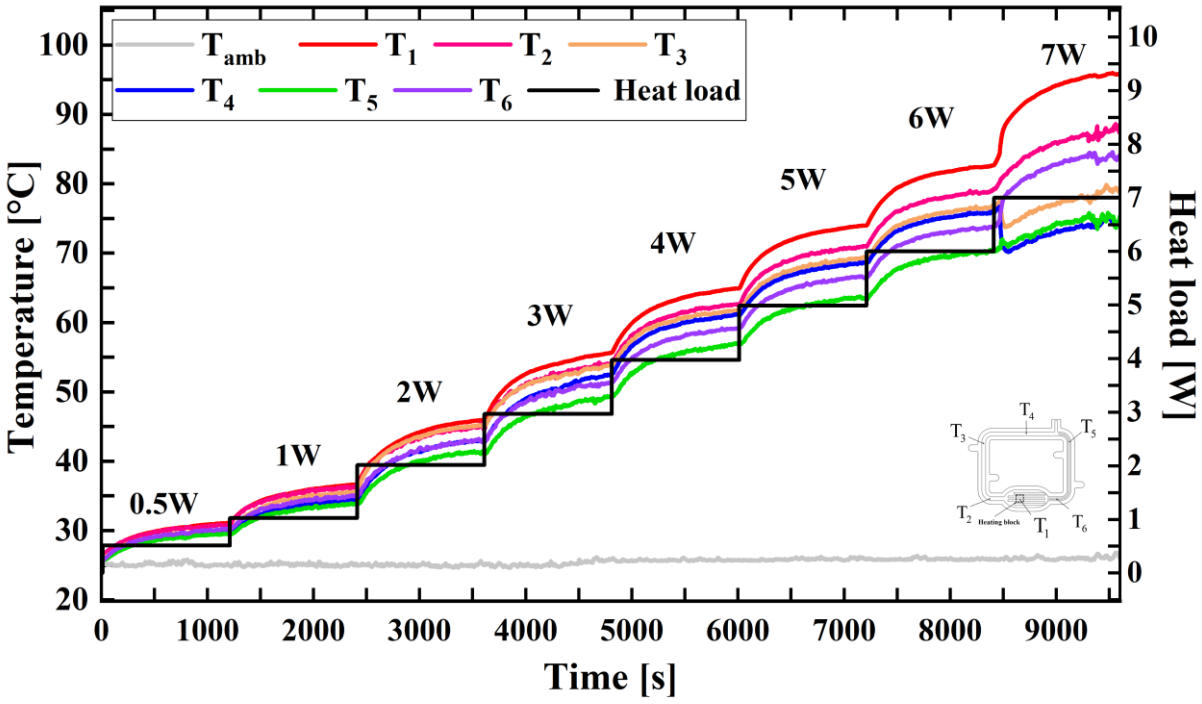

(a)

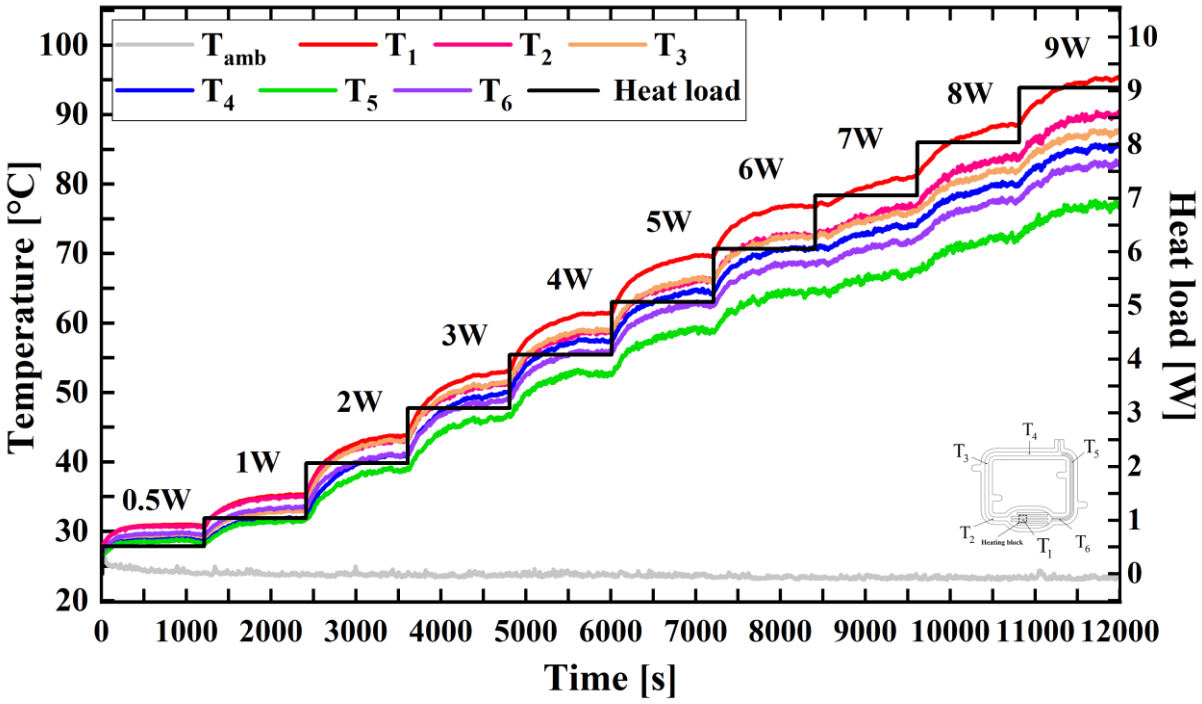

(b)

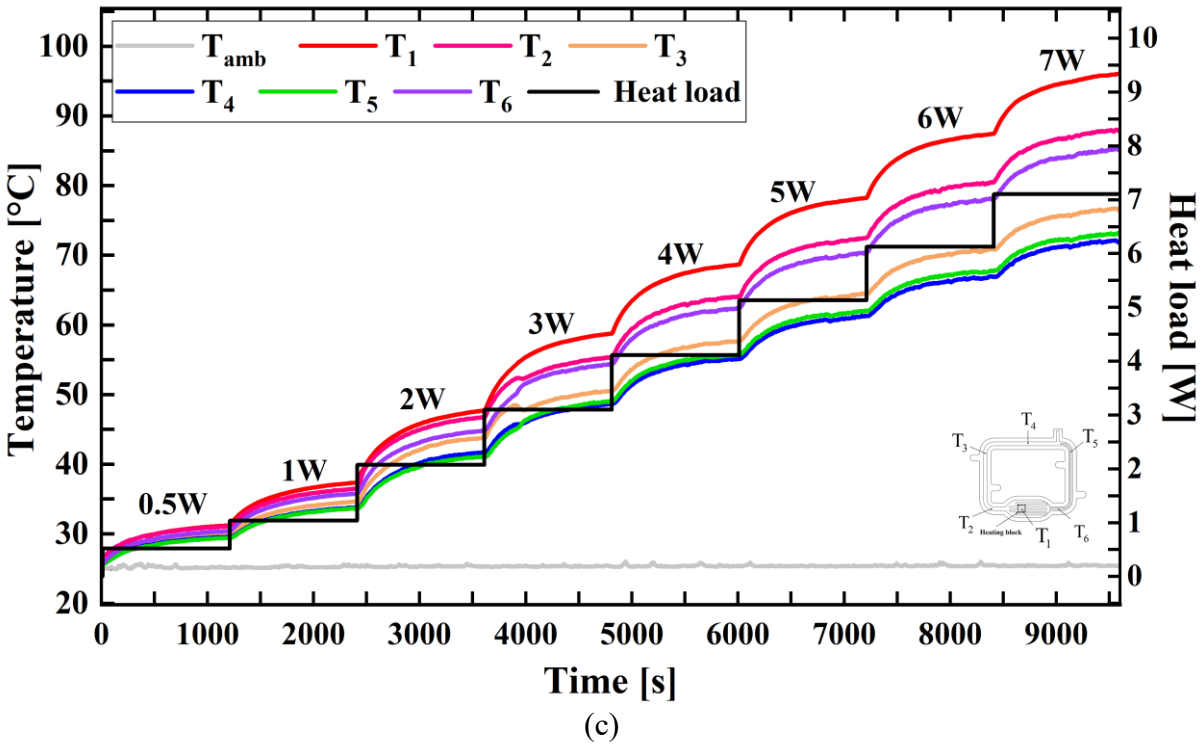

(c)

Souce: Own authorship.

Figure A21 - UTLHP - C (FR=52%) behavior during a power cycle in the horizontal orientation.

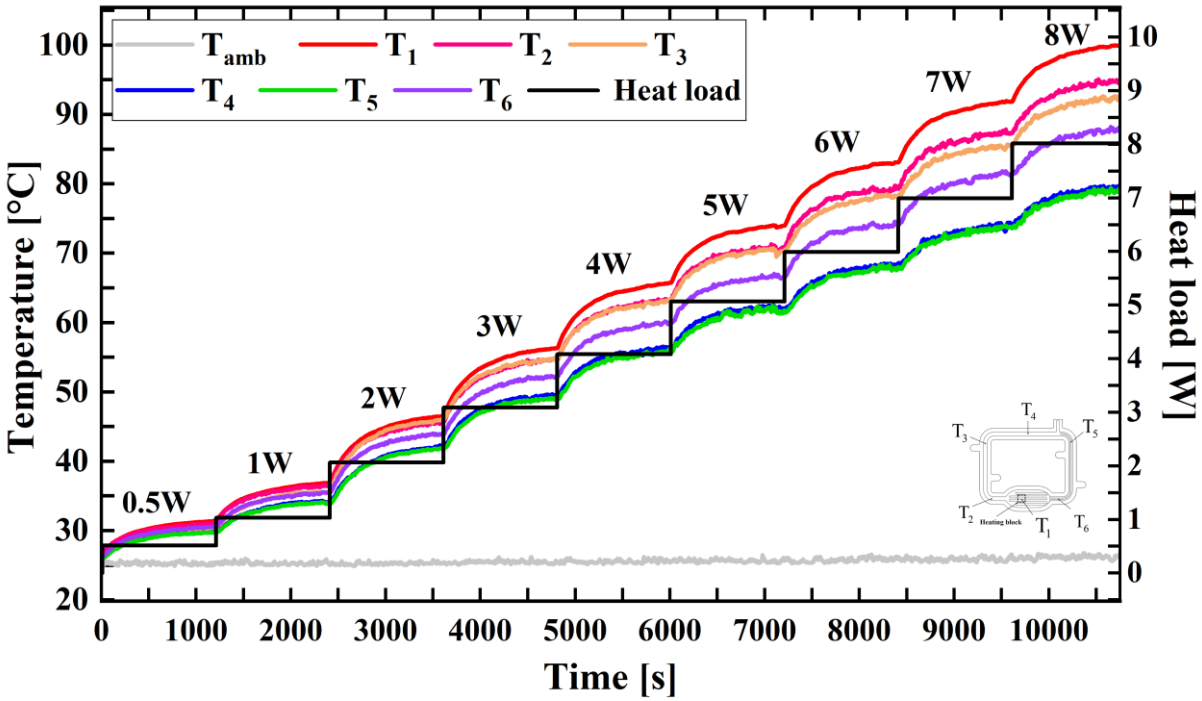

Souce: Own authorship.

- UTLHP - C (Working fluid: Water)

Figure A22 - UTLHP - C (FR=65%) behavior during a power cycle in the horizontal orientation.

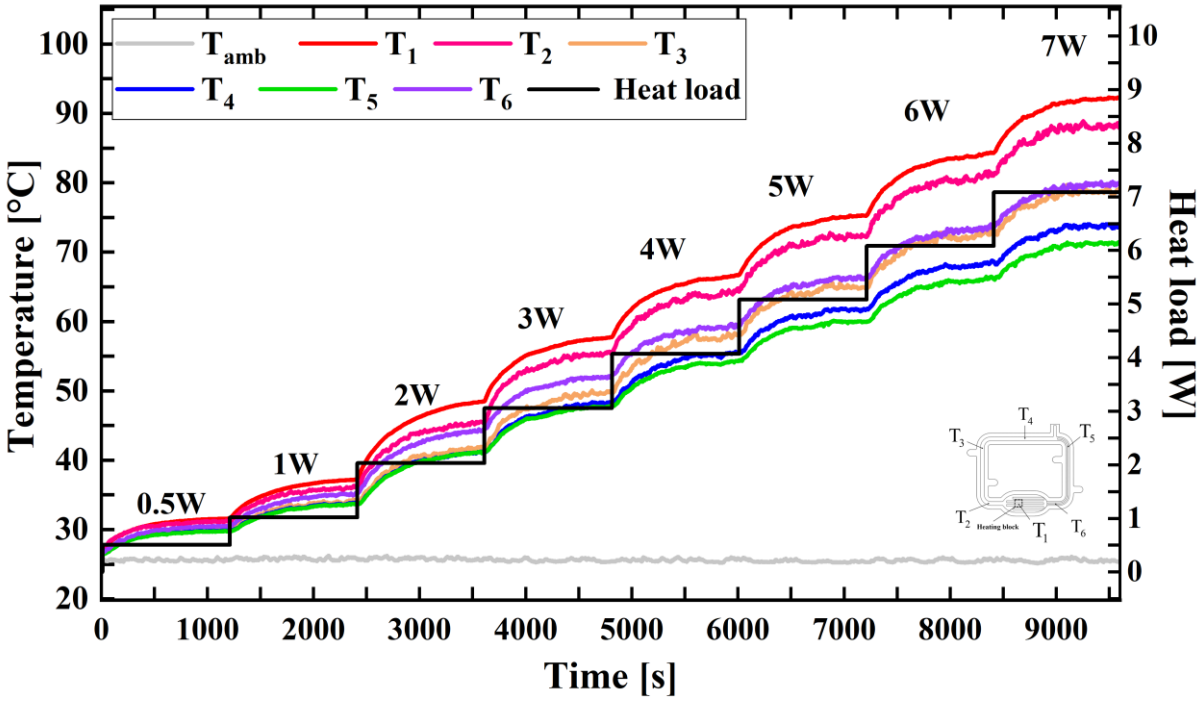

Souce: Own authorship.

APPENDIX B – Uncertainty analysis

Measurements can be classified as direct or indirect. The values in the indirect measurements are calculated from mathematical expressions, using two or more direct measurements performed in the experiment.

The uncertainties associated to the direct measurements are associated with the device imprecisions and this information is usually provided by the measurement equipment supplier. The uncertainties associated with indirect measurements are more difficult to obtain, as they derive from a combination of several measurement uncertainties.

Usually, measurement errors can be considered a random variable. To propagate these errors to an indirect measurement, two procedures can be adopted: statistical (type A) and non-statistical (type B). The statistical method consists of the estimation of the standard uncertainty associate with each one of the two or more measurement source errors, by repeating the same measuring. The most common procedure is the type B, which estimate the standard uncertainty from uncertainty information previously known. In the present work, for safety, rectangular distribution is assumed for all unknown distributions, used when there is an equal chance of any value between -a and +a to occur (ALBERTAZZI; SOUSA, 2008). In this case, the standard uncertainty can be expressed as:

$$u = \frac{a}{2\sqrt{3}} \tag{95}$$

The result of the combination of several source uncertainties is called combined uncertainty. For direct uncorrelated measurements, this parameter can be calculated as:

$$u_{co}^2 = \sum_{i=1}^{n} u_i^2 \tag{96}$$

where, u_{co} is the combined uncertainty and u_i is the standard uncertainty of the i-th source of uncertainty. If H is a continuous and derivable mathematical function, $H = f(X_1, X_2, ..., X_n)$, composed of statistically independent quantities, the combined uncertainty for indirect measurements and uncorrelated is estimate as:

$$u_{co}^2(H) = \sum_{i=1}^{n} \left[\frac{\partial f}{\partial X_i} u(X_i) \right]^2 \quad (97)$$

The combined uncertainty corresponds to the standard deviation of all source's uncertainties together. To obtain the range of values, which corroborates with a certainty probability to find the aleatory error of the measurement process, it is necessary to multiply the combined uncertainty by the respective t-student coefficient, which gives the expanded uncertainty (U):

$$U = t \cdot u_{co} \quad (98)$$

Commonly in engineering, a probability of 95.45% is adopted, providing good results. The t-student coefficient represents the chance that the aleatory error is actually within the range (combined uncertainty). In the present work, it is considered that the probability distribution of each measurement is known, which consists of infinity degrees of freedom. Therefore, for a t-student distribution with confidence interval of 95.45% and infinity degrees freedom, the t-student coefficient is t=2.

7.1.1 Temperature uncertainty

The temperature is directly measured by Type T (copper-constantan) thermocouples with 0.07 mm diameter connected to the data acquisition system. The temperature readings are processed through a computer by LabVIEW™ program. The uncertainties involved in the temperature measurement is summarized in Table 13.

Table 13 - Uncertainties of the temperature measuraments.

Source of uncertainty	Expanded uncertainty	Distribution	Standard uncertainty
Resolution	±0.10 ºC	Rectangular	±0.0577 ºC
Acquisition system	±0.77 ºC	Rectangular	±0.445 ºC
Thermocouple T	±1.00 ºC	Rectangular	±0.577 ºC
Combined standard uncertainty			±0.73 ºC
Expanded uncertainty (t=2)			±1.46 ºC

Souce: Own authorship.

7.1.2 Thermal resistance uncertainty

The thermal resistance uncertainty consists by an indirect measurement through the equations (12) and (97). Therefore, the combined standard uncertainty of this parameter is calculated as follow:

$$u_{co}(R_{lhp})^2 = 2\left[\frac{1}{q_{in}}u(T)\right]^2 + \left[\frac{1}{q_{in}^{\ 2}}u(q_{in})\Delta T\right]^2 \tag{99}$$

where q is the heat load (power input), u(T) is the standard uncertainty of temperature measurement, u(q) is the power input standard uncertainty and ΔT is the difference between the evaporator and condenser temperature.

The power input is the transfer heat rate applied in the evaporator surface (heat load) and it is defined as:

$$P = q_{in} = U \cdot I \tag{100}$$

where U is the voltage output and I is the current output of the power supply. This indirect measurement uncertainty is calculated as:

$$u_{co}(q_{in})^2 = \left(I \cdot u(U)\right)^2 + \left(U \cdot u(I)\right)^2 \tag{101}$$

The standard uncertainty of voltage and current are provided by the power supply manufacturer. The maximum uncertainties for both parameters were taken into account, applying the type B procedure and a rectangular distribution, the standard uncertainties for the voltage and current are ±0.15 V and ±0.034 A, respectively.